

22 AUG 1997

REPORT DOCUMENTATION PAGE

Form Approved
OMB No. 0704-0188

Public reporting burden for this collection of information is estimated to average 1 hour per response. Responses are used for planning purposes, statistical analysis and reporting the results of the collection. Estimated public reporting burden for this collection of information is 1 hour per response. This collection of information is being submitted to the Office of Management and Budget, Office of Information and Regulatory Affairs, 1215 Jefferson Davis Highway, Suite 1204, Arlington, VA 22202-4302, and to the Office of Management and Budget, Government Performance and Results Act Office, 1215 Jefferson Davis Highway, Suite 1204, Arlington, VA 22202-4302.

1. AGENCY USE ONLY (Leave Blank)	2. REPORT DATE	3. REPORT TYPE AND DATES COVERED
	97/7/29	Final Technical 94/2/15 - 97/2/14
4. TITLE AND SUBTITLE (U) Modelling Mixing and Reaction in Turbulent Combustion		5. FUNDING NUMBERS PE - 61102F PR - 2308 SA - 35 G - F49620-94-1-0098
6. AUTHOR(S) S.B. Pope		
7. PERFORMING ORGANIZATION NAME(S) AND ADDRESS(ES) Cornell University Ithaca, NY 14853		8. PERFORMING ORGANIZATION REPORT NUMBER AFOSR-TR 97-040
9. SPONSORING/MONITORING AGENCY NAME(S) AND ADDRESS(ES) AFOSR/NA 110 Duncan Avenue, Suite B115 Bolling AFB DC 20332-0001		10. SPONSORING/MONITORING AGENCY REPORT NUMBER
11. SUPPLEMENTARY NOTES		
12a. DISTRIBUTION/AVAILABILITY STATEMENT Approved for public release; distribution is unlimited		12b. DISTRIBUTION CODE
13. ABSTRACT (Maximum 200 words)		
<p>The overall objective of the research project was to develop, test and demonstrate a combined methodology for modelling turbulent combustion. The method was based on the solution—by a particle/Monte Carlo method—of a modelled transport equation for the joint probability density function (PDF) of velocity, turbulence frequency, and thermochemical composition. New contributions were made to several aspects of the method. An improved turbulent mixing model (EMST) was developed and demonstrated in turbulent flames. A new model for turbulence frequency, and a wavevector model that is exact for rapid distortions was developed. The PDF methodology was also extended for incorporation in large eddy simulations. Overall, the PDF method was substantially advanced and demonstrated to be an effective approach for calculating the turbulent reactive flows encountered in propulsion devices.</p>		
14. SUBJECT TERMS Turbulent combustion, turbulent mixing		15. NUMBER OF PAGES 140
		16. PRICE CODE
17. SECURITY CLASSIFICATION OF REPORT Unclassified	18. SECURITY CLASSIFICATION OF THIS PAGE Unclassified	19. SECURITY CLASSIFICATION OF ABSTRACT Unclassified
		20. LIMITATION OF ABSTRACT UL

NSN 7540-01-280-5500

Standard Form 298 (1890104 Draft
Revised 20 August 1991, GPO 27-510
7700-01

BACKGROUND

The research performed is in the context of computational modelling of turbulent combustion. In the design of combustion chambers for propulsion devices, turbulent combustion models are used in combination with CFD to predict the performance of proposed designs. Such models are required, at a minimum, to calculate the mean flow and temperature fields. It is also desirable that more details be calculated, such as NO_x and CO . Existing models are far from perfect, but they have proved their worth, in reducing design time and the cost of extensive testing.

One of the challenges in constructing models for turbulent combustion is to take due account of the so-called turbulent-combustion interactions. Prime among these is the effect of turbulent temperature and species concentration fluctuations on the chemical reaction rates. In the simplest mean-flow model, the mean reaction rate is evaluated from the mean species concentrations and the mean temperature—with no account of fluctuations. Such an approach is grossly in error (see, e.g., Pope 1990). In contrast, in PDF methods (Pope 1985)—on which this research is focused—all fluctuations are fully represented and their effects accounted for.

In PDF methods a Lagrangian viewpoint is adopted. The flow is represented by a large number N of particles (e.g., $N = 10^5$), each with its own set of properties, namely: mass, $m^{(n)}$; position $\mathbf{X}^{(n)}(t)$; velocity $\mathbf{U}^{(n)}(t)$; composition $\phi^{(n)}(t)$; and turbulence frequency $\omega^{(n)}(t)$. Because of mass conservation, the particle mass $m^{(n)}$ does not vary. The particle moves with its own velocity, $\dot{\mathbf{X}}^{(n)} = \mathbf{U}^{(n)}$. The turbulence modelling aspect of the approach consists of stochastic models for the behavior of the velocity $\mathbf{U}^{(n)}$ and turbulence frequency $\omega^{(n)}$. The composition $\phi^{(n)}(t)$ —which consists of the species mass fractions and enthalpy—evolves according to two processes: reaction (which is treated exactly), and mixing (by molecular transport processes).

As described in the following sections, the research performed is primarily directed towards improving these stochastic models.

EMST MIXING MODEL

The composition field in a turbulent reacting flow changes due to convection, reaction and molecular transport. In the PDF approach, the first two processes are treated exactly (without turbulence modeling approximations) so that the modelling of molecular transport—by a *mixing model*—is critical.

The simplest mixing model is IEM (Interaction by Exchange with the Mean) proposed by Villermaux & Devillon (1972), which is the same as the LMSE model (Linear Mean Square Estimation) of Dopazo (1976). According to these models, the particle composition $\phi^{(n)}(t)$ relaxes to the local mean $\langle \phi \rangle$ at a given turbulent rate $C_\phi \langle \omega \rangle$, i.e.,

$$\frac{d\phi^{(n)}}{dt} = -C_\phi \langle \omega \rangle (\phi^{(n)} - \langle \phi \rangle).$$

In previous AFOSR research we pin-pointed a severe weakness of all existing models including IEM (Norris & Pope 1990), which is that they are “non-local”. This means that the composition of the n th particle $\phi^{(n)}$ is affected by the compositions of other particles $\phi^{(m)}$ that have significantly different compositions. Ideally, a mixing model is “local” in composition space, so that its evolution is affected only by particles of a similar composition. It was shown by Norris & Pope (1990) that existing models’ violation of localness results in their predicting, incorrectly, “distributed” combustion in the “flamelet” regime.

19971006 150

For a single composition, the mapping closure (see e.g., Pope 1991b) provides a local model with many attractive properties. We attempted a direct extension of this closure to many compositions—as is necessary for combustion calculations—but, unfortunately, a tractable model was not obtained.

Inspired by the mapping closure ideas, we developed a local model (Subramaniam & Pope 1997) called the EMST mixing model (Euclidean Minimum Spanning Tree). The central idea is illustrated in Fig. 1. For ease of exposition we consider two compositions, so that the composition space is two-dimensional, i.e., a plane. Each point on Fig. 1 represents the composition of a particle in the two-dimensional composition space. The solid points are connected by lines, and the lines are selected so that their total length is minimized. (This is the definition of an EMST.) For each particle, the EMST identifies one or more near neighbor with which the particle interacts (i.e., mixes). Asymptotically, as the number of particles N tends to infinity, the distance between the identified neighbors tends to zero, so that the model becomes local.

The details of the EMST mixing model, and its testing in simple flows is described by Subramaniam & Pope (1997a).

To test and demonstrate the capabilities of the model, it has been applied to a piloted jet diffusion flame (Masri, Subramaniam and Pope 1996). In this test case the chemistry is fast so that the composition is everywhere close to equilibrium. Figure 2 shows scatter plots of reaction progress variable b and mixture fraction ξ according to the EMST and IEM mixing models. The correct, equilibrium, behavior corresponds to all points lying on the upper two sides of the triangle that is evident in the Figure. Clearly in the EMST model calculations, nearly all of the samples do lie on these lines: but, because of the non-local mixing it involves, the IEM model incorrectly yields a significant fraction of partially burnt fluid.

MODEL FOR TURBULENCE FREQUENCY

In the k - ε turbulence model, the dependent variables can be used to define a lengthscale $L = k^{\frac{3}{2}}/\varepsilon$, a timescale $\tau = k/\varepsilon$ and a rate (or turbulence frequency) $\langle \omega \rangle = \varepsilon/k$. In Wilcox's k - ε model (Wilcox 1993), the turbulence frequency $\langle \omega \rangle$ is represented directly. Information about $\langle \omega \rangle$ is essential for modelling mixing rates and the rates of other turbulent processes. In the PDF method employed in this research, each particle has a value of $\omega^{(n)}$ which allows the mean $\langle \omega \rangle$ to be calculated. Furthermore, the particle values represent the *distribution* of turbulent frequencies.

A stochastic model for ω was developed by Pope & Chen (1990) and used by Pope (1991a). Though physically accurate, this model proved to have several undesirable features in practice: it is computationally expensive to implement; the underlying PDF ω is lognormal, whose long tails lead to substantial statistical errors; and an ad hoc additional term is needed to effect entrainment of non-turbulent fluid.

A different, simpler, model for ω has been developed (Jayesh & Pope 1995) that has favorable properties, and has been found to be robust. The basic model consists of the stochastic differential equation

$$d\omega = -(\omega - \langle \omega \rangle) \frac{dt}{T} + \left(\frac{2\sigma^2 \langle \omega \rangle \omega}{T} \right)^{\frac{1}{2}} dW,$$

where $T^{-1} = C_3 \langle \omega \rangle$, and C_3 and σ^2 are model constants. This results in ω having an exponential autocorrelation, and a gamma-distribution PDF.

In application to inhomogeneous flows, a further important innovation is the definition of the conditional mean frequency

$$\Omega \equiv C_\Omega \langle \omega | \langle \omega \rangle \geq 0 \rangle,$$

where C_Ω is a constant. At the free-stream edge of a free shear flows, there is a turbulent/non-turbulent intermittent region, in which the intermittency factor decreases from 1 in the fully-turbulent fluid to 0 in the irrotational free stream. In these regions, the PDF of ω consists of a turbulent distribution of weight γ , and a non-turbulent delta-function distribution ($\omega = 0$) of weight $(1 - \gamma)$. The conditional mean Ω conditionally samples from the turbulent fluid, and consequently provides a turbulent frequency that is considerably larger than $\langle \omega \rangle$, and that better represents the rates of turbulent processes.

Figure 3 shows calculations using this model for a constant-density temporal shear layer. It may be seen that the profile of Ω is quite different from that of $\langle \omega \rangle$, and provides the required higher value of turbulence frequency at the edge of the flow. It has been used successfully at Allison Engine Company to make calculations of a step-swirl combustor (Anand, Hsu and Pope 1997).

WAVEVECTOR MODEL

In practical combustors, complex mean velocity fields are the norm. Examples are swirling jets and jets into a cross flow. It is well-known that models such as k - ε provide a poor representation of such flows. In Reynolds-stress and PDF methods, the modelling of the “rapid pressure” is crucial for such flows; and a limiting test of rapid-pressure models is rapid distortions.

Recently work of Reynolds & Kassinos (1995) has shown that Reynolds-stress closures are incapable of correctly accounting for rapid distortions with rotation. However, based on their suggestions, we have developed a PDF closure that is *exact for homogeneous rapid distortions*. In this closure, a unit vector—called the wavevector—is introduced. For the n th particle it is $e^{(n)}(t)$, and it evolves by

$$\frac{d}{dt} e_\ell^{(n)} = -\frac{\partial \langle U_m \rangle}{\partial x_\ell} e_m^{(n)} (\delta_{i\ell} - e_i^{(n)} e_\ell^{(n)}),$$

while the fluctuating component of velocity evolves by

$$\frac{du_j^{(n)}}{dt} = -u_k^{(n)} \frac{\partial \langle U_\ell \rangle}{\partial x_k} (\delta_{j\ell} - 2e_j^{(n)} e_\ell^{(n)}).$$

These equations determine the evolution of the Reynolds stresses exactly, for arbitrary rapid distortions of homogeneous turbulence.

The above equations apply to the rapid-distortion limit. They have been extended to be applicable to general flows through the addition of “slow pressure” terms (Van Slooten & Pope 1997). The resulting model has been tested for against the available experimental and DNS data. For example, Fig. 4 shows the predicted evolution of the Reynolds-stress anisotropies in homogeneous shear flow.

NUMERICAL ERRORS IN THE SOLUTION OF PDF EQUATIONS

In conventional numerical methods, truncation errors arise that depend on the grid spacing Δx and on the timestep Δt . In particle methods—such as that used to solve the PDF equations—additional errors arise that depend on the number of particles, N .

Focusing just on these latter errors, let Q_N denote the numerical estimate of a quantity Q based on a particle method calculation with N particles. We assume that the method is convergent so

that

$$\lim_{N \rightarrow \infty} Q_N = Q.$$

But for finite N there are two errors. First there is a deterministic error, bias, defined by

$$B_Q \equiv \langle Q_N \rangle - Q.$$

Second there is a random, statistical error, ε_Q , with zero mean and variance

$$\langle \varepsilon_Q^2 \rangle = \text{var}(Q_N).$$

Simple arguments, confirmed by numerical tests, show that these errors scale as $B_Q \sim N^{-1}$ and $\varepsilon_Q \sim N^{-\frac{1}{2}}$, so that the statistical error is dominant for large N . Nevertheless, in the particle method used to solve the PDF equations it is found that bias is larger than desirable. The reasons for this have been studied (Xu & Pope 1997), and remedies sought.

PDF METHODOLOGY IN LARGE EDDY SIMULATIONS

In large eddy simulations (LES) models are required for the subgrid scale motions. For reactive flows, the straightforward LES approach of solving equations for the filtered composition fields leads to the same formidable closure problem that is encountered in mean flow closures. However, this subgrid closure problem can be circumvented by using PDF methodology. The PI has collaborated with Professor Givi's group at SUNY Buffalo to develop and implement this methodology (Colucci et al. 1997).

The appropriate quantity to consider is the filtered density function (FDF) that was introduced by Pope (1990) and developed by Gao & O'Brien (1993). At any point and time, the FDF gives the density in composition space of fluid around the point, weighted by the filter. Just as reaction is in closed form in the PDF equations, so also reaction is in closed form in the FDF equations.

The first implementation of an LES/FDF methodology is reported by Colucci et al. (1997). For two test flows they compare results from DNS, from LES/FDF and from LES with the neglect of composition fluctuations. The results confirm that the neglect of composition fluctuations can lead to huge errors, and that the LES/PDF approach is both tractable and accurate. Further work is needed to apply the LES/FDF approach to turbulent flames so that direct comparison with experimental data can be made.

References

Anand, M. S., A. T. Hsu, and S. B. Pope (1997). Calculations of swirl combustors using joint velocity-scalar probability density function method. *AIAA J.* 35, 1143–1150.

Colucci, P. J., F. A. Jaber, P. Givi, and S. B. Pope (1997). Filtered density function for large eddy simulation of turbulent reacting flows. *Phys. Fluids*, (submitted).

Dopazo, C. (1976). A probabilistic approach to turbulent flame theory. *Acta Astronaut.* 3, 853–878.

Gao, F. and E. E. O'Brien (1993). A large-eddy simulation scheme for turbulent reacting flows. *Phys. Fluids A* 5, 1282–1284.

Jayesh and S. B. Pope (1995). Stochastic model for turbulent frequency. FDA 95-05, Cornell University.

Masri, A. R., S. Subramaniam, and S. B. Pope (1996). A mixing model to improve PDF simulation of turbulent diffusion flames. In *Twenty-Sixth Symp. (Int'l) on Combust.*, Pittsburg, pp. 49–57. Combustion Institute.

Norris, A. T. and S. B. Pope (1990). Turbulent mixing model based on ordered pairing. *Combust. Flame* 83, 27–42.

Pope, S. B. (1985). PDF methods for turbulent reactive flows. *Prog. Energy Combust. Sci.* 11, 119–192.

Pope, S. B. (1990). Computations of turbulent combustion: progress and challenges. In *Twenty-Third Symp. (Int'l) on Combust.*, Pittsburg, pp. 591–612. Combustion Institute.

Pope, S. B. (1991a). Application of the velocity-dissipation PDF model to inhomogeneous turbulent flows. *Phys. Fluids A* 3, 1947–1957.

Pope, S. B. (1991b). Mapping closures for turbulent mixing and reaction. *Theoretical and Computational Fluid Dynamics* 2, 255–270.

Pope, S. B. and Y. L. Chen (1990). The velocity-dissipation PDF model for turbulent flows. *Phys. Fluids A* 2, 1437–1449.

Reynolds, W. C. and S. C. Kassinos (1995). A one-point model for the evolution of the Reynolds stress and structure tensors in rapidly deformed homogeneous turbulence. *Proc. R. Soc. Lond. A* 451, 87–104.

Subramaniam, S. and S. B. Pope (1997). A mixing model for turbulent reactive flows based on Euclidean minimum spanning trees. *Combust. Flame*, (submitted).

Van Slooten, P. R. and S. B. Pope (1997). PDF modeling of inhomogeneous turbulence with exact representation of rapid distortions. *Phys. Fluids* 9, 1085–1105.

Villermaux, J. and J. C. Devillon (1972). In *Proceedings of the second international symposium on chemical reaction engineering*, New York. Elsevier.

Wilcox, D. C. (1993). *Turbulence modeling for CFD*. La Cañada, CA: DCW Industries.

Xu, J. and S. B. Pope (1997). Sources of bias in particle-mesh methods for PDF models for turbulent flows. FDA 97-01, Cornell University.

PERSONNEL SUPPORTED

Prof. S.B. Pope, P.I.

Dr. Jayesh, post-doc

Dr. A.R. Masri, visitor

S. Subramaniam, P.R. Van Slooten, J. Xu, X. Zheng, graduate students

PUBLICATIONS

Colucci, P. J., F. A. Jaber, P. Givi, and S. B. Pope (1997). Filtered density function for large eddy simulation of turbulent reacting flows. *Phys. Fluids*, (submitted).

Jayesh and S. B. Pope (1995). Stochastic model for turbulent frequency. FDA 95-05, Cornell University.

Masri, A. R., S. Subramaniam, and S. B. Pope (1996). A mixing model to improve PDF simulation of turbulent diffusion flames. In *Twenty-Sixth Symp. (Int'l) on Combust.*, Pittsburg, pp. 49–57. Combustion Institute.

Norris, A. T. and S. B. Pope (1995). Modeling of extinction in turbulent diffusion flames by the velocity-dissipation-composition PDF method. *Combust. Flame* 100, 211–220.

Pope, S. B. (1996). Diffusion by continuous movements: implications for turbulent mixing and the scalar flux. *J. Fluid Mech.*, (submitted).

Pope, S. B. (1997). Turbulence combustion modeling: fluctuations and chemistry. In G. D. Roy, S. M. Frolov, and P. Givi (Eds.), *Advanced computation & analysis of combustion*, pp. 310–320. Moscow: ENAS Publishers.

Subramaniam, S. and S. B. Pope (1997a). Comparison of PDF mixing models for nonpremixed turbulent reacting flows. FDA 97-03, Cornell University.

Subramaniam, S. and S. B. Pope (1997b). A mixing model for turbulent reactive flows based on Euclidean minimum spanning trees. *Combust. Flame*, (submitted).

Van Slooten, P. R. and S. B. Pope (1997). PDF modeling of inhomogeneous turbulence with exact representation of rapid distortions. *Phys. Fluids* 9, 1085–1105.

Welton, W. C. and S. B. Pope (1997). PDF model calculations of compressible turbulent flows using smoothed particle hydrodynamics. *J. Comp. Phys* 134, 150–168.

Xu, J. and S.B. Pope (1997). Sources of bias in particle-mesh methods for PDF models for turbulent flows. FDA 97-01, Cornell University.

SIGNIFICANT INTERACTIONS

Allison Engine Company

The PI has worked closely with Dr. M.S. Anand to incorporate various PDF models and numerics to produce a PDF-based combustor design code. Dr. Andrew Hsu is implementing a PDF method developed by the PI for inclusion in the National Combustor code.

General Electric

The PI has provided advice on the implementation of PDF methodology in GE's CONCERT combustor code.

General Motors

The PI provided Dr. Dan Haworth with code for tracking particles through unstructured grids. In addition, the Ph.D. student Shankar Subramaniam was a summer intern at GM in 1996.

Pratt& Whitney

Dr. Andy Brankovic, in collaboration with Dr. Andrew Norris (of the Ohio Aerospace Institute) have implemented the TGLDM method in the CORSAIR combustor code. The TGLDM (trajectory-generated low dimensional manifold) method, provides a computationally tractable way to incorporate detailed chemistry.

PRESENTATIONS

March, 1994	Argonne National Labs, DOE meeting
June, 1994	AFOSR Contractors meeting, Lake Tahoe
August, 1994	International Combustion Symposium, Irvine, CA (co-author of 3 papers and 1 poster)
October, 1994	Yale, invited seminar
February, 1995	Shell KSLA, Amsterdam, invited lecture
April, 1995	AGTSR Combustion Workshop, (Indianapolis)
May, 1995	British Gas, invited lecture
June, 1995	DOE contractors meeting, Wisconsin
June, 1995	AFOSR contractors meeting, Michigan
August, 1995	Turbulent Shear Flows Symposium, Penn State (2 contributed papers)
August, 1995	EUROMECH workshop on Turbulent Combustion (Delft), invited plenary lecture
November, 1995	Dow Chemicals, Texas, invited lecture
November, 1995	AICHE, Annual Meeting, Miami beach, invited lecture
November, 1995	APS/DFD Annual Meeting, Irvine CA, (3 contributed papers)
January, 1996	Exxon Research & Engineering, invited seminar, NJ
March, 1996	Advanced Gas Turbine System Research, Combustion Workshop, invited talk, Morgantown, VA
May, 1996	Combustion Institute, Central States Section, invited plenary lecture, Indiana
May, 1996	NASA/AFOSR Workshop on Supersonic Combustion, invited talk, VA
June, 1996	AFOSR Contractors Meeting, VA
August, 1996	Turbulent Non-premixed Flame Workshop, invited talk, Italy
August, 1996	International Combustion Symposium, 2 papers, Italy
November, 1996	Advanced Turbine Systems, invited talk, D.C.
November 1996	APS/DFD meeting, 6 talks, NY

INVENTIONS AND PATENTS

None

FIGURES

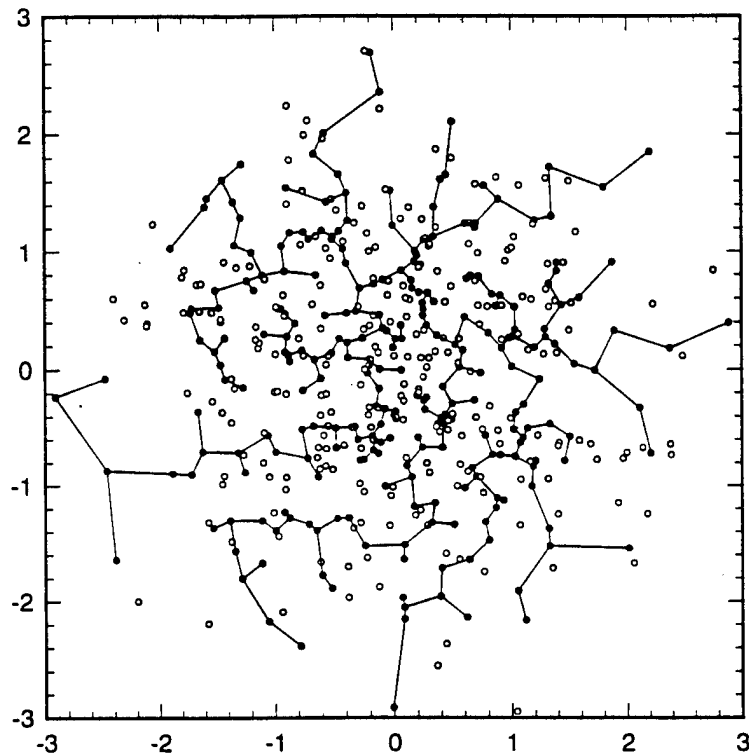


Fig. 1 Sketch of points representing particle compositions in a two-dimensional composition space. The solid points are connected by a Euclidean minimum spanning tree (EMST).

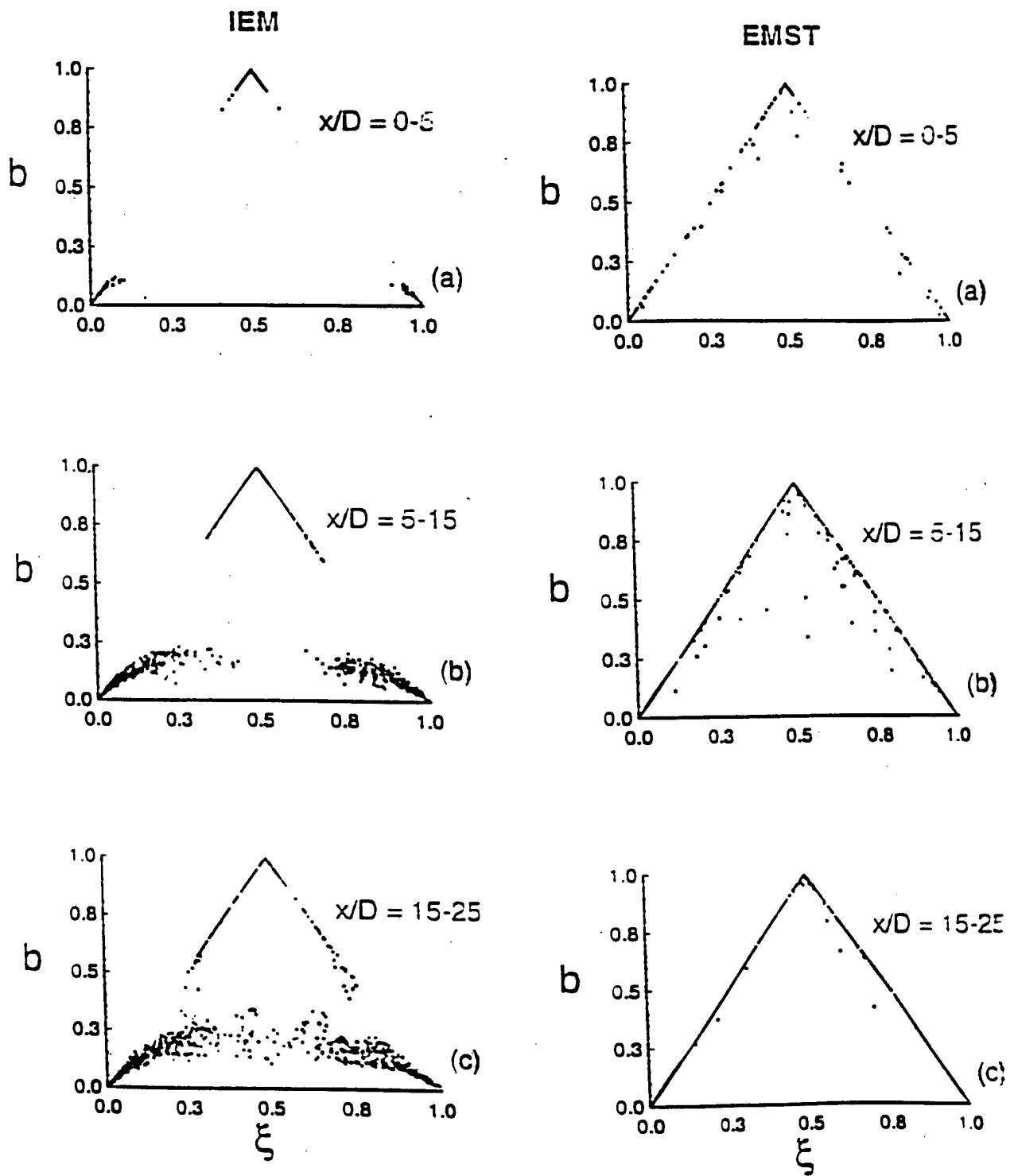


Figure 2: Scatter plots of reaction progress variable b against mixture fraction ξ in a piloted jet diffusion flame according to IEM and EMST mixing models. Each plot covers an axial range of x/D , where D is the jet diameter. The known correct result is for all points to lie on the two upper sides of the triangle. (From Masri et al. 1996.)

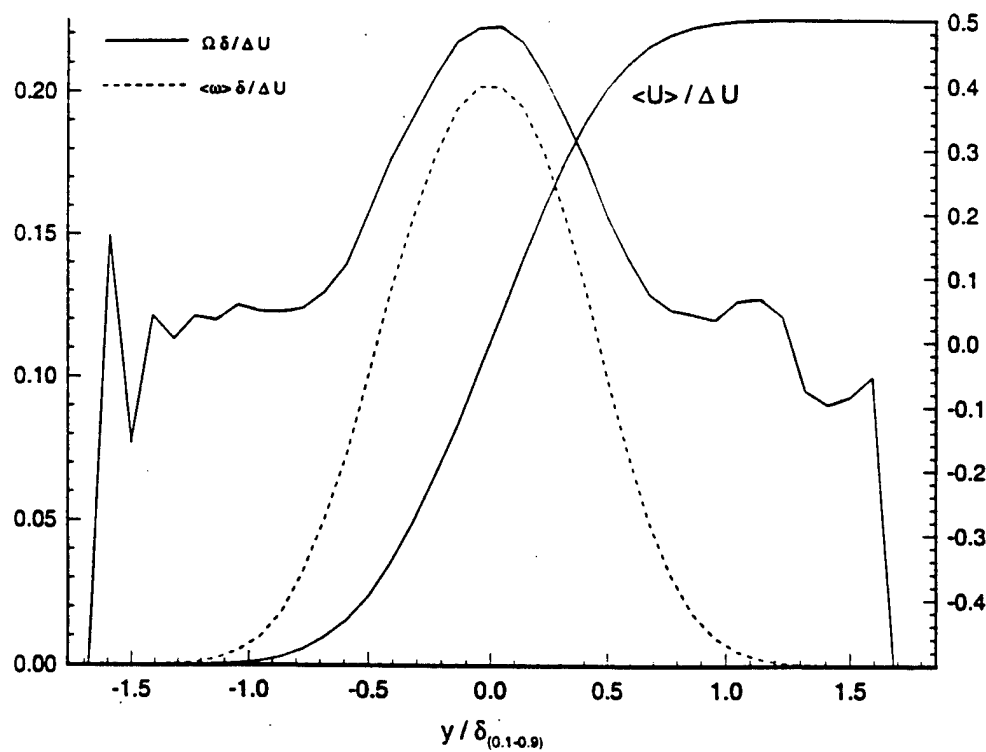


Fig. 3 : Profiles in the self-similar temporal mixing layer obtained from the $U - \omega$ joint PDF method, showing that in the intermittent region the conditional mean Ω remains appreciable, while the unconditional mean $\langle \omega \rangle$ asymptotes to zero. (As the intermittency factor tends to zero, there are large statistical errors in Ω : but there is negligible impact on the calculation in the turbulent region.)

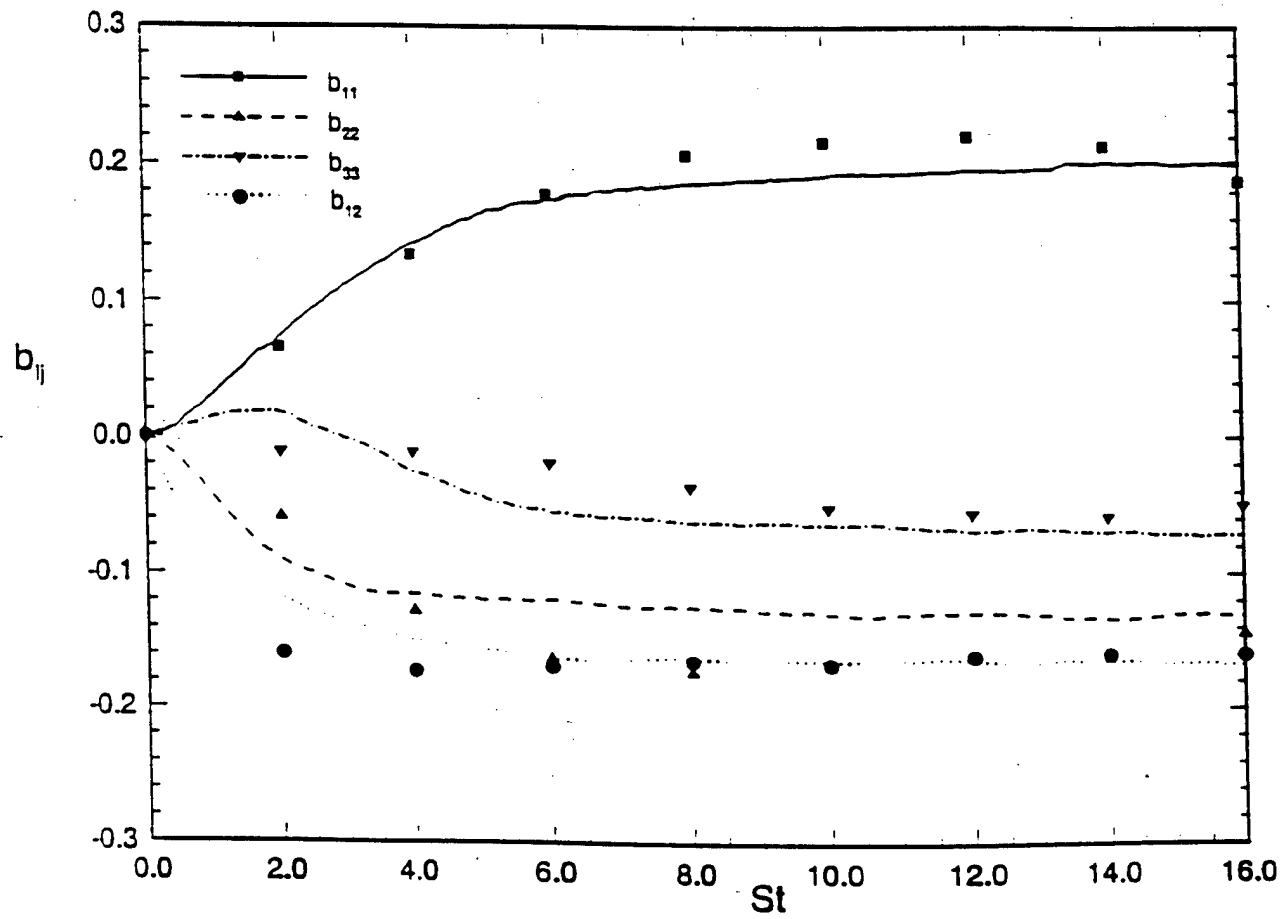


Figure 4 : Velocity-wavenumber joint PDF model applied to homogeneous shear flow. Reynolds-stress anisotropies ($b_{ij} \equiv \langle u_i u_j \rangle / \langle u_\ell u_\ell \rangle - \frac{1}{3} \delta_{ij}$) as a function of the total shear (St). Comparison with DNS (symbols) of Rogers (1986).

PHYSICS OF FLUIDS

Vol. 9, No. 4, April 1997

PDF modeling for inhomogeneous turbulence with exact representation of rapid distortions

P. R. Van Slooten and S. B. Pope

Sibley School of Mechanical and Aerospace Engineering, Cornell University, Ithaca, New York 14853

pp. 1085-1105

PDF modeling for inhomogeneous turbulence with exact representation of rapid distortions

P. R. Van Slooten and S. B. Pope

Sibley School of Mechanical and Aerospace Engineering, Cornell University, Ithaca, New York 14853

(Received 30 August 1996; accepted 5 December 1996)

A model for inhomogeneous turbulence is constructed that provides an exact representation of rapidly distorted homogeneous turbulence (RDT). The fundamental quantity modeled is the joint PDF of the velocity and wave vector which is related to the unit wavenumber vector. This joint PDF provides a model equation for the evolution of the *directional spectrum*, the integral over the wavenumber magnitude of the velocity spectrum. At this level the rapid pressure-rate-of-strain correlation is closed yielding exact equations in RDT. For decaying turbulence, the return-to-isotropy terms are modeled by stochastic diffusion equations for the velocity and wave vector. A general model of this type is constructed along with four simplified versions. The decay models are combined with the RDT model to give complete models for homogeneous turbulence, which are tested for several flows. The homogeneous models are then extended in a general manner to inhomogeneous turbulence. © 1997 American Institute of Physics. [S1070-6631(97)01404-9]

I. INTRODUCTION

A fundamental goal in turbulence modeling is the creation of robust and accurate models for the Reynolds stress equation. Although the present work is in the context of PDF methods, modeled Reynolds stress equations are still derived. The background for PDF methods is then best understood in the context of Reynolds stress models (RSM's).

For a wide range of inhomogeneous and homogeneous turbulent flows the rapid pressure-rate-of-strain correlation is a dominant term, which makes its modeling crucial to all RSM's. The standard modeling approach is based on the exact integral expressions derived by Chou¹ for the case of homogeneous turbulence. The integrals are not closed for RSM's, but are instead modeled as functions of the Reynolds stress anisotropy tensor. The slow or turbulent-turbulent interaction term requires the modeling of a second-order tensor, \mathbf{B} , while for the rapid term a model of a fourth-order tensor, \mathbf{M} , is required. Rotta² created the first model of this form by approximating the slow tensor as a linear function of the anisotropies. Other researchers have since formulated models for both tensors with varying levels of complexity. Some of the rapid models created are presented in the following references: Launder, Reece, and Rodi;³ Shih and Lumley;⁴ Haworth and Pope;⁵ Fu, Launder, and Tselepidakis;⁶ Speziale, Sarkar, and Gatski;⁷ Johansson and Hallbäck;⁸ and Ristorcelli, Lumley, and Abid;⁹ while other slow models are presented in: Lumley and Newman;¹⁰ Sarkar and Speziale;¹¹ and Chung and Kim.¹²

The general results of the rapid models have been mixed. For simple irrotational flows with small anisotropies, the latest models work very well, but for arbitrarily complex inhomogeneous flows RSM's have not performed up to expectations. This is particularly true for flows that contain rotational effects. In fact, recent analysis indicates that all RSM's are fundamentally flawed in certain rotational flows. Reynolds¹³ demonstrated that the rapid rotation of anisotropic turbulence in RSM's has no effect on the invariants of the Reynolds stress anisotropy tensor, while the exact results

from RDT (Cambon and Jacquin¹⁴ and Mansour, Shih, and Reynolds¹⁵) indicate that the invariants decay. Reynolds and Kassinos¹⁶ conclude that the Reynolds stress tensor forms an insufficient basis for modeling the rapid pressure-rate-of-strain correlation. In addition, Speziale, Abid, and Blaisdell¹⁷ have shown that RSM's behave poorly when compared to linear stability analysis for complex rotational cases such as in elliptical flows. For homogeneous turbulence, linear stability theory is equivalent to RDT, so again the Reynolds stress closures fail for rapidly distorted rotating flows.

The study of RDT has a long history dating back to the original work of Prandtl¹⁸ and Taylor.¹⁹ Batchelor and Proudman²⁰ continued this work by deriving an exact expression for the Reynolds stresses in axisymmetric contraction and plane strain. Other references of note include: Townsend;²¹ Lee and Reynolds;²² Lee;²³ Lee, Kim, and Moin,²⁴ and Hunt and Carruthers.²⁵ Although the Reynolds stress equation for RDT includes the *unclosed* rapid pressure-rate-of-strain correlation, a closed and linear representation exists in Fourier space from which the exact solutions for the Reynolds stresses are derived. RSM's are often constructed to yield the correct *initial* response when *isotropic* turbulence is subjected to a particular rapid distortion, but the results for general flows in the RDT limit are typically unsatisfactory.

As a means to introduce improved modeling of the RDT limit Reynolds and Kassinos¹⁶ and Kassinos and Reynolds²⁶ have gone beyond standard RSM approaches by including structural information of the turbulence. For RDT, they have added evolution equations for another second-order tensor, which they call the *structure dimensionality*. This allows increased functionality of the model for \mathbf{M} , but introduces new closure problems in the equation for the dimensionality tensor. Additionally, a new model formulation for RDT based on an eddy axis tensor is presented. The results for this RDT model are very good, and an extension to non-RDT flows is presented in Kassinos and Reynolds.²⁷ Improving the extended model is a topic of their current research.²⁸

The contribution of the present work is the development

of a general PDF model for inhomogeneous turbulence that maintains the exact solution for rapid distortions of homogeneous turbulence. Standard PDF methods for inert flows consist of models for the PDF of velocity (Pope²⁹ and Haworth and Pope⁵) or joint PDF of velocity and turbulent frequency (Pope and Chen³⁰ and Pope³¹), while in reacting flows composition is also included (Pope²⁹). PDF methods have several advantages over traditional moment closures (Pope^{29,32}). In particular, realizability is assured by construction so that a RSM is expressible by a PDF model only if it maintains realizability (Pope,³³ Durbin and Speziale,³⁴ and Wouters, Peeters, and Roekaerts³⁵). Also, convection and reaction are treated exactly which are very important issues for inhomogeneous turbulence and reacting flows, respectively (Pope²⁹). To achieve exact representation for rapid distortions, the standard velocity PDF models are extended by the inclusion of a stochastic vector, \mathbf{e}^* , called the wave vector. The added directional information results in a model for physical space variables that corresponds to the *directional spectrum* in Fourier (wavenumber) space. Thus, the model forms a bridge between Reynolds stress modeling and spectral modeling.

This work begins in Sec. II A with a brief introduction to the issues at the RSM level. Definitions and properties of spectral variables are presented in Sec. II B. A further introduction to the general theory of rapid distortions is presented in Sec. III A, while a wave space PDF formulation for RDT is constructed in Sec. III B. An equivalent PDF formulation for RDT in physical space is described in Sec. III C with a further examination of the correspondences between the stochastic and physical systems given in Sec. III D. The approaches utilized in Secs. III B, III C, and III D are an adaptation of the particle representation model for RDT presented by Kassinos and Reynolds²⁶ and are a Monte Carlo integration of the RDT governing equations. The new construction is designed to contain the formulation used in PDF methods which allows the extension of the method to non-RDT flows.

In Sec. IV A, the approach and motivations for the extension to general (i.e., non-RDT) homogeneous turbulence are examined. The idea is to construct a model for decaying turbulence which is then combined with the RDT model to yield a model for general homogeneous turbulence. In Sec. IV B, a general model for decaying turbulence along with four simplified models are derived and presented. The combined models are tested for several types of flows and the results discussed in Sec. IV C. The further extension of the homogeneous model to inhomogeneous turbulence is introduced in Sec. V, while a brief summary of the results and conclusions are given in Sec. VI.

II. BACKGROUND

A. Reynolds stress closures

The primary issues in turbulence modeling are addressed in homogeneous turbulent flows of Newtonian fluids with constant density, ρ , and kinematic viscosity, ν . The incompressible Navier-Stokes equations govern the evolution of the Eulerian velocity, $\mathbf{U}(\mathbf{x},t)$, which is also expressed in terms of its mean, $\langle \mathbf{U}(\mathbf{x},t) \rangle$, and fluctuation, $\mathbf{u}(\mathbf{x},t)$:

$$\mathbf{U}(\mathbf{x},t) = \langle \mathbf{U}(\mathbf{x},t) \rangle + \mathbf{u}(\mathbf{x},t). \quad (1)$$

For homogeneous turbulence the mean velocity is specified by a spatially uniform mean velocity gradient. The fluctuating velocity is described by continuity and conservation of momentum equations which are derived from the Navier-Stokes equations:

$$\frac{\partial u_i}{\partial x_i} = 0, \quad (2a)$$

and

$$\frac{\partial u_i}{\partial t} + u_l \frac{\partial u_i}{\partial x_l} + u_l \frac{\partial \langle U_i \rangle}{\partial x_l} + \langle U_l \rangle \frac{\partial u_i}{\partial x_l} = - \frac{\partial P'}{\partial x_i} + \nu \frac{\partial^2 u_i}{\partial x_l \partial x_l}. \quad (2b)$$

The Reynolds stresses, $\langle u_i u_j \rangle$, are the primary variable of interest in turbulence modeling. Their evolution is derived from Eq. (2b) with the condition of statistical homogeneity applied:

$$\frac{d \langle u_i u_j \rangle}{dt} = \mathcal{P}_{ij} + \Pi_{ij} - \varepsilon_{ij}, \quad (3a)$$

where the symbolic terms are: production, \mathcal{P}_{ij} ; pressure-rate-of-strain correlation, Π_{ij} ; and dissipation, ε_{ij} . These terms are defined by

$$\mathcal{P}_{ij} = - \langle u_i u_l \rangle \frac{\partial \langle U_j \rangle}{\partial x_l} - \langle u_l u_j \rangle \frac{\partial \langle U_i \rangle}{\partial x_l}, \quad (3b)$$

$$\Pi_{ij} = 2 \langle P' s_{ij} \rangle, \quad (3c)$$

and

$$\varepsilon_{ij} = \nu \left\langle \frac{\partial u_i}{\partial x_k} \frac{\partial u_j}{\partial x_k} \right\rangle, \quad (3d)$$

where the fluctuating pressure, P' , and the fluctuating rate-of-strain, $s_{ij} = \frac{1}{2}(\partial u_i / \partial x_j + \partial u_j / \partial x_i)$, are used.

The Reynolds stresses are split into isotropic and anisotropic parts through the use of the turbulent kinetic energy, $k = \frac{1}{2} \langle u_l u_l \rangle$, and the anisotropy of the Reynolds stresses:

$$b_{ij} = \frac{\langle u_i u_j \rangle}{2k} - \frac{1}{3} \delta_{ij}. \quad (4)$$

For incompressible, homogeneous turbulence the Reynolds stress anisotropy equation is

$$\frac{db_{ij}}{dt} = \mathcal{P}_{ij}^{(b)} + \frac{1}{2k} \Pi_{ij} - \frac{\varepsilon}{k} (e_{ij} - b_{ij}), \quad (5a)$$

where

$$\mathcal{P}_{ij}^{(b)} = \frac{1}{2k} [\mathcal{P}_{ij} - \mathcal{P}_{ll} (b_{ij} + \frac{1}{3} \delta_{ij})], \quad (5b)$$

and

$$e_{ij} = \frac{\varepsilon_{ij}}{2\varepsilon} - \frac{1}{3} \delta_{ij}. \quad (5c)$$

In terms of a RSM, the production of anisotropy, $\mathcal{P}_{ij}^{(b)}$, is in closed form, while models are required for the pressure-rate-of-strain correlation and the dissipation tensor from which both the dissipation, $\varepsilon = \frac{1}{2} \varepsilon_{ll}$, and the deviatoric dissipation, e_{ij} , are derived.

Chou¹ derived integral expressions for the pressure-rate-of-strain correlation in homogeneous turbulence from the exact solution of the Poisson equation for the fluctuating pressure:

$$\frac{\partial^2 P'}{\partial x_i \partial x_l} = -2 \underbrace{\frac{\partial \langle U_l \rangle}{\partial x_m} \frac{\partial u_m}{\partial x_l}}_{\text{rapid}} - \underbrace{\frac{\partial u_l}{\partial x_m} \frac{\partial u_m}{\partial x_l}}_{\text{slow}} \quad (6)$$

Corresponding to the two source terms, the pressure-rate-of-strain correlation is split into rapid and slow parts, $\Pi_{ij} = \Pi_{ij}^{(r)} + \Pi_{ij}^{(s)}$. The rapid correlation is expressed as a function of a fourth-order tensor, \mathbf{M} :

$$\Pi_{ij}^{(r)} = 4k \frac{\partial \langle U_l \rangle}{\partial x_k} (M_{ikjl} + M_{jkl}), \quad (7)$$

which is closed at the level of the two-point velocity correlation, $R_{ik}(\mathbf{r}) = \langle u_i(\mathbf{x}) u_k(\mathbf{x} + \mathbf{r}) \rangle$:

$$M_{ikjl} = -\frac{1}{8\pi k} \int \frac{1}{|\mathbf{r}|} \frac{\partial^2 R_{ik}(\mathbf{r})}{\partial r_j \partial r_l} d\mathbf{r}. \quad (8)$$

The slow correlation is expressed as a function of a second-order tensor, \mathbf{B} :

$$\Pi_{ij}^{(s)} = \varepsilon (B_{ij} + B_{ji}), \quad (9a)$$

which is closed at the level of the two-point triple velocity correlation, $C_{ikl}(\mathbf{r}) = \langle u_i(\mathbf{x}) u_k(\mathbf{x} + \mathbf{r}) u_l(\mathbf{x} + \mathbf{r}) \rangle$:

$$B_{ij} = -\frac{1}{4\pi\varepsilon} \int \frac{1}{|\mathbf{r}|} \frac{\partial^3 C_{ikl}(\mathbf{r})}{\partial r_j \partial r_k \partial r_l} d\mathbf{r}. \quad (9b)$$

The assumption of local isotropy at high Reynolds numbers yields an isotropic dissipation tensor. For lower Reynolds numbers, the slow pressure-rate-of-strain correlation and the deviatoric dissipation are combined to give the return-to-isotropy tensor, ϕ_{ij} :

$$\phi_{ij} = -\frac{1}{\varepsilon} \Pi_{ij}^{(s)} + 2e_{ij}. \quad (10)$$

For the stress anisotropy equation, dissipation effects from the kinetic energy equation scale in a similar manner as the return-to-isotropy tensor, and they are both labeled as *slow* terms. The resulting Reynolds stress anisotropy equation is

$$\frac{db_{ij}}{dt} = \mathcal{P}_{ij}^{(b)} + \frac{1}{2k} \Pi_{ij}^{(r)} - \frac{\varepsilon}{2k} (\phi_{ij} - 2b_{ij}), \quad (11)$$

in which there are three terms that require modeling: the rapid pressure-rate-of-strain correlation; the dissipation; and the return-to-isotropy tensor.

For a rotating reference frame, the Reynolds stress equations are altered in two ways:

- (i) the Coriolis force adds kinematic terms similar to the production;
- (ii) the rapid pressure-rate-of-strain correlation includes the frame rotation rate tensor.

The frame rotation is expressed through either the frame rotation rate tensor, $\mathbf{\Omega}^f$, or the angular velocity of the frame, $\mathbf{\bar{\Omega}}^f$, which are related via $\Omega_{ij}^f = \bar{\Omega}_m^f \epsilon_{imj}$.

B. Wavenumber space variables

In the later development of stochastic PDF models it is crucial to demonstrate the level of correspondence between the stochastic and the physical systems. This correspondence occurs in wavenumber space, and certain spectral variables are required to relate the results to the Reynolds stresses. The velocity spectrum is defined as the Fourier transform of the two-point velocity correlation:

$$\Phi_{ij}(\boldsymbol{\kappa}) = \left(\frac{1}{2\pi} \right)^3 \int R_{ij}(\mathbf{r}) e^{-i\boldsymbol{\kappa} \cdot \mathbf{r}} d\mathbf{r}. \quad (12)$$

The integral of the symmetric part of this tensor, $\Phi_{ij}^s \equiv \frac{1}{2} (\Phi_{ij} + \Phi_{ji})$, over the magnitude of the wavenumber vector, $\kappa \equiv |\boldsymbol{\kappa}|$, defines the *directional spectrum*:

$$\Gamma_{ij}(\mathbf{e}) = \int_0^\infty \kappa^2 \Phi_{ij}^s(\kappa \mathbf{e}) d\kappa, \quad (13)$$

where $\mathbf{e} \equiv \boldsymbol{\kappa}/\kappa$ is the unit wavenumber vector. The directional spectrum is symmetric by definition and real due to conjugate symmetry. Related to the directional spectrum is the *directional energy spectrum*:

$$\Gamma(\mathbf{e}) = \frac{1}{2} \Gamma_{ii}(\mathbf{e}). \quad (14)$$

The spectral variables are related to the Reynolds stresses and the turbulent kinetic energy through the inverse Fourier transform:

$$\langle u_i u_j \rangle = \int \Phi_{ij}(\boldsymbol{\kappa}) d\boldsymbol{\kappa} = \int \Gamma_{ij}(\mathbf{e}) dS(\mathbf{e}), \quad (15a)$$

and

$$k = \int \Gamma(\mathbf{e}) dS(\mathbf{e}), \quad (15b)$$

where $dS(\mathbf{e})$ is the differential element on the surface of the unit sphere. These relationships provide valuable physical interpretations of the spectral variables. The velocity spectrum is the Reynolds stress density in wavenumber space, while the directional spectrum and the directional energy spectrum are the densities on the unit sphere in wavenumber space of the Reynolds stresses and turbulent kinetic energy, respectively.

The form of the spectral variables in isotropic turbulence is a useful property. For the velocity spectrum the isotropic form is well known (Batchelor³⁶):

$$\Phi_{ij}(\boldsymbol{\kappa}) = \frac{E(\kappa)}{4\pi\kappa^2} \left(\delta_{ij} - \frac{\kappa_i \kappa_j}{\kappa^2} \right), \quad (16)$$

where $E(\kappa)$ is the energy spectrum,

$$E(\kappa) = \int \frac{1}{2} \Phi_{ii}(\kappa \mathbf{e}) \kappa^2 dS(\mathbf{e}). \quad (17)$$

The isotropic form of the directional spectrum is independent of the energy spectrum:

$$\Gamma_{ij}(\mathbf{e}) = \frac{k}{4\pi}(\delta_{ij} - e_i e_j), \quad (18)$$

while the directional energy spectrum is uniform over the unit sphere:

$$\Gamma(\mathbf{e}) = \frac{k}{4\pi}. \quad (19)$$

The spectral variables are also related to the fourth-order tensor in the rapid pressure-rate-of-strain correlation:

$$M_{ijkl} = \frac{1}{2k} \int \frac{\kappa_j \kappa_l}{\kappa^2} \Phi_{ik}(\boldsymbol{\kappa}) d\boldsymbol{\kappa} = \frac{1}{2k} \int e_j e_l \Gamma_{ik}(\mathbf{e}) dS(\mathbf{e}), \quad (20)$$

so that knowledge of either the velocity or directional spectrum is sufficient to *close* the rapid pressure-rate-of-strain correlation for *all* homogeneous turbulent flows. Therefore, modeling approaches that are based on either spectrum can provide improved results over RSM's.

III. RAPID DISTORTION THEORY

A. General theory

In turbulence modeling the quantities of interest (i.e., Reynolds stresses) are dominated by the large, energy containing scales of the flow. For these scales, RDT applies when the mean distortion imposes a time scale, $S^{-1} \equiv \|\nabla \langle \mathbf{U} \rangle\|^{-1}$, on the flow that is much smaller than that of the large scales, $\tau \equiv k/\varepsilon$. This condition is expressed through a constraint on the normalized shear- (strain- or rotation-) rate parameter:

$$\left(\frac{Sk}{\varepsilon} \right) \gg 1. \quad (21)$$

The continuity equation, Eq. (2a), is unchanged by this scaling, but the turbulent convection and the viscous terms in Eq. (2b) and the slow pressure term in Eq. (6) are negligible. The momentum and Poisson pressure equations are then linear in the fluctuating velocity:

$$\frac{\partial u_i}{\partial t} + u_i \frac{\partial \langle U_i \rangle}{\partial x_l} + \langle U_l \rangle \frac{\partial u_i}{\partial x_l} = - \frac{\partial P'}{\partial x_i}, \quad (22a)$$

and

$$\frac{\partial^2 P'}{\partial x_i \partial x_l} = -2 \frac{\partial \langle U_l \rangle}{\partial x_m} \frac{\partial u_m}{\partial x_l}. \quad (22b)$$

The Reynolds stress equation, Eq. (3a), and the anisotropy equation, Eq. (5a), are simplified by the elimination of the slow pressure-rate-of-strain correlation and the dissipation tensor:

$$\frac{d\langle u_i u_j \rangle}{dt} = \mathcal{P}_{ij} + \Pi_{ij}^{(r)}, \quad (23a)$$

and

$$\frac{db_{ij}}{dt} = \mathcal{P}_{ij}^{(b)} + \frac{1}{2k} \Pi_{ij}^{(r)}. \quad (23b)$$

For a single Fourier mode a general solution of Eq. (22) exists of the form:

$$\mathbf{u}(\mathbf{x}, t) = \hat{\mathbf{u}}(t) e^{i\hat{\boldsymbol{\kappa}}(t) \cdot \mathbf{x}}, \quad (24)$$

where $\hat{\mathbf{u}}(t)$ is the Fourier velocity mode and $\hat{\boldsymbol{\kappa}}(t)$ is a time varying wavenumber. These variables evolve via

$$\frac{d\hat{u}_i}{dt} = - \frac{\partial \langle U_m \rangle}{\partial x_n} \hat{u}_n (\delta_{im} - 2\hat{e}_i \hat{e}_m), \quad (25a)$$

$$\frac{d\hat{\kappa}_i}{dt} = - \frac{\partial \langle U_m \rangle}{\partial x_i} \hat{\kappa}_m, \quad (25b)$$

and

$$\frac{d\hat{e}_i}{dt} = - \frac{\partial \langle U_m \rangle}{\partial x_n} \hat{e}_m (\delta_{in} - \hat{e}_i \hat{e}_n), \quad (25c)$$

where the evolution of the time varying unit wavenumber vector, $\hat{\mathbf{e}}(t) \equiv \hat{\boldsymbol{\kappa}}(t)/|\hat{\boldsymbol{\kappa}}(t)|$, is also given. The solution maintains continuity through

$$\hat{\mathbf{u}}(t) \cdot \hat{\boldsymbol{\kappa}}(t) = \hat{\mathbf{u}}(t) \cdot \hat{\mathbf{e}}(t) = 0. \quad (26)$$

The time varying wavenumbers are commonly viewed as a deforming space (Rogallo³⁷), but interpreting them as a Lagrangian system of particles evolving in a fixed wave space is equivalent. This viewpoint provides a clearer picture of the modeling in this work.

The velocity spectrum is defined in a fixed wave space and is related to Fourier velocity modes in this fixed wave space. These modes, $\hat{\mathbf{a}}$, are defined in the standard manner by a Fourier series expansion of an assumed periodic velocity field with period L , which results in discrete wavenumbers, ℓ . The definitions of the two-point velocity correlation and the velocity spectrum are then used to give:

$$\Phi_{ij}(\boldsymbol{\kappa}) = \lim_{L \rightarrow \infty} \left(\frac{L}{2\pi} \right)^3 \sum \langle (\hat{\mathbf{a}}_i(\ell))^* \hat{\mathbf{a}}_j(\ell) \rangle \delta(\boldsymbol{\kappa} - \ell), \quad (27)$$

where the complex conjugate operator, $(\cdot)^*$, is used, and a delta operator is defined to give a relationship between the discrete and continuous wavenumbers:

$$\delta(\boldsymbol{\kappa} - \ell) = \begin{cases} 1 & \boldsymbol{\kappa} = \ell, \\ 0 & \text{otherwise.} \end{cases} \quad (28)$$

From Eqs. (25) and (27), the RDT equation for the velocity spectrum is derived through the use of the standard Lagrangian to Eulerian transformation (see also Townsend²¹ and Craya³⁸ for alternative derivations):

$$\begin{aligned} \frac{\partial \Phi_{ij}}{\partial t} &= \kappa_m \frac{\partial \langle U_m \rangle}{\partial x_n} \frac{\partial \Phi_{ij}}{\partial \kappa_n} - \frac{\partial \langle U_j \rangle}{\partial x_m} \Phi_{im} - \frac{\partial \langle U_i \rangle}{\partial x_m} \Phi_{mj} \\ &+ 2 \frac{\partial \langle U_n \rangle}{\partial x_m} \left[\frac{\kappa_i \kappa_n}{\kappa^2} \Phi_{mj} + \frac{\kappa_j \kappa_n}{\kappa^2} \Phi_{im} \right]. \end{aligned} \quad (29)$$

Integrating the symmetric part over the wavenumber magnitude yields the RDT equation for the directional spectrum:

$$\begin{aligned} \frac{\partial \Gamma_{ij}}{\partial t} = & e_m (\delta_{rn} - e_r e_n) \frac{\partial \langle U_m \rangle}{\partial x_r} \frac{\partial \Gamma_{ij}}{\partial e_n} - 3 e_m e_r \frac{\partial \langle U_m \rangle}{\partial x_r} \Gamma_{ij} \\ & - \frac{\partial \langle U_j \rangle}{\partial x_m} \Gamma_{im} - \frac{\partial \langle U_i \rangle}{\partial x_m} \Gamma_{jm} \\ & + 2 \frac{\partial \langle U_n \rangle}{\partial x_m} [e_i e_n \Gamma_{jm} + e_j e_n \Gamma_{im}]. \end{aligned} \quad (30)$$

Both the velocity and directional spectra evolve via *closed* equations in the RDT limit under consideration. Also, the directional spectrum is a compact description of the flow in that no further simplification from it maintains a closed governing equation for RDT.

B. PDF formulation for RDT in Fourier space

In this work, PDF methods are viewed as modeling the exact and generally unclosed one-point, one-time PDF equations that are derived from the Navier-Stokes equations. The model PDF equation is constructed so that it is equivalent to the PDF equation for a simple stochastic system which is easily simulated via Monte Carlo techniques. In this section and the two following sections the particle representation model by Kassinos and Reynolds²⁶ is adapted for PDF methods. From this new construction the method is extendible to non-RDT flows. In addition, the construction illustrates differences between these PDF methods and standard PDF methods.

From the previous section the solution for a single Fourier mode in the RDT limit consists of ordinary differential equations for $\hat{\kappa}$ and \hat{u} . The equations for RDT are closed at the directional spectrum level for which it is sufficient to consider the unit wavenumber vector, \hat{e} , in place of the full vector. For general initial velocity fields, the PDF formulation of the problem is constructed by setting the unit wavenumbers and velocity modes to be the random variables, \hat{e}^* and \hat{u}^* , respectively. These stochastic variables evolve by the deterministic RDT equations, Eq. (25). The fundamental variable is then the joint PDF of unit wavenumber and velocity mode, $\hat{f}(\eta, \mathbf{v})$, where (η, \mathbf{v}) are the state space variables for (\hat{e}^*, \hat{u}^*) . The joint PDF equation as derived via standard approaches:

$$\begin{aligned} \frac{\partial \hat{f}}{\partial t} = & \frac{\partial \langle U_r \rangle}{\partial x_s} \frac{\partial}{\partial \eta_i} \left[\eta_r \left(\delta_{is} - \frac{\eta_i \eta_s}{\eta^2} \right) \hat{f} \right] \\ & + \frac{\partial \langle U_r \rangle}{\partial x_s} \frac{\partial}{\partial v_i} \left[v_s \left(\delta_{ir} - 2 \frac{\eta_i \eta_r}{\eta^2} \right) \hat{f} \right], \end{aligned} \quad (31)$$

is an exact representation of the Navier-Stokes equations in the RDT limit. Therefore, a Monte Carlo simulation based on the stochastic variables, \hat{e}^* and \hat{u}^* , is an exact Monte Carlo integration of the RDT equations.

The PDF approach for RDT in Fourier space is completed by the specification of an initial distribution of \hat{e}^* and \hat{u}^* , while the velocity field requires the distribution of the

stochastic wavenumber vector, $\hat{\kappa}^*$. The velocity field that corresponds to N realizations of $\hat{\kappa}^*$ and \hat{u}^* is equivalent to the sum of $2N$ modes:

$$\mathbf{u}(\mathbf{x}) = \sum_{n=-N}^N \hat{u}^{(n)} e^{i\hat{\kappa}^{(n)} \cdot \mathbf{x}}, \quad (32a)$$

where conjugate symmetry is maintained by

$$\hat{u}^{(-n)} \equiv (\hat{u}^{(n)})^* \quad \text{and} \quad \hat{\kappa}^{(-n)} \equiv -\hat{\kappa}^{(n)}, \quad \text{for } n=1, N. \quad (32b)$$

In Appendix A, a method is developed for specifying the stochastic variables in a manner that results in a random homogeneous vector field with a prescribed spectrum. By comparison of Eqs. (32a) and (A11), a proper initial velocity field is generated, if

$$\hat{u}^{(n)} = \frac{1}{\sqrt{2N}} \hat{\mathbf{Z}}^{(n)}, \quad (33a)$$

and

$$\hat{\kappa}^{(n)} = \kappa^{(n)}, \quad (33b)$$

where $\hat{\mathbf{Z}}^{(n)}$ is a zero-mean random vector whose covariance matrix is determined by the spectrum, Eq. (A12), and $\kappa^{(n)}$ is a random vector with a distribution defined in Eq. (A4).

C. PDF formulation for RDT in physical space

The previous section constructed a PDF method for RDT using Fourier space variables. To extend this method for inhomogeneous turbulent flows, it is necessary to construct a method that is based on physical space variables. A stochastic system consisting of the velocity, \mathbf{u}^* , and a unit vector, \mathbf{e}^* , is written:

$$du_i^* = - \frac{\partial \langle U_r \rangle}{\partial x_s} u_s^* (\delta_{ir} - 2 e_i^* e_r^*) dt, \quad (34a)$$

and

$$de_i^* = - \frac{\partial \langle U_r \rangle}{\partial x_s} e_r^* (\delta_{is} - e_i^* e_s^*) dt. \quad (34b)$$

These equations are identical to the evolution equations for the Fourier amplitude of velocity and the unit wavenumber, Eq. (25), which is the justification for labeling \mathbf{e}^* the wave vector. Therefore, the one-point, one-time joint PDF of velocity and wave vector, $f^*(\mathbf{V}, \eta)$, corresponds identically to $\hat{f}(\mathbf{v}, \eta)$ since they evolve by the same equation:

$$\begin{aligned} \frac{\partial f^*}{\partial t} = & \frac{\partial \langle U_r \rangle}{\partial x_s} \frac{\partial}{\partial \eta_i} \left[\eta_r \left(\delta_{is} - \frac{\eta_i \eta_s}{\eta^2} \right) f^* \right] \\ & + \frac{\partial \langle U_r \rangle}{\partial x_s} \frac{\partial}{\partial V_i} \left[V_s \left(\delta_{ir} - 2 \frac{\eta_i \eta_r}{\eta^2} \right) f^* \right]. \end{aligned} \quad (35)$$

Again, the stochastic system is an exact Monte Carlo integration for RDT, and is called the **u-e** RDT Model. The evolution of the stochastic system defined here, $(\mathbf{u}^*, \mathbf{e}^*)$, is analogous to the system from Kassinos and Reynolds,²⁶ (\mathbf{v}, \mathbf{n}) , where \mathbf{v} is the velocity and \mathbf{n} is the unit gradient vector.

The specification of a stochastic velocity evolution by the velocity Fourier mode equation requires justification which is demonstrated by the correspondence between the Reynolds stresses of the stochastic and physical systems. First, correspondence is established between the spectrum variables of RDT and the stochastic model through a stochastic tensor:

$$\Lambda_{ij}^*(\boldsymbol{\eta}) \equiv \int V_i V_j f^*(\mathbf{V}, \boldsymbol{\eta}) d\mathbf{V} = \langle u_i^* u_j^* | \mathbf{e}^* = \boldsymbol{\eta} \rangle f_e^*(\boldsymbol{\eta}), \quad (36)$$

where the marginal PDF of the wave vector, $f_e^*(\boldsymbol{\eta})$, and the stochastic Reynolds stresses conditional on the wave vector (Kassinos and Reynolds²⁶) are introduced. The evolution equation for the new tensor is found by integrating the joint PDF equation:

$$\begin{aligned} \frac{\partial \Lambda_{ij}^*}{\partial t} &= \eta_m \left(\delta_{rn} - \frac{\eta_r \eta_n}{\eta_t \eta_t} \right) \frac{\partial \langle U_m \rangle}{\partial x_r} \frac{\partial \Lambda_{ij}^*}{\partial \eta_n} \\ &- 3 \frac{\eta_m \eta_r}{\eta_t \eta_t} \frac{\partial \langle U_m \rangle}{\partial x_r} \Lambda_{ij}^* - \frac{\partial \langle U_j \rangle}{\partial x_m} \Lambda_{im}^* \\ &- \frac{\partial \langle U_i \rangle}{\partial x_m} \Lambda_{jm}^* + 2 \frac{\partial \langle U_n \rangle}{\partial x_m} \left[\frac{\eta_i \eta_n}{\eta_t \eta_t} \Lambda_{jm}^* + \frac{\eta_i \eta_n}{\eta_t \eta_t} \Lambda_{im}^* \right]. \end{aligned} \quad (37)$$

By comparison with Eq. (30) the new stochastic tensor is shown to evolve in the exact manner as the directional spectrum. Thus, it is the stochastic model for the directional spectrum (Kassinos and Reynolds²⁶):

$$\Lambda_{ij}^*(\boldsymbol{\eta}) \leftrightarrow \Gamma_{ij}(\mathbf{e}). \quad (38)$$

The spectral correspondence is combined with the relationship between the Reynolds stresses and the directional spectrum, Eq. (15a), to demonstrate the correspondence between the Reynolds stresses from the physical and stochastic systems:

$$\langle u_i u_j \rangle = \int \Gamma_{ij}(\mathbf{e}) dS(\mathbf{e}) \leftrightarrow \int \Lambda_{ij}^*(\boldsymbol{\eta}) d\boldsymbol{\eta} = \langle u_i^* u_j^* \rangle. \quad (39)$$

Therefore, the equation for the Fourier mode of the velocity is an appropriate model for the stochastic velocity.

Both PDF methods based on this RDT approach and standard PDF methods provide a model for the rapid pressure term in the evolution equation for the PDF of velocity. However, standard PDF methods are constructed to correspond to the Reynolds stresses and RSM's, while the new methods correspond to the directional spectrum.

D. Correspondence to Reynolds stress and structure based models

With a PDF model based on the velocity and the wave vector, the evolution of the statistical quantities such as the Reynolds stresses are specified. The model Reynolds stress equation is derived from the stochastic evolution equation for the velocity:

$$\begin{aligned} \frac{d\langle u_i^* u_j^* \rangle}{dt} &= -\langle u_i^* u_l^* \rangle \frac{\partial \langle U_j \rangle}{\partial x_l} - \langle u_l^* u_j^* \rangle \frac{\partial \langle U_i \rangle}{\partial x_l} \\ &+ 2 \frac{\partial \langle U_n \rangle}{\partial x_m} [\langle e_i^* u_j^* e_n^* u_m^* \rangle + \langle e_j^* u_i^* e_n^* u_m^* \rangle]. \end{aligned} \quad (40)$$

From a comparison with the physical Reynolds stress equation for RDT, Eq. (23a), the production is of the same form, while \mathbf{M} is represented by a fourth-order correlation of stochastic variables (Kassinos and Reynolds²⁶):

$$\begin{aligned} 2kM_{imjn} &= \int e_j e_n \Gamma_{im}(\mathbf{e}) dS(\mathbf{e}) \\ &\leftrightarrow \int \frac{\eta_j \eta_n}{\eta_s \eta_s} \Lambda_{im}^*(\boldsymbol{\eta}) d\boldsymbol{\eta} \\ &= \langle u_i^* u_m^* e_j^* e_n^* \rangle. \end{aligned} \quad (41)$$

Reynolds¹³ and Reynolds and Kassinos¹⁶ have defined other tensors which give additional structural information about the turbulence. The structure dimensionality tensor, \mathbf{D} , provides information on directions of dimensional independence, while the structure circulicity tensor, \mathbf{F} , provides information on the structure of the large-scale vorticity field. These variables are defined through the use of a fluctuating vector stream function, $\boldsymbol{\Psi}'$:

$$u_i = \epsilon_{ijk} \frac{\partial \Psi'_k}{\partial x_j}, \quad (42)$$

where ϵ_{ijk} is the alternating tensor. The structure tensors are defined by

$$D_{ij} \equiv \left\langle \frac{\partial \Psi_l}{\partial x_i} \frac{\partial \Psi_l}{\partial x_j} \right\rangle = \int \frac{\kappa_i \kappa_j}{\kappa^2} \Phi_{mm}(\boldsymbol{\kappa}) d\boldsymbol{\kappa}, \quad (43a)$$

and

$$F_{ij} \equiv \left\langle \frac{\partial \Psi_i}{\partial x_l} \frac{\partial \Psi_j}{\partial x_l} \right\rangle = \epsilon_{ilm} \epsilon_{jnp} \int \frac{\kappa_l \kappa_n}{\kappa^2} \Phi_{mp}(\boldsymbol{\kappa}) d\boldsymbol{\kappa}, \quad (43b)$$

where the integral relationships with the velocity spectrum apply for homogeneous turbulence. From the integral relations, the structure tensors correspond to correlations of the stochastic variables (Kassinos and Reynolds²⁶):

$$D_{ij} \leftrightarrow \langle u_l^* u_l^* e_i^* e_j^* \rangle, \quad (44a)$$

and

$$F_{ij} \leftrightarrow \epsilon_{ilm} \epsilon_{jnp} \langle u_m^* u_p^* e_l^* e_n^* \rangle. \quad (44b)$$

The trace of these tensors is twice the turbulent kinetic energy as is evidenced by the stochastic model.

A geometric relation exists between the structure tensors and the Reynolds stress tensor which is shown by expressing the vector product of the alternating tensors in terms of Dirac delta functions:

$$\begin{aligned} \epsilon_{ilm} \epsilon_{jnp} &= \delta_{ij} (\delta_{ln} \delta_{mp} - \delta_{lp} \delta_{mn}) + \delta_{in} (\delta_{lp} \delta_{mj} - \delta_{lj} \delta_{mp}) \\ &+ \delta_{ip} (\delta_{lj} \delta_{mn} - \delta_{ln} \delta_{mj}). \end{aligned} \quad (45)$$

The relation which applies for homogeneous turbulence (Kassinos and Reynolds²⁶) is

$$F_{ij} + D_{ij} + \langle u_i u_j \rangle = 2k \delta_{ij}. \quad (46)$$

In summary, the inclusion of directional information from the evolution equation for the wave vector results in an exact PDF model for RDT, which is expressible as a model for the directional spectrum. With this model the rapid pressure-rate-of-strain correlation and the structure dimensionality and circulicity tensors are all exactly represented in the RDT limit.

IV. PDF MODEL FOR HOMOGENEOUS TURBULENCE

A. Motivation

RDT governs the behavior of turbulence in the limiting case of very strong mean distortions and is exactly represented by the **u-e** RDT Model. In the opposing limit, the energy containing scales of the turbulence have time to equilibrate with the slowly changing mean flows. This is again expressed as a condition on the normalized shear-(strain- or rotation-) rate parameter:

$$\left(\frac{Sk}{\varepsilon} \right) \ll 1. \quad (47)$$

The most basic flow of this type is decaying turbulence where there is no mean velocity gradient. Typical engineering flows are neither rapidly nor slowly distorted, but have turbulent time scales that are of the same order as the mean distortion time scale:

$$\left(\frac{Sk}{\varepsilon} \right) \sim 1. \quad (48)$$

In this section, **u-e** joint PDF models are first developed for decaying turbulence, which are combined with the **u-e** RDT Model to give general models for homogeneous turbulence.

The Reynolds stress anisotropy equation, Eq. (11), is simplified for decaying turbulence by the elimination of the production and rapid pressure-rate-of-strain correlation:

$$\frac{db_{ij}}{dt} = - \left(\frac{\varepsilon}{2k} \right) (\phi_{ij} - 2b_{ij}). \quad (49)$$

The dissipation and return-to-isotropy are new terms over the RDT case and both require modeling.

The behavior of \mathbf{e}^* is known for RDT, while in decaying turbulence experiments demonstrate that the return-to-isotropy tensor causes a reduction in the anisotropy of the Reynolds stresses (see Warhaft;³⁹ Choi and Lumley;⁴⁰ Chung and Kim¹²). A return to isotropy in the directional energy spectrum is a diffusion of the kinetic energy from some arbitrary distribution back to the isotropic, uniform distribution. This motivates the modeling of the stochastic variables, \mathbf{e}^* and \mathbf{u}^* , by diffusional processes. When applied to the Reynolds stress equation, the diffusion of \mathbf{e}^* alters the rapid pressure-rate-of-strain correlation and may be involved in modeling the return-to-isotropy tensor.

B. **u-e** PDF models for decaying turbulence

A general model for \mathbf{u}^* and \mathbf{e}^* in decaying turbulence is created from which four simplified models are also constructed. The general form for the two coupled vector-valued diffusion processes is expressed using two independent, isotropic Wiener processes, $d\mathbf{W}$ and $d\mathbf{W}'$, which gives a system of Ito stochastic differential equations (SDE's):

$$du_i^* = a_i(\mathbf{u}^*, \mathbf{e}^*) dt + A_{ij}(\mathbf{u}^*, \mathbf{e}^*) dW_j + B_{ij}(\mathbf{u}^*, \mathbf{e}^*) dW'_j, \quad (50a)$$

and

$$de_i^* = g_i(\mathbf{u}^*, \mathbf{e}^*) dt + G_{ij}(\mathbf{u}^*, \mathbf{e}^*) dW_j + H_{ij}(\mathbf{u}^*, \mathbf{e}^*) dW'_j, \quad (50b)$$

where one of the diffusion tensors (\mathbf{A} , \mathbf{B} , \mathbf{G} , or \mathbf{H}) may be arbitrarily set to zero.

Constraints on the general diffusion process are required to construct a model that is physically meaningful for decaying turbulence. Two constraints that apply for every realization of the stochastic system are required to maintain the analogy with the unit wavenumber and Fourier mode of velocity begun in the RDT model. These deterministic constraints are:

- (1) \mathbf{e}^* remains of unit length (by definition);
- (2) \mathbf{e}^* and \mathbf{u}^* maintain orthogonality due to the continuity equation in Fourier space.

In addition, two statistical constraints based on physical arguments for decaying turbulence are imposed as well. They are:

- (1) the PDF of velocity tends to an isotropic joint-normal distribution;
- (2) the evolution of the turbulent kinetic energy is known:

$$\frac{dk}{dt} = -\varepsilon. \quad (51)$$

With these constraints the stochastic system provides realizable models for the directional spectrum and the Reynolds stresses. Also, the form of the directional spectrum model maintains continuity.

The details of the derivation are given in Appendix B, and the resulting model is summarized here:

$$du_i^* = \left(\frac{\varepsilon}{k} \right) \left[\tilde{a}_1 \sqrt{k} e_i^* + \tilde{a}_2^{(1)} u_i^* + 2\tilde{a}_2^{(2)} \frac{k}{u_s^* u_s} u_i^* + \tilde{a}_i^a \sqrt{k} \right] dt + A_{ij} dW_j + B_{ij} dW'_j, \quad (52a)$$

and

$$de_i^* = \left(\frac{\varepsilon}{k} \right) \left[\tilde{g}_1 e_i^* + \tilde{g}_2 \frac{u_i^*}{\sqrt{k}} + (\delta_{ij} - e_i^* e_j^*) \tilde{g}_j^a \right] dt + G_{ij} dW_j + H_{ij} dW'_j, \quad (52b)$$

where the coefficients are defined in Eqs. (B13), (B14), and (B16), and one constraint remains on the anisotropic drift terms:

$$\sqrt{k}\tilde{a}_l^a e_l^* + \tilde{g}_l^a u_l^* = 0. \quad (53)$$

This model is called the General **u-e** Decay Model, and its main purpose is to serve as a guide for the construction of simplified models that are based on assumptions into the evolution of either \mathbf{u}^* or \mathbf{e}^* . The simplified models that are tested in this paper are given below.

1. Isotropic Diffusion of \mathbf{e} Model (Iso)

In this model the evolution of \mathbf{e}^* is taken to be an isotropic diffusion which is equivalent to a random walk of \mathbf{e}^* on the unit sphere. The model has two parameters, a_u and a_e , which govern the time scales of the decay for \mathbf{u}^* and \mathbf{e}^* , respectively. The stochastic equations are

$$du_i^* = -\frac{1}{2}\left(\frac{\varepsilon}{k}\right)[1 + \frac{3}{2}a_u + a_e]u_i^* dt + \frac{1}{2}(a_u\varepsilon)\frac{u_i^*}{u_s^* u_s^*} dt \\ - \left(\frac{a_e\varepsilon}{k}\right)^{1/2} e_i^* u_l^* dW_l + (a_u\varepsilon)^{1/2} [\delta_{il} - e_i^* e_l^*] dW_l', \quad (54a)$$

and

$$de_i^* = -\left(\frac{a_e\varepsilon}{k}\right)e_i^* dt + \left(\frac{a_e\varepsilon}{k}\right)^{1/2} [\delta_{il} - e_i^* e_l^*] dW_l. \quad (54b)$$

The return-to-isotropy tensor based on this model is a function of \mathbf{e}^* ,

$$\phi_{ij} = (2 + 3a_u)b_{ij} + 2a_e(b_{ij} - d_{ij}^a) \\ + a_u \left[\langle e_i^* e_j^* \rangle - \left\langle \frac{u_i^* u_j^*}{u_s^* u_s^*} \right\rangle \right], \quad (55)$$

where the anisotropy of the structure dimensionality tensor is defined as

$$d_{ij}^a \equiv \frac{D_{ij}}{2k} - \frac{1}{3}\delta_{ij}. \quad (56)$$

2. Modified Isotropic Diffusion of \mathbf{e} Model (Miso)

In an effort to improve the Isotropic Diffusion of \mathbf{e} Model, anisotropic drift terms are introduced that are proportional to the Reynolds stress anisotropy through a constant parameter, γ . The stochastic equations are

$$du_i^* = -\frac{1}{2}\left(\frac{\varepsilon}{k}\right)[1 + \frac{3}{2}a_u + a_e]u_i^* dt \\ + \left(\frac{\gamma\varepsilon}{k}\right)[b_{ij} - b_{mn}b_{mn}\delta_{ij}]u_j^* dt \\ + \frac{1}{2}(a_u\varepsilon)\frac{u_i^*}{u_s^* u_s^*} dt - \left(\frac{a_e\varepsilon}{k}\right)^{1/2} e_i^* u_l^* dW_l \\ + (a_u\varepsilon)^{1/2} [\delta_{il} - e_i^* e_l^*] dW_l', \quad (57a)$$

and

$$de_i^* = -\left(\frac{a_e\varepsilon}{k}\right)e_i^* dt - \left(\frac{\gamma\varepsilon}{k}\right)[\delta_{ij} - e_i^* e_j^*]b_{jl}e_l^* dt \\ + \left(\frac{a_e\varepsilon}{k}\right)^{1/2} [\delta_{il} - e_i^* e_l^*] dW_l. \quad (57b)$$

The return-to-isotropy tensor based on this model is again a function of \mathbf{e}^* :

$$\phi_{ij} = (2 + 3a_u)b_{ij} + 2a_e(b_{ij} - d_{ij}^a) + a_u \left[\langle e_i^* e_j^* \rangle - \left\langle \frac{u_i^* u_j^*}{u_s^* u_s^*} \right\rangle \right] \\ - 4\gamma[(\frac{1}{3} - b_{mn}b_{mn})b_{ij} + (b_{il}b_{lj} - \frac{1}{3}b_{mn}b_{mn}\delta_{ij})]. \quad (58)$$

3. Langevin Velocity Model (Lang)

In this model the equation for the velocity is specified as the Langevin equation with an anisotropic drift term that is proportional to the Reynolds stress anisotropy. For this model, the velocity evolution is independent of \mathbf{e}^* . Again, there are three parameters: a_u , a_e , and γ , which are related to the decay time scales. The stochastic equations are

$$du_i^* = -\frac{1}{2}\left(\frac{\varepsilon}{k}\right)[1 + \frac{3}{2}a_u]u_i^* dt + \left(\frac{\gamma\varepsilon}{k}\right) \\ \times [b_{ij} - b_{mn}b_{mn}\delta_{ij}]u_j^* dt + (a_u\varepsilon)^{1/2} dW_i, \quad (59a)$$

and

$$de_i^* = -\frac{1}{2}\left(\frac{\varepsilon}{k}\right)\left[a_e + a_u \frac{k}{u_s^* u_s^*}\right]e_i^* dt - \left(\frac{\gamma\varepsilon}{k}\right) \\ \times [\delta_{ij} - e_i^* e_j^*]b_{jl}e_l^* dt - (a_u\varepsilon)^{1/2} \left[\frac{u_i^* e_l^*}{u_s^* u_s^*}\right] dW_l \\ + \left(\frac{a_e\varepsilon}{k}\right)^{1/2} \left(\delta_{il} - e_i^* e_l^* - \frac{u_i^* u_l^*}{u_s^* u_s^*}\right) dW_l'. \quad (59b)$$

The return-to-isotropy model takes the standard form found in Reynolds stress closures and matches any RSM with an appropriate specification of the model parameters:

$$\phi_{ij} = (2 + 3a_u)b_{ij} \\ - 4\gamma[(\frac{1}{3} - b_{mn}b_{mn})b_{ij} + (b_{il}b_{lj} - \frac{1}{3}b_{mn}b_{mn}\delta_{ij})]. \quad (60)$$

The diffusion of \mathbf{e}^* affects only the rapid pressure-rate-of-strain correlation in non-decaying turbulence.

4. Structure Langevin Velocity Model (SLang)

In this model the basic Langevin equation is kept, but new anisotropic drift terms that are proportional to the anisotropic part of the structure dimensionality tensor are included. This model then has four parameters: a_u , a_e , γ_1 , and γ_2 ; and the stochastic equations are

$$du_i^* = -\frac{1}{2}\left(\frac{\varepsilon}{k}\right)[1 + \frac{3}{2}a_u]u_i^* dt + \left(\frac{\gamma_1\varepsilon}{k}\right)[b_{ij} - b_{mn}b_{mn}\delta_{ij}]u_j^* dt \\ + \left(\frac{\gamma_2\varepsilon}{k}\right)[d_{ij}^a - b_{mn}d_{mn}^a\delta_{ij}]u_j^* dt + (a_u\varepsilon)^{1/2} dW_i, \quad (61a)$$

and

$$\begin{aligned}
de_i^* = & -\frac{1}{2}\left(\frac{\varepsilon}{k}\right)\left[a_e + a_u \frac{k}{u_s^* u_s^*}\right]e_i^* dt - \left(\frac{\gamma_1 \varepsilon}{k}\right) \\
& \times [\delta_{ij} - e_i^* e_j^*]b_{jl}e_l^* dt - \left(\frac{\gamma_2 \varepsilon}{k}\right)[\delta_{ij} \\
& - e_i^* e_j^*]d_{jl}^a e_l^* dt - (a_u \varepsilon)^{1/2} \left[\frac{u_i^* e_l^*}{u_s^* u_s^*}\right] dW_l \\
& - \left(\frac{a_e \varepsilon}{k}\right)^{1/2} \left(\delta_{il} - e_i^* e_l^* - \frac{u_i^* u_l^*}{u_s^* u_s^*}\right) dW_l'. \quad (61b)
\end{aligned}$$

The return-to-isotropy tensor is then modeled as

$$\begin{aligned}
\phi_{ij} = & (2 + 3a_u)b_{ij} \\
& - 4\gamma_1 \left[\left(\frac{1}{3} - b_{mn}b_{mn}\right)b_{ij} + (b_{il}b_{lj} - \frac{1}{3}b_{mn}b_{mn}\delta_{ij}) \right] \\
& - 4\gamma_2 \left[\frac{1}{3}d_{ij}^a - b_{mn}d_{mn}^a(b_{ij} + \frac{1}{3}\delta_{ij}) + \frac{1}{2}(d_{il}^a b_{lj} + d_{jl}^a b_{li}) \right]. \quad (62)
\end{aligned}$$

C. Model performance

The models for homogeneous turbulence consist of one of the four simplified decay models combined with the RDT model. Additional closure information is also required, and it is provided by a simple dissipation model:

$$\frac{d\varepsilon}{dt} = \frac{\varepsilon^2}{k} \left(C_{\varepsilon 1} \frac{\mathbf{P}}{\varepsilon} - C_{\varepsilon 2} \right). \quad (63)$$

The parameters, $C_{\varepsilon 1}$ and $C_{\varepsilon 2}$, are set to 1.5625 and 1.9, respectively, which yield an asymptotic production-to-dissipation ratio that is representative of many flows:

$$(\mathbf{P}/\varepsilon)_\infty = \frac{C_{\varepsilon 2} - 1}{C_{\varepsilon 1} - 1} = 1.6. \quad (64)$$

This model does not take into account the decrease in dissipation that is known to occur in rotational flows, and the kinetic energy is expected to be underpredicted in these cases. Further information on modeling of the dissipation is contained in: Hanjalic and Launder⁴¹ and Launder, Reece, and Rodi.³

The purpose of this work is to introduce a new methodology in turbulence modeling, and not to formulate the *ideal* model of this type. For this reason, the specification of model parameters is governed by convenience rather than the desire for optimal values. The parameters are set to yield accurate asymptotic values for the Reynolds stress anisotropy invariants for homogeneous shear flows which are important in many common engineering applications. In fact, the set of model parameters given below is not unique in its level of accuracy.

Where possible the anisotropy budgets from the models and DNS data are compared. These budgets are properly scaled and have several advantages over the unscaled Reynolds stress budgets:

- the anisotropy budgets for flows with different initial shear-rate parameters are directly comparable;

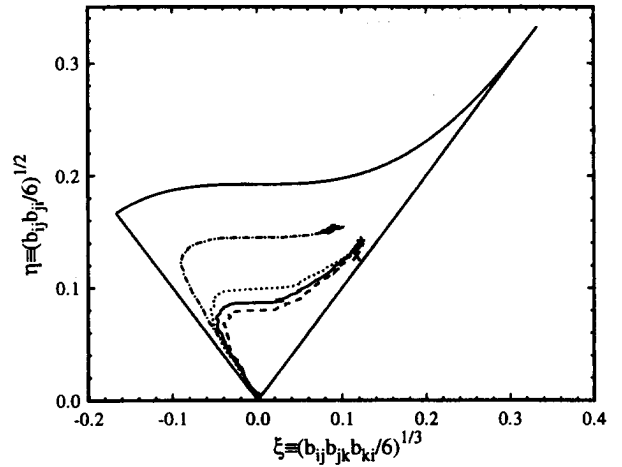


FIG. 1. Mapping of Reynolds stress anisotropy invariants in homogeneous shear with $(Sk/\varepsilon)_0 = 1.0$ for models: —, Lang; - - -, SLang; - · -, Iso; - · · -, MISO; compared to asymptotic states from experiments: \times , Tavoularis and Karnik (Ref. 43); and DNS: +, Rogers *et al.* (Ref. 42).

- the asymptotic balances between terms are more apparent in the anisotropy budgets.

The anisotropy budgets also provide more rigorous tests for turbulence models than the evolution of the anisotropy, because the models for the slow and rapid terms are examined separately.

1. Homogeneous shear

Homogeneous shear flows are defined by the mean velocity gradient:

$$\frac{\partial \langle U_i \rangle}{\partial x_j} = S \begin{bmatrix} 0 & 1 & 0 \\ 0 & 0 & 0 \\ 0 & 0 & 0 \end{bmatrix}. \quad (65)$$

In Fig. 1, the trajectories of the Reynolds stress anisotropy invariants from the four models: Lang, SLang, Iso, and MISO; are presented for homogeneous shear, and the asymptotic states are compared to the DNS data from Rogers *et al.*⁴² and the experimental data from Tavoularis and Karnik.⁴³ The model parameters are specified to yield good results for the comparison and are:

- Lang: $a_e = 0.03$, $a_u = 2.1$, $\gamma = 2.0$;
- SLang: $a_e = 0.2$, $a_u = 2.1$, $\gamma_1 = 2.4$, $\gamma_2 = 0.2$;
- Iso: $a_e = 0.3$, $a_u = 0.3$;
- MISO: $a_e = 0.65$, $a_u = 1.7$, $\gamma = 2.5$.

The asymptotic states are further examined in Table I which summarizes the experimental and DNS data as well. The Lang, SLang, and MISO models are within the experimental range given, while the Iso model does not provide the proper distribution of energy between the 22 and 33 components.

Further comparisons with the DNS data of Rogers *et al.*⁴² are made. In Fig. 2, the kinetic energy from the models is shown to grow much faster than that of the DNS. This defect is due to the dissipation modeling. The evolution of the Reynolds stress anisotropies for the Lang model are

TABLE I. Asymptotic values for homogeneous shear flows from: Tavoularis and Karnik (Ref. 43) (TK), Rogers, Moin, and Reynolds (Ref. 42) (RMR); Isotropic Diffusion of ϵ Model (Iso); Modified Isotropic Diffusion of ϵ Model (MIso); Langevin Velocity Model (Lang); Structure Langevin Velocity Model (SLang).

	TK	RMR	Iso	MIso	Lang	SLang
b_{11}^{∞}	0.18 ± 0.04	0.215	0.223	0.195	0.194	0.185
b_{12}^{∞}	-0.16 ± 0.01	-0.158	-0.156	-0.170	-0.165	-0.173
b_{22}^{∞}	-0.11 ± 0.02	-0.153	-0.203	-0.132	-0.131	-0.118
b_{33}^{∞}	-0.06 ± 0.03	-0.062	-0.020	-0.063	-0.063	-0.067
$(P/\epsilon)_{\infty}$	1.47 ± 0.14	1.80	1.6	1.6	1.6	1.6
$(Sk/\epsilon)_{\infty}$	4.60 ± 0.14	5.7	5.12	4.72	4.83	4.62

given in Fig. 3, while their complete budgets are presented in Fig. 4. The transient results for the evolution of the anisotropies are quite good, while the asymptotic values are very good. In the anisotropy budget comparisons, the results are also quite good, especially for the asymptotic balance of terms, which are not directly forced by the selection of model parameters.

2. Homogeneous shear with frame rotation

Adding frame rotation perpendicular to the plane of the shear is a common test of turbulence models. The angular velocity is:

$$\bar{\Omega}_i^f = [0, 0, \Omega^f]. \quad (66)$$

The effects of frame rotation are compared to the large-eddy simulations by Bardina, Ferziger, and Reynolds.⁴⁴ From Speziale and Mac Giolla Mhuiris,⁴⁵ the solution depends on the initial shear-rate parameter and on the rotation-to-rate-of-strain ratio, Ω^f/S . Linear stability analysis (i.e., RDT) shows that the flow is unstable with exponential growths in kinetic energy roughly in the range, $0 \leq \Omega^f/S \leq 0.5$.

The evolution of the kinetic energy for the Lang model is representative of all four models and is shown in Fig. 5. The model gives the correct qualitative behavior with all three cases being unstable and the energy in the Ω^f/S

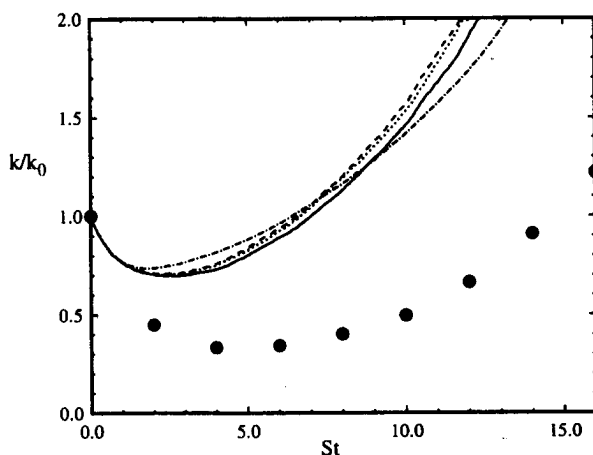


FIG. 2. Evolution of kinetic energy in homogeneous shear flow with $(Sk/\epsilon)_0 = 2.36$: ●, DNS of Rogers *et al.* (Ref. 42); —, Lang; - - -, SLang; · · ·, ISO; · · · ·, MIso.

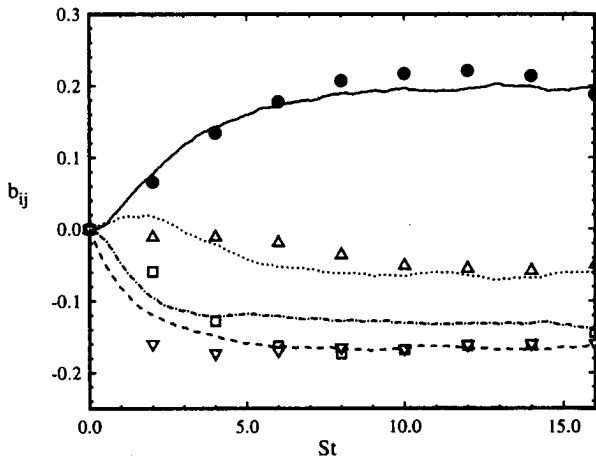


FIG. 3. Evolution of Reynolds stress anisotropy for homogeneous shear flows with $(Sk/\epsilon)_0 = 2.36$. Comparison between Langevin Velocity Model (lines) and DNS of Rogers *et al.* (Ref. 42) (symbols): (—, ●), b_{11} ; (- - -, △), b_{12} ; (· · ·, □), b_{22} ; (· · · ·, ▽), b_{33} .

=0.25 case growing the fastest. However, the quantitative comparison is poor which is a problem common with many second-order closures. This problem is largely attributable to the dissipation modeling.

3. Axisymmetric contraction and expansion

Axisymmetric flows are specified by

$$\frac{\partial \langle U_i \rangle}{\partial x_j} = S \begin{bmatrix} 1 & 0 & 0 \\ 0 & -\frac{1}{2} & 0 \\ 0 & 0 & -\frac{1}{2} \end{bmatrix}, \quad (67)$$

with $S > 0$ for contraction and $S < 0$ for expansion. From symmetry the Reynolds stress anisotropy produced by these flows remains in an axisymmetric form where the only non-zero components are related by $b_{22} = b_{33} = -\frac{1}{2}b_{11}$. In addition only one component of the fourth-order tensor, \mathbf{M} , is required to fully specify the rapid pressure-rate-of-strain correlation:

$$\Pi_{11}^{(r)} = 12kSM_{1111}. \quad (68)$$

With these simplifications axisymmetric contraction and expansion form the two most basic irrotational flows.

The results from the models are first compared to the experimental data from Tucker⁴⁶ for axisymmetric contraction. The evolution of the kinetic energy and Reynolds stress anisotropies are presented in Figs. 6 and 7. The kinetic energy from all of the models compares with the experimental data quite well, while the anisotropies from the Lang, SLang, and MIso models yield better comparisons than the ISO model.

The case of axisymmetric contraction is also examined through the use of DNS data. The evolution of the kinetic energy from all of the models and the Reynolds stress anisotropies from the Lang and ISO models for varying initial strain-rate parameters are compared to the DNS data of Lee and Reynolds²² in Figs. 8 and 9. The anisotropy budgets for

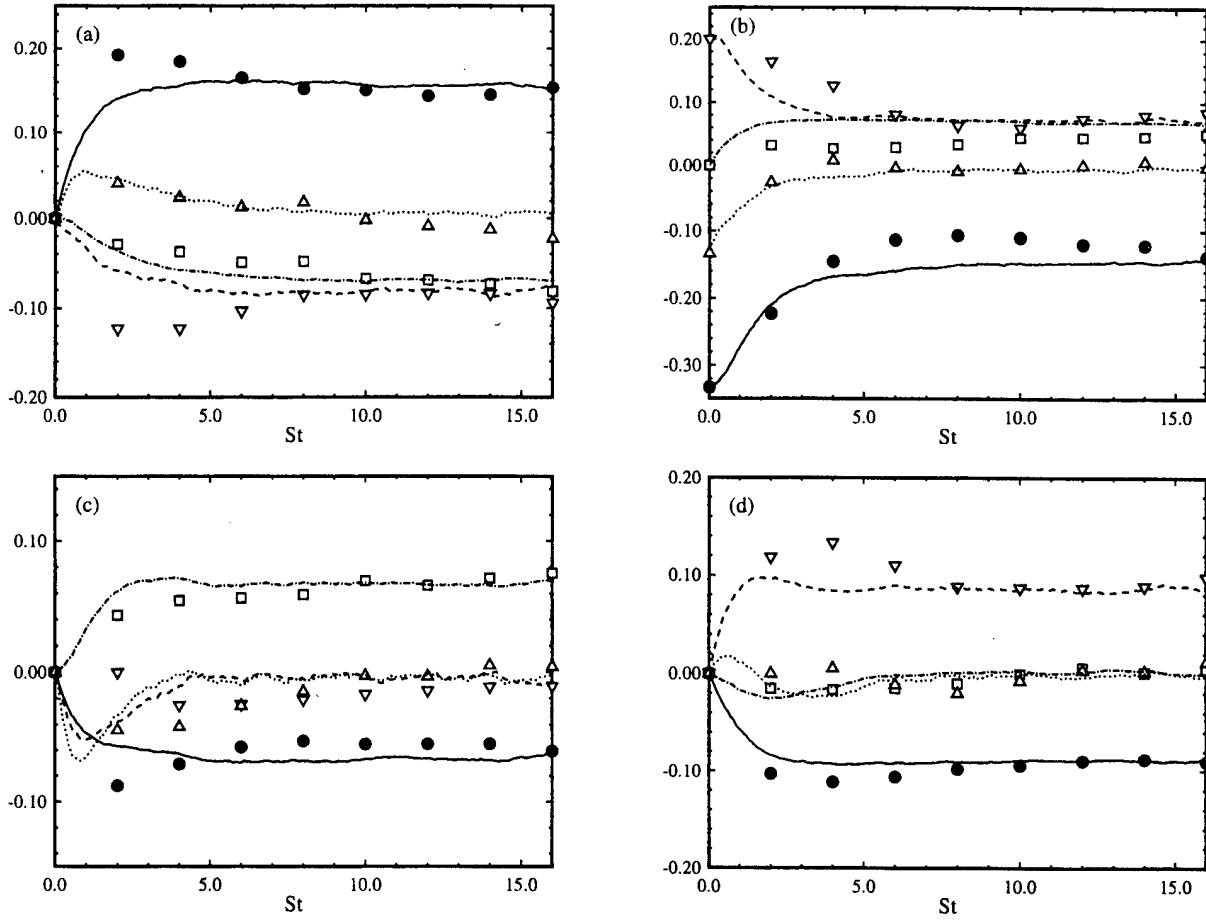


FIG. 4. Evolution of Reynolds stress anisotropy budget for homogeneous shear flows with $(Sk/\varepsilon)_0 = 2.36$. Comparison between Langevin Velocity Model (lines) and DNS of Rogers *et al.* (Ref. 42) (symbols): (—, ●), $\mathbf{P}_{ij}^{(b)}/S$; (---, ∇), $\Pi_{ij}^{(r)}/(2kS)$; (---, \square), $-(\varepsilon/Sk)^{\frac{1}{2}}(\phi_{ij} - 2b_{ij})$; (···, Δ), db_{ij}/Sdt ; for: (a) 11 component; (b) 12 component; (c) 22 component; (d) 33 component.

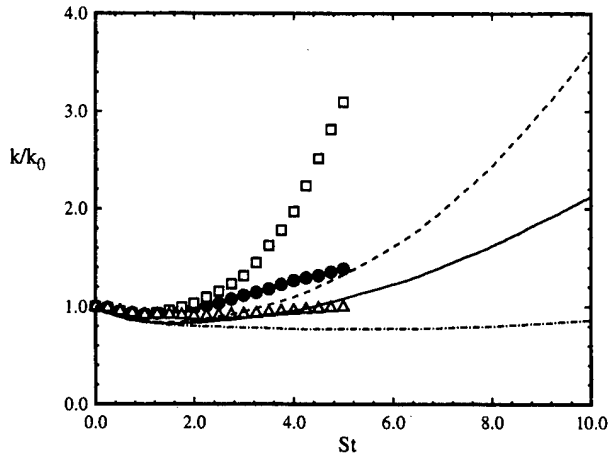


FIG. 5. Evolution of kinetic energy in homogeneous shear with a rotating frame and $(Sk/\varepsilon)_0 = 3.38$. Comparison between Langevin Velocity Model (lines) and LES of Bardina, Ferziger, and Reynolds (Ref. 44) (symbols): (—, ●), $\Omega^f/S = 0.0$; (---, \square), $\Omega^f/S = 0.25$; (---, Δ), $\Omega^f/S = 0.5$.

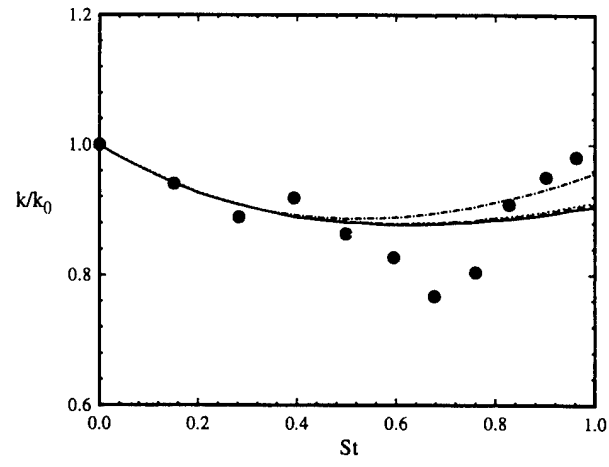


FIG. 6. Evolution of kinetic energy in axisymmetric contraction with $(Sk/\varepsilon)_0 = 2.1$. Comparison between the experimental data of Tucker (Ref. 46): (●, k/k_0), and the models: —, Lang; ---, SLang; - - -, Iso; ···, MIso.

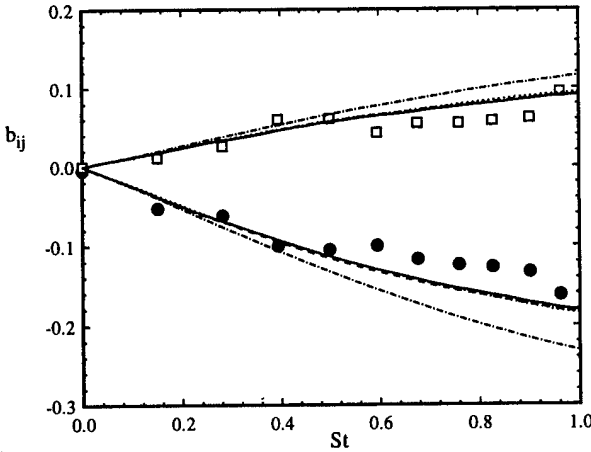


FIG. 7. Evolution of Reynolds stress anisotropy in axisymmetric contraction with $(Sk/\varepsilon)_0 = 2.1$. Comparison between experimental data of Tucker (Ref. 46): ●, b_{11} ; □, b_{22} ; and models: —, Lang; - - -, SLang; - · -, Iso; · · ·, MIso.

the Iso model and the DNS data are also presented for two strain-rates in Fig. 10. In Fig. 11, the rapid pressure-rate-of-strain correlation is examined more closely by comparisons between the Lang and Iso models and the DNS data of Lee.²³

The effects of the different decay models become negligible as the strain-rate increases toward the RDT limit. For this reason, all of the test results at the highest strain-rates compare with the DNS data very well. At the lower strain-rates the effects of the decay models become significant, and the models yield different results. Here, the Iso model provides the best comparisons with the DNS data, because the other models deviate from the RDT values of the rapid pressure-rate-of-strain correlation more rapidly than the DNS data indicate (see Fig. 11).

The comparisons between the models and the DNS data for axisymmetric expansion show some interesting effects. The evolution of the kinetic energy from all of the models

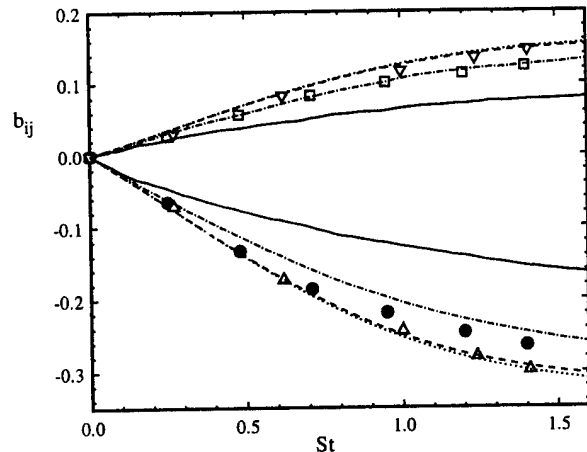


FIG. 9. Evolution of Reynolds stress anisotropies in axisymmetric contraction. Comparison between DNS of Lee and Reynolds (Ref. 22) (symbols) and models (lines) for $(Sk/\varepsilon)_0 = 0.557$; ●, b_{11} ; □, b_{22} ; —, Lang; - - -, Iso; and $(Sk/\varepsilon)_0 = 55.7$: △, b_{11} ; ▽, b_{22} ; - - -, Lang; · · ·, Iso.

and the Reynolds stress anisotropies from the Lang and Iso models for varying initial strain-rate parameters are compared to the DNS data of Lee and Reynolds²² in Figs. 12 and 13. In the energy comparison the models do very well for $St < 1.0$, but deviate even for the highest strain-rate for $St > 1.0$. This degradation of the solution is due to an instability that exists for axisymmetric expansion in RDT which was described by Kassinos and Reynolds.²⁷

The models give anisotropies that decrease as the initial strain-rate parameter decreases, while DNS shows the non-intuitive tendency to have increased anisotropies for decreased strain-rates. To understand the evolution of the anisotropies, their budgets for the Iso model and the DNS data are compared in Fig. 14. The modeled rapid pressure-rate-of-strain correlation and the closed production terms compare very well. This point is further emphasized in Fig. 15 by comparing the rapid pressure-rate-of-strain correlation from the Lang and Iso models to the DNS data of Lee.²³ Although the Iso model performs better, the Lang model is still reasonable. It is actually the slow terms that cause the difference in the anisotropy evolutions. For the DNS data these terms *increase* the anisotropy; i.e., drive the system from isotropy.

The slow terms include the return-to-isotropy tensor and the Reynolds stress anisotropy which is a scaling term due to the dissipation of the kinetic energy. In Fig. 16, the differences between the Iso model and the DNS data are apparent. Since the anisotropy is a closed term, the source of the trouble is the modeling for the return-to-isotropy tensor.

These results have significant implications for the modeling of the return-to-isotropy tensor. In Reynolds stress closures, this tensor is modeled as a function of the anisotropy. Some of the latest models (Chung and Kim¹²) include model coefficients that depend on the Reynolds number and anisotropy invariants. However, the resulting parameters are specified with comparisons to decaying turbulence and maintain slow terms that strictly reduce the anisotropy for all Reynolds numbers. The DNS results of Lee and Reynolds²² in-

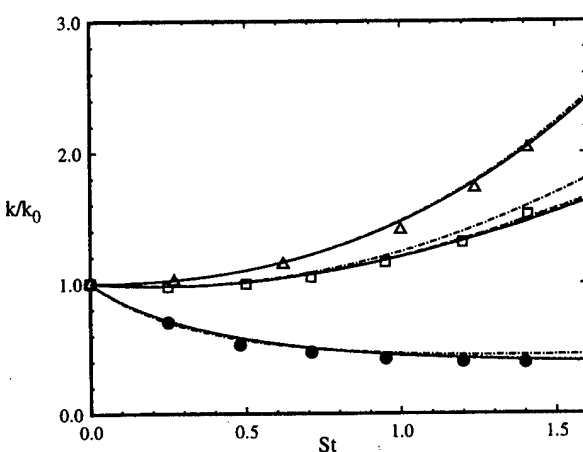


FIG. 8. Evolution of kinetic energy in axisymmetric contraction. Comparison between DNS of Lee and Reynolds (Ref. 22): ●, $(Sk/\varepsilon)_0 = 0.557$; □, $(Sk/\varepsilon)_0 = 5.7$; △, $(Sk/\varepsilon)_0 = 55.7$; and models: —, Lang; - - -, SLang; - · -, Iso; · · ·, MIso.

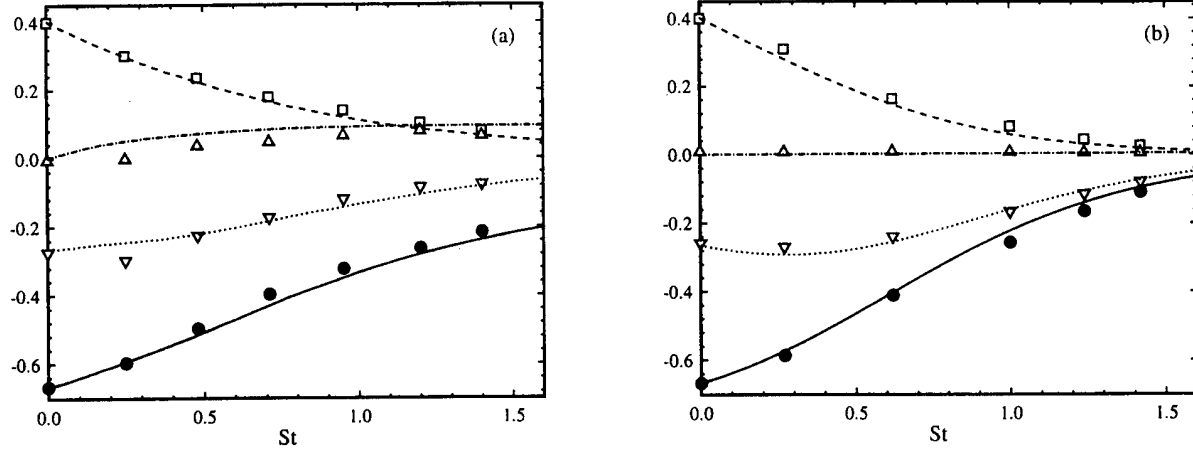


FIG. 10. Evolution of Reynolds stress anisotropy budget in axisymmetric contraction. Comparison between Isotropic Diffusion of ϵ Model (lines) and DNS of Lee and Reynolds (Ref. 22) (symbols): (—●), $\mathbf{P}_{11}^{(b)}/S$; (---□), $\Pi_{11}^{(r)}/(2kS)$; (---△), $-(\epsilon/Sk)\frac{1}{2}(\phi_{11}-2b_{11})$; (···▽), db_{11}/Sdt ; for: (a) $(Sk/\epsilon)_0=0.557$; (b) $(Sk/\epsilon)_0=55.7$.

dicate that this is not always the case for homogeneous turbulence.

4. Elliptical flows

Flows with elliptical streamlines are generated by the mean velocity gradient:

$$\frac{\partial \langle U_i \rangle}{\partial x_j} = \begin{bmatrix} 0 & S + \omega & 0 \\ S - \omega & 0 & 0 \\ 0 & 0 & 0 \end{bmatrix}, \quad (69)$$

with $|\omega| > |S|$, while $|\omega| < |S|$ generates hyperbolic streamlines. The flow is a combination of plane strain and solid body rotation and is also parameterized through the aspect ratio of the elliptical streamlines, $E \equiv \sqrt{(S + \omega)/(\omega - S)}$, and the rotation frequency, $\Omega \equiv \sqrt{(S + \omega)(\omega - S)}$ (Blaisdell and Shariff⁴⁷). Stability issues for the elliptical flows were addressed in the following references: Cambon, Teissèdre, and

Jeandel;⁴⁸ Pierrehumbert;⁴⁹ Bayly;⁵⁰ Landman and Saffman;⁵¹ and Waleffe;⁵² and the results show that the flow is unstable with exponential growths in kinetic energy for all values of $(\omega/S) = (E^2 + 1)/(E^2 - 1) > 1$. However, Speziale, Abid, and Blaisdell¹⁷ have shown that current second-order closures predict that the flows restabilize for $\omega/S \leq 2$ for any initial mean rotation-rate parameter, $(\Omega k/\epsilon)_0$.

The models were tested in a case with nearly circular streamlines, $E = 1.1$, and a high initial rotation-rate parameter, $(\Omega k/\epsilon)_0 = 270$. In this case, the rotation-to-rate-of-strain ratio is large, $(\omega/S) = 10.5$, for which all second-order closures erroneously predict decaying kinetic energy. Figure 17 does show growing kinetic energy in all four models, but the rates are far lower than the exponential growth found in the DNS data of Blaisdell and Shariff⁴⁷ for $(\Omega k/\epsilon)_0 = 4.05$ (not shown). The poor quantitative results are at least partially due to the dissipation model which ignores the known decrease in dissipation due to rotation.

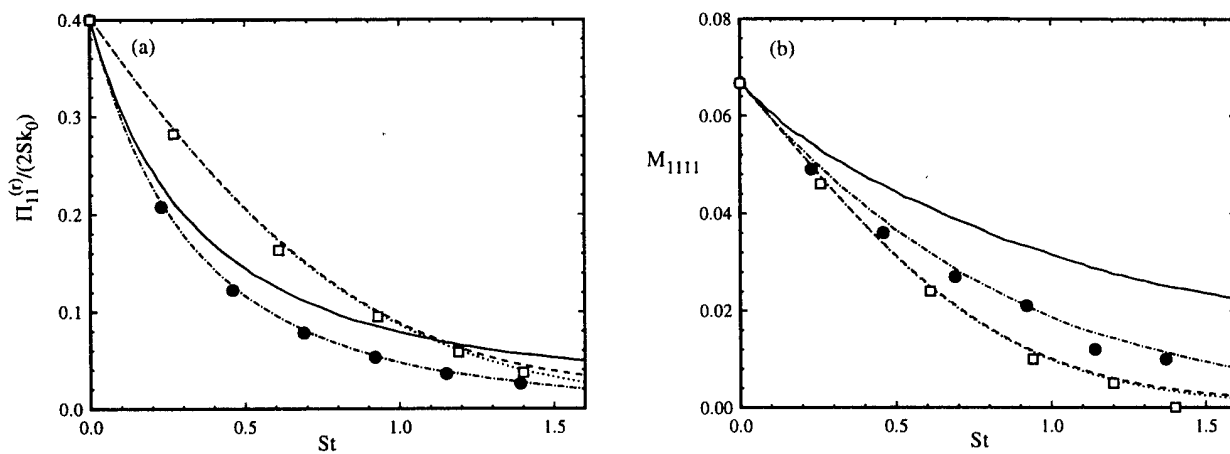


FIG. 11. Evolution of (a) normalized rapid pressure-rate-of-strain correlation; (b) Fourth-order correlation; in axisymmetric contraction. Comparison between DNS of Lee (Ref. 23) and models with $(Sk/\epsilon)_0 = 0.5$: ●, DNS; —, Lang; ---, Iso; and $(Sk/\epsilon)_0 = 50.0$ □, DNS; ---, Lang ···, Iso.

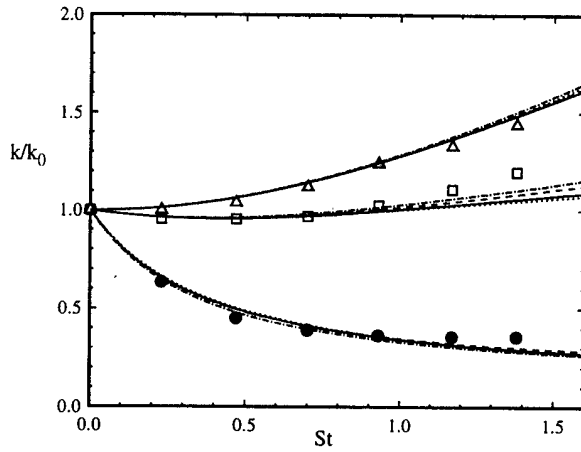


FIG. 12. Evolution of kinetic energy in axisymmetric expansion. Comparison between DNS of Lee and Reynolds (Ref. 22): ●, $(Sk/\varepsilon)_0=0.408$; □, $(Sk/\varepsilon)_0=4.08$; △, $(Sk/\varepsilon)_0=40.8$; and models: —, Lang; - - -, SLang; ---, Iso; · · ·, MIso.

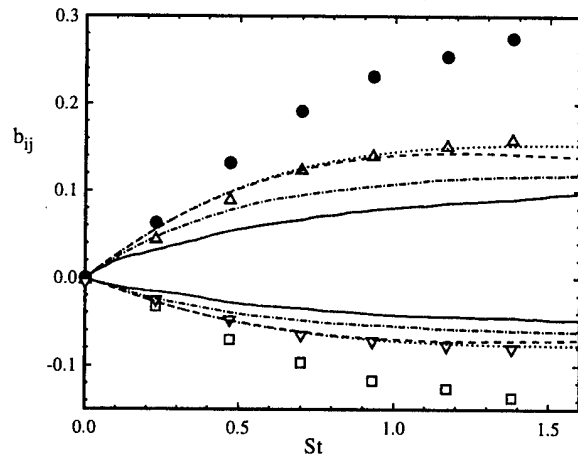


FIG. 13. Evolution of Reynolds stress anisotropies in axisymmetric expansion. Comparison between DNS of Lee and Reynolds (Ref. 22) (symbols) and models (lines) for $(Sk/\varepsilon)_0=0.408$: ●, b_{11} ; □, b_{22} ; —, Lang; - - -, Iso; and $(Sk/\varepsilon)_0=40.8$: △, b_{11} ; ▽, b_{22} ; - - -, Lang; · · ·, Iso.

5. Model comparison

In summary, the four models with their specified sets of parameters provide very good results in all test flows at the highest strain-rates where the flows are nearly in the RDT limit. At lower strain-rates, all the models provide quite good results in all of the test flows except axisymmetric expansion. It has been shown in this case that the problems are caused by poor modeling of the return-to-isotropy tensor and that RSM's which are based on decaying turbulence share these problems. Because the models directly impact the anisotropy budgets, the differences between the models are more apparent in the anisotropies than in the kinetic energies.

The Lang, Slang, and MIso models yield similar results due to the comparable parameter values for the anisotropic drift terms that are proportional to the Reynolds stress anisotropy. These models perform better in homogeneous shear

and axisymmetric contraction when compared to experimental data, while the Iso model performs better in axisymmetric expansion and contraction when compared to DNS data. The Iso model is better in these cases, because it matches the DNS data in deviating from RDT more slowly than the other three models. It is possible that the very low Reynolds numbers of the DNS is a factor in this result. Because of its inferior performance for the important case of homogeneous shear, the Iso model is not recommended for future use.

The modeled return-to-isotropy tensors are one way to differentiate between the four models. The modeled tensors from the Iso and MIso models contain expectations which do not have good physical interpretations, while the tensor from the Lang model takes the general form for RSM's if the parameters are allowed to be functions of the anisotropy invariants and Reynolds number. The Slang model includes effects of the structure dimensionality anisotropy tensor, but

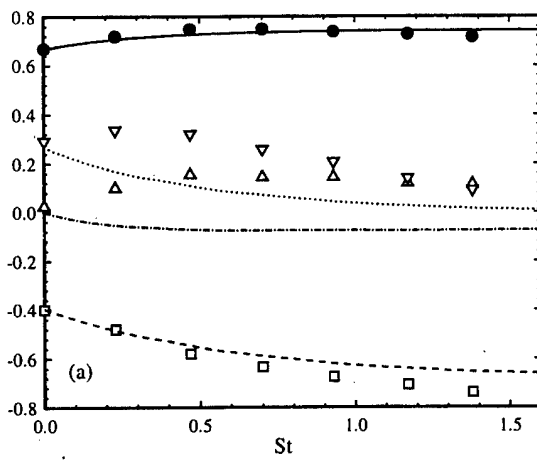


FIG. 14. Evolution of Reynolds stress anisotropy budget in axisymmetric expansion. Comparison between Isotropic Diffusion of e Model (lines) and DNS of Lee and Reynolds (Ref. 22) (symbols): (—, ●), $\mathbf{P}_{11}^{(b)}/|S|$; (---, □), $\mathbf{\Pi}_{11}^{(r)}/(2k|S|)$; (- · - ·, △), $-(\varepsilon/|S|k)^{1/2}(\phi_{11}-2b_{11})$; (···, ▽), $db_{11}/|S|dt$; for: (a) $(Sk/\varepsilon)_0=0.408$; (b) $(Sk/\varepsilon)_0=40.8$.

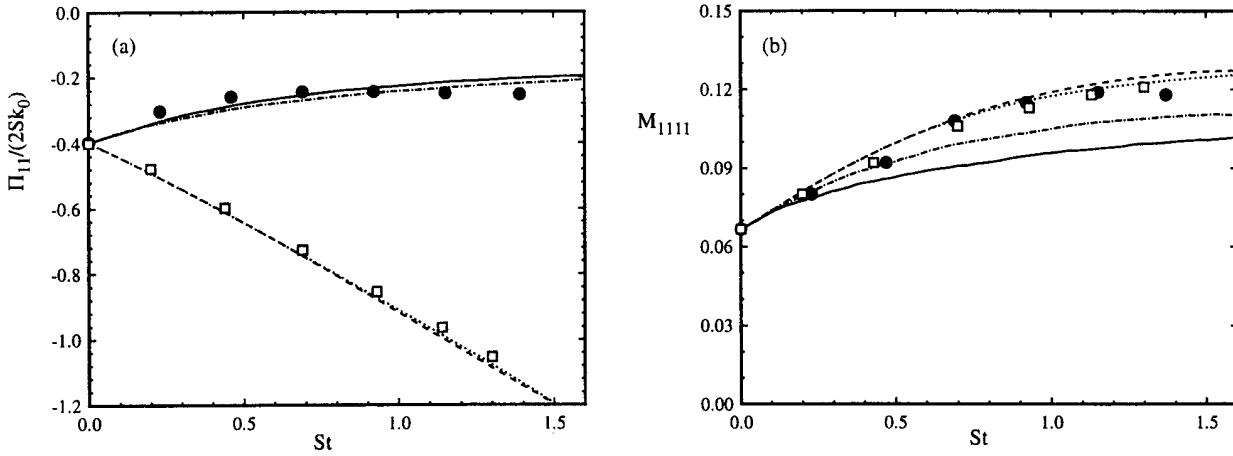


FIG. 15. Evolution of (a) normalized rapid pressure-rate-of-strain correlation; (b) Fourth-order correlation; in axisymmetric expansion. Comparison between DNS of Lee (Ref. 23) and models with $(Sk/\varepsilon)_0=0.5$: ●, DNS; —, Lang; - - -, Iso; and $(Sk/\varepsilon)_0=50.0$ □, DNS; - - -, Lang · · ·, Iso.

does not provide a general model of the form: $\phi_{ij} = \phi_{ij}(\mathbf{b}, \mathbf{d}^a)$. A general model of this form could be created and might provide improved modeling for the return-to-isotropy tensor. However, the SLang model in its current form does not significantly improve over the Lang model. For our future work in inhomogeneous turbulence, the Lang model will be used, because the evidence so far does not indicate an advantage in using the more complicated SLang or MIso models.

V. PDF MODEL FOR INHOMOGENEOUS TURBULENCE

In this section the \mathbf{u} - \mathbf{e} PDF model for rapidly distorted inhomogeneous turbulence is constructed based on the RDT model for the homogeneous case from Sec. III C. The general PDF models for non-rapid inhomogeneous turbulence are not presented but follow directly by adding a decay model from Sec. IV B.

In PDF methods of inhomogeneous turbulence it is useful to view the stochastic equations as models for Lagrangian fluid particles. In a Lagrangian system, the particle position, $\mathbf{X}^+(t, \mathbf{Y})$, evolves by the particle velocity, $\mathbf{U}^+(t, \mathbf{Y}) \equiv \mathbf{U}(\mathbf{X}^+[t, \mathbf{Y}], t)$:

$$\frac{\partial \mathbf{X}_i^+}{\partial t} = \mathbf{U}_i^+, \quad (70)$$

where \mathbf{Y} is the particle position at a reference time. Also, the local Lagrangian excess velocity is defined by

$$\begin{aligned} \mathbf{u}^+(t, \mathbf{Y}) &\equiv \mathbf{U}^+(t, \mathbf{Y}) - \langle \mathbf{U}(\mathbf{x}, t) \rangle_{\mathbf{x}=\mathbf{X}^+(t, \mathbf{Y})} \\ &= \mathbf{u}(\mathbf{X}^+[t, \mathbf{Y}], t), \end{aligned} \quad (71)$$

where $\mathbf{u}(\mathbf{x}, t)$ is the Eulerian fluctuating velocity.

From the Navier-Stokes equations expressed as

$$\frac{D \mathbf{U}_i}{D t} = - \frac{\partial \langle P \rangle}{\partial x_i} - \frac{\partial P'}{\partial x_i} + \nu \frac{\partial^2 U_i}{\partial x_l \partial x_l} \equiv - \frac{\partial \langle P \rangle}{\partial x_i} + a_i, \quad (72)$$

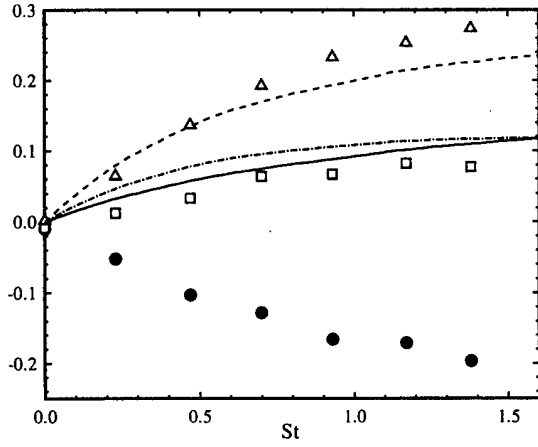


FIG. 16. Evolution of the slow terms in axisymmetric expansion. Comparison between DNS of Lee and Reynolds (Ref. 22) (symbols) and Iso model (lines) with $(Sk/\varepsilon)_0=0.408$: (—, ●), $\frac{1}{2}(\phi_{11} - 2b_{11})$; (- - -, □), $\phi_{11}/2$; (- - -, Δ), b_{11} .

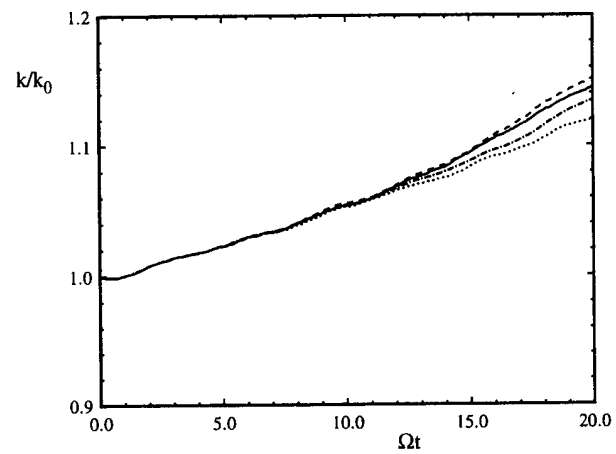


FIG. 17. Evolution of kinetic energy in an elliptical flow with $\omega/S=10.5$: —, Lang model; - - -, Slang model; - - -, Iso model; · · ·, MIso model.

the equation for the Lagrangian velocity is

$$\frac{\partial U_i^+}{\partial t} = \left\{ \frac{DU_i}{Dt} \right\}_{\mathbf{x}=\mathbf{X}^+(t, \mathbf{Y})} = \left\{ -\frac{\partial \langle P \rangle}{\partial x_i} \right\}_{\mathbf{x}=\mathbf{X}^+(t, \mathbf{Y})} + a_i(\mathbf{X}^+[t, \mathbf{Y}], t). \quad (73)$$

The effects of viscosity on the mean velocity is negligible at high Reynolds numbers which results in $\langle \mathbf{a} \rangle = 0$. The equation for the Lagrangian excess velocity is then

$$\frac{\partial u_i^+}{\partial t} = \left\{ \frac{Du_i}{Dt} \right\}_{\mathbf{x}=\mathbf{X}^+(t, \mathbf{Y})} = \left\{ \frac{\partial \langle u_i u_l \rangle}{\partial x_l} - u_l \frac{\partial \langle U_i \rangle}{\partial x_l} \right\}_{\mathbf{x}=\mathbf{X}^+(t, \mathbf{Y})} + a_i(\mathbf{X}^+[t, \mathbf{Y}], t), \quad (74)$$

where the first two terms account for the changing velocity due to the particle's movement.

The stochastic representation of $(\mathbf{X}^+, \mathbf{U}^+, \mathbf{u}^+)$ is $(\mathbf{X}^*, \mathbf{U}^*, \mathbf{u}^*)$ for which a model of \mathbf{a} is required. The evolution of the stochastic position is simply

$$dX_i^* = U_i^* dt. \quad (75)$$

The equations for \mathbf{U}^* are constructed in a manner that yields the RDT model for \mathbf{u}^* in homogeneous turbulence, Eq. (34a). The velocity model is

$$dU_i^* = -\frac{\partial \langle P \rangle}{\partial x_i} dt + 2 \frac{\partial \langle U_m \rangle}{\partial x_n} [e_i^* e_m^* u_n^* - \langle e_i^* e_m^* u_n^* \rangle] dt, \quad (76)$$

where the corresponding model of \mathbf{u}^* is

$$du_i^* = -\frac{\partial \langle U_m \rangle}{\partial x_n} u_n^* (\delta_{im} - 2 e_i^* e_m^*) dt - 2 \frac{\partial \langle U_m \rangle}{\partial x_n} \langle e_i^* e_m^* u_n^* \rangle dt + \frac{\partial \langle u_i u_j \rangle}{\partial x_j} dt. \quad (77)$$

This equation reduces to the velocity RDT equation, Eq. (34a), in homogeneous turbulence because the gradients of the Reynolds stress are zero and the triple correlation, $\langle e_i^* e_m^* u_n^* \rangle$, is also zero by symmetry in the velocity distribution. The triple correlation term was added to Eq. (76) to force the exact evolution equation for the mean Eulerian velocity, which is equivalent to forcing the mean of the modeled \mathbf{a} to be zero.

The evolution equation for the wave vector follows by maintaining a unit length and orthogonality with \mathbf{u}^* :

$$de_i^* = -\frac{\partial \langle U_m \rangle}{\partial x_n} e_m^* (\delta_{in} - e_i^* e_n^*) dt - \left[\frac{\partial \langle u_i u_j \rangle}{\partial x_j} - 2 \frac{\partial \langle U_m \rangle}{\partial x_n} \langle e_i^* e_m^* u_n^* \rangle \right] \frac{e_i^* u_i^*}{u_s^* u_s^*} dt. \quad (78)$$

The final term in this equation corresponds to the inhomogeneous terms in Eq. (77) and has the purpose of maintaining the wave vector in the plane orthogonal to the excess velocity. A direct calculation of this projection during the Monte Carlo simulation is equally valid and preferable numerically due to the high statistical error inherent in calculating the gradients of the Reynolds stresses.

VI. CONCLUSIONS

A new approach to PDF modeling of inhomogeneous turbulence has been developed that provides exact representation of rapidly distorted homogeneous turbulence. The construction is based on the particle representation model by Kassinos and Reynolds.²⁶ Their approach is adapted into a PDF formulation that begins with a model for the joint PDF of a velocity Fourier mode and unit wavenumber vector. This is an exact representation of RDT at the level of the directional spectrum. To provide an initial condition for the Monte Carlo solution of this PDF method, an algorithm is also presented that generates a stochastic system in Fourier space that corresponds to a homogeneous vector field with a prescribed spectrum.

An equivalent formulation of the RDT model using physical space variables is required for the extension of the method to the inhomogeneous case. The result is a model for the joint PDF of the velocity and wave vector, the $\mathbf{u}\cdot\mathbf{e}$ RDT Model, which is based on the integral relationship between the directional spectrum and the Reynolds stresses (Kassinos and Reynolds²⁶). A difference between PDF methods based on the $\mathbf{u}\cdot\mathbf{e}$ RDT Model and standard PDF methods is that the model for the rapid pressure term in the PDF of velocity equation corresponds to a model for the directional spectrum and not just the Reynolds stresses. Because the directional spectrum is a complete description for RDT, this limit is now treated exactly.

Models for general homogeneous turbulence are constructed by combining the $\mathbf{u}\cdot\mathbf{e}$ RDT Model with a $\mathbf{u}\cdot\mathbf{e}$ model for decaying turbulence. The decay models maintain the analogy with the directional spectrum through two deterministic constraints: \mathbf{e} is of unit length and $\mathbf{u}\cdot\mathbf{e}$ are orthogonal; and the analogy with the particle velocities through two statistical constraints: the joint PDF of \mathbf{u} tends to a joint normal distribution in isotropic turbulence and the kinetic energy evolves by the dissipation. By maintaining these analogies the PDF method can be viewed either as stochastic model for fluid particles in physical space or as a realizable spectral model at the level of the directional spectrum.

Five models for decaying turbulence are constructed: General $\mathbf{u}\cdot\mathbf{e}$ Decay Model, Isotropic Diffusion of \mathbf{e} Model (Iso), Modified Isotropic Diffusion of \mathbf{e} Model (MISO), Langevin Velocity Model (Lang), and Structure-Langevin Velocity Model (SLang). The Lang, SLang, Iso, and MISO models perform quite well in the cases of homogeneous turbulence that are tested. The Lang, SLang, and MISO models provide very similar results in all cases and are better than the Iso model in the important case of homogeneous shear. The Lang model is currently preferable, because it yields the general form for the return-to-isotropy tensor used in RSM's. A future version of the SLang model may provide better modeling of this tensor.

The extension of the homogeneous turbulence models to models for inhomogeneous turbulence is accomplished by adding a stochastic variable representing the particle location and through the use of the full particle velocity. The resulting models maintain the exact solution for RDT of homogeneous turbulence.

While testing the homogeneous models, several general

observations were made about turbulence modeling. It was argued that the anisotropy budgets are important means of comparing turbulence models to DNS data, because they are properly scaled and allow separate comparisons for the slow and rapid models. Therefore, they form a more rigorous test than the anisotropy evolutions. From the anisotropy budgets of axisymmetric expansion, it is shown that the increase in anisotropy for lower initial strain-rates is caused by the slow terms. In particular, the scaling term from the dissipation of kinetic energy is larger than the return-to-isotropy tensor. This presents a problem for all models of the return-to-isotropy tensor that are based on decaying turbulence where this effect has not been observed. Also, the need for an improved dissipation model is apparent, especially in the cases where rotational effects are important.

ACKNOWLEDGMENTS

This work was supported in part by the Department of Defense through the Air Force Graduate Fellowship Program and in part by the Air Force Office of Scientific Research, Grant F49620-94-1-0098.

APPENDIX A: SYNTHESIS OF HOMOGENEOUS RANDOM VECTOR FIELDS WITH A PRESCRIBED SPECTRUM

The purpose of this appendix is to show how to synthesize a random field as the sum of N conjugate pairs of independent modes such that its two-point correlation converges to a specified one as N tends to infinity.

Let $\mathbf{u}(\mathbf{x})$ be a real, zero-mean, statistically-homogeneous random vector field with spectrum function, $\Phi_{ij}(\boldsymbol{\kappa})$. The two-point correlation and the spectrum are related by Eq. (12) or its inverse

$$R_{ij}(\mathbf{r}) \equiv \langle u_i(\mathbf{x}) u_j(\mathbf{x} + \mathbf{r}) \rangle = \int \Phi_{ij}(\boldsymbol{\kappa}) e^{i\boldsymbol{\kappa} \cdot \mathbf{r}} d\boldsymbol{\kappa}. \quad (\text{A1})$$

From conjugate symmetry and an additional symmetry condition from homogeneity, the real and symmetric parts of the spectrum are equivalent:

$$\text{Re}\{\Phi_{ij}(\boldsymbol{\kappa})\} = \Phi_{ij}^s(\boldsymbol{\kappa}) \equiv \frac{1}{2}[\Phi_{ij}(\boldsymbol{\kappa}) + \Phi_{ji}(\boldsymbol{\kappa})], \quad (\text{A2a})$$

while the imaginary and anti-symmetric part are related by

$$\iota \text{Im}\{\Phi_{ij}(\boldsymbol{\kappa})\} = \Phi_{ij}^a(\boldsymbol{\kappa}) \equiv \frac{1}{2}[\Phi_{ij}(\boldsymbol{\kappa}) - \Phi_{ji}(\boldsymbol{\kappa})]. \quad (\text{A2b})$$

The terms in Eq. (A2a) are called the co-spectrum, while the terms in Eq. (A2b) are called the quadrature spectrum. These relations show that the spectrum tensor forms a Hermitian matrix. Further, because the spectrum is a representation of the energy at a particular location in Fourier space, the matrix is also positive semi-definite (Batchelor³⁶).

The energy of the random vector field is defined via

$$k \equiv \int \frac{1}{2} \Phi_{ll}(\boldsymbol{\kappa}) d\boldsymbol{\kappa}, \quad (\text{A3})$$

with which a normalized spectrum is defined by

$$f(\boldsymbol{\kappa}) \equiv \frac{1}{2} \Phi_{ll}(\boldsymbol{\kappa}) / k. \quad (\text{A4})$$

The normalized spectrum is non-negative and integrates to unity; i.e., it has the properties of a joint PDF. Another normalized spectrum is also defined by

$$\Psi_{ij}(\boldsymbol{\kappa}) \equiv \Phi_{ij}(\boldsymbol{\kappa}) / \Phi_{ll}(\boldsymbol{\kappa}). \quad (\text{A5})$$

In terms of these the normalized spectra, Eq. (A1) is re-written:

$$R_{ij}(\mathbf{r}) = 2k \int \Psi_{ij}(\boldsymbol{\kappa}) e^{i\boldsymbol{\kappa} \cdot \mathbf{r}} f(\boldsymbol{\kappa}) d\boldsymbol{\kappa}. \quad (\text{A6})$$

If $\boldsymbol{\kappa}^*$ is defined to be a random vector with a joint PDF of $f(\boldsymbol{\kappa})$, then the integral in Eq. (A6) is equivalent to an expectation:

$$R_{ij}(\mathbf{r}) = 2k \langle \Psi_{ij}(\boldsymbol{\kappa}^*) e^{i\boldsymbol{\kappa}^* \cdot \mathbf{r}} \rangle. \quad (\text{A7})$$

The synthetic field, $\tilde{\mathbf{u}}(\mathbf{x})$, is defined for a given N by

$$\tilde{\mathbf{u}}(\mathbf{x}) \equiv \frac{1}{\sqrt{2N}} \sum_{n=-N}^N \mathbf{Z}^{(n)} e^{i\boldsymbol{\kappa}^{(n)} \cdot \mathbf{x}}, \quad (\text{A8})$$

where $\boldsymbol{\kappa}^{(n)}$ are independent and identically distributed wave-number vectors with distribution $f(\boldsymbol{\kappa})$ and $\mathbf{Z}^{(n)}$ are identically distributed zero-mean random vectors, dependent on $\boldsymbol{\kappa}^{(n)}$, whose covariance matrix is deduced below, Eq. (A12). In addition, conjugate symmetry is guaranteed by using conjugate pairs:

$$\mathbf{Z}^{(-n)} \equiv (\mathbf{Z}^{(n)})^* \quad \text{and} \quad \boldsymbol{\kappa}^{(-n)} \equiv -\boldsymbol{\kappa}^{(n)}, \quad \text{for } n = 1, N. \quad (\text{A9})$$

The complex conjugate of Eq. (A8) provides an alternate definition of the field:

$$\tilde{\mathbf{u}}(\mathbf{x}) \equiv \frac{1}{\sqrt{2N}} \sum_{n=-N}^N (\mathbf{Z}^{(n)})^* e^{-i\boldsymbol{\kappa}^{(n)} \cdot \mathbf{x}}. \quad (\text{A10})$$

From Eqs. (A8) and (A10), the two-point correlation of the synthetic field is

$$\begin{aligned} \tilde{R}_{ij}(\mathbf{r}) &\equiv \langle \tilde{u}_i(\mathbf{x}) \tilde{u}_j(\mathbf{x} + \mathbf{r}) \rangle \\ &= \frac{1}{2N} \sum_{n=-N}^N \langle (\mathbf{Z}_i^{(n)})^* \mathbf{Z}_j^{(n)} e^{i\boldsymbol{\kappa}^{(n)} \cdot \mathbf{r}} \rangle. \end{aligned} \quad (\text{A11})$$

By comparing Eqs. (A7) and (A11), we observe that $\tilde{R}_{ij}(\mathbf{r}, t)$ equals $R_{ij}(\mathbf{r}, t)$ (for all $N \geq 1$) provided $\mathbf{Z}^{(n)}$ satisfies

$$\langle (\mathbf{Z}_i^{(n)})^* \mathbf{Z}_j^{(n)} | \boldsymbol{\kappa}^{(n)} = \boldsymbol{\kappa} \rangle = 2k \Psi_{ij}(\boldsymbol{\kappa}). \quad (\text{A12})$$

The complex random vectors, $\mathbf{Z}^{(n)}$, must have a covariance matrix given by Eq. (A12), but their distribution is not determined. It is convenient to specify $\mathbf{Z}^{(n)}$ as Gaussian random vectors, because the distribution is then determined from the covariance matrix. In practice, $\mathbf{Z}^{(n)}$ can be constructed from real, standard, isotropic Gaussian random vectors, $\boldsymbol{\xi}^{(n)}$, by

$$\mathbf{Z}^{(n)} = (\mathbf{L})^* \boldsymbol{\xi}^{(n)}, \quad (\text{A13})$$

where \mathbf{L} is a complex triangular matrix with a real diagonal that is uniquely defined by

$$\langle (\mathbf{Z}^{(n)})^* \mathbf{Z}^{(n)T} | \boldsymbol{\kappa}^{(n)} = \boldsymbol{\kappa} \rangle = \mathbf{L}(\mathbf{L})^{*T} = 2k \Psi_{ij}(\boldsymbol{\kappa}). \quad (\text{A14})$$

This is simply the complex version of the Cholesky factorization for positive, semi-definite, Hermitian matrices.

APPENDIX B: CONSTRUCTION OF GENERAL u-e DECAY MODEL

A general model for \mathbf{u}^* and \mathbf{e}^* in decaying turbulence is constructed based on the form for coupled stochastic diffusion processes:

$$du_i^* = a_i(\mathbf{u}^*, \mathbf{e}^*)dt + A_{ij}(\mathbf{u}^*, \mathbf{e}^*)dW_j + B_{ij}(\mathbf{u}^*, \mathbf{e}^*)dW'_j, \quad (B1a)$$

and

$$de_i^* = g_i(\mathbf{u}^*, \mathbf{e}^*)dt + G_{ij}(\mathbf{u}^*, \mathbf{e}^*)dW_j + H_{ij}(\mathbf{u}^*, \mathbf{e}^*)dW'_j, \quad (B1b)$$

and the four constraints given in Sec. IV B. In applying these constraints to the diffusion process some simplifying assumptions are made in order to achieve a tractable model. As a result the General u-e Decay Model is not in the *most* general form, but maintains more than sufficient generality for our purposes.

Before the constraints are applied to the diffusion process, its coefficients are re-expressed using the isotropic functions of \mathbf{u}^* and \mathbf{e}^* :

$$a_i(\mathbf{u}^*, \mathbf{e}^*) = a_1 e_i^* + a_2 u_i^* + a_i^a, \quad (B2a)$$

$$g_i(\mathbf{u}^*, \mathbf{e}^*) = g_1 e_i^* + g_2 u_i^* + g_i^a, \quad (B2b)$$

$$A_{ij}(\mathbf{u}^*, \mathbf{e}^*) = \mathcal{A}_1 \delta_{ij} + \mathcal{A}_2 e_i^* e_j^* + \mathcal{A}_3 \frac{u_i^* u_j^*}{u_s^* u_s^*} + \mathcal{A}_4 e_i^* u_j^* + \mathcal{A}_5 e_j^* u_i^* + A_{ij}^a, \quad (B2c)$$

$$B_{ij}(\mathbf{u}^*, \mathbf{e}^*) = \mathcal{B}_1 \delta_{ij} + \mathcal{B}_2 e_i^* e_j^* + \mathcal{B}_3 \frac{u_i^* u_j^*}{u_s^* u_s^*} + \mathcal{B}_4 e_i^* u_j^* + \mathcal{B}_5 e_j^* u_i^* + B_{ij}^a, \quad (B2d)$$

$$G_{ij}(\mathbf{u}^*, \mathbf{e}^*) = \mathcal{G}_1 \delta_{ij} + \mathcal{G}_2 e_i^* e_j^* + \mathcal{G}_3 \frac{u_i^* u_j^*}{u_s^* u_s^*} + \mathcal{G}_4 e_i^* u_j^* + \mathcal{G}_5 e_j^* u_i^* + G_{ij}^a, \quad (B2e)$$

$$H_{ij}(\mathbf{u}^*, \mathbf{e}^*) = \mathcal{H}_1 \delta_{ij} + \mathcal{H}_2 e_i^* e_j^* + \mathcal{H}_3 \frac{u_i^* u_j^*}{u_s^* u_s^*} + \mathcal{H}_4 e_i^* u_j^* + \mathcal{H}_5 e_j^* u_i^* + H_{ij}^a, \quad (B2f)$$

where a_γ and g_γ for $\gamma=1,2$ and \mathcal{A}_γ , \mathcal{B}_γ , \mathcal{G}_γ , and \mathcal{H}_γ for $\gamma=1,2,3,4,5$ are functions of $u_s^* u_s^*$ and the time varying statistics of \mathbf{u}^* and \mathbf{e}^* . Also, a_i^a , g_i^a , A_{ij}^a , B_{ij}^a , G_{ij}^a , and H_{ij}^a are anisotropic functions of \mathbf{u}^* and \mathbf{e}^* . The deterministic constraints are expressed via Ito calculus which applies for the Ito SDE's:

$$d(e_l^* e_l^*) = 2e_l^* de_l^* + de_l^* de_l^* = 0, \quad (B3a)$$

and

$$d(u_l^* e_l^*) = u_l^* de_l^* + e_l^* du_l^* + du_l^* de_l^* = 0. \quad (B3b)$$

The unit length of \mathbf{e}^* constraint applied to the general diffusion process imposes conditions on the model:

$$e_i^* G_{ij} = e_i^* H_{ij} = 0, \quad (B4a)$$

and

$$g_i e_i^* = -\frac{1}{2} [G_{ij} G_{ij} + H_{ij} H_{ij}], \quad (B4b)$$

while the orthogonality constraint imposes

$$e_i^* A_{ij} + u_i^* G_{ij} = e_i^* B_{ij} + u_i^* H_{ij} = 0, \quad (B5a)$$

and

$$a_i e_i^* + g_i u_i^* = -[A_{ij} G_{ij} + B_{ij} H_{ij}]. \quad (B5b)$$

In the above conditions the independence of the Wiener processes is used to set each of their coefficients to zero.

The conditions in Eqs. (B4a) and (B5a) impose constraints on the tensorial form of the diffusion coefficients. The results for the isotropic parts are

$$A_{ij}(\mathbf{u}^*, \mathbf{e}^*) = \mathcal{A}_1 \delta_{ij} + \mathcal{A}_2 e_i^* e_j^* + \mathcal{A}_3 \frac{u_i^* u_j^*}{u_s^* u_s^*} - (\mathcal{G}_1 + \mathcal{G}_3) e_i^* u_j^* + \mathcal{A}_5 e_j^* u_i^* + A_{ij}^a, \quad (B6a)$$

$$B_{ij}(\mathbf{u}^*, \mathbf{e}^*) = \mathcal{B}_1 \delta_{ij} + \mathcal{B}_2 e_i^* e_j^* + \mathcal{B}_3 \frac{u_i^* u_j^*}{u_s^* u_s^*} - (\mathcal{H}_1 + \mathcal{H}_3) e_i^* u_j^* + \mathcal{B}_5 e_j^* u_i^* + B_{ij}^a, \quad (B6b)$$

$$G_{ij}(\mathbf{u}^*, \mathbf{e}^*) = \mathcal{G}_1 (\delta_{ij} - e_i^* e_j^*) + \mathcal{G}_3 \frac{u_i^* u_j^*}{u_s^* u_s^*} - (\mathcal{A}_1 + \mathcal{A}_2) \frac{u_i^* e_j^*}{u_s^* u_s^*} + G_{ij}^a, \quad (B6c)$$

$$H_{ij}(\mathbf{u}^*, \mathbf{e}^*) = \mathcal{H}_1 (\delta_{ij} - e_i^* e_j^*) + \mathcal{H}_3 \frac{u_i^* u_j^*}{u_s^* u_s^*} - (\mathcal{B}_1 + \mathcal{B}_2) \frac{u_i^* e_j^*}{u_s^* u_s^*} + H_{ij}^a. \quad (B6d)$$

For the anisotropic diffusion coefficients, the unit length constraint is applied without assumption, while in the orthogonality constraint each term is individually assumed to be zero. The results are conditions on the tensorial form of the anisotropic diffusion coefficients:

$$A_{ij}^a \equiv (\delta_{il} - e_i^* e_l^*) \mathcal{A}_{lj}^a, \quad (B7a)$$

$$B_{ij}^a \equiv (\delta_{il} - e_i^* e_l^*) \mathcal{B}_{lj}^a, \quad (B7b)$$

$$G_{ij}^a \equiv t_i^* t_l^* \mathcal{G}_{lj}^a, \quad (B7c)$$

$$H_{ij}^a \equiv t_i^* t_l^* \mathcal{H}_{lj}^a, \quad (B7d)$$

where a vector, \mathbf{t}^* , mutually orthogonal to \mathbf{u}^* and \mathbf{e}^* is used, and \mathcal{A}_{lj}^a , \mathcal{B}_{lj}^a , \mathcal{G}_{lj}^a , and \mathcal{H}_{lj}^a are new anisotropic functions. From geometrical considerations a relationship between three orthogonal unit vectors exists:

$$t_i^* t_j^* = \delta_{ij} - e_i^* e_j^* - \frac{u_i^* u_j^*}{u_s^* u_s^*}. \quad (\text{B8})$$

With the functional form of the drift coefficients substituted into Eqs. (B4b) and (B5b), expressions and conditions on the coefficients are found. Also, it is assumed that the terms consisting of the anisotropic drift coefficients are zero independent of the isotropic terms. The results are

$$g_i^a \equiv (\delta_{il} - e_i^* e_l^*) \bar{g}_i^a, \quad (\text{B9a})$$

$$a_i^a e_i^* + \bar{g}_i^a u_i^* = 0, \quad (\text{B9b})$$

$$\begin{aligned} a_1 = & -g_2(u_s^* u_s^*) - \{(2\mathcal{G}_1 + \mathcal{G}_3)\mathcal{A}_1 + (\mathcal{G}_1 + \mathcal{G}_3)\mathcal{A}_3 \\ & + (\mathcal{A}_1 + \mathcal{A}_2)\mathcal{A}_5 + t_i^* t_l^* \mathcal{A}_1 \mathcal{G}_{li}^a \\ & + (2\mathcal{H}_1 + \mathcal{H}_3)\mathcal{B}_1 + (\mathcal{H}_1 + \mathcal{H}_3)\mathcal{B}_3 \\ & + (\mathcal{B}_1 + \mathcal{B}_2)\mathcal{B}_5 + t_i^* t_l^* \mathcal{B}_1 \mathcal{H}_{li}^a\}, \end{aligned} \quad (\text{B9c})$$

and

$$\begin{aligned} g_1 = & -\mathcal{G}_1(\mathcal{G}_1 + \mathcal{G}_3) - \mathcal{H}_1(\mathcal{H}_1 + \mathcal{H}_3) - \frac{1}{2}(\mathcal{G}_3^2 + \mathcal{H}_3^2) \\ & - \frac{1}{2u_s^* u_s^*} [(\mathcal{A}_1 + \mathcal{A}_2)^2 + (\mathcal{B}_1 + \mathcal{B}_2)^2] \\ & - \frac{1}{2} t_i^* t_l^* (\mathcal{G}_1 \mathcal{G}_{li}^a + \mathcal{H}_1 \mathcal{H}_{li}^a). \end{aligned} \quad (\text{B9d})$$

The constraint of a joint normal solution in isotropic, decaying turbulence is applied by comparison with the Langevin equation whose solution for the PDF is known to

be joint normal. The actual comparison is made between the SDE's for speed from the different equations. The Langevin equation is

$$du_i = -au_i dt + bdW_i, \quad (\text{B10})$$

which when expressed for the speed, $u \equiv |\mathbf{u}|$, is

$$du = \left(\frac{b^2}{u} - au \right) dt + bdW. \quad (\text{B11})$$

In isotropic turbulence the SDE for speed from the general model with the stochastic constraints applied is

$$du = E_1 dt + E_2 dW, \quad (\text{B12a})$$

where

$$E_1 = [\mathcal{A}_1(\mathcal{A}_1 + \mathcal{A}_2) + \mathcal{B}_1(\mathcal{B}_1 + \mathcal{B}_2) + \frac{1}{2}(\mathcal{A}_2^2 + \mathcal{B}_2^2)] \frac{1}{u}$$

$$+ [a_2 + \frac{1}{2}(\mathcal{G}_1 + \mathcal{G}_3)^2 + \frac{1}{2}(\mathcal{H}_1 + \mathcal{H}_3)^2] u, \quad (\text{B12b})$$

$$E_2 = [(\mathcal{A}_1 + \mathcal{A}_3)^2 + (\mathcal{B}_1 + \mathcal{B}_3)^2 + (\mathcal{A}_5^2 + \mathcal{B}_5^2)u^2]^{1/2}. \quad (\text{B12c})$$

This equation must be forced into the form of Eq. (B11). A fully general model would consist of diffusion coefficients which are power or Laurent series in \mathbf{u} , but to avoid this complexity the coefficients are assumed independent of u where possible. Thus, by scaling with ε and k all the coefficients are re-expressed with non-dimensional parameters and the appropriate u dependencies where necessary:

$$\begin{aligned} a_i^a & \equiv \tilde{a}_i^a \left(\frac{\varepsilon}{\sqrt{k}} \right), \quad a_1 \equiv \tilde{a}_1 \left(\frac{\varepsilon}{\sqrt{k}} \right), \quad a_2 \equiv \tilde{a}_2^{(1)} \left(\frac{\varepsilon}{k} \right) + \tilde{a}_2^{(2)} \left(\frac{2\varepsilon}{u^2} \right), \\ \bar{g}_i^a & \equiv \tilde{g}_i^a \left(\frac{\varepsilon}{k} \right), \quad g_1 \equiv \tilde{g}_1 \left(\frac{\varepsilon}{k} \right), \quad g_2 \equiv \tilde{g}_2 \frac{\varepsilon}{\sqrt{k^3}}, \\ \mathcal{A}_1 & \equiv \tilde{\mathcal{A}}_1 \sqrt{\varepsilon}, \quad \mathcal{A}_2 \equiv \tilde{\mathcal{A}}_2 \sqrt{\varepsilon}, \quad \mathcal{A}_3 \equiv \tilde{\mathcal{A}}_3 \sqrt{\varepsilon}, \quad \mathcal{A}_5 \equiv \tilde{\mathcal{A}}_5 \frac{\sqrt{2\varepsilon}}{u}, \quad \mathcal{A}_{lj}^a \equiv \tilde{\mathcal{A}}_{lj}^a \sqrt{\varepsilon}, \\ \mathcal{B}_1 & \equiv \tilde{\mathcal{B}}_1 \sqrt{\varepsilon}, \quad \mathcal{B}_2 \equiv \tilde{\mathcal{B}}_2 \sqrt{\varepsilon}, \quad \mathcal{B}_3 \equiv \tilde{\mathcal{B}}_3 \sqrt{\varepsilon}, \quad \mathcal{B}_5 \equiv \tilde{\mathcal{B}}_5 \frac{\sqrt{2\varepsilon}}{u}, \quad \mathcal{B}_{lj}^a \equiv \tilde{\mathcal{B}}_{lj}^a \sqrt{\varepsilon}, \\ \mathcal{G}_1 & \equiv \tilde{\mathcal{G}}_1 \sqrt{\frac{\varepsilon}{k}}, \quad \mathcal{G}_3 \equiv \tilde{\mathcal{G}}_3 \sqrt{\frac{\varepsilon}{k}}, \quad \mathcal{G}_{lj}^a \equiv \tilde{\mathcal{G}}_{lj}^a \sqrt{\frac{\varepsilon}{k}}, \\ \mathcal{H}_1 & \equiv \tilde{\mathcal{H}}_1 \sqrt{\frac{\varepsilon}{k}}, \quad \mathcal{H}_3 \equiv \tilde{\mathcal{H}}_3 \sqrt{\frac{\varepsilon}{k}}, \quad \mathcal{H}_{lj}^a \equiv \tilde{\mathcal{H}}_{lj}^a \sqrt{\frac{\varepsilon}{k}}. \end{aligned}$$

The joint normal condition is now applied giving an expression for one of the velocity drift coefficients:

$$\tilde{a}_2^{(2)} = \frac{1}{2} [\tilde{\mathcal{A}}_3(2\tilde{\mathcal{A}}_1 + \tilde{\mathcal{A}}_3) - \frac{1}{2}\tilde{\mathcal{A}}_2(2\tilde{\mathcal{A}}_1 + \tilde{\mathcal{A}}_2) + 2\tilde{\mathcal{A}}_5^2 + \tilde{\mathcal{B}}_3(2\tilde{\mathcal{B}}_1 + \tilde{\mathcal{B}}_3) - \frac{1}{2}\tilde{\mathcal{B}}_2(2\tilde{\mathcal{B}}_1 + \tilde{\mathcal{B}}_2) + 2\tilde{\mathcal{B}}_5^2]. \quad (\text{B13})$$

The evolution of the kinetic energy constraint is applied by forcing the kinetic energy equation from the stochastic model into the same form as Eq. (51), which results in an expression for the remaining velocity drift coefficient:

$$\begin{aligned}
\tilde{a}_2^{(1)} = & -\frac{1}{2} \left\{ 1 + \frac{1}{\sqrt{k}} \langle u_s^* \tilde{a}_l^a \rangle + (\mathcal{G}_1 + \mathcal{G}_3)^2 + (\mathcal{H}_1 + \mathcal{H}_3)^2 + \frac{3}{2} (\mathcal{H}_1 + \mathcal{H}_3)^2 + 3 \mathcal{H}_5^2 + \mathcal{H}_1 \langle (\delta_{jl} - e_j^* e_l^*) \mathcal{H}_{lj}^a \rangle + \mathcal{H}_3 \left\langle \frac{u_j^* u_l^*}{u_s^* u_s^*} \mathcal{H}_{lj}^a \right\rangle \right. \\
& + \sqrt{2} \mathcal{H}_5 \left\langle \frac{e_j^* u_l^*}{(u_s^* u_s^*)^{1/2}} \mathcal{H}_{lj}^a \right\rangle + \frac{1}{2} \langle (\delta_{ln} - e_l^* e_n^*) \mathcal{H}_{lj}^a \mathcal{H}_{nj}^a \rangle + \frac{3}{2} (\mathcal{B}_1 + \mathcal{B}_3)^2 + 3 \mathcal{B}_5^2 + \mathcal{B}_1 \langle (\delta_{jl} - e_j^* e_l^*) \mathcal{B}_{lj}^a \rangle \\
& \left. + \mathcal{B}_3 \left\langle \frac{u_j^* u_l^*}{u_s^* u_s^*} \mathcal{B}_{lj}^a \right\rangle + \sqrt{2} \mathcal{B}_5 \left\langle \frac{e_j^* u_l^*}{(u_s^* u_s^*)^{1/2}} \mathcal{B}_{lj}^a \right\rangle + \frac{1}{2} \langle (\delta_{ln} - e_l^* e_n^*) \mathcal{B}_{lj}^a \mathcal{B}_{nj}^a \rangle \right\}. \quad (B14)
\end{aligned}$$

The final form for the General **u-e** Model is now summarized:

$$\begin{aligned}
du_i^* = & \left(\frac{\varepsilon}{k} \right) \left[\tilde{a}_1 \sqrt{k} e_i^* + \tilde{a}_2^{(1)} u_i^* + 2 \tilde{a}_2^{(2)} \frac{k}{u_s^* u_s^*} u_i^* \right. \\
& \left. + \tilde{a}_i^a \sqrt{k} \right] dt + A_{ij} dW_j + B_{ij} dW_j', \quad (B15a)
\end{aligned}$$

and

$$\begin{aligned}
de_i^* = & \left(\frac{\varepsilon}{k} \right) \left[\tilde{g}_1 e_i^* + \tilde{g}_2 \frac{u_i^*}{\sqrt{k}} + (\delta_{ij} - e_i^* e_j^*) \tilde{g}_j^a \right] dt \\
& + G_{ij} dW_j + H_{ij} dW_j', \quad (B15b)
\end{aligned}$$

where some of the coefficients were previously given in Eqs. (B13) and (B14), and the following coefficients are re-expressed in non-dimensional form:

$$\begin{aligned}
\tilde{a}_1 = & -\tilde{g}_2 \frac{u_s^* u_s^*}{k} - \{ (2\mathcal{G}_1 + \mathcal{G}_3) \mathcal{H}_1 + (\mathcal{G}_1 + \mathcal{G}_3) \mathcal{H}_3 \\
& + (\mathcal{H}_1 + \mathcal{H}_2) \mathcal{H}_5 + t_i^* t_l^* \mathcal{H}_1 \mathcal{G}_{li}^a + (2\mathcal{H}_1 + \mathcal{H}_3) \mathcal{B}_1 \\
& + (\mathcal{H}_1 + \mathcal{H}_3) \mathcal{B}_3 + (\mathcal{B}_1 + \mathcal{B}_2) \mathcal{B}_5 + t_i^* t_l^* \mathcal{B}_1 \mathcal{H}_{li}^a \}, \\
& \quad (B16a)
\end{aligned}$$

$$\begin{aligned}
\tilde{g}_1 = & -\mathcal{G}_1 (\mathcal{G}_1 + \mathcal{G}_3) - \mathcal{H}_1 (\mathcal{H}_1 + \mathcal{H}_3) - \frac{1}{2} (\mathcal{G}_3^2 + \mathcal{H}_3^2) \\
& - \frac{k}{2 u_s^* u_s^*} [(\mathcal{H}_1 + \mathcal{H}_2)^2 + (\mathcal{B}_1 + \mathcal{B}_2)^2] \\
& - \frac{1}{2} t_i^* t_l^* (\mathcal{G}_1 \mathcal{G}_{li}^a + \mathcal{H}_1 \mathcal{B}_{li}), \quad (B16b)
\end{aligned}$$

$$\begin{aligned}
A_{ij}(\mathbf{u}^*, \mathbf{e}^*) = & \sqrt{\varepsilon} \left[\mathcal{H}_1 \delta_{ij} + \mathcal{H}_2 e_i^* e_j^* + \mathcal{H}_3 \frac{u_i^* u_j^*}{u_s^* u_s^*} \right. \\
& - \frac{1}{\sqrt{k}} (\mathcal{G}_1 + \mathcal{G}_3) e_i^* u_j^* + \sqrt{2} \mathcal{H}_5 \frac{e_j^* u_i^*}{(u_s^* u_s^*)^{1/2}} \\
& \left. + (\delta_{il} - e_i^* e_l^*) \tilde{A}_{lj}^a \right], \quad (B16c)
\end{aligned}$$

$$\begin{aligned}
B_{ij}(\mathbf{u}^*, \mathbf{e}^*) = & \sqrt{\varepsilon} \left[\mathcal{B}_1 \delta_{ij} + \mathcal{B}_2 e_i^* e_j^* + \mathcal{B}_3 \frac{u_i^* u_j^*}{u_s^* u_s^*} \right. \\
& - \frac{1}{\sqrt{k}} (\mathcal{H}_1 + \mathcal{H}_3) e_i^* u_j^* + \sqrt{2} \mathcal{B}_5 \frac{e_i^* u_i^*}{(u_s^* u_s^*)^{1/2}} \\
& \left. + (\delta_{il} - e_i^* e_l^*) \tilde{B}_{lj}^a \right], \quad (B16d)
\end{aligned}$$

$$\begin{aligned}
G_{ij}(\mathbf{u}^*, \mathbf{e}^*) = & \sqrt{\frac{\varepsilon}{k}} \left[\mathcal{G}_1 (\delta_{ij} - e_i^* e_j^*) + \mathcal{G}_3 \frac{u_i^* u_j^*}{u_s^* u_s^*} \right. \\
& \left. - \sqrt{k} (\mathcal{H}_1 + \mathcal{H}_2) \frac{u_i^* e_j^*}{u_s^* u_s^*} + t_i^* t_l^* \tilde{G}_{lj}^a \right], \quad (B16e)
\end{aligned}$$

$$\begin{aligned}
H_{ij}(\mathbf{u}^*, \mathbf{e}^*) = & \sqrt{\frac{\varepsilon}{k}} \left[\mathcal{H}_1 (\delta_{ij} - e_i^* e_j^*) + \mathcal{H}_3 \frac{u_i^* u_j^*}{u_s^* u_s^*} \right. \\
& \left. - \sqrt{k} (\mathcal{B}_1 + \mathcal{B}_2) \frac{u_i^* e_j^*}{u_s^* u_s^*} + t_i^* t_l^* \tilde{H}_{lj}^a \right]. \quad (B16f)
\end{aligned}$$

In addition, one constraint remains on the anisotropic drift terms:

$$\sqrt{k} \tilde{a}_l^a e_l^* + \tilde{g}_l^a u_l^* = 0. \quad (B17)$$

¹P. Y. Chou, "On velocity correlations and the solutions of the equations of turbulent fluctuation," *Q. Appl. Math.* **3**, 38 (1945).

²J. Rotta, "Statistische theorie nichthomogener turbulenz," *Z. Phys.* **129**, 547 (1951).

³B. E. Launder, G. J. Reece, and W. Rodi, "Progress in the development of a Reynolds-stress turbulence closure," *J. Fluid Mech.* **68**, 537 (1975).

⁴T. H. Shih and J. L. Lumley, "Modeling of pressure correlation terms in Reynolds stress and scalar flux equations," Technical Report FDA-85-3, Cornell University, 1985.

⁵D. C. Haworth and S. B. Pope, "A generalized Langevin model for turbulent flows," *Phys. Fluids* **29**, 387 (1986).

⁶S. Fu, B. E. Launder, and D. P. Tselepidakis, "Accommodating the effects of high strain rates in modelling the pressure-strain correlation," Technical Report TFD/87/5, UMIST Mech. Eng. Dept. Report TFD/89/1, 1987.

⁷C. G. Speziale, S. Sarkar, and T. B. Gatski, "Modelling the pressure-strain correlation of turbulence: an invariant dynamical systems approach," *J. Fluid Mech.* **227**, 245 (1991).

⁸A. V. Johansson and M. Hällberg, "Modelling of rapid pressure-strain in Reynolds-stress closures," *J. Fluid Mech.* **269**, 143 (1994).

⁹J. R. Ristorcelli, J. L. Lumley, and R. Abid, "A rapid-pressure covariance representation consistent with the Taylor-Proudman theorem materially indifferent in the two-dimensional limit," *J. Fluid Mech.* **292**, 111 (1995).

¹⁰J. L. Lumley and G. R. Newman, "The return to isotropy of homogeneous turbulence," *J. Fluid Mech.* **82**, 161 (1977).

¹¹S. Sarkar and C. G. Speziale, "A simple nonlinear model for the return to isotropy in turbulence," *Phys. Fluids A* **2**, 84 (1990).

¹²M. K. Chung and S. K. Kim, "A nonlinear return-to-isotropy model with Reynolds number and anisotropy dependency," *Phys. Fluids A* **7**, 1425 (1995).

¹³W. C. Reynolds, "Effects of rotation on homogeneous turbulence," in *Proceedings of the Tenth Australasian Fluid Mechanics Conference*, 1989.

¹⁴C. Cambon and L. Jacquin, "Spectral approach to non-isotropic turbulence subjected to rotation," *J. Fluid Mech.* **202**, 295 (1989).

¹⁵N. N. Mansour, T. H. Shih, and W. C. Reynolds, "The effects of rotation on initially anisotropic homogeneous flows," *Phys. Fluids A* **3**, 2421 (1991).

¹⁶W. C. Reynolds and S. C. Kassinos, "A one-point model for the evolution of the Reynolds stress and structure tensors in rapidly deformed homogeneous turbulence," *Proc. R. Soc. London A* **451** (1941), 87 (1995).

¹⁷C. G. Speziale, R. Abid, and G. A. Blaisdell, "On the consistency of Reynolds stress turbulence closures with hydrodynamic stability theory," *Phys. Fluids A* **8**, 781 (1996).

¹⁸L. Prandtl, in *NACA Technical Memo*, 1933.

¹⁹G. I. Taylor, "Turbulence in a contracting stream," *Z. Angew. Math. Mech.* **15**, 91 (1935).

²⁰G. K. Batchelor and I. Proudman, "The effect of rapid distortion of a fluid in turbulent motion," *Q. J. Mech. Appl. Math.* **7**, 83 (1954).

²¹A. A. Townsend, *The Structure of Turbulent Shear Flow*, 2nd ed. (Cambridge University Press, Cambridge, 1976).

²²M. J. Lee and W. C. Reynolds, "Numerical experiments on the structure of homogeneous turbulence," Technical Report TF-24, Stanford University, November 1985.

²³M. J. Lee, "Distortion of homogeneous turbulence by axisymmetric strain and dilatation," *Phys. Fluids A* **1**, 1541 (1989).

²⁴M. J. Lee, J. Kim, and P. Moin, "Structure of turbulence at high shear rate," *J. Fluid Mech.* **216**, 561 (1990).

²⁵J. C. R. Hunt and D. J. Carruthers, "Rapid distortion theory and the 'problems' of turbulence," *J. Fluid Mech.* **212**, 497 (1990).

²⁶S. C. Kassinos and W. C. Reynolds, "A structure-based model for rapid distortion of homogeneous turbulence," Technical Report TF-61, Stanford University, 1994.

²⁷S. C. Kassinos and W. C. Reynolds, "An extended structure-based model based on a stochastic eddy-axis evolution equation," *Annual Research Briefs: Center for Turbulence Research* (1995), pp. 133–148.

²⁸S. C. Kassinos and W. C. Reynolds (private communication, April 1996).

²⁹S. B. Pope, "Pdf methods for turbulent reactive flows," *Prog. Energy Combust. Sci.* **11**, 119 (1985).

³⁰S. B. Pope and Y. L. Chen, "The velocity-dissipation probability density function model for turbulent flows," *Phys. Fluids A* **2**, 1437 (1990).

³¹S. B. Pope, "Application of the velocity-dissipation probability density function model to inhomogeneous turbulent flows," *Phys. Fluids A* **3**, 1947 (1991).

³²S. B. Pope, "Lagrangian pdf methods for turbulent flows," *Annu. Rev. Fluid Mech.* **26**, 23 (1994).

³³S. B. Pope, "On the relationship between stochastic Lagrangian models of turbulence and second-moment closures," *Phys. Fluids A* **6**, 973 (1994).

³⁴P. A. Durbin and C. G. Speziale, "Realizability of second-moment closure via stochastic analysis," *J. Fluid Mech.* **280**, 395 (1994).

³⁵H. A. Wouters, T. W. J. Peeters, and D. Roekaerts, "On the existence of a stochastic Lagrangian model representation for second-moment closures," *Phys. Fluids A* **8**, 1702 (1996).

³⁶G. K. Batchelor, *The Theory of Homogeneous Turbulence* (Cambridge University Press, Cambridge, 1953).

³⁷R. S. Rogallo, "Numerical experiments in homogeneous turbulence," Technical Report 81315, NASA, 1981.

³⁸A. Craya, "Contribution à l'analyse de la turbulence associée à des vitesses moyennes," 1958. P.S.T. no. 345.

³⁹Z. Warhaft, "An experimental study of the effect of uniform strain on thermal fluctuations in grid-generated turbulence," *J. Fluid Mech.* **99**, (1980).

⁴⁰K. S. Choi and J. L. Lumley, "Return to isotropy of homogeneous turbulence revisited," in *Turbulence and Chaotic Phenomena in Fluids*, edited by T. Tatsumi (Elsevier, New York, 1984), pp. 267–272.

⁴¹K. Hanjalić and B. E. Launder, "A Reynolds stress model of turbulence and its applications," *J. Fluid Mech.* **52**, 609 (1972).

⁴²M. M. Rogers, P. Moin, and W. C. Reynolds, "The structure and modeling of the hydrodynamic and passive scalar fields in homogeneous turbulent shear flow," Technical Report TF-25, Stanford University, August 1986.

⁴³S. Tavoularis and U. Karnik, "Further experiments on the evolution of turbulent stresses and scales in uniformly sheared turbulence," *J. Fluid Mech.* **204**, 457 (1989).

⁴⁴J. Bardina, J. H. Fersiger, and W. C. Reynolds, "Improved turbulence models based on large-eddy simulation of homogeneous, incompressible turbulent flows," Technical Report TF-19, Stanford University, 1983.

⁴⁵C. G. Speziale and N. Mac Giolla Mhuiris, "On the prediction of equilibrium states in homogeneous turbulence," *J. Fluid Mech.* **209**, 591 (1989).

⁴⁶H. J. Tucker, Ph.D. thesis, McGill University, Montreal, 1970.

⁴⁷G. A. Blaisdell and K. Shariff, "Homogeneous turbulence subjected to mean flow with elliptic stream lines," in *Studying Turbulence Using Numerical Simulation Databases - V*, December 1994. Center for Turbulence Research: Proceedings of the Summer Program 1994.

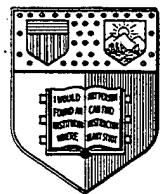
⁴⁸C. Cambon, C. Teissèdre, and D. Jeandel, "Etude d'effets couplés de déformation et de rotation sur une turbulence homogène," *J. Méc. Théor. Appl.* **4**, 629 (1985).

⁴⁹R. T. Pierrehumbert, "Universal short-wave instability of two-dimensional eddies in an inviscid fluid," *Phys. Rev. Lett.* **57**, 2157 (1986).

⁵⁰B. J. Bayly, "Three-dimensional instability of elliptical flow," *Phys. Rev. Lett.* **57**, 2160 (1986).

⁵¹M. J. Landman and P. G. Saffman, "The three-dimensional instability of strained vortices in a viscous fluid," *Phys. Fluids* **30**, 2339 (1987).

⁵²F. Waleffe, "The three-dimensional instability of strained vortices," *Phys. Fluids A* **2**, 76 (1990).



Fluid Dynamics and Aerodynamics Program

**Sibley School of
Mechanical and Aerospace Engineering**

Cornell University Ithaca, New York 14853

**COMPARISON OF PDF MIXING MODELS FOR
NONPREMIXED TURBULENT REACTING FLOW**

by

S. Subramaniam and S. B. Pope

FDA 97-03

March, 1997

Abstract

A spatially inhomogeneous model problem for studying turbulent nonpremixed reacting flow with reversible reaction is proposed that admits stationary solutions which are periodic in physical space. The thermochemical state of the fluid is characterized by two composition variables: mixture fraction $\xi(\mathbf{x}, t)$ and reaction progress variable $Y(\mathbf{x}, t)$. A linear gradient in the mean mixture fraction field is imposed such that, in a forced stationary velocity field, the mixture fraction field also attains statistical stationarity. The solutions are parametrized by the Damköhler number and the reaction zone thickness parameter. At sufficiently high Damköhler number there is stable reaction, but as the Damköhler number is decreased below a critical value, global extinction occurs. The range of parameter values is chosen such that the model problem reproduces important phenomena such as stable near-equilibrium reaction, local extinction and global extinction. A self-similar model thermochemistry is proposed which allows access to the parameter range of interest at reasonable computational expense. Monte Carlo simulations are performed to solve for the joint probability density function of velocity, turbulent frequency and composition. The predictions for critical Damköhler number are compared for two different mixing models: the interaction by exchange with the mean (IEM) model, and the Euclidean Minimum Spanning Tree (EMST) model. The results obtained using the simpler conditional moment closure (CMC) model are also presented for comparison. The model problem is formulated to permit direct numerical simulations (DNS) using pseudo-spectral methods which require periodic boundary conditions. The DNS study of this model problem, which is currently underway, will provide validation for the model predictions and additional insight into the phenomenon of extinction in inhomogeneous turbulent reactive flows.

1 Introduction

Prediction of the extinction characteristics of turbulent nonpremixed flames is an important and challenging area of current research. An important parameter in nonpremixed flames is the Damköhler number:

$$\text{Da} \equiv \tau_\phi / \tau^*, \quad (1)$$

which is the ratio of the characteristic mixing timescale τ_ϕ to the characteristic chemical timescale τ^* .

When the Damköhler number is very large, the fluid composition almost everywhere in the physical domain is very close to chemical equilibrium because reaction is rapid compared to the time taken to mix with neighboring fluid. In such situations models based on the equilibrium assumption or those based on small departures from equilibrium may be used with confidence. However, in most turbulent flames there is a range of turbulent timescales (or, in other words, mixing timescales) and there is a corresponding range of Damköhler numbers. As the Damköhler number decreases at any given physical location (as a result of an increase in the local scalar dissipation rate), departures from equilibrium become significant and may result in local extinction. If the Damköhler number is too small to sustain stable combustion in a sufficiently large fraction of the fluid volume, global extinction occurs.

Experiments on piloted jet diffusion flames by Masri et al. [9] provide direct evidence of these phenomena. Clearly, modeling such jet diffusion flames based on equilibrium or near-equilibrium assumptions is questionable. Computations of piloted jet flames using PDF transport equations have been performed using finite-rate chemistry [4], [19], [11]. While the calculations of Norris & Pope [11] are successful in predicting the jet velocity at which global extinction occurs, the details of local extinction are not well represented. These discrepancies were attributed to three factors; deficiencies in the mixing model; differential diffusion effects which were neglected; and, experimental error. In spite of establishing the overall success of the PDF approach in modeling turbulent nonpremixed flames, these calculations highlight the need for a better understanding of such reactive flows.

While the comparison of model predictions with experimental data is the ultimate test of a model, it is difficult to pinpoint the model deficiencies in comparisons with experiment for several reasons. In real flows there are many complex coupled processes and it is difficult to isolate the effects of the physical process being modeled. The modeled terms, e.g. Lagrangian time series of composition or conditional scalar dissipation, are often not amenable to direct measurement.

On the other hand direct numerical simulations (DNS) can be used to perform controlled numerical experiments on simple turbulent reactive flows and all flow properties of interest can be extracted. Since many features characteristic of turbulent flames can be represented in a simpler model problem, a satisfactory model for turbulent flames should perform comparably in a simpler turbulent reactive flow. Modeling deficiencies may be identified more easily in the model problem setting. Furthermore, the model behavior in the simpler flow problem can be used to gain valuable insight into the model performance in real turbulent flames. In fact, such computations of practical combusting flows are an ongoing part of this research effort and this work is intended as an important complement thereof.

The present contribution constitutes a valuable intermediate step to the comparison of model predictions with DNS. The objectives of the present work are two-fold: the first is to construct a simple inhomogeneous, nonpremixed reactive flow model problem that is amenable to direct numerical simulation (DNS); the second is to study the effect of PDF models of molecular mixing on model predictions over a range of flow conditions including those close to extinction. In particular it is of interest to determine whether the new principle of localness [18] required of mixing models enables a more accurate representation of mixing in reactive flows.

In general a constant-density, constant-diffusivity (equal for all species), nonpremixed turbulent reactive flow may be characterized by a Reynolds number (say the Taylor-scale Reynolds number R_λ), Damköhler number and a reaction zone thickness parameter defined as:

$$\hat{\xi}_r \equiv \Delta\xi_r/\xi', \quad (2)$$

where $\Delta\xi_r$ is the characteristic width of the reaction zone in mixture fraction space and ξ' is the r.m.s. mixture fraction. These parameters may be functions of space and time.

In order to obtain a quantitative description of extinction in this $(R_\lambda, \text{Da}, \hat{\xi}_r)$ parameter space with finite computer resources, the model problem is necessarily very simple both in terms of flow and thermochemistry. The velocity field in this model problem is constant-density, statistically stationary, homogeneous isotropic turbulence. A simple thermochemical model for one-step reversible reaction is employed, with the thermochemical state of the fluid described by two variables: the mixture fraction and reaction progress variable. It is advantageous to consider a model problem which admits statistically stationary solutions. This removes the temporal dependence of the parameters and also allows study of flow characteristics independent of the influence of initial conditions. Even with these simplifications a statistical description of extinction using numerical simulations is subject to statistical variability and is dependent on the duration of the simulation [8].

In previous studies of extinction by Lee & Pope [8], stationarity was achieved by forcing the mixture fraction field, but in this model problem stationarity is achieved by imposing a linear mean gradient in the mixture fraction. The mean gradient in mixture fraction also results in a “flame brush” which is a more realistic case than that considered in Lee & Pope [8]. The flow under consideration has statistical inhomogeneity only in the reaction progress variable, and only in the spatial dimension along which the linear mean gradient is imposed.

At high Reynolds number, the extinction characteristics are expected to become independent of the Reynolds number. One of the goals of these simulations (both the PDF simulations presented here and the anticipated DNS) will be a characterization of global extinction by means of a stability diagram in $\text{Da} - \hat{\xi}_r$ parameter space similar to that shown in Lee & Pope [8].

The following section describes the model problem and governing equations. This is followed by the definition of the parameter range of interest in $(\text{Da}, \hat{\xi}_r)$ space and the associated flow regimes in Section 3. Following this is a description of the self-similar thermochemistry (SSTC) in Section 4. Section 5 describes the conditional moment closure (CMC) model and determination of the range of self-similarity of the SSTC. It concludes with estimates for the computational cost to perform PDF simulations of the periodic reaction zone model problem with the SSTC. Results for a range of parameters using

the PDF approach with the IEM mixing model and the EMST mixing model are then presented. It is found that the models are in good agreement for large values of the reaction zone thickness parameter $\hat{\xi}_r$, but there are significant differences for small values of $\hat{\xi}_r$. These differences are discussed in the light of the modeling assumptions inherent in each model and summarized in the final section.

2 Periodic reaction zones model problem

The velocity field in this model problem is constant-density, statistically stationary, homogeneous isotropic turbulence. At high Reynolds number the velocity field can be characterized by ϵ , the mean dissipation rate and k , the kinetic energy of the turbulence. A mean turbulent frequency $\langle \omega \rangle$ ($\langle \omega \rangle \equiv \epsilon/k$), and a velocity scale $u' (= \sqrt{2k/3})$ can be defined in terms of k and ϵ . These quantities can then be used to define a characteristic lengthscale $l = u'^3/\epsilon$ and timescale $\tau = k/\epsilon$ of the turbulence.

The thermochemical state of the fluid is characterized by two composition variables: the mixture fraction $\xi(\mathbf{x}, t)$ and the reaction progress variable $Y(\mathbf{x}, t)$. The mixture fraction is a conserved passive scalar and evolves by

$$\frac{D\xi}{Dt} = \Gamma \nabla^2 \xi, \quad (3)$$

where Γ is the molecular diffusivity. The fluctuating mixture fraction field is defined as

$$\xi(\mathbf{x}, t) = \xi(\mathbf{x}, t) - \langle \xi \rangle(\mathbf{x}, t).$$

In Lee & Pope [8], the mean mixture fraction field is homogeneous, and a statistically homogeneous, periodic, statistically stationary fluctuating mixture fraction field is generated by artificial forcing. In the present work a gradient in the mean mixture fraction field is imposed in the x_2 direction which results in a more realistic “flame brush”. The simplest way to achieve this is to impose a linear gradient $\partial \langle \xi \rangle / \partial x_2 = \text{constant}$. This results in a periodic, statistically homogeneous fluctuating mixture fraction field, which attains statistical stationarity after sufficient time has evolved for the flow to equilibrate. The mixture fraction variance evolution is given by

$$\frac{\partial \langle \xi^2 \rangle}{\partial t} = -2 \langle \xi u_2 \rangle \frac{\partial \langle \xi \rangle}{\partial x_2} - \langle \chi \rangle, \quad (4)$$

where the terms on the r.h.s. are production of mixture fraction variance due to the imposed mean mixture fraction gradient, and scalar dissipation

$$\langle \chi \rangle \equiv 2\Gamma \left(\frac{\partial \xi}{\partial x_k} \frac{\partial \xi}{\partial x_k} \right).$$

In stationary isotropic turbulence, the fluctuating mixture fraction field decays in the absence of mean gradient production. The mixing timescale, which is the characteristic timescale for decay of mixture fraction variance $\xi'^2 = \langle \xi^2 \rangle$, is given by

$$\tau_\phi \equiv \xi'^2 / \langle \chi \rangle. \quad (5)$$

For non-zero values of the imposed linear gradient, the mixture fraction variance attains a stationary value when there is a balance between production and scalar dissipation [12]. It is also found that the pdf of mixture fraction is close to a Gaussian.

The reaction progress variable evolution is given by

$$\frac{DY}{Dt} = \Gamma \nabla^2 Y + S(\xi, Y), \quad (6)$$

where $S(\xi, Y)$ is the reaction rate and the molecular diffusivity Γ is taken to be equal to the mixture fraction diffusivity.

A new thermochemical model is developed for a one-step reversible reaction (fuel + oxidant \rightleftharpoons product), which is similar to the one used in Lee and Pope [8]. For the sake of clarity, only the features of the thermochemistry pertinent to this section are presented here. A more complete description is given in Ref. [8]. The reaction progress variable Y is the mass fraction of product. At chemical equilibrium, Y adopts the value $Y_e(\xi)$ which is specified as an analytic expression in terms of ξ and the stoichiometric value of the mixture fraction ξ_s ($0 < \xi_s < 1$). The reaction rate as a function of composition (ξ, Y) is also given by an analytic expression. (The exact specification of these functions and the rationale for developing this thermochemical model is deferred until Sections 3 & 4.) For a stoichiometric mixture fraction of 0.5, Fig. 1 shows a sketch of the equilibrium function and the reaction rate contours.

In combustion problems with two uniform reactant streams, ξ is usually defined as a conserved scalar that goes from zero in one reactant stream (say the oxidant stream) to unity in the second reactant stream (fuel). For the purposes of numerical simulation (either for DNS or PDF) a linear gradient in $\langle \xi \rangle$ can be imposed in a computational box of length L in the x_2 direction with $\partial \langle \xi \rangle / \partial x_2 = \Delta \xi_L / L$, with $\langle \xi \rangle(x_2 = 0) = 0$, and $\langle \xi \rangle(x_2 = L) = \Delta \xi_L$ (if the mean mixture fraction is to range from 0 to 1 in the computational box, the jump in mean mixture fraction $\Delta \xi_L$ over length L is unity). However, within the domain $0 \leq x_2 \leq L$, the mixture fraction takes on values $\xi < 0$ and $\xi > \Delta \xi_L$ (if $\Delta \xi_L \geq 1$, then ξ can also be greater than unity). In DNS, periodic boundary conditions are applied which is equivalent to extending the solution domain periodically in all spatial directions. In particular, the periodic boundary condition on ξ implies

$$\xi(x_1, x_2 + mL, x_3, t) = \xi(x_1, x_2, x_3, t), \quad m \text{ integer.}$$

Consequently, for the general interval $mL \leq x_2 \leq (m+1)L$, the mean mixture fraction $\langle \xi \rangle$ ranges from $m\Delta \xi_L$ to $(m+1)\Delta \xi_L$, and hence for any finite $\Delta \xi_L$, ξ is an unbounded variable over the whole domain. Consequently for this model problem it is necessary to extend the definition of the thermochemistry for all values of ξ such that

- (i) periodic boundary conditions may be applied to Y also, so that Y is periodic in ξ space.
- (ii) within each interval $[mL, (m+1)L]$ there is a flame brush.
- (iii) at sufficiently high Da (far from extinction) Y becomes statistically stationary.

One way to attempt to do this is to simply extend the thermochemistry by periodically repeating the thermochemistry in the $[0,1]$ mixture fraction interval as depicted in Fig. 2,

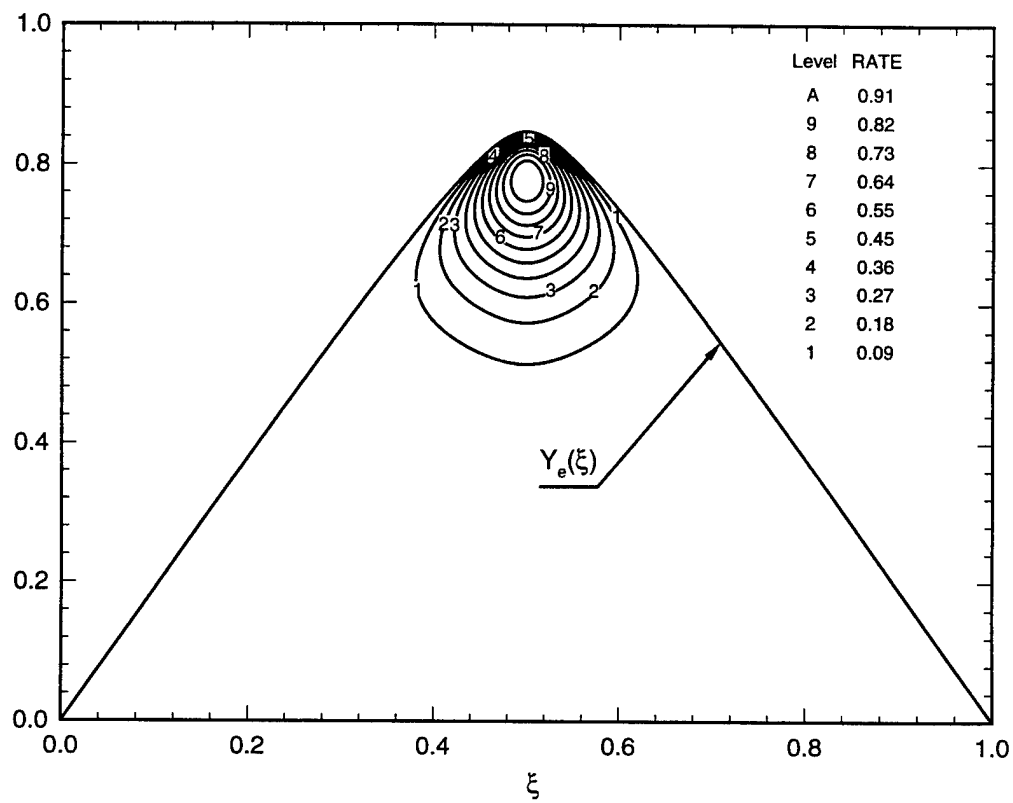


Figure 1: Sketch of the equilibrium function $Y_e(\xi)$ and reaction rate contours $S(\xi, Y)$ for model thermochemistry.

namely

$$Y_e(\xi) = Y_e(\xi - \lfloor \xi \rfloor), \xi \notin [0, 1], \quad (7)$$

$$S(\xi, Y) = S(\xi - \lfloor \xi \rfloor, Y), \xi \notin [0, 1], \quad (8)$$

where $\lfloor \xi \rfloor$ is the largest integer smaller than ξ . However, this simple periodic extension

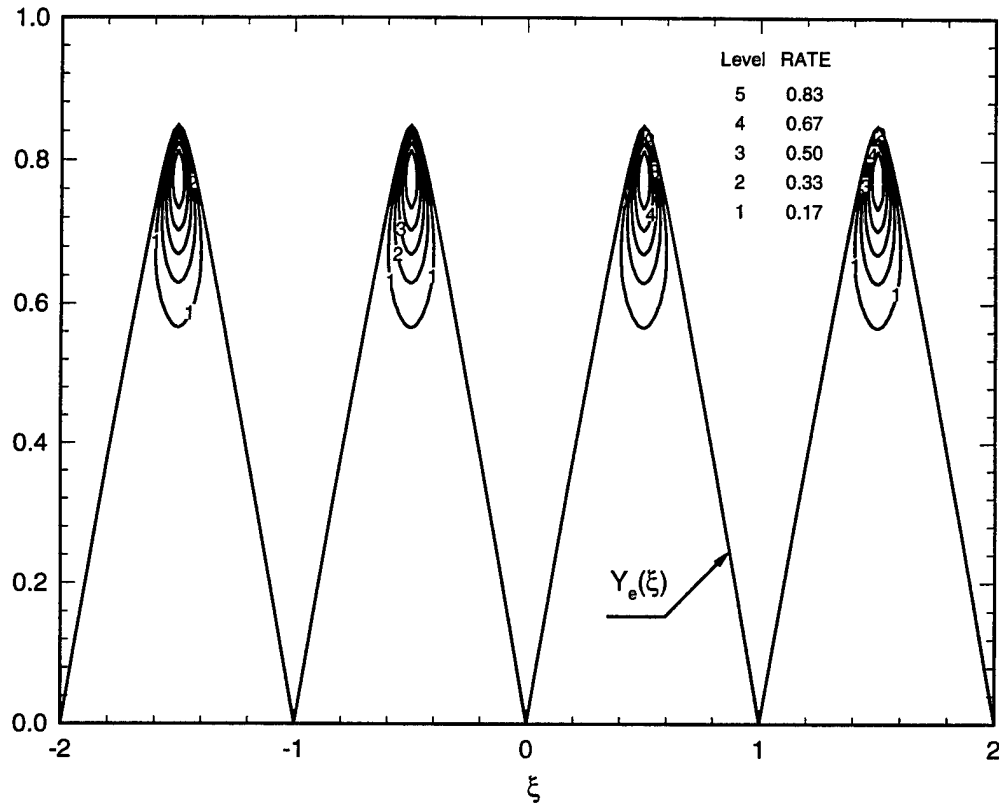


Figure 2: Symmetric extension of the thermochemistry: equilibrium function and reaction rate contours are shown.

is unsuitable since it cannot result in a non-trivial stationary solution corresponding to stable reaction (cf. (iii)). Consider the volume average of the mean progress variable

$$[\langle Y \rangle]_L(t) \equiv \frac{1}{L} \int_0^L \langle Y \rangle(x_2, t) dx_2.$$

Since in this periodic extension the reaction rate function is always non-negative ($S(\xi, Y) \geq 0$), the volume average of $\langle Y \rangle$ must always increase (except for the case where the reaction rate is zero everywhere). This implies that there are only two trivial stationary solutions to the problem: either the flow is in chemical equilibrium everywhere ($Y = Y_e$) or there is no product anywhere ($Y = 0$ everywhere). Clearly this extension procedure is not useful for studying the range of combustion phenomena which are of interest.

The alternative extension procedure that is used here is to first extend the thermochemistry in the $[0,1]$ mixture fraction interval “anti-symmetrically” to the $[-1,0]$ interval, and then periodically repeat the structure in the mixture fraction interval $[-1,1]$ as depicted in Fig. 3, specifically

$$Y_e(\xi) = Y_e(\xi - \lfloor \xi \rfloor), \xi \in [2m, 2m+1], \quad (9)$$

$$Y_e(\xi) = -Y_e(\lceil \xi \rceil - \xi), \xi \in [2m-1, 2m], \quad (10)$$

$$S(\xi, Y) = S(\xi - \lfloor \xi \rfloor, Y), \xi \in [2m, 2m+1], \quad (11)$$

$$S(\xi, Y) = -S(\lceil \xi \rceil - \xi, Y), \xi \in [2m-1, 2m], \quad (12)$$

where $\lceil \xi \rceil$ is the smallest integer larger than ξ . In order for the mean mixture fraction to

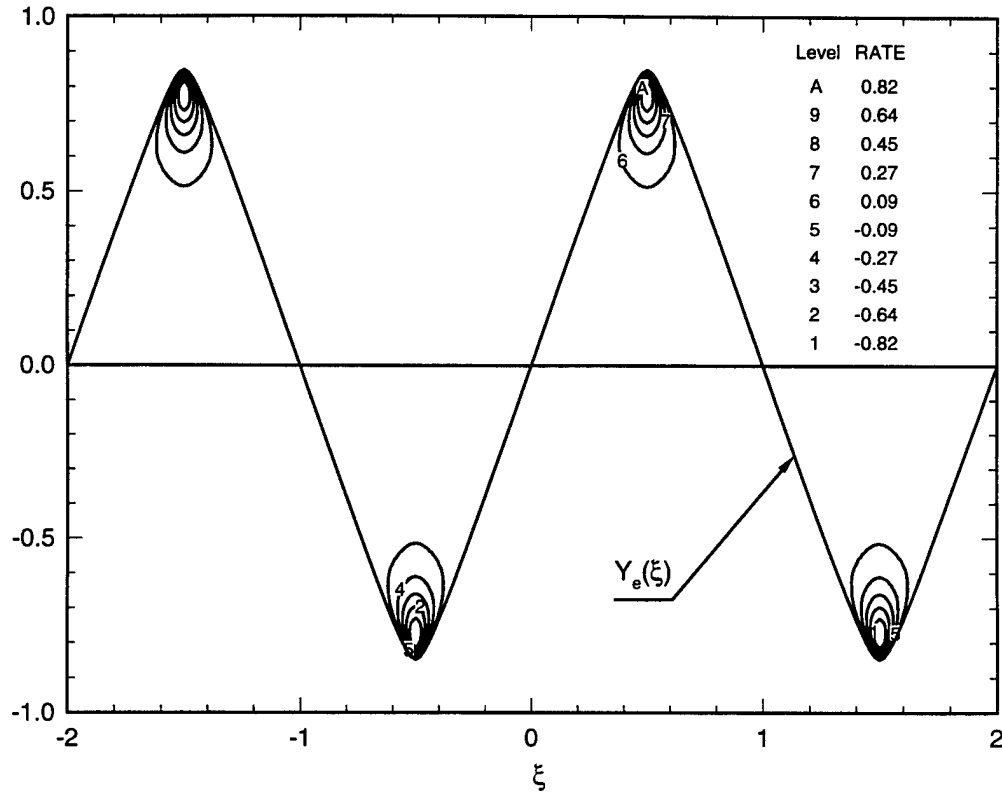


Figure 3: Antisymmetric extension of the thermochemistry: equilibrium function and reaction rate contours are shown.

extend over one period of the antisymmetric extension of the thermochemistry ($\langle \xi \rangle(x_2 = 0) = 0, \langle \xi \rangle(x_2 = L) = 2$), the jump in the mean mixture fraction over the length L is given by

$$\Delta\xi_L = 2. \quad (13)$$

This implies that the gradient in the mean mixture fraction is $\partial\langle \xi \rangle / \partial x_2 = \Delta\xi_L / L = 2/L$. Since each reaction zone period is statistically identical, it is sufficient to simulate only one such period.

The alternating positive and negative equilibrium functions can be interpreted as zones corresponding to flames and “anti–flames”. In the interval $\xi \in [2m, 2m + 1]$, which is interpreted as a flame, reactants enter from either end of the interval and are converted to product which leaves the interval due to transport. In the interval $\xi \in [2m - 1, 2m]$, which is interpreted as an “anti–flame”, “anti–reactants” (which are products leaving the adjacent flame zones) enter from either end of the interval and are converted to “anti–product” (which is reactant) which again leaves the interval due to transport. See Fig 3. Each interval in mixture fraction space $\xi \in [2m, 2m + 1]$, is a statistically identical copy of the interval $\xi \in [0, 1]$ and similarly for the “anti–flame” intervals – each interval in mixture fraction space $\xi \in [2m - 1, 2m]$, is a statistically identical copy of the interval $\xi \in [-1, 0]$. Furthermore, each fluid particle in the “anti–flame” interval with composition (ξ, Y) is statistically identical to a fluid particle in the mixture fraction interval $[0, 1]$ with composition $([\xi] - \xi, -Y)$. See Fig 3. As a consequence, even though in this model problem the mixture fraction and progress variable take on seemingly “unphysical” values outside the interval $[0, 1]$, they can be interpreted in physical terms by the mathematical relations in the preceding paragraph.

Flames and anti–flames are separated by the constant–property surfaces, $\xi(\mathbf{x}, t) = \text{integer}$. (These surfaces are time–dependent and each one is not necessarily connected.) In order to conform with the idea that $\xi = 0$ and $\xi = 1$ correspond to pure reactants (i.e., $Y = 0$), the boundary condition ($Y = 0$) is imposed on the surfaces $\xi = \text{integer}$.

3 Parameters determining the reacting flow regime

In this section the accessible parameter range for performing PDF simulations of the periodic reaction zone problem is determined, and the development of the self–similar thermochemistry is motivated. These considerations are also central to determining the accessible range for the associated DNS study which is currently underway.

At fixed Reynolds number, the extinction characteristics of a turbulent nonpremixed reactive flow are determined by the reaction zone thickness parameter $\hat{\xi}_r$ ($\equiv \Delta\xi_r / \xi'$) and the Damköhler number. The reaction zone thickness $\Delta\xi_r$, is a measure of the width of the reaction rate function in mixture fraction space (details are provided in Section 4). For low values of $\hat{\xi}_r$ the fluctuations in mixture fraction are large relative to the reaction zone thickness and the reaction is confined to thin reaction sheets in physical space. Large values of $\hat{\xi}_r$ correspond to broad reaction zones where fluctuations in mixture fraction at a physical location with $\langle \xi \rangle = \xi_s$ are contained entirely within the reaction zone.

Direct numerical simulations of *homogeneous* nonpremixed combustion [8] indicate that the critical Damköhler number (the smallest Damköhler number, or range of Damköhler number values, below which stable combustion cannot be sustained) scales like $\hat{\xi}_r^{-2.3}$, while simpler models such as CMC (and simple scaling arguments) predict a scaling like $\hat{\xi}_r^{-2}$. It has been shown that the small difference in the exponents could be due to statistical variability [8]. In spite of the spatial inhomogeneity present in the current model problem, it is reasonable to expect similar scalings for the periodic reaction zones problem. In other words, higher critical Damköhler numbers may be expected for thin reaction sheets compared to broad reaction zones. It is also expected that the model for molecular mixing will have a significant effect on the prediction of critical Damköhler corresponding to extinction in the thin reaction sheet limit [16].

The objective of this study is to perform simulations for reaction zone thickness values varying from a few tenths to as much as ten times the r.m.s. mixture fraction. Specifically, the aim is to access the range $0.3 \leq \hat{\xi}_r \leq 10$.

In order to gain a better understanding of the influence of the Damköhler number and $\hat{\xi}_r$ on extinction in the model problem, it is necessary to perform spatio-temporally well-resolved simulations for a broad range of these parameters. The implication of the scaling $Da \sim \hat{\xi}_r^{-2}$ is that once a desired range of $\hat{\xi}_r$ is chosen, the range of Damköhler numbers to be investigated for extinction is automatically determined by the physics of the problem. The rest of this section is devoted to determining the broadest parameter range in $Da-\hat{\xi}_r$ space that is accessible to simulation at reasonable computational expense.

The reaction zone thickness parameter $\hat{\xi}_r$ may be varied by changing either the stationary value of the r.m.s. mixture fraction ξ' , or the reaction zone thickness in mixture fraction space $\Delta\xi_r$. If $\hat{\xi}_r$ is varied by changing ξ' , keeping $\Delta\xi_r$ fixed, then it is legitimate to compare the results obtained for each $\hat{\xi}_r$ value. This is the approach adopted by Lee & Pope [8]. However, for the periodic reaction zone model problem there are limits on both the maximum and minimum values of the r.m.s. mixture fraction ξ' .

3.1 Upper limit on ξ'

The limitation on maximum ξ' arises from the requirement that flame brushes not overlap in physical space which is in accord with the physical picture of reacting flows. In mixture fraction space the flame brush (of $\xi \approx \xi_s$) is in the interval $[\xi_s - \Delta\xi_r/2, \xi_s + \Delta\xi_r/2]$. At any given x_2 location in physical space, there is a non-negligible probability of the instantaneous mixture fraction lying in this flame brush (i.e., $\xi \in [\xi_s - \Delta\xi_r/2, \xi_s + \Delta\xi_r/2]$) if

$$\langle \xi \rangle(x_2) \pm 2\xi' \in [\xi_s - \frac{\Delta\xi_r}{2}, \xi_s + \frac{\Delta\xi_r}{2}],$$

which may be restated as

$$\langle \xi \rangle(x_2) \in [\xi_s - \frac{\Delta\xi_r}{2} - 2\xi', \xi_s + \frac{\Delta\xi_r}{2} + 2\xi'].$$

See Fig. 4. In mixture fraction space the flame brushes are centered at the mixture fraction values $\xi = \dots - \xi_s, \xi_s, 2 - \xi_s, 2 + \xi_s, \dots$. The requirement that the probability of adjacent flame brushes (located in mixture fraction space at say ξ_s and $2 - \xi_s$) overlapping at the same physical location x_2 be negligible, may be quantified as follows:

$$2 - \xi_s - \frac{1}{2}\Delta\xi_r - 2\xi' \geq \xi_s + \frac{1}{2}\Delta\xi_r + 2\xi'.$$

The largest possible ξ' corresponding to non-overlapping (distinct) flame brushes in physical space is achieved by choosing $\xi_s = 0.5$, and is determined by the inequality

$$4\xi' \leq 1 - \Delta\xi_r. \quad (14)$$

For a given value of the reaction zone thickness $\Delta\xi_r$ in mixture fraction space (corresponding to a particular fixed choice of parameters in the model thermochemistry), the limitation on maximum r.m.s. mixture fraction ξ' in Eq. 14 imposes a lower bound on the reaction zone thickness parameter $\hat{\xi}_r$. Choosing a representative value of $\Delta\xi_r = 0.232$ (corresponding to that used in the simulations of Lee & Pope [8]) results in a minimum

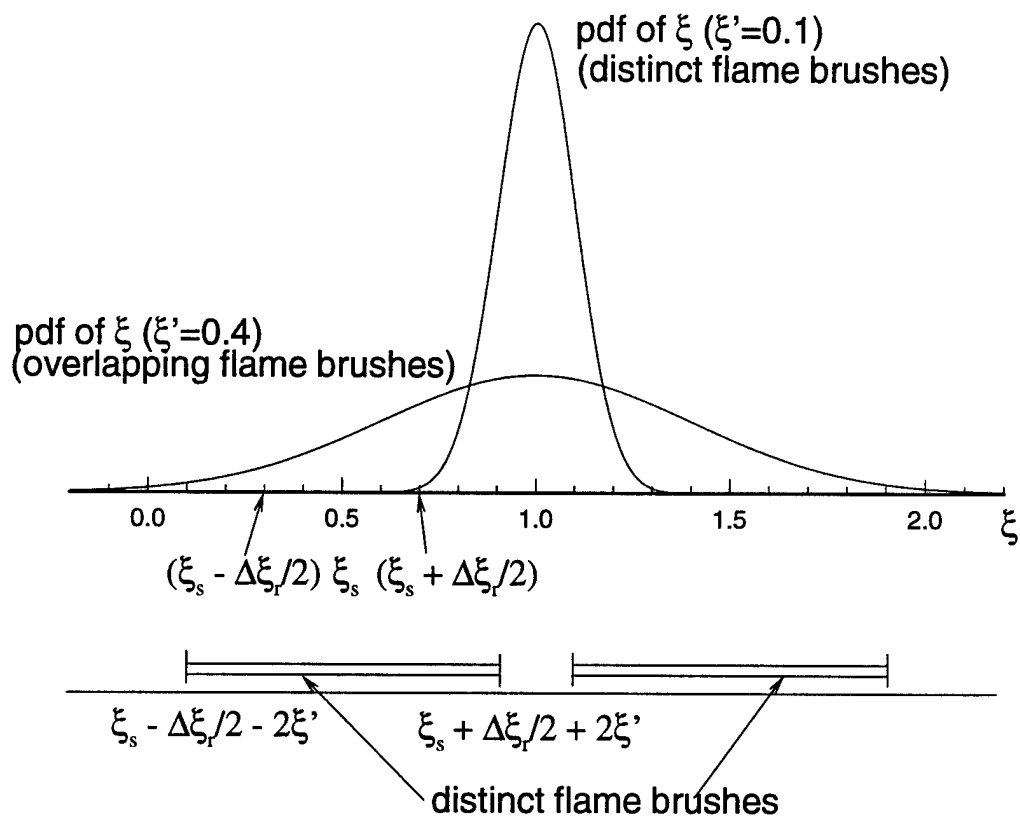


Figure 4: Sketch showing the variation in the width of the flame brush for different values of the stationary r.m.s. mixture fraction ξ' .

$\hat{\xi}_r$ value of 1.2. Since the objective of this study is to perform simulations for reaction zone thickness values down to a few tenths of the r.m.s. mixture fraction, the only way to access this parameter range is by changing the reaction zone thickness $\Delta\xi_r$ itself.

3.2 Lower limit on ξ'

The limitation on minimum ξ' arises from considerations of computational expense. In the periodic reaction zones problem the mixture fraction variance attains a stationary value when the production due to mean gradient balances the scalar dissipation in Eq. 4. The r.m.s. value of the stationary mixture fraction scales as:

$$\xi' \sim \frac{\partial \langle \xi \rangle}{\partial x_2} \times l. \quad (15)$$

If the length of the computational domain in the x_2 direction is L and $\Delta\xi_L$ is the jump in mean mixture fraction across the domain, then substituting

$$\frac{\partial \langle \xi \rangle}{\partial x_2} = \frac{\Delta\xi_L}{L},$$

the r.m.s. mixture fraction scaling can be written as

$$\xi' \sim \Delta\xi_L \frac{l}{L}. \quad (16)$$

Since there is only a single reaction zone period in $[0, L]$ (Eq. 13), the stationary r.m.s. mixture fraction can be varied only by changing l/L , the ratio of the turbulence length scale to the computational box-length. However, increasing the ratio l/L results in an increase in computational cost of the simulation. This becomes apparent on examining the evolution equation for $\langle Y \rangle$, which is obtained by taking the expectation of both sides of Eq. 6:

$$\frac{\partial \langle Y \rangle}{\partial t} = -\frac{\partial \langle u_2 Y \rangle}{\partial x_2} + \langle S \rangle. \quad (17)$$

The mean reaction progress variable evolves due to transport (first term on the r.h.s.) and mean reaction rate. Assuming simple gradient transport, one may write

$$\langle u_2 Y \rangle = -\gamma_t \frac{\partial \langle Y \rangle}{\partial x_2}, \quad (18)$$

where γ_t is a turbulent diffusivity. The transport term can now be written as

$$\frac{\partial \langle u_2 Y \rangle}{\partial x_2} = -\gamma_t \frac{\partial^2 \langle Y \rangle}{\partial x_2^2}. \quad (19)$$

If Y_0 is the characteristic scale for $\langle Y \rangle$, and L is the box-length, then the transport term in the $\langle Y \rangle$ equation can be estimated as

$$\frac{\partial \langle u_2 Y \rangle}{\partial x_2} \sim -\gamma_t \frac{Y_0}{L^2}.$$

Following standard eddy–viscosity modeling assumptions, the turbulent diffusivity may be estimated by the relation

$$\begin{aligned}\gamma_t &= \frac{\nu_t}{\text{Pr}} \\ &= \frac{C_\mu}{\text{Pr}} \frac{k^2}{\epsilon} \\ &= \frac{C_\mu}{\text{Pr}} \left(\frac{3}{2}\right)^3 \frac{l^2}{\tau},\end{aligned}$$

where Pr is the turbulent Prandtl number. The timescale for transport can be estimated to be:

$$T_t \sim \frac{L^2}{\gamma_t} \approx C_t \left(\frac{L}{l}\right)^2 \tau, \quad (20)$$

where C_t is a constant, empirically determined to be 0.04 by fitting to data obtained from simulations of the inert flow ($S = 0$) for different box-lengths L . For $L = 9.34$, this empirical relation yields $T_t = 5.23$. See Fig. 5.

Using the relation in Eq. 16, the transport timescale can be shown to vary inversely with the mixture fraction variance:

$$T_t \sim \left(\frac{1}{\xi'}\right)^2. \quad (21)$$

In order to obtain stationary solutions to the periodic reaction zones problem the simulations must be run to a time T_s , which is larger than the largest physical timescale in the problem. In this problem, for the range of parameters being considered, the largest physical timescale is the transport timescale T_t . Therefore it is required that the simulations be run for 3 to 4 times the transport timescale ($T_s \sim [3 - 4]T_t$). Given finite computational resources, Eq. 21 imposes a limit on the minimum ξ' that can be achieved in the simulations.

3.3 Variation of $\Delta\xi_r$

These limits on the extreme values of ξ' imply that the variation in $\hat{\xi}_r$ will have to be accomplished in part by changing the reaction zone thickness $\Delta\xi_r$. Since the reaction zone thickness $\Delta\xi_r$ is a derived thermochemical parameter (i.e., it is not one of the parameters used to define the thermochemistry, but is implied by the choice of defining parameters and the thermochemical functions), it can only be specified indirectly. However, even a simple two-variable thermochemistry such as the Lee–Pope thermochemistry [8] requires the specification of many such secondary parameters in order to define the thermochemistry.

The primary parameters are the reaction zone thickness ($\Delta\xi_r$) and the chemical timescale (τ^*), which in turn determine the non-dimensional reaction zone thickness $\hat{\xi}_r$ and the Damköhler number (Da) respectively. Since the solutions to the periodic reaction zones model problem are to be parametrized only by these two non-dimensional quantities ($\hat{\xi}_r$ and Da), the thermochemistry needs to be specified such that the solutions are the same for a given value of $\hat{\xi}_r$ ($= \Delta\xi_r / \xi'$), for different values of $\Delta\xi_r$. This requires that the secondary parameters in the thermochemistry specification change with

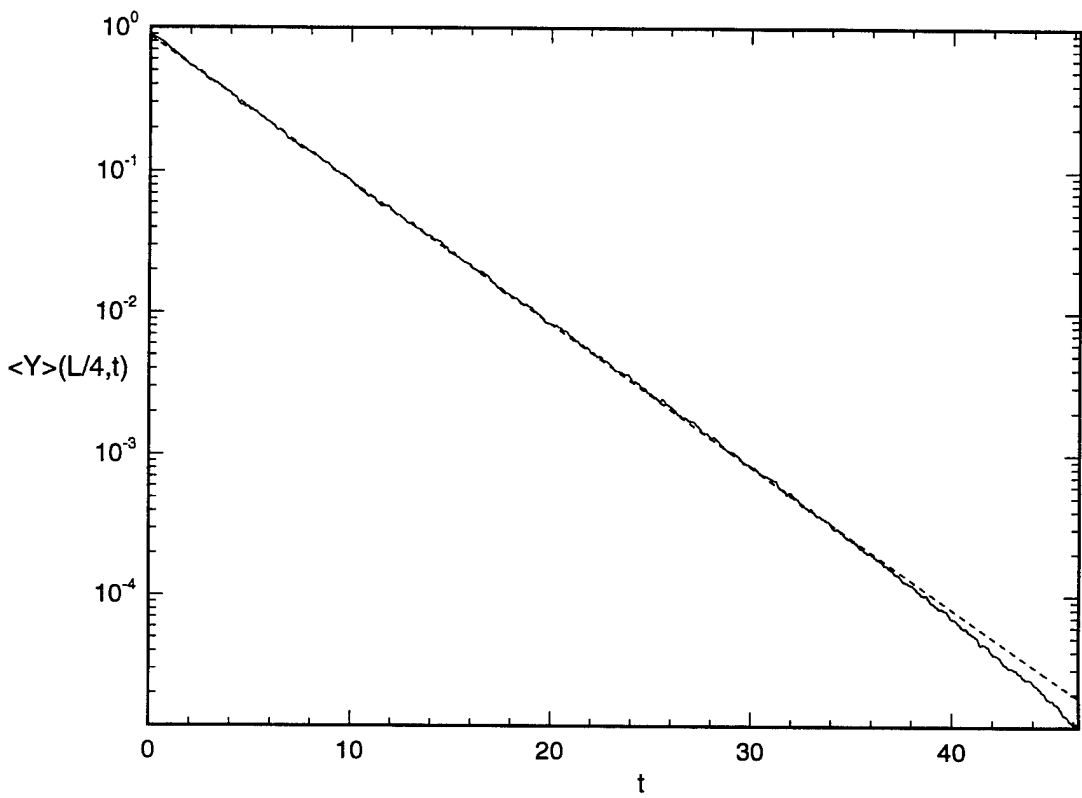


Figure 5: Inert case $\langle Y \rangle$ decay test: — $\langle Y \rangle(L/4, t)$, - - - $\langle Y \rangle(L/4, 0) \times \exp(-t/4.3)$. The length of the domain $L = 9.34$ and the transport timescale estimated from the plot is 4.3. The characteristic timescale of the turbulence τ is 1.5 time units. The empirical relation $T_t = C_t(L/l)^2 \tau$ gives $T_t = 5.23$.

$\Delta\xi_r$ such that indeed $\Delta\xi_r$ and τ^* completely determine the thermochemistry. Thermochemistry specifications that do not possess this property will result in solutions that differ, depending on the choice of secondary thermochemical parameters, even for the same values of $\hat{\xi}_r$ and τ^* . Since the Lee–Pope thermochemistry [8] does not possess the feature that $\Delta\xi_r$ and τ^* completely determine the thermochemistry, a new thermochemistry specification is developed. This self-similar thermochemistry, which possesses the desired features (to an extent), is now described in the next section.

4 Self-similar thermochemistry

The self-similar thermochemical model consists of a specification for the equilibrium function $Y_e(\xi)$, ($0 \leq \xi \leq 1$) and the reaction rate function $S(\xi, Y)$ (or equivalently, $S(\xi, y)$, where $y = Y_e - Y$). In any two-variable thermochemistry there are two important mixture fraction scales in the reaction zone in composition space. One of these is the reaction zone thickness $\Delta\xi_r$ which measures the width of the reaction rate function. The other mixture fraction scale, denoted $\Delta\xi_e$, is associated with the curvature of the equilibrium function in mixture fraction space:

$$Y_e''(\xi) \equiv \frac{d^2Y_e(\xi)}{d\xi^2}.$$

The quantity $Y_e''(\xi)$ plays a central role in the theory of turbulent diffusion flames and this is made clear when the evolution equation for the perturbation-from-equilibrium field $y(\mathbf{x}, t) = Y_e(\xi[\mathbf{x}, t]) - Y(\mathbf{x}, t)$, is considered. The perturbation field $y(\mathbf{x}, t)$ is always non-negative in the “flame” intervals and is always non-positive in the “anti-flame” intervals. The equation for the perturbation in the progress variable reveals the influence of the thermochemistry on the evolution equations clearly, and is derived by substituting the definition of y in Eq. (6) and using Eq. (3) to arrive at:

$$\frac{\partial y}{\partial t} = -\frac{\partial(u_2 y)}{\partial x_2} + \Gamma \nabla^2 y - \Gamma \nabla \xi \cdot \nabla \xi Y_e''(\xi) - S, \quad (22)$$

where $Y_e''(\xi)$ is the second derivative of the equilibrium function with respect to ξ . Taking expectations of Eq. 22 results in the evolution equation of $\langle y \rangle$:

$$\frac{\partial \langle y \rangle}{\partial t} = -\frac{\partial \langle u_2 y \rangle}{\partial x_2} + \Gamma \nabla^2 \langle y \rangle - \Gamma \langle \nabla \xi \cdot \nabla \xi \rangle Y_e''(\xi) - \langle S \rangle. \quad (23)$$

The terms on the r.h.s. of Eq. 23 are turbulent transport in the x_2 direction, molecular transport, the microscale mixing term

$$Z \equiv -\Gamma \langle \nabla \xi \cdot \nabla \xi \rangle Y_e''(\xi),$$

and mean reaction respectively. The molecular transport term is negligible at high Peclét number. The stability of combustion is determined by the relative magnitudes of the transport in the x_2 direction, the microscale mixing term, and the reaction term. Confining our attention to the “flame” zones, it is seen that the transport term $\partial \langle u_2 y \rangle / \partial x_2$ is always negative, such that it transports reacting fluid out of the reaction zones, forcing y toward positive values. The microscale mixing term is positive and also drives $\langle y \rangle$ away

from zero to positive values. Reaction restores $\langle y \rangle$ toward its equilibrium value of zero at stable combustion.

In order to make sensible comparisons across different $\hat{\xi}_r$ values (which correspond to combinations of different $\Delta\xi_r$ values and ξ' values) it is important that the relative influence of the two mixture fraction scales $\Delta\xi_e$ and $\Delta\xi_r$, as they manifest themselves in Eq. 23, be maintained across the range of $\hat{\xi}_r$ values. This can be accomplished if the reaction zone thickness $\Delta\xi_r$ can be varied while keeping the ratio $\Delta\xi_r / \Delta\xi_e$ constant and also preserving the scaling of each of the terms in Eq. 23. The Lee–Pope thermochemistry [8] does not permit such a variation of $\Delta\xi_r$ through variation of its thermochemical parameters.

In the self-similar thermochemistry it is required that these thermochemical functions $[Y_e(\xi), S(\xi, y)]$ be specified in such a way that they preserve the ratio of mixture fraction scales $\Delta\xi_r / \Delta\xi_e$ and the relative magnitude of the terms in Eq. 23. With this objective in mind, first the scaled version of Eq. 23 is derived. Following this is a brief recapitulation of the important features of the Lee–Pope thermochemistry. This is done with two objectives in mind. First it elucidates the fact that the family of Lee–Pope thermochemical functions does not possess the desired scaling. Secondly, since the SSTC has several other features in common with the Lee–Pope thermochemistry, it facilitates understanding the new thermochemistry. Finally it is shown how the two thermochemistry specifications may be matched.

The scale for the mixture fraction ξ in the thermochemical functions is chosen to be $\Delta\xi_e$. The scaled mixture fraction $\hat{\xi}$ is defined as follows:

$$z = \xi - \xi_{ss} \quad (24)$$

$$\hat{\xi} = z / \Delta\xi_e, \quad (25)$$

where $\xi_{ss} \in [0, 1]$ which is the origin of the similarity variable $\hat{\xi}$ will be defined later in the section. The perturbation variable y is scaled with respect to y_0 (which is to be determined from the condition for similarity) such that

$$\hat{y} = \frac{y}{y_0}. \quad (26)$$

The thermochemical functions will be specified in terms of the similarity variables $(\hat{\xi}, \hat{y})$ such that for fixed parameters in the thermochemistry, Eq. 23 will become self-similar. Following this idea, the curvature of the equilibrium function $Y_e''(\xi)$ is scaled by its maximum value, such that

$$Y_e''(\xi) = |Y_e''_{\max}| F(\hat{\xi}). \quad (27)$$

The reaction rate function is written as

$$S(\xi, y) = \bar{S}(\xi, y) / \tau_c, \quad (28)$$

where τ_c is a chemical timescale which determines the magnitude of the reaction rate. Thus for a fixed shape of the reaction rate function $\bar{S}(\xi, y)$, the magnitude of the reaction rate term in Eq. 23 can be changed by specifying τ_c . Thus different Damköhler numbers can be simulated easily by simply changing τ_c . The shape of the function $\bar{S}(\xi, y)$ has an implicit dependence on the two thermochemical mixture fraction scales $\Delta\xi_r$ and $\Delta\xi_e$:

$$\bar{S}(\xi, y) = \bar{S}(\xi, y; \Delta\xi_r, \Delta\xi_e).$$

The ratio $\Delta\xi_r/\Delta\xi_e$ is to be maintained constant. Then the thermochemistry is determined by one scale, say $\Delta\xi_e$, and variations in $\Delta\xi_r$ are achieved by varying $\Delta\xi_e$. In short, it is required that

$$\bar{S}(\xi, y; \Delta\xi_r/\Delta\xi_e, \Delta\xi_e) = \bar{S}(\hat{\xi}, \hat{y}; \Delta\xi_e).$$

The microscale mixing term Z can be expressed as

$$\begin{aligned} Z &= -\Gamma \langle \nabla \xi \cdot \nabla \xi \rangle Y_e''(\xi) \\ &= -\left\{ \Gamma \left(\frac{\Delta\xi_L}{L} \right)^2 + \frac{1}{2} \langle \chi \rangle \right\} Y_e''(\xi) \\ &\approx -\frac{1}{2} \langle \chi \rangle Y_e''(\xi), \end{aligned}$$

the approximation being valid at high Péclet number. This approximate expression for the microscale mixing term may be scaled as

$$Z \approx -\frac{1}{2} \frac{\xi'^2}{\tau_\phi} \widehat{\langle \chi \rangle} |Y_e''_{\max}| F(\hat{\xi}) \quad (29)$$

$$= -\frac{1}{2} \widehat{\langle \chi \rangle} F(\hat{\xi}) \frac{1}{\tau_\phi \hat{\xi}_r^2} \left(\frac{\Delta\xi_r}{\Delta\xi_e} \right)^2 \Delta\xi_e^2 |Y_e''_{\max}|, \quad (30)$$

where $\widehat{\langle \chi \rangle}$ is the scaled scalar dissipation. Again in the above equation, the ratio $\Delta\xi_r/\Delta\xi_e$ is to be maintained constant.

Substituting the relations in Eqs. 25–30 into the mean perturbation evolution equation Eq. 23 yields the evolution of the mean scaled perturbation \hat{y} in terms of the similarity variables:

$$\frac{\partial \langle \hat{y} \rangle}{\partial t} = -\frac{\partial \langle u_2 \hat{y} \rangle}{\partial x_2} + \Gamma \nabla^2 \hat{y} - \frac{(\Delta\xi_e)^2 |Y_e''_{\max}|}{y_0} F(\hat{\xi}) \widehat{\langle \chi \rangle} \frac{1}{\tau_\phi \hat{\xi}_r^2} \left(\frac{\Delta\xi_r}{\Delta\xi_e} \right)^2 - \frac{\bar{S}(\hat{\xi}, \hat{y}; \Delta\xi_e)}{\tau_c y_0}. \quad (31)$$

The conditions for similarity implied by Eq. 31 are that the groups

$$\frac{(\Delta\xi_e)^2 |Y_e''_{\max}|}{y_0}$$

and

$$\frac{\bar{S}(\hat{\xi}, \hat{y}; \Delta\xi_e)}{y_0}$$

be independent of $\Delta\xi_e$. First the appropriate scaling of $|Y_e''_{\max}|$ with respect to $\Delta\xi_e$ will be determined based on the asymptotic behavior of the equilibrium function (and its curvature) as $\Delta\xi_e \rightarrow 0$. This will lead to the specification of the equilibrium function. From this scaling of $|Y_e''_{\max}|$ and the similarity condition on the group $(\Delta\xi_e)^2 |Y_e''_{\max}| / y_0$, the appropriate scale y_0 will be determined. Finally the second similarity condition on the group \bar{S}/y_0 will determine the scaling of \bar{S} with respect to $\Delta\xi_e$. In order to explain the asymptotic behavior of the equilibrium function, some details of the Lee–Pope thermochemistry are reproduced from Ref. [8].

4.1 Lee–Pope thermochemistry

In the Lee–Pope thermochemistry, the value of the progress variable at equilibrium Y_e is determined by the specified stoichiometric mixture fraction ξ_s ($0 \leq \xi_s \leq 1$) and by the specified equilibrium constant K of the one-step reversible reaction



where Y_F , Y_O and Y_P represent the mass fraction of fuel, oxidizer and product respectively, r being the stoichiometric proportion of the oxidizer to fuel mass fraction. At chemical equilibrium Y_P adopts the value Y_e , and the reactant mass fractions can be written as:

$$Y_F = \xi - \xi_s Y_e \quad (33)$$

$$Y_O = (1 - \xi) - (1 - \xi_s) Y_e. \quad (34)$$

Noting that the equilibrium constant is given by

$$K = \frac{Y_e^2}{Y_F Y_O}, \quad (35)$$

yields the relation that determines $Y_e(\xi)$:

$$K = \frac{Y_e^2}{\{\xi - \xi_s Y_e\} \{(1 - \xi) - (1 - \xi_s) Y_e\}}. \quad (36)$$

From Eq. 36 one can deduce that the maximum value of Y_e , Y_{\max} , is

$$Y_{\max} = \frac{1}{1 + 2/\sqrt{K}}, \quad (37)$$

which occurs at $\xi = \xi_{\max}$:

$$\xi_{\max} = \frac{\xi_s + 1/\sqrt{K}}{1 + 2/\sqrt{K}}. \quad (38)$$

As K tends to infinity, Y_{\max} approaches unity and ξ_{\max} tends to ξ_s .

The curvature of the equilibrium function $Y_e''(\xi)$ (and its maximum value $|Y_{e\max}''|$) is determined by the values of K and ξ_s . For a given value of ξ_s , $Y_e(\xi; K)$ is a family of curves which asymptotes to straight lines in the limit of infinite K (which is the limiting case of irreversible reaction [1]). See Fig. 6. In this limit of irreversible reaction the curvature of the equilibrium function $Y_e''(\xi)$ is everywhere zero but for at $\xi = \xi_s$ where $|Y_{e\max}''|$ is infinite.

The reaction rate in the Lee–Pope thermochemistry, which is denoted S_L , is specified by

$$S_L(\xi, y) = f_L(y)g_L(\xi)/\tau_c, \quad (39)$$

where y is again the perturbation from equilibrium, τ_c is a specified timescale, and the functions f_L and g_L are given by

$$f_L(y) = B_L y \exp(1 - B_L y), \quad (40)$$

$$g_L(\xi) = \exp\{-B_L(Y_{\max} - Y_e(\xi))\}, \quad (41)$$

where B_L is a thermochemical parameter.

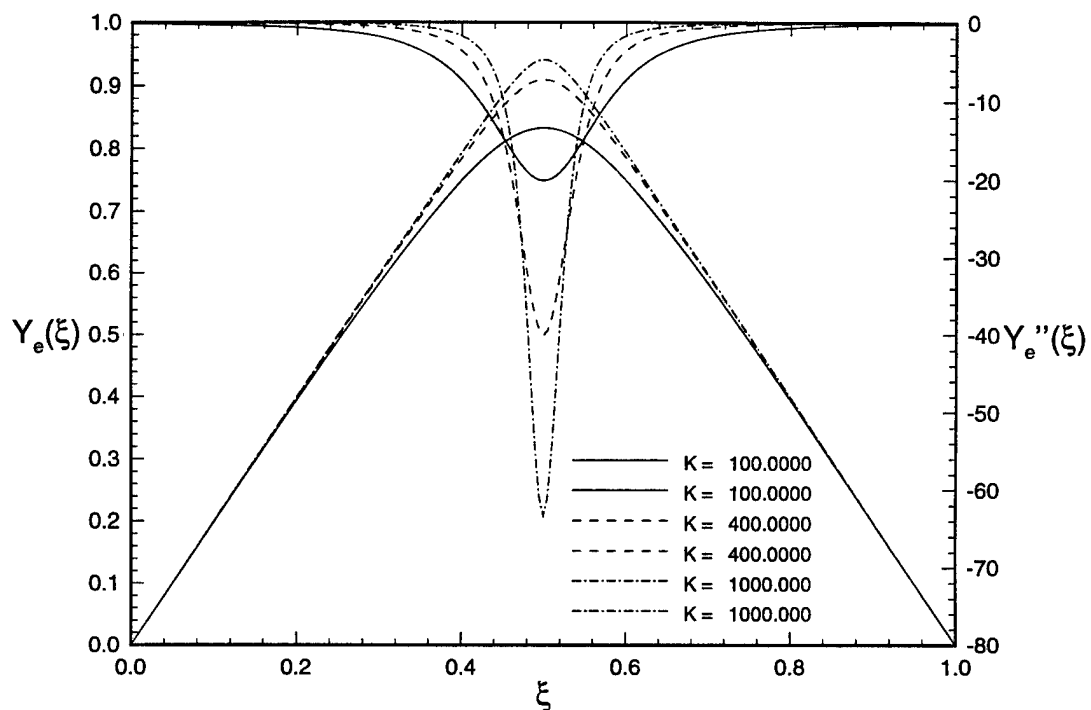


Figure 6: Equilibrium function $Y_e(\xi)$ and its second derivative $Y_e''(\xi)$ for different values of the parameter K in the Lee–Pope thermochemistry. The stoichiometric value of the mixture fraction is 0.5.

For fixed ξ_s , the parameter K controls the scale $\Delta\xi_e$. For a given equilibrium function specification (fixed ξ_s and K) the parameter B_L controls $\Delta\xi_r$. However, it is not possible to vary $\Delta\xi_r$ using K , while maintaining a fixed ratio of $\Delta\xi_r$ to $\Delta\xi_e$ with a constant value of B_L . A one-parameter family of thermochemical functions which enables such a variation of $\Delta\xi_r$ is now described.

4.2 Self-similar equilibrium function

The self-similar family of equilibrium functions is constructed such that it satisfies the following conditions. The function $Y_e(\xi)$ is zero at $\xi = 0$ and $\xi = 1$. Let ξ_{\max} denote the value of ξ where Y_e reaches its maximum value Y_{\max} . The equilibrium function increases monotonically from $\xi = 0$ to ξ_{\max} and then decreases monotonically till it reaches zero at $\xi = 1$. Consequently the second derivative Y_e'' is always non-positive. Further it must be of the form given in Eq. 27.

The nature of the function $Y_e''(\xi)$ is revealed by considering its integral, $dY_e/d\xi$, in the limit $\Delta\xi_e \rightarrow 0$. In this limit let the maximum value attained by $Y_e(\xi)$ be unity. Further let the slopes of the straight-line asymptotes to $Y_e(\xi)$ at $\xi = 0$ and $\xi = 1$ be m_1 and m_2 respectively. Then

$$\lim_{\Delta\xi_e \rightarrow 0} \left[\frac{dY_e}{d\xi} \right] = \begin{cases} m_1 = 1/\xi_s & \xi < \xi_s \\ m_2 = -1/(1 - \xi_s) & \xi > \xi_s \end{cases} \quad (42)$$

Clearly in the limit $\Delta\xi_e \rightarrow 0$, $dY_e/d\xi$ is a step function at ξ_s . It follows then that in the same limit $Y_e''(\xi)$ is proportional to a δ -function located at ξ_s . First the specification of $Y_e(\xi)$ for $\xi_s = 0.5$ is given since the expressions are simpler. The general unsymmetric case ($\xi_s \neq 0.5$) is also documented, though the simulations are performed only for the symmetric case. The symmetric case is chosen for two reasons. As already noted in Section 3, the choice of $\xi_s = 0.5$ maximizes the minimum distance between adjacent reaction zones in periodic extension of the thermochemistry. Secondly, for $\xi_s \neq 0.5$ the magnitude of the slopes of the asymptotes to the equilibrium function at $\xi = 0$ and $\xi = 1$ are not equal, whereas they are for the symmetric case. This inequality in the magnitude of the slopes results in a discontinuous $Y_e''(\xi)$ at integer values of ξ . For the symmetric case, for sufficiently small $\Delta\xi_e$, the curvature of the equilibrium function goes to zero at the integer values of ξ .

4.3 Equilibrium function $Y_e(\xi)$ for the symmetric case

When the stoichiometric mixture fraction is $\xi_s = 0.5$, the equilibrium function is symmetric. For the symmetric case, ξ_{ss} , the origin of the similarity variable, is ξ_s . The equilibrium function Y_e is specified as a function of $z = \xi - \xi_{ss} = \xi - \xi_s$. The zeros of the equilibrium function occur at $z = \pm 1/2$. The slopes of the straight-line asymptotes to $Y_e(z)$ at $z = -1/2$ and $z = 1/2$ must be $m (= 2)$ and $-m (= -2)$ respectively. In the limit of $\Delta\xi_e \rightarrow 0$, the slope of the equilibrium function is given by

$$\frac{dY_e}{dz} = 1 - 2H(z), \quad (43)$$

where $H(z)$ is the Heaviside unit step function:

$$H(z) = \begin{cases} 0 & z < 0 \\ 1 & z > 0 \end{cases}.$$

This defines the integral of d^2Y_e/dz^2 (which is proportional to a δ -function) to be -2 .

If the characteristic width of a δ -sequence function is ϵ , then its magnitude scales like $1/\epsilon$. This means that one can express a family of δ -sequence functions (parametrized by ϵ) which asymptote to a Dirac δ -function as

$$Y_e(z) \sim \frac{1}{\epsilon} F\left(\frac{z}{\epsilon}\right).$$

Comparing this with the requirement for self-similarity that $Y_e''(\xi) = |Y_{e \text{ max}}''| F(\hat{\xi})$, one can identify $\Delta\xi_e = \epsilon$ and $|Y_{e \text{ max}}''| \sim 1/\epsilon \sim 1/\Delta\xi_e$.

We choose the Cauchy distribution for representing the δ -function since it is analytically integrable twice. Thus the specification for $Y_e''(z)$ is

$$\frac{d^2Y_e}{dz^2} = -\frac{4}{\pi\Delta\xi_e} \frac{1}{\left[1 + (z/\Delta\xi_e)^2\right]}. \quad (44)$$

The maximum value of the second derivative $|Y_{e \text{ max}}''|$ is $4/(\pi\Delta\xi_e)$. Integrating Eq. (44) once with respect to z yields $Y_e'(z)$ to be

$$\frac{dY_e}{dz} = -\frac{4}{\pi} \arctan\left(\frac{z}{\Delta\xi_e}\right). \quad (45)$$

In the limit

$$\lim_{\Delta\xi_e \rightarrow 0} Y_e'(z) = 1 - 2H(z),$$

the limiting value of the slopes (cf. 43) are recovered.

Integrating Eq. (44) twice with respect to z we get $Y_e(z)$ to be

$$Y_e(z) = -\frac{4}{\pi} z \arctan\left(\frac{z}{\Delta\xi_e}\right) + \frac{2\Delta\xi_e}{\pi} \ln\left[1 + \left(\frac{z}{\Delta\xi_e}\right)^2\right] + c, \quad (46)$$

where c is a constant of integration which is determined by the requirement that Y_e go to zero at $z = 1/2$. This gives the value of c to be

$$c = - \int_0^{1/2} \frac{dY_e}{dz} dz = \frac{2}{\pi} \arctan\left(\frac{1}{2\Delta\xi_e}\right) - \frac{2\Delta\xi_e}{\pi} \ln\left[1 + \left(\frac{1}{2\Delta\xi_e}\right)^2\right].$$

This completes the specification of the equilibrium function for the symmetric case. Fig. 7 shows the self-similar equilibrium function with $\xi_s = 0.5$ for different values of $\Delta\xi_e$. Details of the equilibrium function for the general case are given in Appendix A.

4.4 Reaction rate function

Now that the scaling of $|Y_{e \text{ max}}''| (\sim 1/\Delta\xi_e)$ has been established, using the similarity condition on the group $(\Delta\xi_e)^2 |Y_{e \text{ max}}''| / y_0$ yields

$$\frac{(\Delta\xi_e)^2 |Y_{e \text{ max}}''|}{y_0} = \left(\frac{-b\Delta\xi_e^2}{\pi\Delta\xi_e y_0}\right).$$

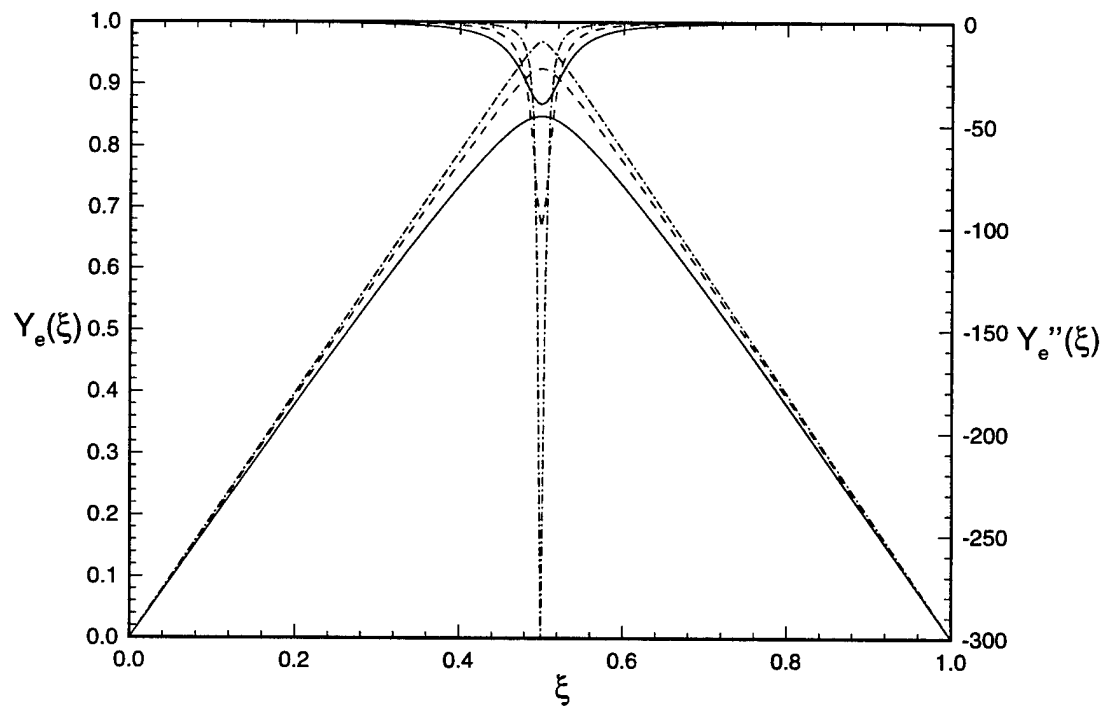


Figure 7: Equilibrium function $Y_e(\xi)$ and its second derivative $Y_e''(\xi)$ for different values of the parameter $\Delta\xi_e$ in the self-similar thermochemistry: — $\Delta\xi_e = 0.03183$ ($Y_e''_{\max} = -40$); - - - $\Delta\xi_e = 1.27324 \times 10^{-2}$ ($Y_e''_{\max} = -100$); - · - · $\Delta\xi_e = 4.244 \times 10^{-3}$ ($Y_e''_{\max} = -300$); The stoichiometric value of the mixture fraction is 0.5.

For this group to be independent of $\Delta\xi_e$, it is necessary that

$$y_0 \sim \Delta\xi_e.$$

Now the second similarity condition can be used to determine the scaling of \bar{S} with respect to $\Delta\xi_e$, which results in

$$\bar{S}(\hat{\xi}, \hat{y}; \Delta\xi_e) \sim \Delta\xi_e.$$

This is achieved by specifying the \bar{S} to be of the form:

$$\bar{S}(\hat{\xi}, \hat{y}; \Delta\xi_e) = \Delta\xi_e \hat{S}(\hat{\xi}, \hat{y}). \quad (47)$$

In a manner analogous to the Lee–Pope thermochemistry, the function $\hat{S}(\hat{\xi}, \hat{y})$ is expressed as a product of two functions:

$$\hat{S}(\hat{\xi}, \hat{y}) = f(\hat{y})g(\hat{\xi}). \quad (48)$$

These functions are chosen similar to those in the Lee–Pope thermochemistry. They are

$$f(\hat{y}) = B\hat{y} \exp(1 - B\hat{y}) \quad (49)$$

$$g(\hat{\xi}) = \exp\{-CG(\hat{\xi})\}, \quad (50)$$

where $G(\hat{\xi})$, given by

$$G(\hat{\xi}) \equiv \frac{Y_{\max} - Y_e(z)}{\Delta\xi_e} = \frac{4}{\pi} \hat{\xi} \arctan(\hat{\xi}) - \frac{2}{\pi} \ln [1 + \hat{\xi}^2], \quad (51)$$

is independent of $\Delta\xi_e$. A contour plot of the scaled reaction rate $\hat{S}(\hat{\xi}, \hat{y})$ as a function of the similarity variables is shown in Fig. 8. The constants B and C are thermochemical parameters that determine the width of the reaction rate function in y and ξ space, respectively. The variation of f with y for different values of the parameter B is shown in Fig. 9. The parameter B plays the role of activation energy. The reaction rate in a typical combustion process is significantly large close to equilibrium and rapidly decays far from equilibrium. This trend is captured by the shape of the function $f(y)$ for suitable choices of the parameter B and $\Delta\xi_e$. The variation of g with ξ for different values of the parameter C is shown in Fig. 10. The peak of the function g at stoichiometric mixture fraction is also characteristic of the variation of reaction rate in typical combustion systems.

The characteristic reaction timescale τ^* associated with this reaction rate specification can be ascertained by considering the Taylor series expansion of $S(\xi, y)$ in powers of y about the point $(\xi, y = 0)$:

$$S(\xi, y) = S(\xi, 0) + y \left[\frac{\partial S(\xi, y)}{\partial y} \right]_{y=0} + \dots$$

Since $S(\xi, 0)$ is zero (the reaction rate is zero at equilibrium), for small y , the reaction rate is approximately $y [\partial S(\xi, y)/\partial y]_{y=0}$. Noting that

$$\left[\frac{\partial S(\xi, y)}{\partial y} \right]_{y=0} = g(\xi)Be/\tau_c,$$

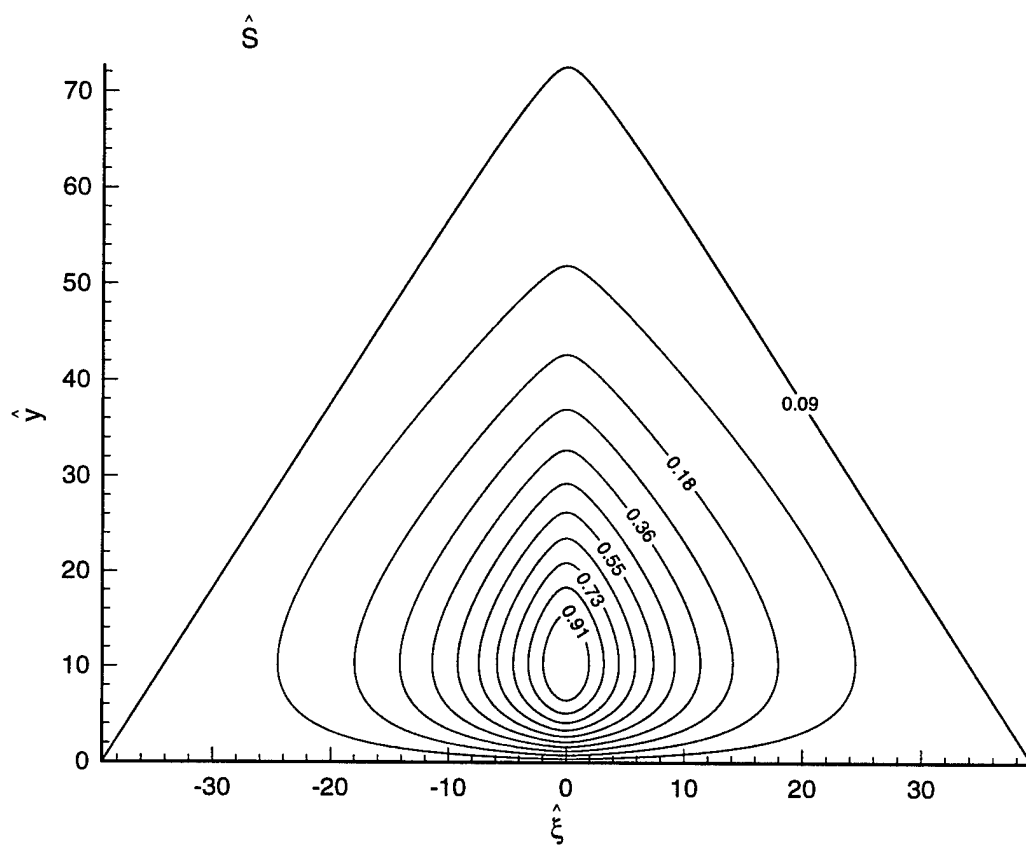


Figure 8: Contours of the reaction rate function $\hat{S}(\hat{\xi}, \hat{y})$ in the self-similar thermochemistry; $B = 0.0964$, $C = 0.055$.

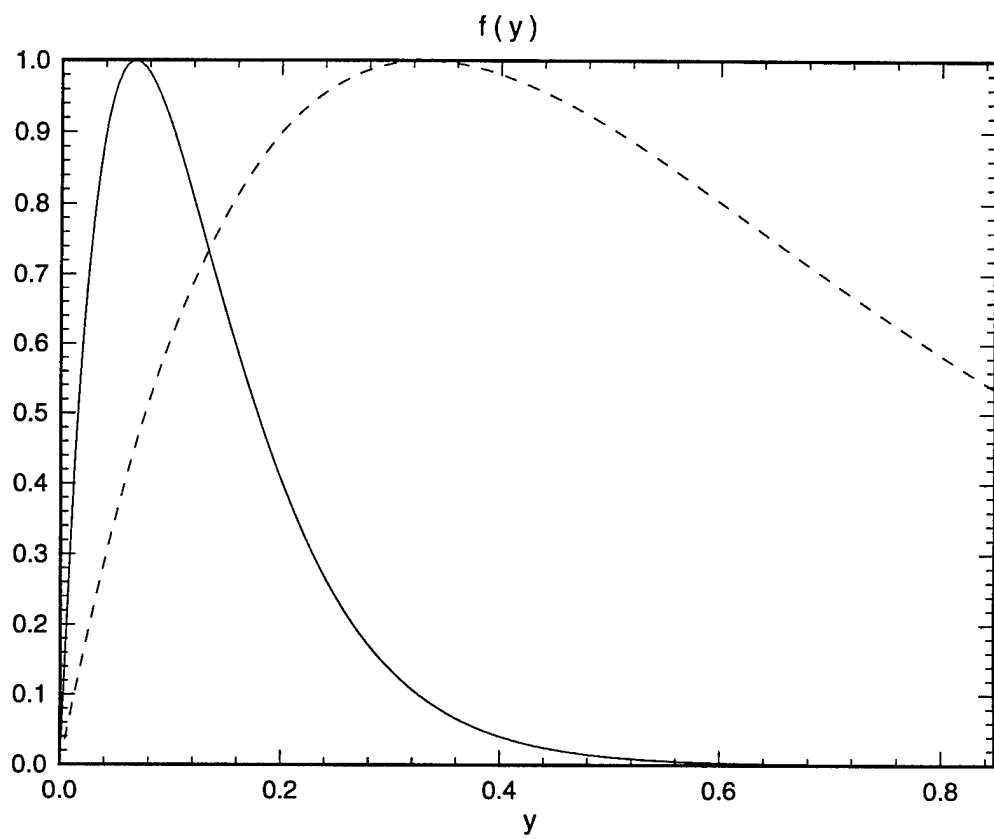


Figure 9: Plot of the function $f(y)$ for different values of the parameter B in the self-similar thermochemistry; — $B = 0.477$; - - - $B = 0.096$. The value of the parameter $\Delta\xi_e$ is chosen to be 0.03183 ($Y_e''_{\max} = -40$).

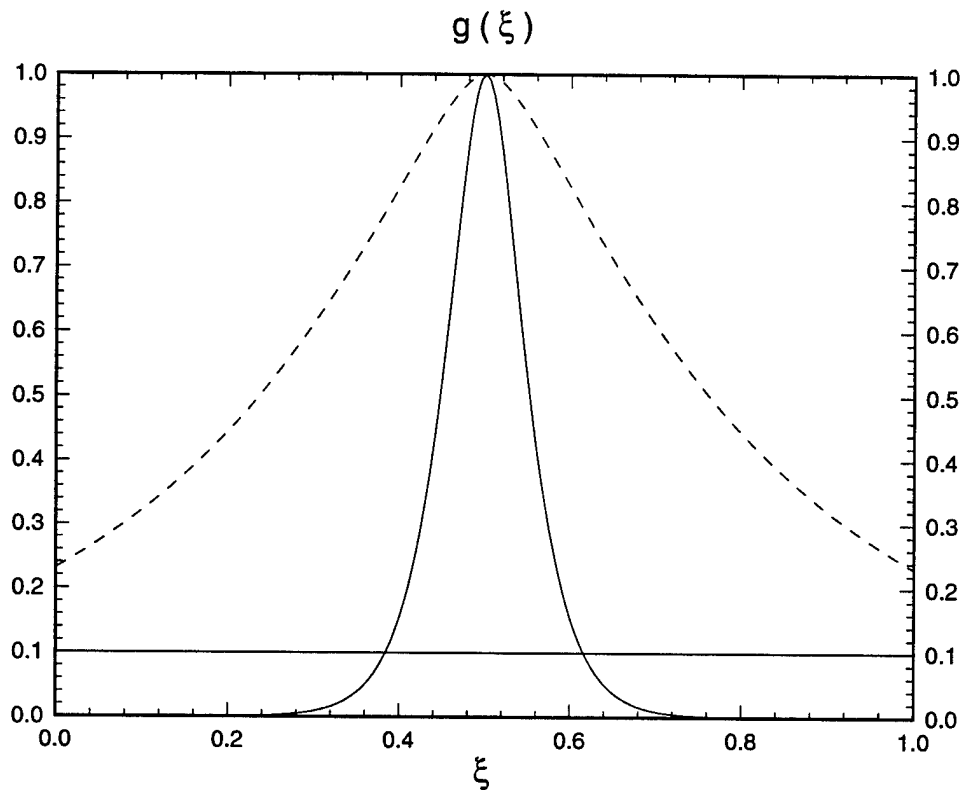


Figure 10: Plot of the function $g(\xi)$ for different values of the parameter C in the self-similar thermochemistry; — $C = 0.529$; - - - $C = 0.055$. The value of the parameter $\Delta\xi_e$ is chosen to be 0.03183 ($Y_e''_{\max} = -40$). The intersection of the horizontal line at height 0.1 with the function $g(\xi)$ defines the reaction zone thickness $\Delta\xi_r$.

the reaction rate for small y at $\xi = \xi_{\max}$ (note $g(\xi_{\max}) = 1$) is given by yBe/τ_c . From this relation the characteristic reaction timescale τ^* is deduced to be

$$\tau^* \equiv \tau_c/(Be). \quad (52)$$

It may be noted that the maximum reaction rate is $S_{\max} = 1/\tau_c = Be/\tau^*$. Since both f and g are maximized by unity, τ_c can be used to adjust the actual magnitude of the reaction rate. This completes the specification of the self-similar thermochemistry.

4.5 Reaction zone thickness $\Delta\xi_r$

In the Lee–Pope thermochemistry, the reaction zone thickness in mixture fraction space was defined as

$$\Delta\xi_r = \xi_r - \xi_l, \quad (53)$$

where the lean and rich limits of the reaction zone in mixture-fraction space (ξ_l and ξ_r respectively) are defined to be the lower and upper values of ξ at which $g_L(\xi)$ equals 0.1. Here an alternative definition of the reaction zone thickness, denoted $\Delta\xi_{rss}$, is proposed, which bears a one-to-one relation with the Lee–Pope definition of $\Delta\xi_r$. In the next sub-section it is also shown how the Lee–Pope reaction zone thickness specification can be translated into a specification of parameters for the self-similar thermochemistry. The purpose of this alternative definition of the reaction zone thickness is to demonstrate the fact that in the self-similar thermochemistry, the ratio $\Delta\xi_{rss}/\Delta\xi_e$ is unchanged (for fixed thermochemical constants B and C), even as $\Delta\xi_e$ is varied. It is also shown that the ratio $\Delta\xi_r/\Delta\xi_e$ changes by less than 1.5% over the range of $\Delta\xi_e$ considered in this study.

In order to define $\Delta\xi_{rss}$, the g function is expanded in a Taylor series about $z = 0$ (which is where g attains its maximum value of 1 for the symmetric case; the definition is easily extended to the general case but not shown here)

$$g(z) = 1 + z \frac{dg}{dz} + \frac{1}{2} z^2 \frac{d^2g}{dz^2} + \dots \quad (54)$$

Since the first derivative of g is zero at $z = 0$, the second derivative at $z = 0$ is used to define a mixture-fraction scale based on the half-width of the g function. This scale, $\Delta\xi_{rss}$, is given by

$$\Delta\xi_{rss} = \left| \frac{d^2g}{dz^2} \right|_{z=0}^{-1/2} = \Delta\xi_e \left(\frac{\pi}{4C} \right)^{1/2}. \quad (55)$$

From the above it is clear that if the parameter C is maintained constant, then the ratio $\Delta\xi_{rss}/\Delta\xi_e$ is also maintained constant.

4.6 Matching the Lee–Pope thermochemistry

The thermochemical parameters used by Lee & Pope in their simulations of homogeneous combustion were $K = 400$ and $B_L = 15$. It is shown here that the parameters of the self-similar thermochemistry can be chosen to match the important derived parameters of the Lee–Pope thermochemistry, though the details of the two thermochemistry specifications may differ.

The equilibrium function in the Lee–Pope thermochemistry is determined by ξ_s and K . The self-similar thermochemistry equilibrium function is determined by ξ_s and $\Delta\xi_e$.

The self-similar equilibrium function is matched to the Lee–Pope equilibrium function by specifying the same value of ξ_s (which is 0.5) and by specifying the value of $\Delta\xi_e$ such that it yields the same value of $|Y_e''_{\max}|$ as that of the Lee–Pope equilibrium function. For $\xi_s = 0.5$ and $K = 400$, the value of $|Y_e''_{\max}|$ is 40. Using the relation between $|Y_e''_{\max}|$ and $\Delta\xi_e$ in the self-similar thermochemistry ($|Y_e''_{\max}| = 4/(\pi\Delta\xi_e)$) gives the matching value of $\Delta\xi_e$ to be 0.03183. The solid line curves in Fig. 7 show the self-similar equilibrium function and its second derivative for the choice of parameters ($\xi_s = 0.5, \Delta\xi_e = 0.03183$) that match the Lee–Pope equilibrium function.

In order to match the important derived parameters of the reaction rate function, the parameter C in the function $g(\hat{\xi})$ (Eq. 50) is specified so as to match the reaction zone thickness $\Delta\xi_r$ of the Lee–Pope thermochemistry. The value of $\Delta\xi_r$ (=0.232) used in the Lee–Pope simulations corresponds to a lean reactive limit (ξ_l) in mixture–fraction space of 0.384. The corresponding value of C is computed using the relation (cf. Eq. 50)

$$C = \frac{-\ln(0.1)}{G(\hat{\xi}_l)}, \quad (56)$$

where $\hat{\xi}_l = \xi_l/\Delta\xi_e$ and $G(\hat{\xi})$ is given by Eq. 51. This yields a value of $C = 0.529$. The function $g(\hat{\xi})$ for the choice of parameters ($\Delta\xi_e = 0.03183, C = 0.529$) that match the Lee–Pope reaction zone thickness is the solid line curve in Fig. 10. Comparing Eqs. 41 and 49, it may be noted that

$$B = B_L \Delta\xi_e. \quad (57)$$

For the value of $B_L = 15$ and $\Delta\xi_e = 0.03183$, this yields the matching value of B to be 0.477. The solid line curve in Fig. 9 shows the function $f(y)$ for this choice of parameters.

In summary, the self-similar thermochemistry is a one-parameter family of $(Y_e(\xi), S(\xi, y))$ functions that preserves the scaling of the terms in Eq. 23 and maintains the ratio of reaction zone thickness to $\Delta\xi_e$. Thus even as the reaction zone thickness changes, the scaling underlying the thermochemistry remains unchanged. In the self-similar thermochemistry the maximum curvature of the equilibrium function $|Y_e''_{\max}|$ and the reaction zone thickness are controlled directly through the parameter $\Delta\xi_e$.

5 The Conditional Moment Closure Model

In Section 3 it was shown that in order to access the parameter range of interest in $\Delta\xi_r$ space subject to the considerations discussed therein, a self-similar thermochemical model is needed. This model has been described in the previous section. With this in hand it now remains to specify the values of the physical parameters that are to be used in the PDF simulations over the range $0.3 \leq \hat{\xi}_r \leq 10$. Prior to describing the results obtained by the PDF simulations (Section 6), solutions to the periodic reaction zone problem using the conditional moment closure (CMC) model of Bilger [2] are presented in this section. One of the advantages of the CMC model, which involves the solution of only one ordinary differential equation, is its simplicity. Apart from providing useful comparisons with the PDF simulation results, the CMC model is also used to test the self-similarity of the SSTC over a range of values of the thermochemical parameter $\Delta\xi_e$. The results of this test are necessary in order to decide the values of the physical parameters that are to be used in the PDF simulations. It is found that the CMC solutions are

asymptotically self-similar in the limit $\Delta\xi_e \rightarrow 0$. Based on the CMC results, a threshold value of $\Delta\xi_e$ is determined, below which the level of self-similarity is deemed acceptable. This acceptable level of self-similarity criterion is then used to determine the appropriate thermochemical and flow parameters that permit access to the $\text{Da} - \hat{\xi}_r$ range of interest at minimum computational expense.

In the CMC model, as applied in this context, the equation for the evolution of the mean progress variable conditioned on the mixture-fraction is derived and modeled. Introducing this conditioning variable adds to the dimensionality of the problem, but there is an overall advantage by reduction in the spatial dimensionality.

A simple way to derive the CMC equation is based on the idea that if the fluctuations of the progress variable arise mainly from fluctuations in the mixture fraction field, then the difference between $Y(\mathbf{x}, t)$ and its mean conditioned on the mixture fraction will be small. Consequently Y can be approximated by its mean conditioned on the mixture fraction. The important features of the CMC model are reproduced from Ref. [2] for clarity of exposition. Then the simplified equations for the periodic reaction zone problem are obtained from this closure.

The starting point for the derivation of the CMC model equation is the evolution of the mixture-fraction and progress variable fields (Eqs. 3, 6). In a turbulent flow, both $Y(\mathbf{x}, t)$ and $\xi(\mathbf{x}, t)$ are random fields. The sample space variable of ξ is denoted by η . The expectation of $Y(\mathbf{x}, t)$ conditional on $\xi(\mathbf{x}, t) = \eta$ is denoted $Q(\eta, \mathbf{x}, t)$, i.e.,

$$Q(\eta, \mathbf{x}, t) \equiv \langle Y(\mathbf{x}, t) | \xi(\mathbf{x}, t) = \eta \rangle. \quad (58)$$

For brevity $\langle Y(\mathbf{x}, t) | \xi(\mathbf{x}, t) = \eta \rangle$ is denoted by $\langle Y | \eta \rangle$. The deviation $\tilde{y}(\mathbf{x}, t)$ of the progress variable $Y(\mathbf{x}, t)$ from its conditional mean is defined as

$$\tilde{y}(\mathbf{x}, t) = Y(\mathbf{x}, t) - Q(\xi[\mathbf{x}, t], \mathbf{x}, t). \quad (59)$$

The evolution equation for $Q(\eta, \mathbf{x}, t)$ is

$$\frac{\partial Q}{\partial t} + \langle U_i | \eta \rangle \frac{\partial Q}{\partial x_i} = S(\eta, Q) + \Gamma \langle \nabla \xi \cdot \nabla \xi | \eta \rangle \frac{\partial^2 Q}{\partial \eta^2} + e_Q + e_{\tilde{y}}, \quad (60)$$

where

$$e_Q = \Gamma \left[\frac{\partial}{\partial x_i} \left(\frac{\partial Q}{\partial x_i} \right) + \frac{\partial^2 Q}{\partial \eta \partial x_i} \left\langle \frac{\partial \xi}{\partial x_i} \mid \eta \right\rangle \right] \quad (61)$$

and

$$e_{\tilde{y}} = - \left\langle \left(\frac{\partial \tilde{y}}{\partial t} + U_i \frac{\partial \tilde{y}}{\partial x_i} - \Gamma \frac{\partial^2 \tilde{y}}{\partial x_i \partial x_i} \right) \mid \eta \right\rangle. \quad (62)$$

Consistent with the basic assumption that the difference between $Y(\mathbf{x}, t)$ and its mean conditioned on the mixture fraction is small, the terms in $e_{\tilde{y}}$ are assumed to be negligible compared to the other terms in the equation for Q . At sufficiently high Reynolds number, the terms in e_Q are also negligible [2].

If fluctuations in Y arise from fluctuations in ξ and if the fluctuating mixture fraction field is statistically homogeneous, then $\partial Q / \partial x_i$ must be negligible. Using these closure hypotheses Eq. (60) can be written as

$$\frac{\partial Q}{\partial t} = S(\eta, Q) + \frac{\langle \chi \mid \eta \rangle}{2} \frac{\partial^2 Q}{\partial \eta^2}, \quad (63)$$

where $\chi = 2\Gamma\nabla\xi\cdot\nabla\xi$ is defined to be the scalar dissipation. The conditional mean scalar dissipation, $\langle\chi|\eta\rangle$ is assumed to be equal to the unconditional mean scalar dissipation $\langle\chi\rangle$. Furthermore for stationary solutions the temporal derivative must be zero and the resulting final form of the equation for Q is

$$\frac{\partial^2 Q}{\partial\eta^2} + \frac{2S(\eta, Q)}{\langle\chi\rangle} = 0. \quad (64)$$

The boundary conditions on Q are $Q(\eta = 0) = 0$ and $Q(\eta = 1) = 0$.

The reaction rate expression corresponding to the self-similar thermochemistry (Eqs. 28, 47, 48) can be substituted into Eq. 64 to obtain

$$\frac{\partial^2 Q}{\partial\eta^2} + \frac{2}{\langle\chi\rangle} \frac{\Delta\xi_e f(\hat{q})g(\hat{\eta})}{\tau_c} = 0, \quad (65)$$

where $\hat{q} = q/\Delta\xi_e$ and $q = Y_e(\eta) - Q(\eta)$. Substituting the expression for the mixing timescale in terms of the scalar dissipation (Eq. 5) and the expressions for the functions f and g (Eqs. 49 and 50) in Eq. 65 results in

$$\frac{\partial^2 Q}{\partial\eta^2} + \frac{2}{\xi'^2} \Delta\xi_e \hat{q} \exp\{[-B\hat{q} - CG(\hat{\eta})]\} \frac{\tau_\phi Be}{\tau_c} = 0. \quad (66)$$

The CMC equation (Eq. 66) can be rewritten in terms of the non-dimensional parameters Da and $\hat{\xi}_{rs}$ using the relations in Eqs. 55, 52 and 1 as

$$\frac{\partial^2 Q}{\partial\eta^2} + \frac{1}{\Delta\xi_e} \hat{q} \exp\{[-B\hat{q} - CG(\hat{\eta})]\} \text{Da} \hat{\xi}_{rs}^2 \left(\frac{8C}{\pi}\right) = 0, \quad (67)$$

where $\hat{\xi}_{rs} = \Delta\xi_{rs}/\xi'$. This equation admits stable solutions only for a limited range of parameter values Da and $\hat{\xi}_{rs}$. For given $\hat{\xi}_{rs}$, there is a critical value of Da , $\text{Da}_{\text{crit}}(\hat{\xi}_{rs})$, below which Eq. 67 admits no solutions, while for Da greater than Da_{crit} there are two solutions: one of which is stable and the other which is unstable. By solving for the critical Damköhler number corresponding to the desired range of values in $\hat{\xi}_{rs}$ space (while keeping the thermochemical constants B and C fixed), the global extinction boundary as predicted by the CMC model can be determined in Da – $\hat{\xi}_{rs}$ space.

5.1 Self-similarity and the CMC model

As noted in the previous section, in the self-similar thermochemistry the reaction rate function $S(\xi, y)$ (and the associated reaction zone thickness $\Delta\xi_{rs}$) is determined by a single parameter $\Delta\xi_e$ (for fixed values of the thermochemical constants B and C) and is expressible as one member of a family of functions $S(\hat{\xi}, \hat{y}; \Delta\xi_e)$ where $(\hat{\xi}$ and $\hat{y})$ are the similarity variables independent of $\Delta\xi_e$. This scaling of the composition variables was chosen so as to make the terms in Eq. 23 independent of $\Delta\xi_e$. It is of interest to determine whether solutions to the CMC equation (Eq. 67) can be expressed in terms of the same similarity variables, independent of $\Delta\xi_e$. In the range of parameters where such a scaling is valid, the reaction zone thickness may be varied by simply changing $\Delta\xi_e$ without changing the underlying structure of the thermochemistry and this will be reflected in the self-similar nature of the solution. In this self-similar range, legitimate

comparisons can be made of solutions from models or DNS for different $\hat{\xi}_r$ (or equivalently $\hat{\xi}_{rss}$) values generated using different reaction zone thickness from the same family of thermochemical functions.

Since the same value of $\hat{\xi}_{rss}$ may correspond to different choices of ξ' and $\Delta\xi_{rss}$, and since we are interested in generating different values of $\hat{\xi}_r$ (or equivalently $\hat{\xi}_{rss}$) by changing $\Delta\xi_e$, it is of interest to determine whether the CMC model predictions for critical Damköhler at a given $\hat{\xi}_{rss}$ are independent of $\Delta\xi_e$. Toward this end it is instructive to rewrite Eq. 67 in terms of the similarity variables, in the following form:

$$\Delta\xi_e \frac{\partial^2 Q}{\partial\eta^2} + \hat{q} \exp\{[-B\hat{q} - CG(\hat{\eta})]\} \text{Da}_{rss} \left(\frac{8C}{\pi} \right) = 0. \quad (68)$$

Since $\partial^2 Q/\partial\eta^2$ scales like $|Y_e''|$ (which in turn scales like $1/\Delta\xi_e$), the first term is independent of $\Delta\xi_e$. Since the second term in Eq. 68 depends only on the similarity variables \hat{q} and $\hat{\eta}$, it is also independent of $\Delta\xi_e$. The non-dimensional group ($\text{Da}_{rss} \hat{\xi}_{rss}^2$) must be a constant, revealing the well-known scaling $\text{Da}_{crit} \sim 1/\hat{\xi}_{rss}^2$, independent of $\Delta\xi_e$. However, the solutions to Eq. 68 will depend on the boundary conditions imposed on the similarity variables which, corresponding to $Q(\eta = 0) = 0$ and $Q(\eta = 1) = 0$, are $\hat{q}(\hat{\eta} = -1/\Delta\xi_e) = 0$ and $\hat{q}(\hat{\eta} = 1/\Delta\xi_e) = 0$. Since the boundary conditions are not independent of the similarity parameter $\Delta\xi_e$, in general the solutions to Eq. 68 will not be self-similar. However, since the magnitude of the reaction rate function becomes negligibly small at $\hat{\xi} = \pm 1/(2\Delta\xi_e)$, and this value decreases with decreasing $\Delta\xi_e$, it turns out that for $\Delta\xi_e$ below a limiting value, the critical Damköhler predicted by the CMC model does indeed become independent of $\Delta\xi_e$. The details of the numerical technique used to solve Eq. 68 are given in Appendix B.

5.2 CMC results for the self-similar thermochemistry

The baseline test case is chosen to be the SSTC specification that matches the Lee-Pope thermochemistry. The thermochemical constants for this case are $B = 0.477$ and $C = 0.529$. The baseline value of $\Delta\xi_e$ is 0.03183 which corresponds to $|Y_e''| = 40$. These values correspond to a reaction zone thickness $\Delta\xi_r$ of 0.232 ($\hat{\xi}_{rss} = 0.03878$). Choosing the r.m.s mixture fraction to be 0.232 results in $\hat{\xi}_r = 1$ (or $\hat{\xi}_{rss} = 5.98$). For this baseline test case the CMC model prediction for Da_{crit} is 30.41 which corresponds closely to the ($\xi^* \equiv \xi'/\Delta\xi_r = 1$) predictions in Lee & Pope [8] where $\text{Da}_{crit} \sim 30$.

Having established this baseline result for $|Y_e''| = 40$ ($\Delta\xi_e = 0.03183$), the maximum curvature of the equilibrium function was progressively increased in steps of 20 (corresponding to a decrease in $\Delta\xi_e$) to a value of $|Y_e''| = 120$ ($\Delta\xi_e = 0.0106$), while keeping the parameter $\hat{\xi}_{rss}$ fixed at the value of 5.98. As $|Y_e''|$ is increased, higher grid density in the neighborhood of $\eta = \xi_s$ is required to resolve the solution to the CMC equation accurately. Details of the non-uniform grid for this purpose are given in Appendix B.

The principal features of the CMC model solution are captured by the critical Damköhler and

$$\hat{q}_M = [Y_e(\xi_s) - Q(\xi_s)]/\Delta\xi_e,$$

namely, the scaled maximum departure of the conditional mean from equilibrium. The variation of these quantities with varying $|Y_e''|$ is shown in Fig. 11. It is clear that

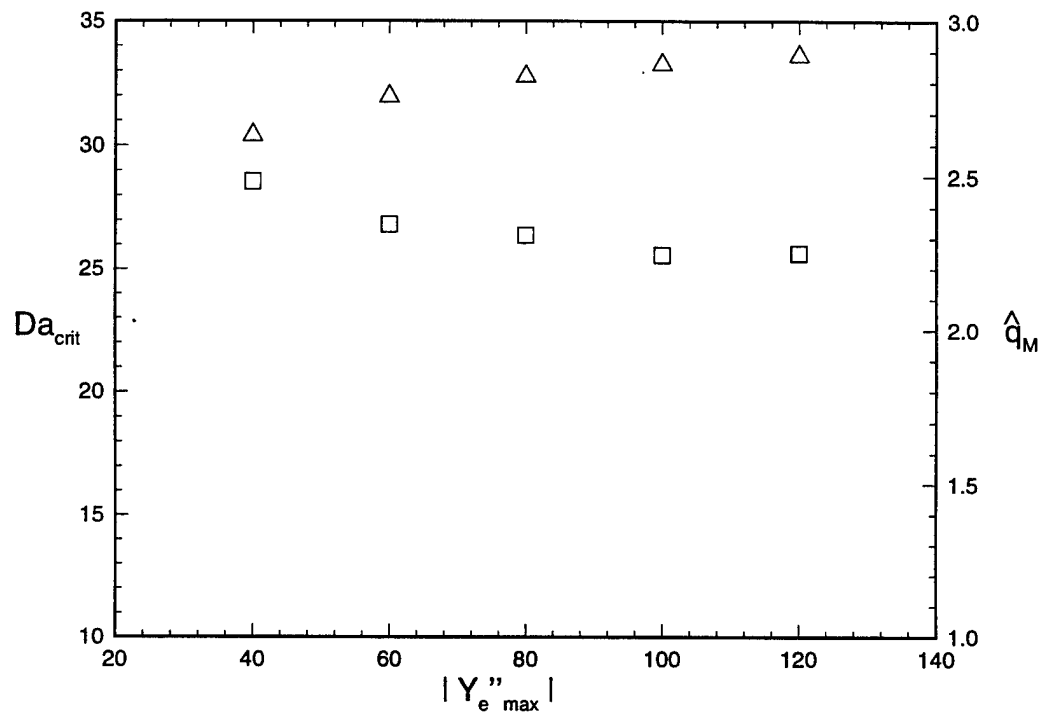


Figure 11: Variation of the CMC model prediction for $Da_{crit}(\Delta)$ with $|Y_e''_{max}|$ for $\hat{\xi}_{rss} = 5.98$. The scaled maximum perturbation $\hat{q}_M(\square)$ is also shown with its corresponding scale on the right.

for values of $|Y_e''_{\max}| < 100$ there is some variation in the CMC solution, but the values tend to asymptote around $|Y_e''_{\max}| = 100$. From this result we conclude that for $|Y_e''_{\max}| \geq 100$ ($\Delta\xi_e \leq 0.0127$) the CMC model solutions are self-similar and independent of variations in $|Y_e''_{\max}|$ (or $\Delta\xi_e$).

5.3 Choice of parameters for the simulation

Given the range of $\Delta\xi_e$ where the CMC model solutions exhibit self-similar behavior, the physical parameters can now be chosen to access the parameter range $0.3 \leq \hat{\xi}_r \leq 10$. The requirement that the values of $\Delta\xi_e$ lie in the self-similar range i.e. $\Delta\xi_e \leq 0.0127$ ($|Y_e''_{\max}| \geq 100$), is added to the list of considerations in Section 3. For each case the maximum value of ξ' allowed by Eq. 14 is chosen, thus minimizing the largest timescale T_t and the computational cost. All these constraints are summarized in the plot shown in Fig 12. The values of the physical and thermochemical parameters of the simulations

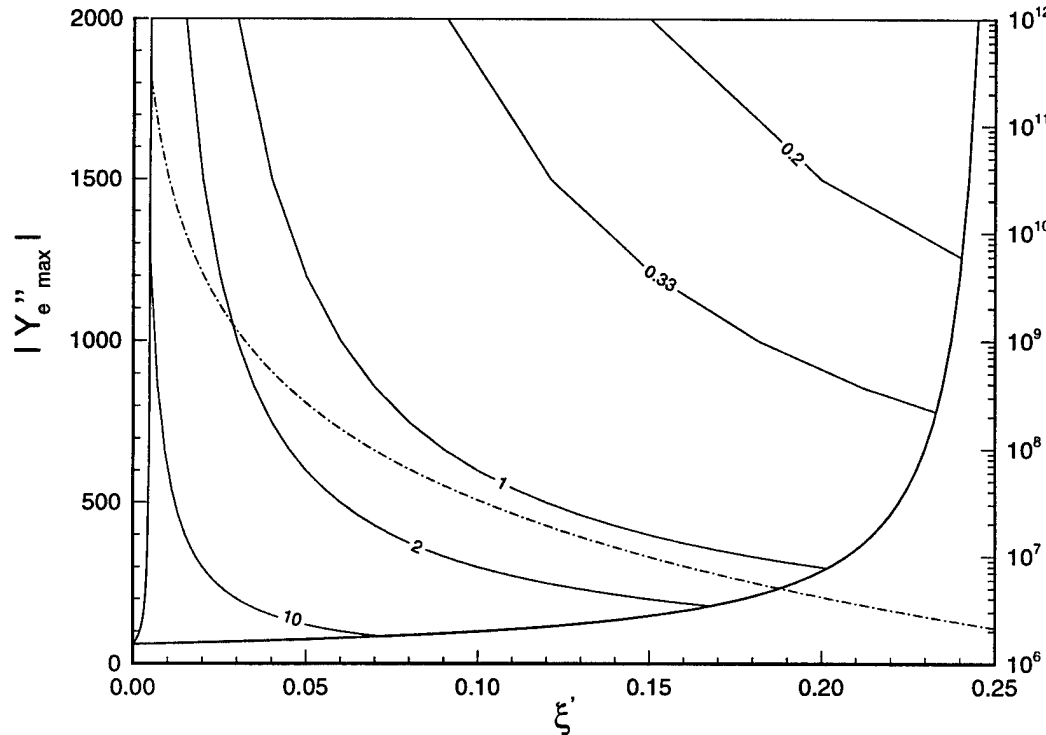


Figure 12: Plot of the contours of $\hat{\xi}_r$ in the $\xi' - Y_e''_{\max}$ plane with ξ' limited by the relation $\xi' \leq (1 - \Delta\xi_r)/4$. The region above $|Y_e''_{\max}| = 100$ is deemed self-similar. The dash-dot ($-\cdot-\cdot-$) curve shows the estimated computational cost in arbitrary units (scale on the right vertical axis) based on estimated nominal resolution requirements. The self-similar thermochemistry is used with $B = 0.096, C = 0.055$.

are given in Section 6.

The thermochemical constant C determines the ratio between $\Delta\xi_e$ and the reaction

zone thickness $\Delta\xi_{r,ss}$ (or $\Delta\xi_r$). Its value is determined based on considerations at the thick reaction zone limit ($\hat{\xi}_r = 10$). In order to simulate this case at minimum computational cost it is desirable to use the maximum value of ξ' subject to the constraint expressed in Eq. 14. This implies that the reaction zone thickness should be at its maximum value for this case. The reaction zone thickness is in turn determined by $\Delta\xi_e$ and the thermochemical constant C . The maximum value of $\Delta\xi_e$ is determined by the self-similarity requirement which dictates that $\Delta\xi_e \leq 0.0127$. The thermochemical constant C is determined on the basis that for the broadest reaction zone (which corresponds to the largest value of $\Delta\xi_e$ that is in the self-similar range) the function $g(\xi)$ be negligibly small (arbitrarily chosen to be less than 2% of the maximum value of g which is unity) at $\xi = 0$ and $\xi = 1$. See Fig 13. This results in a value of $C = 0.055$. Ideally the

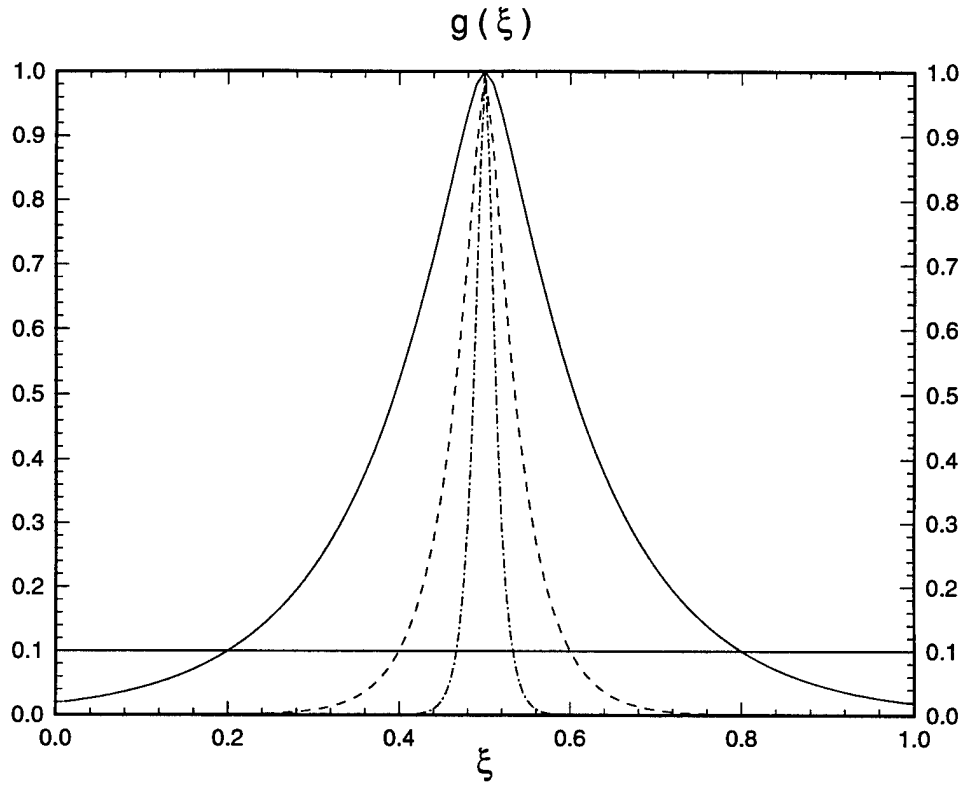


Figure 13: Plot of the function $g(\xi)$ in the self-similar thermochemistry specification, showing the reaction zone thickness for the three cases that are investigated in the simulations. For $\hat{\xi}_r = 10$ and $\hat{\xi}_r = 1$ the value of C is 0.055, while for $\hat{\xi}_r = 0.27$ it is 0.197. The values of the parameter $\Delta\xi_e$ corresponding to the different reaction zone thickness are: — $\Delta\xi_e = 1.27324 \times 10^{-2}$ (Y_e'' max = -100), $\Delta\xi_r = 0.6$, $\hat{\xi}_r = 10$; - - - $\Delta\xi_e = 4.244 \times 10^{-3}$ (Y_e'' max = -300), $\Delta\xi_r = 0.2$, $\hat{\xi}_r = 1$; - - - - $\Delta\xi_e = 4.244 \times 10^{-3}$ (Y_e'' max = -300), $\Delta\xi_r = 0.067$, $\hat{\xi}_r = 0.27$. The intersection of the horizontal line at height 0.1 with the function $g(\xi)$ defines the reaction zone thickness $\Delta\xi_r$.

same value of C should be used for all the different values of $\hat{\xi}_r$. However, as previously noted the parameter C fixes the ratio between $\Delta\xi_e$ and $\Delta\xi_r$. For the smallest value of

$\hat{\xi}_r$ ($=0.27$), which corresponds to the thinnest reaction zone, the value of $\Delta\xi_e$ implied by $C = 0.055$ is so small that the numerical resolution requirements are prohibitive. (The details of convergence and numerical resolution requirements are given in Appendix D). Consequently, for the $\hat{\xi}_r = 0.27$ case, $\Delta\xi_e$ is fixed at the same value as for the $\hat{\xi}_r = 1$ and the value of C is chosen to be 0.197.

The thermochemical constant B is determined on the basis that for the largest value of $\Delta\xi_e$ used in the simulation ($\Delta\xi_e = 0.0127$) the function $f(y)$ be negligibly small (arbitrarily chosen to be less than 2% of the maximum value of f which is unity) at $y = Y_{\max}$. See Fig 14. This results in a value of $B = 0.096$ which is used for all values of $\hat{\xi}_r$.

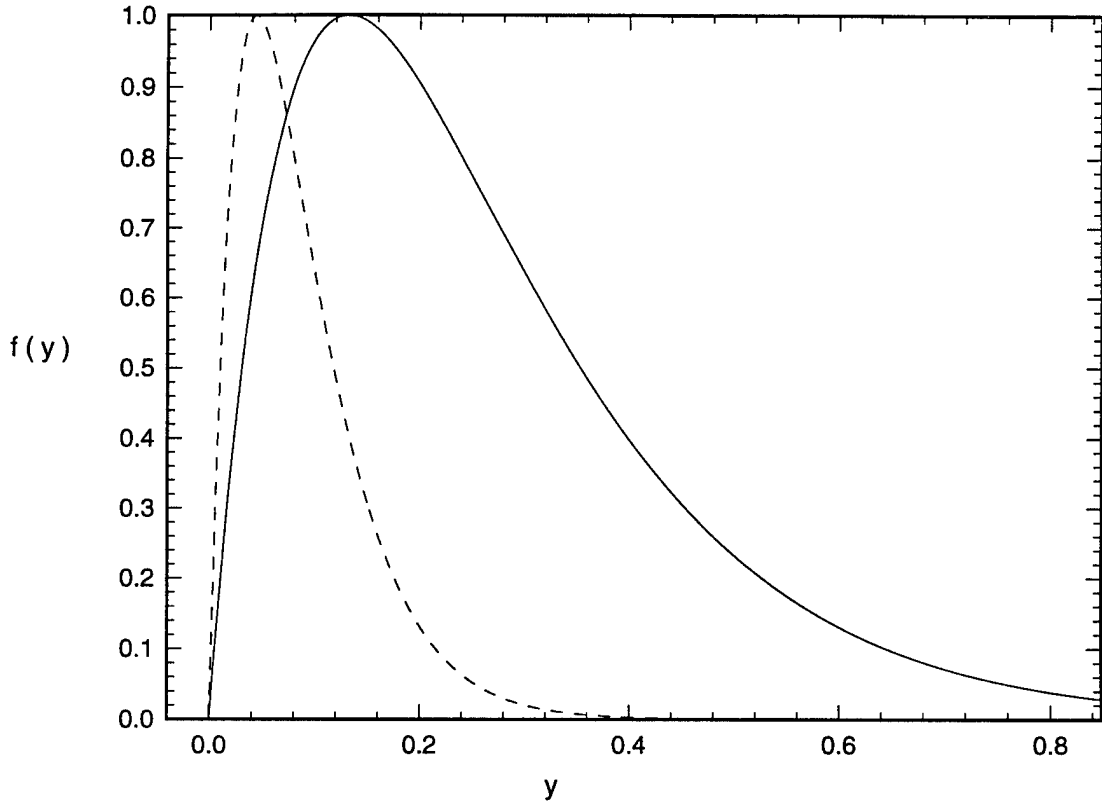


Figure 14: Plot of the function $f(y)$ showing the reaction zone thickness for the cases that are investigated in the simulations. The self-similar thermochemistry is used with $B = 0.096$. The curves correspond to different values of the parameter $\Delta\xi_e$: — $\Delta\xi_e = 1.27324 \times 10^{-2}$ ($Y_e''_{\max} = -100$), for $\hat{\xi}_r = 10$; - - - $\Delta\xi_e = 4.244 \times 10^{-3}$ ($Y_e''_{\max} = -300$), for $\hat{\xi}_r = 1$ and $\hat{\xi}_r = 0.27$.

6 Model predictions

In this section the simulation results for three different reaction zone thickness parameter ($\hat{\xi}_r$) values using the CMC, IEM and EMST models are described. The section begins

with a description of the numerical solution procedure for the PDF models. The CMC model and the numerical procedure used to solve the CMC model equation have already been described in detail in Section 5. This is followed by a description of the three different cases that are to be investigated. Then a simulation strategy is outlined which permits rough estimation of the critical Damköhler number corresponding to global extinction. The results obtained using each model are then presented for each of the three cases. The section concludes with a discussion of the results.

6.1 Numerical solution of PDF model equations

In Monte Carlo simulations of inhomogeneous flows the solution domain in physical space is discretized into a number of cells for the purpose of extracting local mean quantities which appear in the particle evolution equations. Within each cell at any given time t , the joint pdf of velocity, composition and turbulent frequency is represented by an ensemble of N particles. The position, velocity and turbulent frequency of the i^{th} particle are denoted by $\mathbf{X}^{(i)}$, $\mathbf{U}^{(i)}$ and $\omega^{(i)}$ respectively. If the number of compositions is D , then $\phi_{\beta i}$ ($\beta = 1, \dots, D$) represents the composition of the i^{th} particle ($i = 1, \dots, N$). Each particle is assigned an importance weight w_i (such that the particle weights sum to unity) which determines its relative contribution in estimates of the means and higher order moments of the particle properties.

6.1.1 Physical sub-models

The evolution equations of the particle properties are:

$$d\mathbf{X}^{(i)} = \mathbf{U}^{(i)} dt \quad (69)$$

$$d\mathbf{U}^{(i)} = -\frac{3}{4}C_0\langle\omega\rangle (\mathbf{U}^{(i)}(t) - \langle\mathbf{U}\rangle) dt + \sqrt{C_0 k\langle\omega\rangle} d\mathbf{W} \quad (70)$$

$$d\omega^{(i)} = -(\omega^{(i)} - \langle\omega\rangle)C_3\langle\omega\rangle dt - \langle\omega\rangle\omega^{(i)}S_\omega dt \quad (71)$$

$$+ \sqrt{2\sigma^2\langle\omega\rangle\omega^{(i)}C_3\langle\omega\rangle} dW^* \quad (72)$$

$$\frac{d\phi_{\beta i}}{dt} = \Theta_\beta^{(i)} + S_\beta([\phi_i]), \quad \beta = 1, 2. \quad (73)$$

The position equation simply states that each particle moves with its own velocity. The velocity evolves by the simplified Langevin model for *stationary* isotropic turbulence with the constant-density simplification [14] [6]. The model constant C_0 is fixed at its standard value of 2.1. The term $d\mathbf{W}$ represents an increment in the isotropic Wiener process $\mathbf{W}(t)$. The details of this model and its performance may be found in Pope [15]. The turbulent frequency evolves by the Jayesh & Pope [7] model with simplifications resulting from the homogeneity assumption incorporated in Eq. 73. In the equation for turbulent frequency (Eq. 73), the term dW^* represents an increment in the Wiener process $W^*(t)$ which is independent of the Wiener process in the velocity equation. For stationary homogeneous turbulence the modeled source term S_ω is set to zero, thus ensuring that $\langle\omega\rangle$ is stationary. The values of the model constants in the turbulent frequency equation are $C_3 = 1$ and $C_4 = 0.25$. The pdf of the stationary and homogeneous turbulent frequency is a gamma distribution. Further details of the turbulent frequency model may be found in Ref. [7]. The composition variables are defined as $\phi_1 = \xi$ and $\phi_2 = Y$. In the composition evolution

equation (Eq. 73) Θ_β represents the mixing model and $S_\beta([\phi_i])$ represents the reaction rate of the β^{th} scalar (which is non-zero only for $\beta = 2$) and $[\phi_i]$ represents the vector of compositions corresponding to the location of the i^{th} particle in composition space. The self-similar model thermochemistry specification for the reaction rate is used. The two different mixing models used in this study, IEM and EMST, are now described.

6.1.2 Mixing models

In the IEM model [5], the i^{th} particle's compositions evolve by

$$\frac{d\phi_{\beta i}}{dt} = -\frac{1}{2} C_\phi \langle \omega \rangle (\phi_{\beta i} - \langle \phi_\beta \rangle), \quad (74)$$

where C_ϕ is a model constant chosen to be 2.0. While this model is attractive on account of its simplicity it is known to perform unsatisfactorily in certain reactive flows [10], [11].

The EMST mixing model is based on interactions between particles that are local in composition space. It is an extension of the mapping closure particle model to multiple scalars. Only the salient features of the model are presented here for completeness. A complete description of the EMST model and its validation in inert and reactive tests may be found in Subramaniam & Pope [18].

At any given time a subset of N_T particles is chosen for mixing from the ensemble of N particles in the cell, based on an age property associated with each particle. A Euclidean minimum spanning tree is constructed on this subset of N_T particles so that each particle is connected with at least one neighbor particle. See Fig. 15. The vector of particle compositions $\underline{\phi}_{(i)} = \phi_{\beta(i)}$, $i = 1, \dots, N_T$ evolves as:

$$w_{(i)} \frac{d\underline{\phi}_{(i)}}{dt} = -\alpha \sum_{\nu=1}^{N_T-1} B_\nu \left\{ (\underline{\phi}_{(i)} - \underline{\phi}_{n_\nu}) \delta_{im_\nu} + (\underline{\phi}_{(i)} - \underline{\phi}_{m_\nu}) \delta_{in_\nu} \right\}, \quad (75)$$

where the ν^{th} edge connects the particle pair (m_ν, n_ν) and δ represents the Kronecker delta. The specification of the model constants B_ν and α is described in Ref. [18].

6.1.3 The PDF2DV program

These physical sub-models are incorporated in a FORTRAN program called PDF2DV developed by Pope [13] to calculate the properties of statistically two-dimensional (plane or axi-symmetric) turbulent reactive flows. The problem under consideration has spatial structure in only the x_2 direction. Periodic boundary conditions are imposed at $x_2 = 0$ and $x_2 = L$ on the fluctuating velocity, turbulent frequency, fluctuating mixture fraction and progress variable. The flow parameters for the simulations are given in Tables 1, 2.

The grid is chosen to be uniform in the computational domain $0 \leq x_2 \leq L$ and the grid spacing is chosen such that there are at least 5 computational cells per integral scale l (See Table 3). Only the mean progress variable field $\langle Y(\mathbf{x}, t) \rangle$ has a spatial variation in x_2 that has to be resolved. This is guaranteed provided the fluctuating mixture fraction field (i.e. the flame brush) is resolved spatially. Using the relation between the r.m.s. mixture fraction ξ' and the integral scale l (Eq. 16), it is clear that resolving the integral scale l ensures that all the composition mean fields are spatially well resolved.

The important flow timescales are the convective timescale $\Delta x_2 / (2u')$ (where Δx_2 is the length of a computational cell in the x_2 direction and u' is the r.m.s. velocity), the

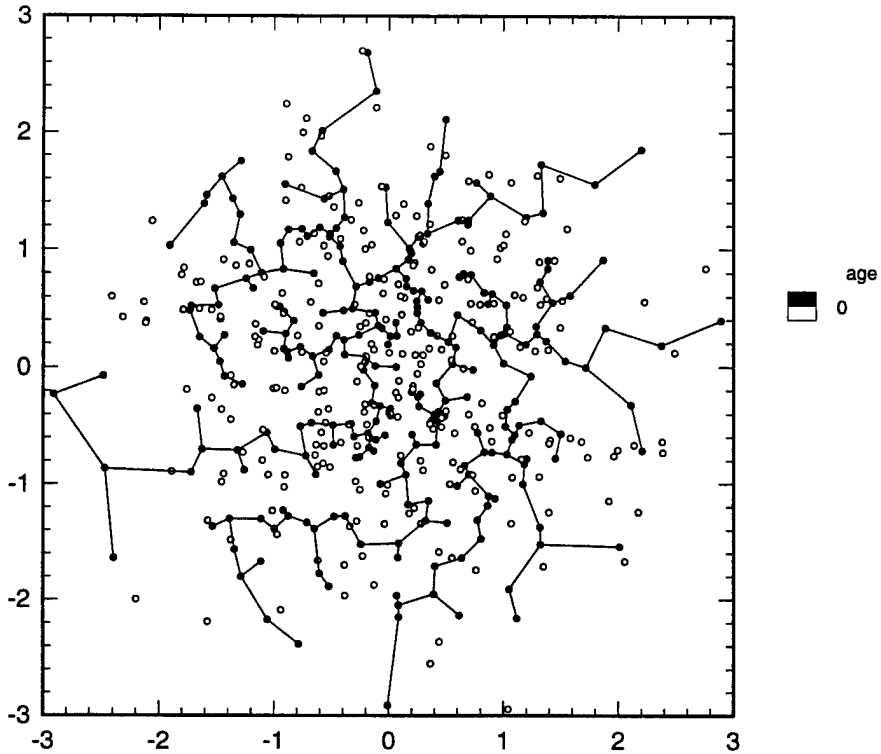


Figure 15: Euclidean Minimum Spanning Tree constructed on the mixing subset of an ensemble of particles in 2-D composition space (open circles represent particles in the non-mixing state); $N = 512$ particles, joint-normal distribution.

Table 1: Summary of velocity-field statistics which are common to all the cases in the PDF simulations.

l —integral length scale	1.0
k —turbulent kinetic energy	1.5
u' —turbulence intensity ($\sqrt{2k/3}$)	1.0
ϵ —mean dissipation rate	1.0
$\langle \omega \rangle$ —mean turbulent frequency (ϵ/k)	0.67
τ —turbulence timescale	1.5
τ_ϕ —mixing timescale	0.75

Table 2: Summary of case-specific flow parameters in the PDF simulations.

	$\hat{\xi}_r = 10$	$\hat{\xi}_r = 1$	$\hat{\xi}_r = 0.27$
L —computational box-length	31.13	9.34	7.78
ξ' —nominal r.m.s. mixture fraction	0.06	0.2	0.24
T_t —transport timescale	58.1	5.23	3.63

Table 3: Summary of numerical parameters for each case in the PDF simulations.

	$\hat{\xi}_r = 10$	$\hat{\xi}_r = 1$	$\hat{\xi}_r = 0.27$
N_c —number of cells in $[0, L]$	156	50	40
$\Delta x_2/l$ —spatial resolution	0.2	0.19	0.19
N_{pc} —nominal number of particles per cell:	80	750	1120
$C_{\Delta t m}$ — $\Delta t \leq C_{\Delta t m} \tau_\phi$	0.1	0.1	0.1
$C_{\Delta t u}$ — $\Delta t \leq C_{\Delta t u} \Delta x_2 / (2u')$	0.4	0.4	0.4
Δt —time step	0.036	0.036	0.038

mixing timescale τ_ϕ , and the transport timescale T_t . Particle properties are advanced over a time step Δt , chosen such that all important flow timescales are resolved (see Table 3), using the method of fractional steps [14]. The time step restriction on Δt arises from the convective timescale which is the smallest of the flow timescales. The effects of mixing and reaction on the reactive scalar Y are implemented through a first-order splitting strategy [20]. The change in Y due to reaction over a time step Δt is computed analytically thus avoiding the need for expensive sub-stepping of the chemical timescale which would have made the high Damköhler calculations prohibitive. The details of the analytic integration of the reaction rate are provided in Appendix C. The particle number density is uniform in both physical space and in composition space (namely the $\xi - Y$ plane). For small values of $\hat{\xi}_r$, within a computational cell, the thermochemical composition scales ($\Delta\xi_e$ and $\Delta\xi_r$) are a small fraction of the region accessed by the particle compositions (which is determined by the r.m.s. mixture fraction ξ'). For these cases, the number of particles per cell N_{pc} has to be increased to ensure that the thermochemical scales are adequately resolved. The details of the convergence of important flow statistics with respect to N_{pc} are provided in Appendix D.

6.2 Description of test cases

The turbulent velocity field parameters which are the same for all the cases are tabulated in Table 1. The different value of stationary mixture fraction standard deviation for each case is generated by changing L , the length of the computational domain. Since the jump in the mean mixture fraction over the computational box-length L is held fixed at 2, changing L effectively changes the imposed mean mixture fraction gradient. The different computational box-lengths, mixture fraction standard deviation and associated transport timescale are tabulated in Table 2. The fundamental and derived thermochemical parameters for each case are given in Table 4. The case with $\hat{\xi}_r = 10$ ($\xi' \approx 0.06$, $\Delta\xi_r = 0.6$)

Table 4: Summary of thermochemical parameters for each case. The thermochemical constant B is 0.096 for all cases.

	$\hat{\xi}_r = 10$	$\hat{\xi}_r = 1$	$\hat{\xi}_r = 0.27$
$\Delta\xi_e$	1.27×10^{-2}	2.24×10^{-3}	2.24×10^{-3}
$ Y_e''_{\max} $	100	300	300
$\Delta\xi_r$	0.6	0.2	0.067
$\Delta\xi_{rss}$	0.048	0.016	8.46×10^{-3}
C	0.055	0.055	0.197

corresponds to broad reaction zones. Consider fluid at a physical location where the mean mixture fraction is stoichiometric. The fluctuations in mixture fraction at this location

are small compared to $\Delta\xi_r$ and are almost always confined within the reaction zone in composition space. The case with $\hat{\xi}_r = 1$ ($\xi' \approx 0.2, \Delta\xi_r = 0.2$) corresponds to moderate reaction zone thickness parameter. The mixture fraction fluctuations are of the order of the reaction zone thickness $\Delta\xi_r$. The case with $\hat{\xi}_r = 0.27$ ($\xi' \approx 0.24, \Delta\xi_r = 0.067$) corresponds to thin reaction zones. The mixture fraction fluctuations are large compared to the reaction zone thickness $\Delta\xi_r$. This is expected to be a severe test of the mixing models.

6.3 Simulation strategy

The objective is to perform simulations for each of the three cases (corresponding to fixed values of $\hat{\xi}_r$) for a range of Damköhler numbers spanning the range of physical states from stable reaction to global extinction. One important outcome of these simulations will be an estimate of the critical Damköhler corresponding to global extinction.

In order to obtain these estimates it is necessary to quantitatively characterize global extinction in a PDF simulation. In the DNS of homogeneous combustion Lee & Pope [8] used an imbalance index, which is a non-dimensional measure of the imbalance between mixing and reaction terms in the evolution equation of the volume-averaged-perturbation $[y(\mathbf{x}, t)]$ [8], to characterize global extinction. In the present study an extinction index is defined based on the temporal evolution of the particle composition values in the PDF simulation.

6.3.1 Extinction index

All the simulations are evolved from the initial condition of chemical equilibrium. In composition space all the particles initially lie along the equilibrium line $Y_e(\xi)$. See Figure 16. After sufficient time has elapsed for the effect of initial conditions to be negligible, the particle properties reach statistical stationarity.

At very high Da , reaction forces these particles to remain close to the equilibrium line, while mixing tends to draw them away from equilibrium. At the other extreme if there is no reaction (inert case), then mixing forces the particles to the $Y = 0$ line, which corresponds to global extinction. Intermediate values of the Da number result in particles populating the composition plane somewhere between these two extreme states. At any time t , one measure of the departure of particles from the equilibrium line in composition space is the expectation of the progress variable conditioned on mixture fraction $\langle Y | \xi \rangle(t)$. However, it is preferable to characterize extinction by a single variable rather than a function. An alternative measure could be the mean progress variable evaluated at the physical location where the mean mixture fraction is stoichiometric, $[\langle Y \rangle(x_2, t)]_{\langle \xi \rangle(x_2) = \xi_s}$. This physical location is always at $x_2 = L/4$ in the simulations and the mean progress variable at this location is denoted $\langle Y \rangle_s(t) \equiv \langle Y \rangle(L/4, t) = [\langle Y \rangle(x_2, t)]_{\langle \xi \rangle(x_2) = \xi_s}$. Using the evolution equation of $\langle Y \rangle$, the decay of the mean progress variable can be estimated for the inert case. Once stationarity is reached, the ratio of the change in $\langle Y \rangle_s(t)$ from its value at $t = T_t$ to the change in $\langle Y \rangle_s(t)$ from its value at $t = T_t$ for the decaying inert case can be used to quantify extinction.

If the characteristic lengthscale of variation of $\langle Y \rangle$ in x_2 is L , then the mean progress

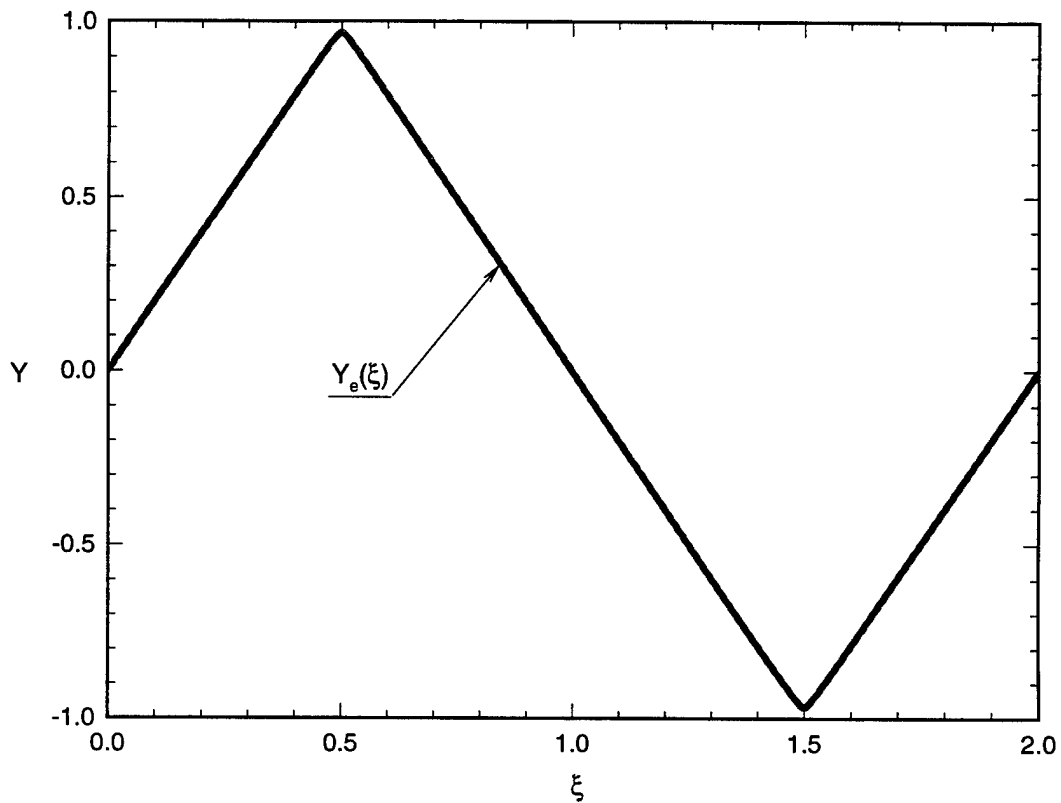


Figure 16: Initial condition for the PDF simulations: mixture fraction ξ is uniformly distributed in $[0,2]$; progress variable Y is initially at equilibrium $Y_e(\xi)$.

variable evolution equation (Eq. 17) for the inert case can be written as

$$\begin{aligned}\frac{\partial \langle Y \rangle}{\partial t} &= -\frac{\partial \langle u_2 Y \rangle}{\partial x_2} \\ &= -\gamma_t \frac{\partial^2 \langle Y \rangle}{\partial x_2^2} \\ &\sim -\frac{L^2}{T_t} \frac{\langle Y \rangle}{L^2} \\ &= -\frac{\langle Y \rangle}{T_t}.\end{aligned}$$

The solution to the equation

$$\frac{\partial \langle Y \rangle}{\partial t} = -\frac{\langle Y \rangle}{T_t},$$

is simple exponential decay with a timescale T_t . Consequently to a good first approximation, for the inert case one may write

$$\langle Y \rangle(x_2, t) = \langle Y \rangle(x_2, 0) \exp(-t/T_t).$$

Numerical simulations confirm this behavior with $T_t \approx 0.04 (L/l)^2 \tau$. See Fig. 5.

Using this relation the following quantity may be used to quantify global extinction:

$$\frac{[\langle Y \rangle_s(t) - \langle Y \rangle_s(T_t)]}{[\langle Y \rangle_s(T_t) (\exp(1 - t/T_t) - 1)]}, \quad t > T_t. \quad (76)$$

The denominator is the change in the mean progress variable at $L/4$ from $t = T_t$ if the flow were inert, and the numerator is the corresponding change in mean progress variable for non-zero reaction at the Damköhler specified in the simulation. The changes in $\langle Y \rangle_s$ are computed with respect to the $t = T_t$ instant so as to ensure that the effect of initial conditions is negligible by $t = T_t$, the largest timescale in the flow.

However, this measure suffers from two drawbacks. Firstly, it is subject to relatively large statistical variations (since only the particles in the cell located at $x_2 = L/4$ contribute to this quantity, see Fig. 17) and secondly for the broad reaction zones case this quantity is not truly representative of the state of particles in the reaction zone. To alleviate both these difficulties, instead of using $\langle Y \rangle_s$ it is preferable to use the reaction-zone-conditioned mean progress variable $\langle Y | \xi_R \rangle$. For $0 \leq \xi \leq 1$ this is defined as

$$\langle Y | \xi_R \rangle \equiv \langle Y^{(i)} | \xi_l \leq \xi^{(i)} \leq \xi_r \rangle. \quad (77)$$

This quantity is a direct measure of the state of particles in the reaction zone.

Furthermore, noting that each fluid particle in the “anti-flame” interval with composition (ξ, Y) is statistically identical to a fluid particle in the mixture fraction interval $[0, 1]$ with composition $([\xi] - \xi, -Y)$, the particle composition values $(|Y^{(i)}|)$ in the “anti-reaction zone” may be used in computing $\langle Y | \xi_R \rangle$, thereby reducing the statistical error. The temporal evolution of $\langle Y | \xi_R \rangle$ is shown in Fig. 18.

Using $\langle Y | \xi_R \rangle$ the extinction index ($E.I.(t)$) is defined as

$$E.I.(t) \equiv \frac{[\langle Y | \xi_R \rangle(t) - \langle Y | \xi_R \rangle(T_t)]}{[\langle Y | \xi_R \rangle(T_t) (\exp(1 - t/T_t) - 1)]}, \quad t > T_t. \quad (78)$$

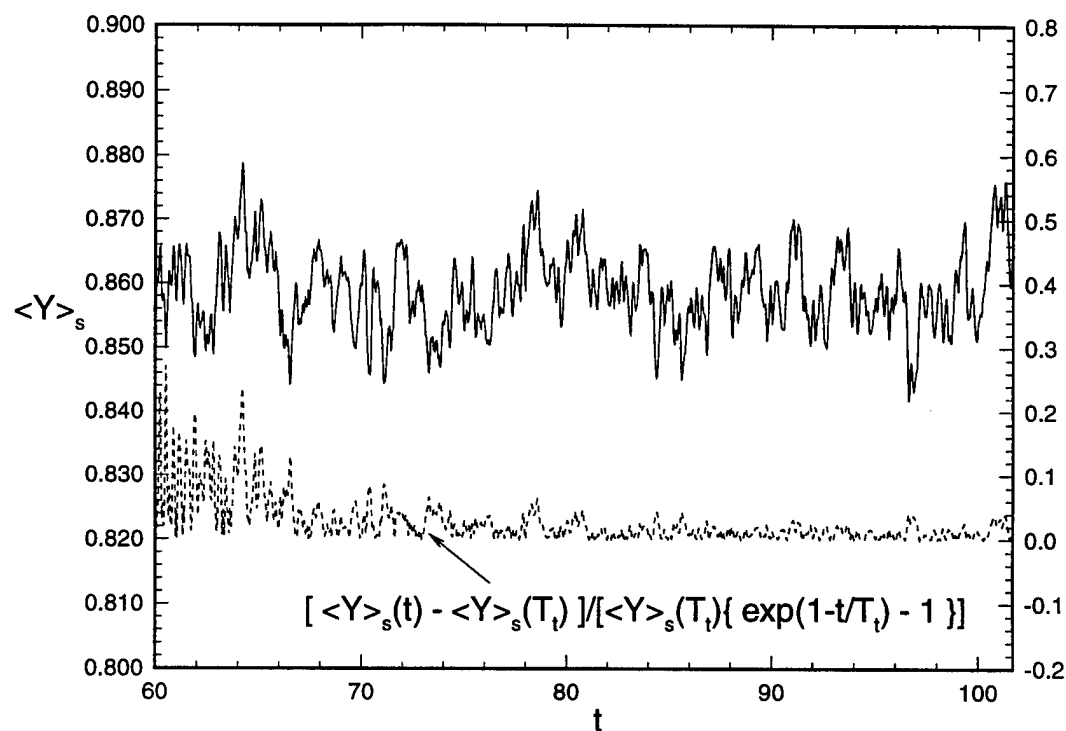


Figure 17: Evolution of $\langle Y \rangle_s(t)$ (—) and the quantity $[\langle Y \rangle_s(t)/\langle Y \rangle_s(T_t) - 1]/[\exp(1 - t/T_t) - 1]$ (---) for the $\xi_r = 10$ case: $Da = 5$ (stable reaction).

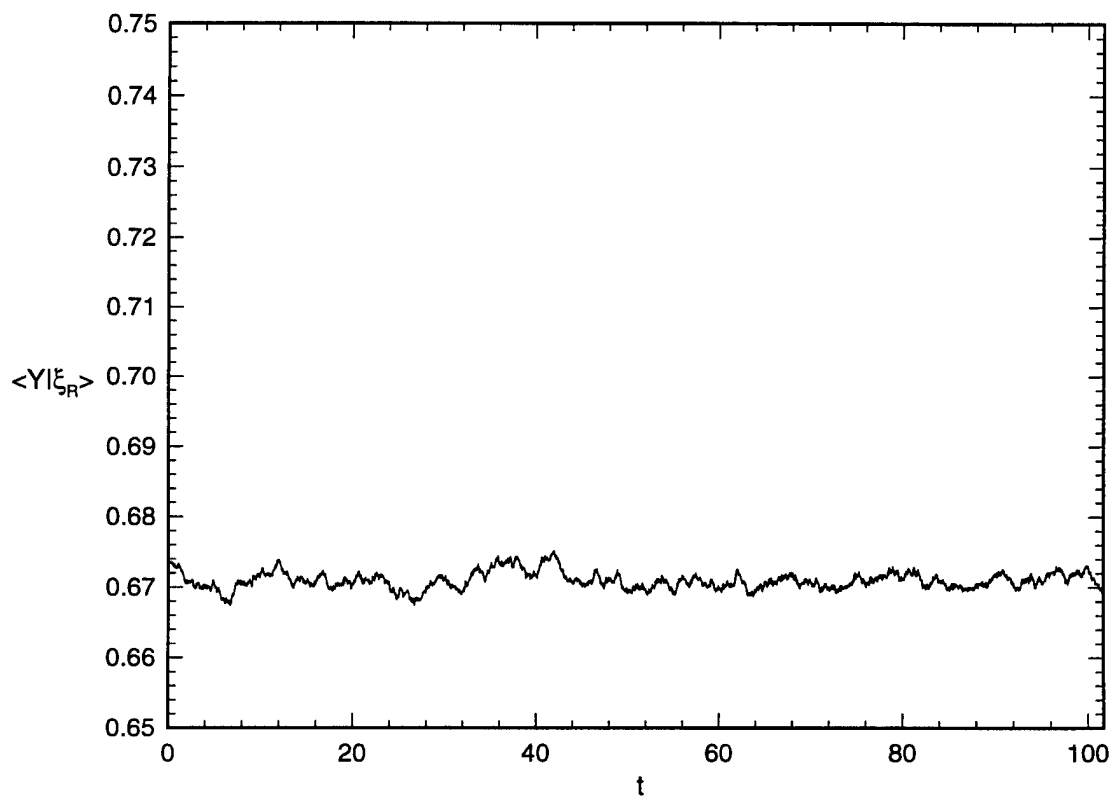


Figure 18: Evolution of $\langle Y | \xi_R \rangle$ for the $\hat{\xi}_r = 10$ case: $\text{Da} = 5$ (stable reaction).

Given the statistical variability inherent in turbulent flows, global extinction can only be quantified probabilistically. In Lee & Pope [8] the authors suggest two possible ways to quantify global extinction: (i) the probability of extinction at a normalized time and (ii) the normalized mean time to extinction in the context of DNS. Both these quantities are beyond the scope of current computational capabilities for either PDF or DNS. In this light, an imprecise definition of extinction for practical purposes is used based on the extinction index. At any Da^* , after the simulation has evolved for a time T_s (where $T_s > T_t$ and is usually 2 to 4 times T_t)

$$\begin{aligned} \text{if } E.I.(T_s) &\geq 0.25 : \text{global extinction } \forall Da \leq Da^* \\ \text{else if } E.I.(T_s) &< 0.25 : \text{stable reaction } \forall Da \geq Da^*. \end{aligned}$$

The evolution of the extinction index for representative cases showing stable reaction and extinction is presented in Fig. 19. By performing simulations for a range of Da , starting

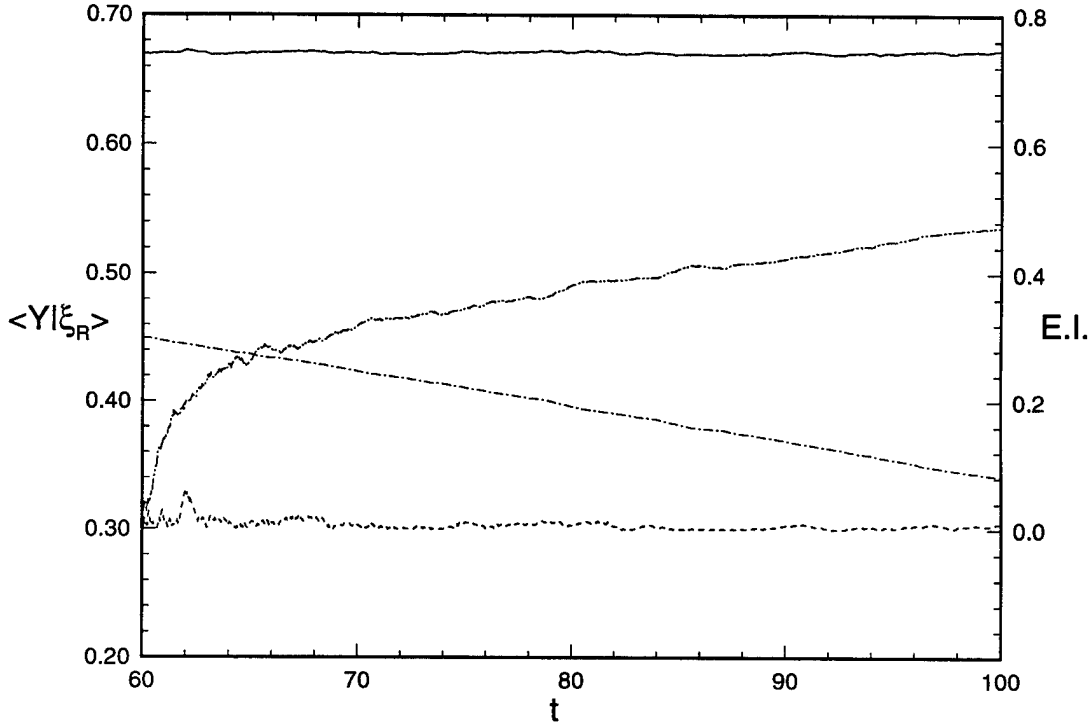


Figure 19: Evolution of $\langle Y | \xi_R \rangle$ and $E.I.$ for the $\hat{\xi}_r = 10$ case. $Da = 5$ (stable reaction): — $\langle Y | \xi_R \rangle$, - - - $E.I.$; $Da = 0.35$ (extinction): - - - - $E.I.$, - - - - $\langle Y | \xi_R \rangle$

from a very high value of Da which is evolved for $T_s \sim [2 - 4]T_t$ and then progressively reducing the Da in steps by a fixed fraction (and evolving the flow for T_s at each Da), a rough bracket of the critical Damköhler number $[Da_l, Da_u]$ corresponding to global extinction can be determined using the criterion expressed in Eq. 78. This then implies that for $Da > Da_u$ there is stable reaction with high probability and that for $Da < Da_l$

there is a high probability of global extinction. A sketch of the variation of probability of stable reaction with Damköhler is shown in Fig. 20.

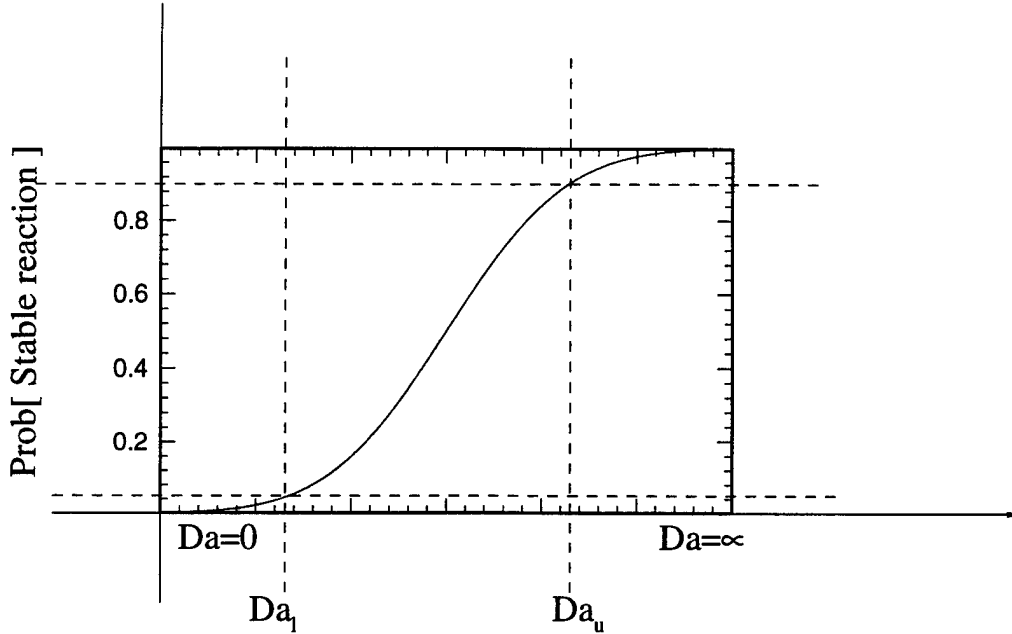


Figure 20: Sketch of the probability of stable combustion showing plausible locations for the lower and upper brackets on the critical Damköhler number.

6.3.2 Simulation algorithm

The simulations and the prediction of global extinction based on *E.I.* are sensitive to the initial condition from which the run is started and are also subject to statistical variability. The effect of statistical variability can be quantified, within the bounds of the computational expense-accuracy trade-off, by performing multiple independent simulations (MIS) at a given Damköhler number. Thus by performing say M MIS at Da_u and Da_l , the probability of extinction (or stable reaction) can be estimated at Da_l and Da_u .

The sensitivity to initial conditions requires that the ratio by which the Damköhler is reduced in the search for $[Da_l, Da_u]$ not be so large as to cause extinction when a smaller ratio would have led to stable reaction. An acceptable value for this ratio is determined empirically to be 0.7.

The considerations of statistical variability and sensitivity to initial conditions dictate the formulation of the following simulation algorithm, which enables extracting the $[Da_l, Da_u]$ estimates from the simulations accurately, at minimum computational cost.

Algorithm:

0. Establish stable reaction at a high Damköhler denoted Da_0 (estimated from the CMC predictions) by evolving the flow for $T_s = 3T_t$.
1. Reduce the Damköhler by a pre-determined factor (0.5) in a series of steps, evolving each Da for $T_s = 2.1T_t$ till global extinction is observed. Thus obtain preliminary estimates for $[Da_l, Da_u]$.
2. Perform multiple ($M = 4$) independent simulations¹ starting at the preliminary estimate Da_u , reducing the Da by a factor of 0.7, evolving the flow for $T_s = 3T_t$ or to extinction, whichever is earlier. Thus obtain refined estimates of $[Da_l, Da_u]$ and estimates of the probability of extinction at these Damköhler numbers.

6.4 Results

The model predictions for the stability limits in $Da-\hat{\xi}_r$ space are shown in Fig. 21. See Table 5. The CMC model predictions for the critical Damköhler corresponding to ex-

Table 5: Global extinction predictions.

	$\hat{\xi}_r = 10$	$\hat{\xi}_r = 1$	$\hat{\xi}_r = 0.27$
Da_{crit} (CMC)	0.527	56.02	204.2
$[Da_l, Da_u]$ (IEM)	[0.35, 0.5]	[1260, 1500]	$[8 \times 10^5, 1.6 \times 10^6]$
$[Da_l, Da_u]$ (EMST)	[0.35, 0.5]	[122.5, 175]	[700, 1000]

tinction scale as $\hat{\xi}_r^{-2}$ for the $\hat{\xi}_r = 10$ and $\hat{\xi}_r = 1$ cases, as expected. The prediction for the thin reaction zone case ($\hat{\xi}_r = 0.27$) deviates from this scaling since the thermochemical constant C is different for this case. While there is reasonably good agreement among the models for broad reaction zones, it is found that the predictions diverge with decreasing reaction zone thickness parameter. The definition of global extinction used in this study is largely insensitive to the effect of statistical variability. For the cases where MIS were performed (the only exception being the IEM for $\hat{\xi}_r = 0.27$ for reasons noted earlier), it is found that all 4 simulations exhibited stable combustion at Da_u and global extinction at Da_l . However, these results must be cautiously interpreted within the limited definition of global extinction used in this study.

Quantitative comparisons of the model predictions are also made and the statistic that is compared is defined in terms of the mean perturbation from equilibrium of the

¹For the $\hat{\xi}_r = 0.27$ case the IEM model prediction for critical Damköhler number differs from the CMC and EMST predictions by several orders of magnitude. Multiple independent simulations were not performed for this case since the IEM model is grossly in error.

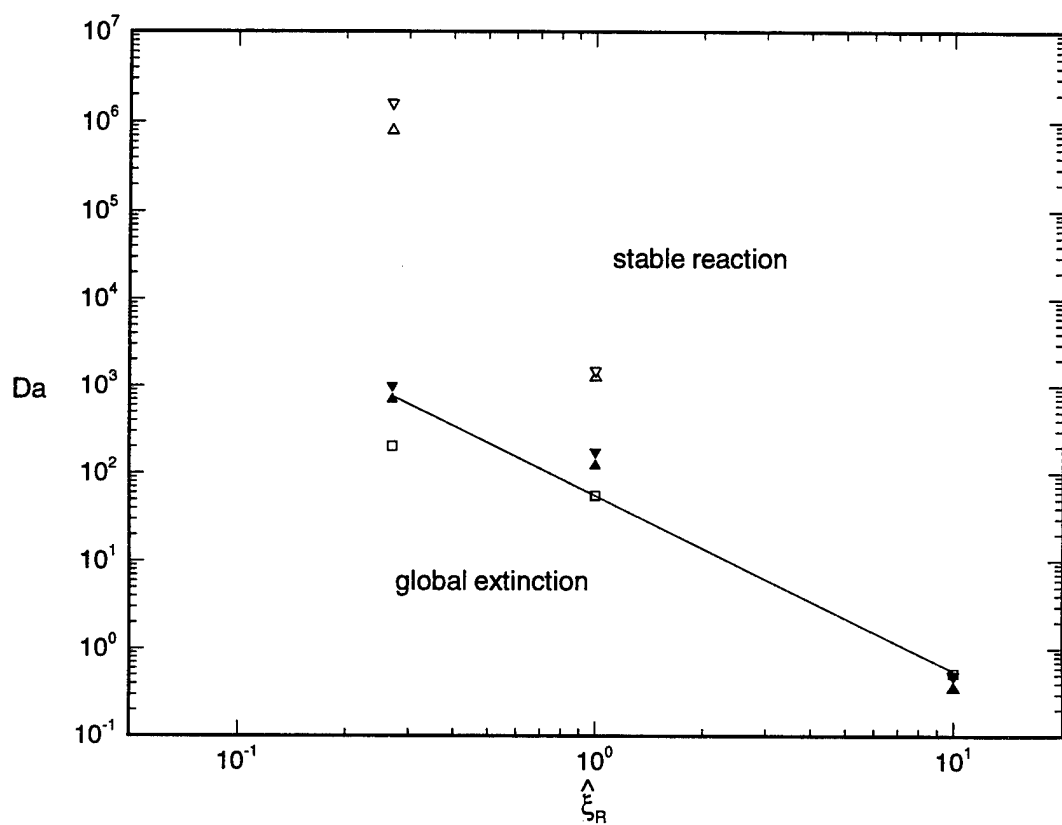


Figure 21: Stability diagram in the $Da - \xi_r$ plane showing the different model predictions for the stability boundary: \square CMC; open triangles IEM; solid triangles EMST. The line represents $Da = 56.02 \xi_r^{-2}$.

progress variable conditioned on the reaction zone $\langle y|\xi_R \rangle(t)$, which is defined as

$$\langle y|\xi_R \rangle(t) \equiv \langle (Y_e(\xi^{(i)}(t)) - Y^{(i)}(t)) | \xi_l \leq \xi^{(i)}(t) \leq \xi_r \rangle. \quad (79)$$

This quantity attains a stationary state after one transport timescale T_t has elapsed and time-averaging may be performed for $t > T_t$. The predictions of the PDF models for this time-averaged quantity, $[\langle y|\xi_R \rangle]_T$ are compared with the average value of $q(\eta)$ in the reaction zone obtained from the CMC predictions in Table 6. The results are now discussed on a case-by-case basis.

6.4.1 Broad reaction zone case: $\hat{\xi}_r = 10$

For this case the numerical parameters used to obtain the CMC result are tabulated in Table 7. The CMC model prediction for the critical Damköhler number for $\hat{\xi}_r = 10$ is 0.527. The perturbation of the conditional mean progress variable from equilibrium (q_M) at Da_{crit} is shown in Fig. 22. The perturbation of the conditional mean progress variable

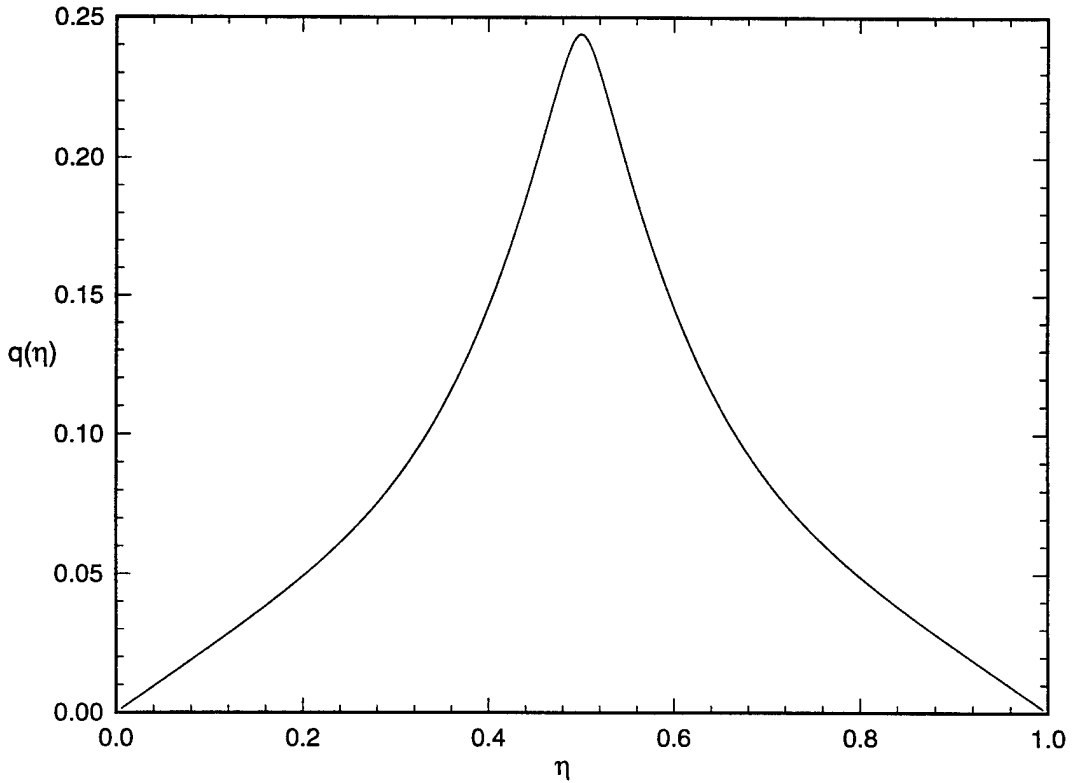


Figure 22: Perturbation $q(\eta) = Y_e(\eta) - Q(\eta)$ obtained from the CMC model at $\text{Da}_{\text{crit}}=0.527$ for the $\hat{\xi}_r=10$ case.

from equilibrium (q_M) at Da_{crit} for the cases $\hat{\xi}_r=10$ and $\hat{\xi}_r=1$ is presented in terms of the scaled similarity variables ($\hat{q}_M = q_M/\Delta\xi_e$ and $\hat{\eta} = (\xi - \xi_s)/\Delta\xi_e$) in Fig. 23. (The case

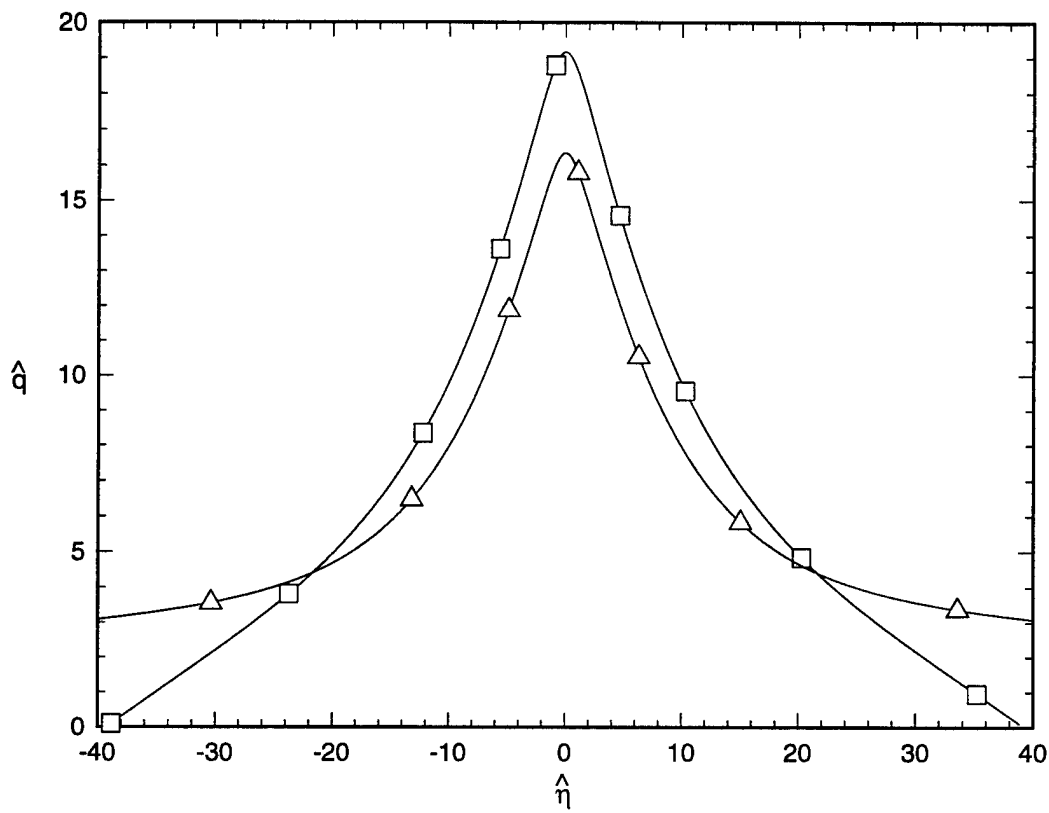


Figure 23: Scaled perturbation $\hat{q}(\hat{\eta}) = q(\eta/\Delta\xi_e)/\Delta\xi_e$ obtained from the CMC model at Da_{crit} for $\hat{\xi}_r = 10$ (\square) and $\hat{\xi}_r = 1$ (\triangle).

$\hat{\xi}_r = 0.27$ is not shown because it is not expected to obey the same scaling, given that the value of the thermochemical constant C is different for that case). While the solutions are not exactly self-similar, they do show an approximate collapse under this scaling. The IEM prediction for this case is ($Da_l = 0.35$, $Da_u = 0.5$). The scatter plots for $Da = 0.5$ and $Da = 0.35$ are shown in Figs. 24 and 25 respectively. The EMST prediction for this case

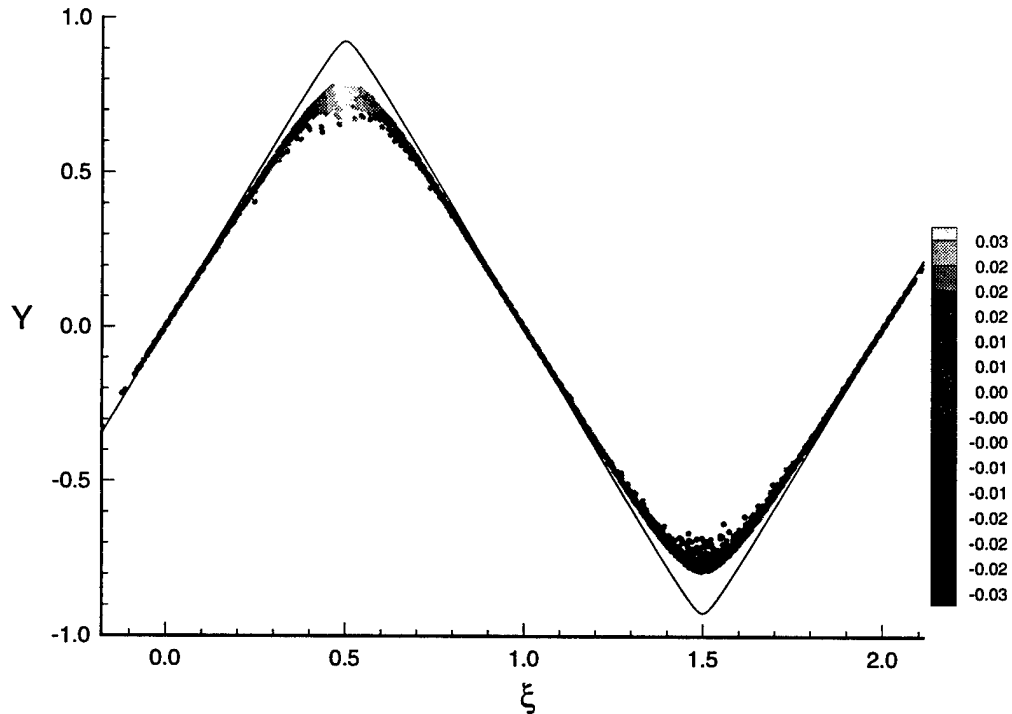


Figure 24: Scatter plot of progress variable Y vs. mixture fraction ξ for the $\hat{\xi}_r = 10$ case at $t = 163$ ($2.8T_t$) using the IEM mixing model. The Damköhler number for this simulation ($Da = 0.5$) corresponds to stable reaction. The solid line is the equilibrium line $Y_e(\xi)$. The grayscale intensity of each particle represents the magnitude of the reaction rate S_Y whose scale is shown in the table on the right.

is also ($Da_l = 0.35$, $Da_u = 0.5$). The scatter plots for $Da_u = 0.5$ and $Da_l = 0.35$ are shown in Figs. 26 and 27 respectively. The IEM model result for $Da = 0.5$ shows a slightly higher degree of scatter which may be attributed to the non-local nature of the model. However, apart from this the IEM and EMST results are very similar for this case, and the critical Damköhler number predictions are in good agreement with the CMC result.

6.4.2 Moderate reaction zone case: $\hat{\xi}_r = 1$

The CMC model prediction for the critical Damköhler number for $\hat{\xi}_r = 1$ is 56.02 (numerical parameters used to obtain this solution are shown in Table 7). The perturbation of the conditional mean progress variable from equilibrium (q_M) at Da_{crit} is shown in Fig. 28. The IEM prediction for this case is ($Da_l = 1260$, $Da_u = 1500$), while the EMST prediction

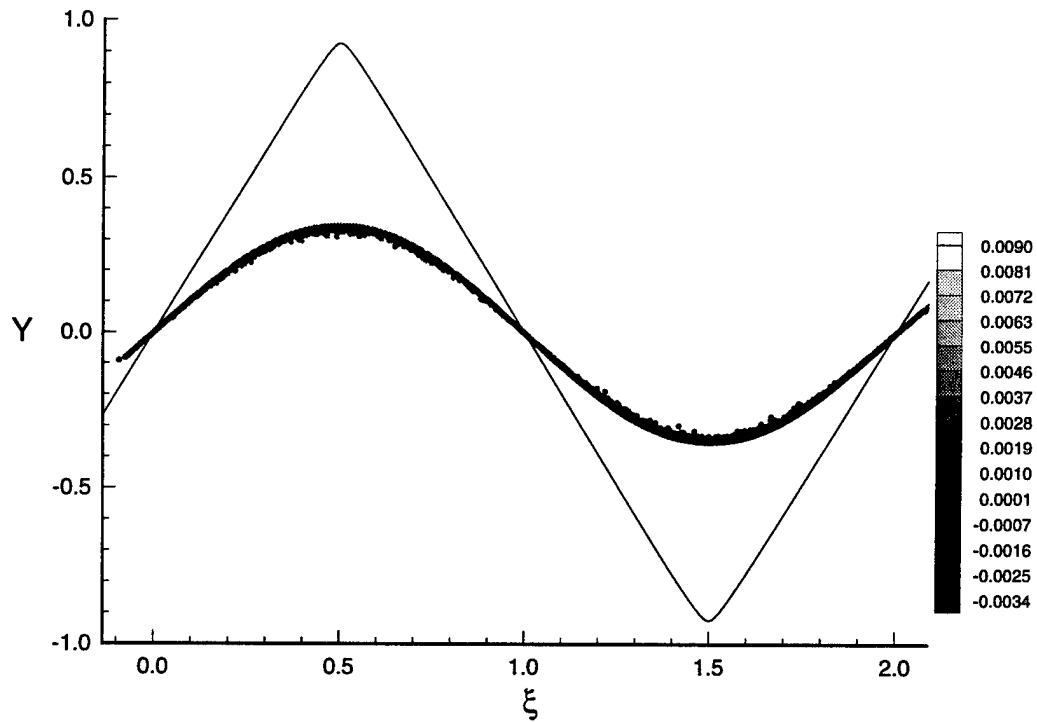


Figure 25: Scatter plot of progress variable Y vs. mixture fraction ξ for the $\hat{\xi}_r = 10$ case at $t = 116.3$ ($2T_t$) using the IEM mixing model. The Damköhler number for this simulation ($Da = 0.35$) corresponds to global extinction. The solid line is the equilibrium line $Y_e(\xi)$. The grayscale intensity of each particle represents the magnitude of the reaction rate S_Y whose scale is shown in the table on the right.

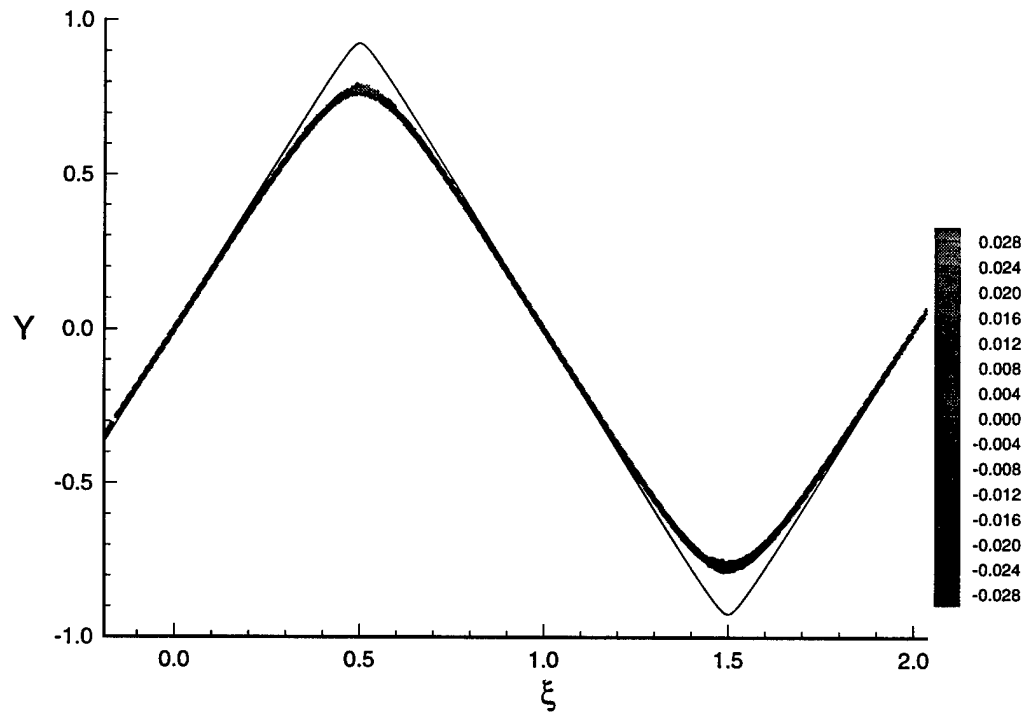


Figure 26: Scatter plot of progress variable Y vs. mixture fraction ξ for the $\hat{\xi}_r = 10$ case at $t = 115.2$ ($1.98T_t$) using the EMST mixing model. The Damköhler number for this simulation ($Da = 0.5$) corresponds to stable reaction. The solid line is the equilibrium line $Y_e(\xi)$. The grayscale intensity of each particle represents the magnitude of the reaction rate S_Y whose scale is shown in the table on the right.

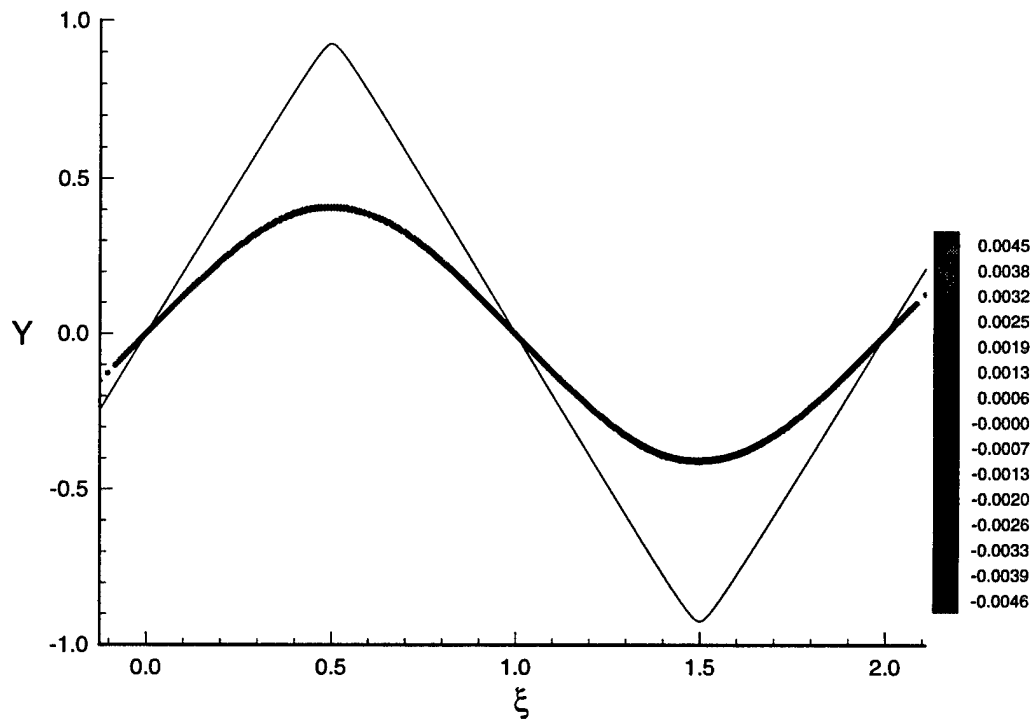


Figure 27: Scatter plot of progress variable Y vs. mixture fraction ξ for the $\hat{\xi}_r = 10$ case at $t = 115.4$ ($1.98T_t$) using the EMST mixing model. The Damköhler number for this simulation ($Da = 0.35$) corresponds to global extinction. The solid line is the equilibrium line $Y_e(\xi)$. The grayscale intensity of each particle represents the magnitude of the reaction rate S_Y whose scale is shown in the table on the right.

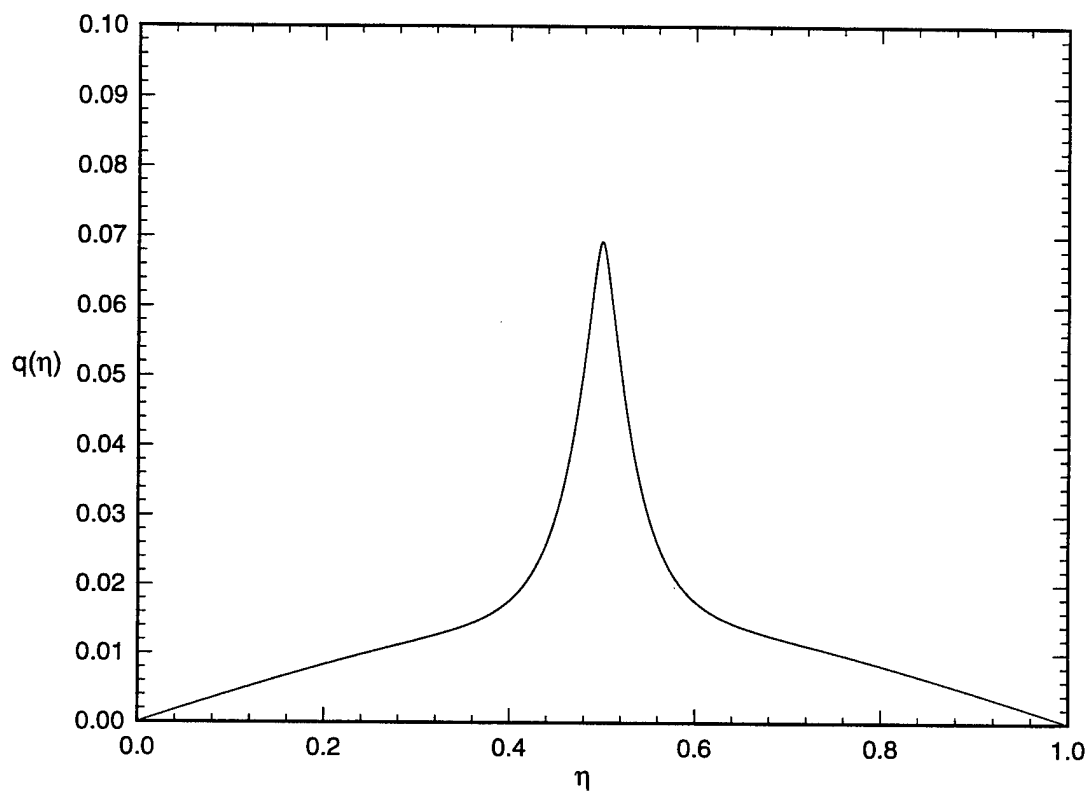


Figure 28: Perturbation $q(\eta) = Y_e(\eta) - Q(\eta)$ obtained from the CMC model at $Da_{crit}=56.02$ for the $\hat{\xi}_r=1$ case.

for this case is ($Da_l = 122.5$, $Da_u = 175$). Both PDF models predict significantly higher critical Damköhler numbers than the CMC model. This may be due to the fact that in the CMC model spatial homogeneity is assumed, whereas in the physical problem there is a “flame brush”. The PDF models account for transport of progress variable flux in closed form and presumably constitute a better model of the physical problem. The difference between the IEM and EMST predictions can be traced to the fact that the IEM model is non-local in composition space, whereas the EMST model is local in composition space. The scatter plots for $Da = 1500$ and $Da = 1260$ using the IEM model are shown in Figs. 29 and 30 respectively. For the stable reaction case (Fig. 29), the IEM model

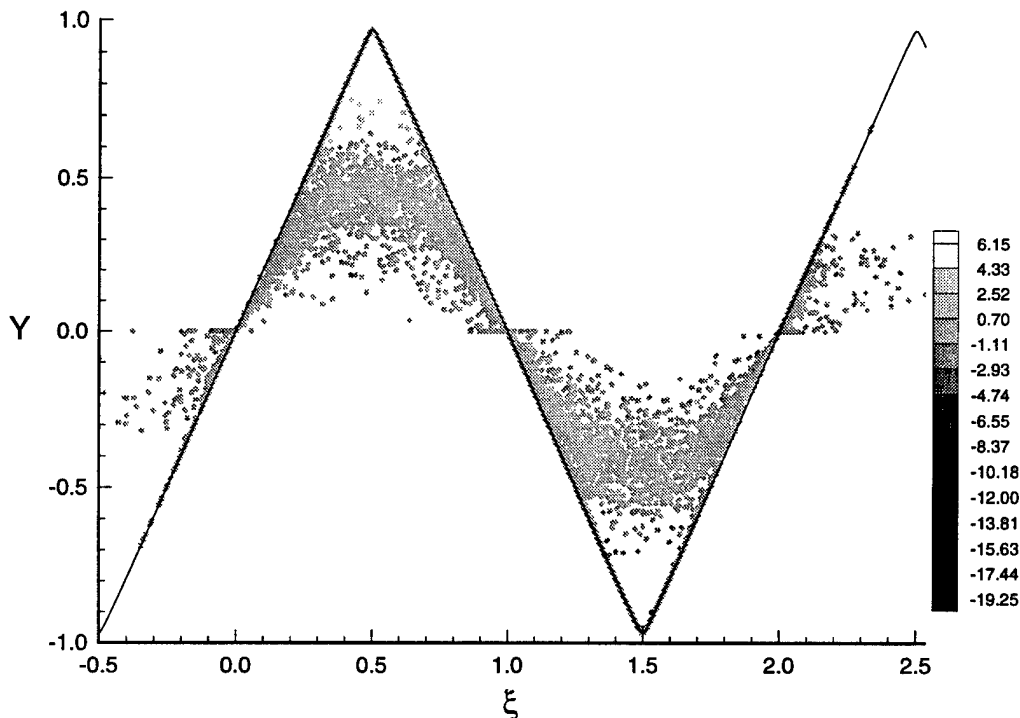


Figure 29: Scatter plot of progress variable Y vs. mixture fraction ξ for the $\hat{\xi}_r = 1$ case at $t = 15.7$ ($3T_t$) using the IEM mixing model. The Damköhler number for this simulation ($Da = 1500$) corresponds to stable reaction. The solid line is the equilibrium line $Y_e(\xi)$. The grayscale intensity of each particle represents the magnitude of the reaction rate S_Y whose scale is shown in the table on the right.

suggests that the pdf in composition space in the reaction zone is composed of 3 distinct regions: (i) a δ -function at equilibrium, (ii) relatively low probability density regions close to equilibrium corresponding to reaction terms being dominant, and (iii) region of high probability density corresponding to a dynamic balance between reaction, mixing and transport. For the case corresponding to global extinction (Fig. 30), the particles are found to be collapsing to the $Y = 0$ line. The scatter plots for $Da_u = 175$ and $Da_l = 122.5$ using the EMST model are shown in Figs. 31 and 32 respectively. In this case for stable reaction, there is considerably less scatter of particles away from the equilibrium

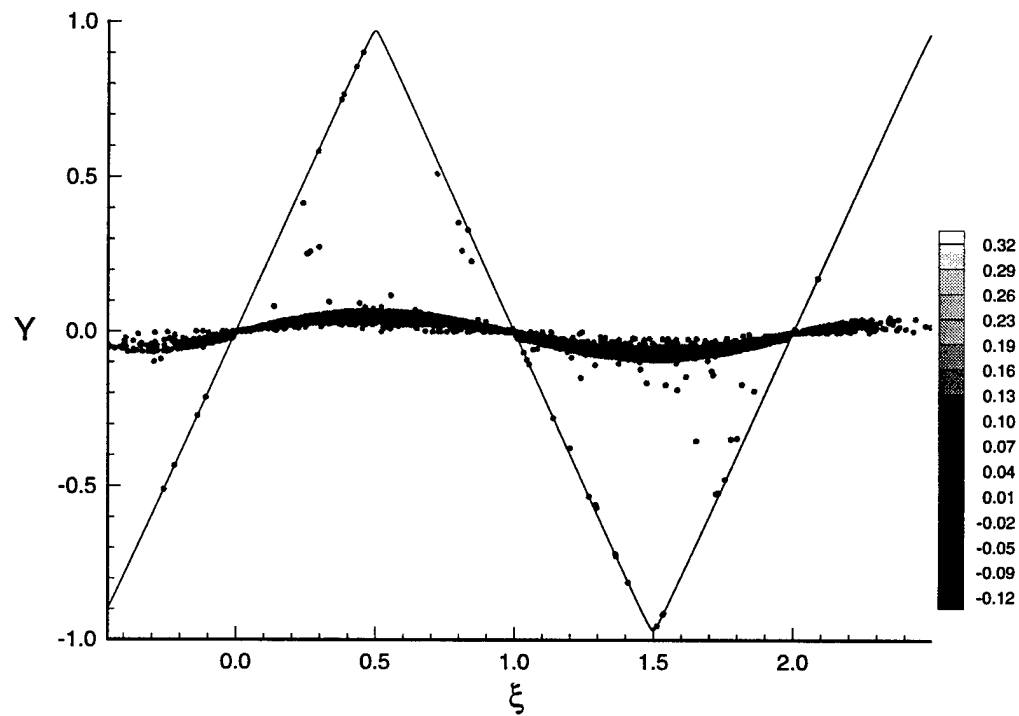


Figure 30: Scatter plot of progress variable Y vs. mixture fraction ξ for the $\hat{\xi}_r = 1$ case at $t = 19.8$ ($3.78T_t$) using the IEM mixing model. The Damköhler number for this simulation ($Da = 1260$) corresponds to global extinction. The solid line is the equilibrium line $Y_e(\xi)$. The grayscale intensity of each particle represents the magnitude of the reaction rate S_Y whose scale is shown in the table on the right.

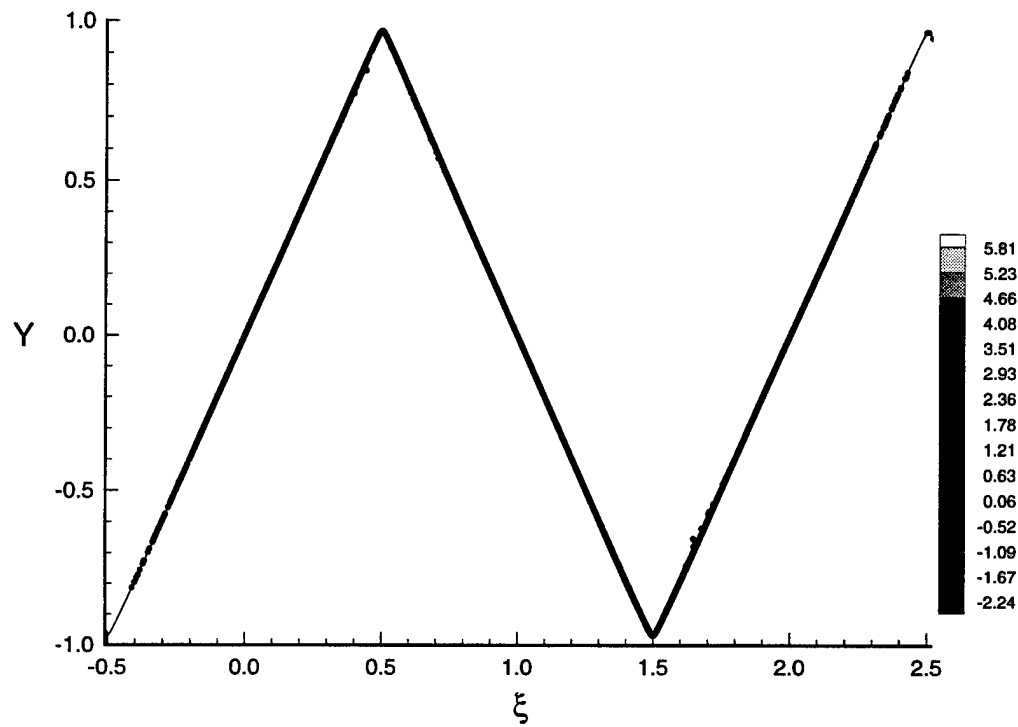


Figure 31: Scatter plot of progress variable Y vs. mixture fraction ξ for the $\hat{\xi}_r = 1$ case at $t = 15.67$ ($2.99T_t$) using the EMST mixing model. The Damköhler number for this simulation ($Da = 500$) corresponds to stable reaction. The solid line is the equilibrium line $Y_e(\xi)$. The grayscale intensity of each particle represents the magnitude of the reaction rate S_Y whose scale is shown in the table on the right.

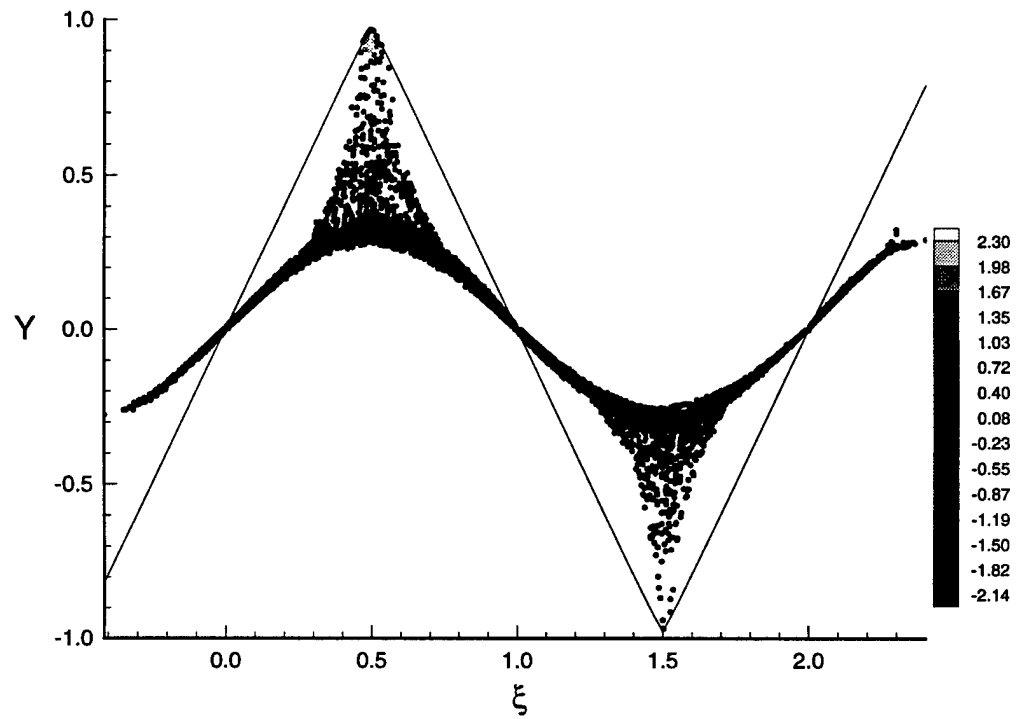


Figure 32: Scatter plot of progress variable Y vs. mixture fraction ξ for the $\hat{\xi}_r = 1$ case at $t = 7.77(1.48T_t)$ using the EMST mixing model. The Damköhler number for this simulation ($Da = 122.5$) corresponds to global extinction. The solid line is the equilibrium line $Y_e(\xi)$. The grayscale intensity of each particle represents the magnitude of the reaction rate S_Y whose scale is shown in the table on the right.

line. The EMST model consistently predicts higher $\langle Y | \xi_R \rangle$ for stable reaction compared to IEM for all the cases. For the extinguishing case (cf. Figs. 32 and. 30), there is a significant difference between the EMST and IEM model behavior. As opposed to the uniform collapse from equilibrium seen in the IEM scatter plot, the EMST model shows distinctly different behavior depending on whether or not the particles are in the reaction zone in mixture fraction space. Within the reaction zone there is a balance between mixing and reaction, with transport moving reactive particles out of the reaction zone into cells where the mean composition ($\langle \xi \rangle, \langle Y \rangle$) lies outside the reaction zone in composition space ($\xi \in [\xi_s - \Delta \xi_r / 2, \xi_s + \Delta \xi_r / 2], Y \in [Y_l, Y_e(\xi)]$ (where Y_l corresponds to $f(y) = 0.1$). In the IEM model these reactive particles are mixed toward the cell mean resulting in extinction at higher critical Damköhler numbers. In the EMST model, the reactive particles are mixed with their neighbors in composition space, and as a consequence they may remain in the reaction zone longer. This accounts for the lower critical Damköhler predictions which seem to be more consistent with the problem physics.

6.4.3 Thin reaction zone case: $\hat{\xi}_r = 0.27$

The CMC model prediction for the critical Damköhler number for $\hat{\xi}_r = 0.27$ is 204.2 (see Fig. 33 and Table 7). This case constitutes a severe test for the PDF mixing models. The reaction zone in composition space is small and it is expected that reaction can be sustained only at Damköhler numbers higher than the CMC prediction. However, it is seen that while the EMST model prediction is within an order of magnitude of the CMC result, the IEM prediction is several orders of magnitude higher. For the IEM model, stable reaction could be sustained only at a Damköhler number of 1.6×10^6 . The EMST prediction for this case is ($Da_l = 700$, $Da_u = 1000$). The scatter plot for stable reaction (Fig. 34) shows more particles departing from the equilibrium line compared to the stable reaction scatter plot for the moderate reaction zone thickness case (Fig 31). This may be attributed to the fact that while the Damköhler number in the thin reaction zone scatter plot is equal to the upper bracket of the critical Damköhler number for that case ($Da_u = 1000$), the Damköhler number in the moderate reaction zone scatter plot ($Da = 500$ in Fig 31) is higher than the upper bracket of the critical Damköhler number ($Da_u = 175$). The scatter plot corresponding to global extinction (Fig. 35) is not significantly different from the moderate reaction zone thickness case.

7 Appendix A: Equilibrium function $Y_e(\xi)$ for the general case

For the general case, given $\xi_s \in [0, 1]$, and the parameter $\Delta \xi_e$, the equilibrium function is defined as follows. As for the symmetric case the equilibrium function is specified as a function of $z = \xi - \xi_{ss}$ and $\Delta \xi_e$. However, in this case the origin of the similarity variable, ξ_{ss} , has to be determined from the solution to a transcendental equation. With this in mind two constants a and b are defined as follows:

$$a \equiv \frac{1}{2} \left[\frac{1}{\xi_s} - \frac{1}{1 - \xi_s} \right] \quad (80)$$

$$b \equiv \left[\frac{1}{\xi_s} + \frac{1}{1 - \xi_s} \right] \quad (81)$$

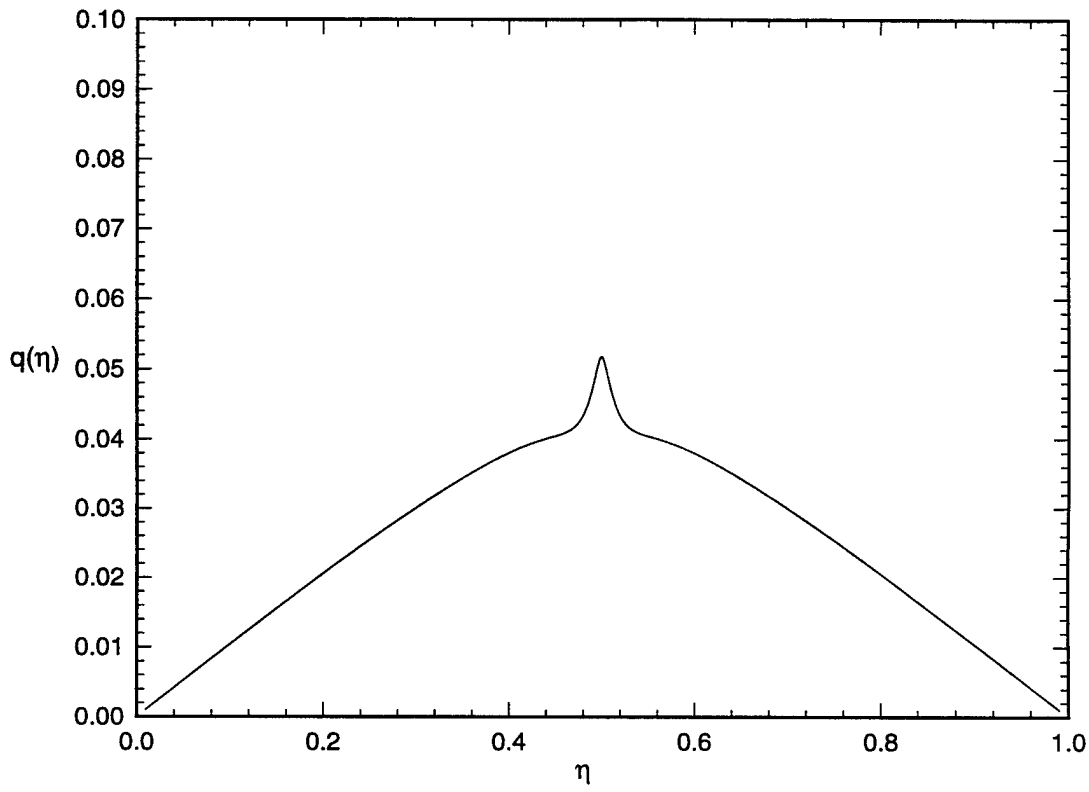


Figure 33: Perturbation $q(\eta) = Y_e(\eta) - Q(\eta)$ obtained from the CMC model at $Da_{crit}=204.2$ for the $\hat{\xi}_r=0.27$ case.

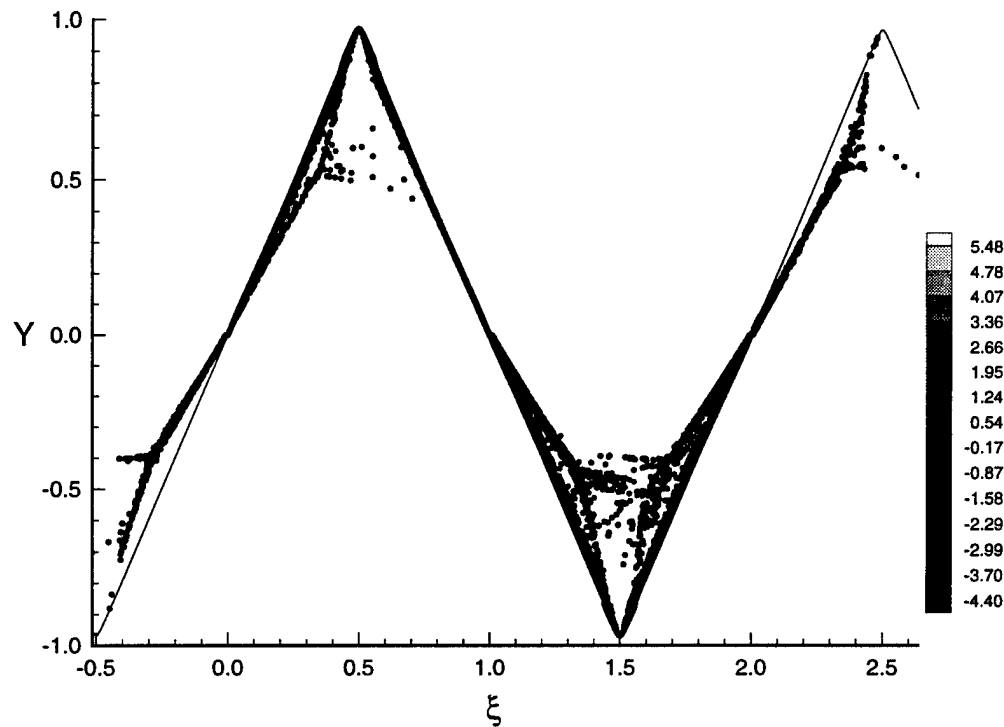


Figure 34: Scatter plot of progress variable Y vs. mixture fraction ξ for the $\hat{\xi}_r = 0.27$ case at $t = 10.87$ ($3T_t$) using the EMST mixing model. The Damköhler number for this simulation ($Da = 1000$) corresponds to stable reaction. The solid line is the equilibrium line $Y_e(\xi)$. The grayscale intensity of each particle represents the magnitude of the reaction rate S_Y whose scale is shown in the table on the right.

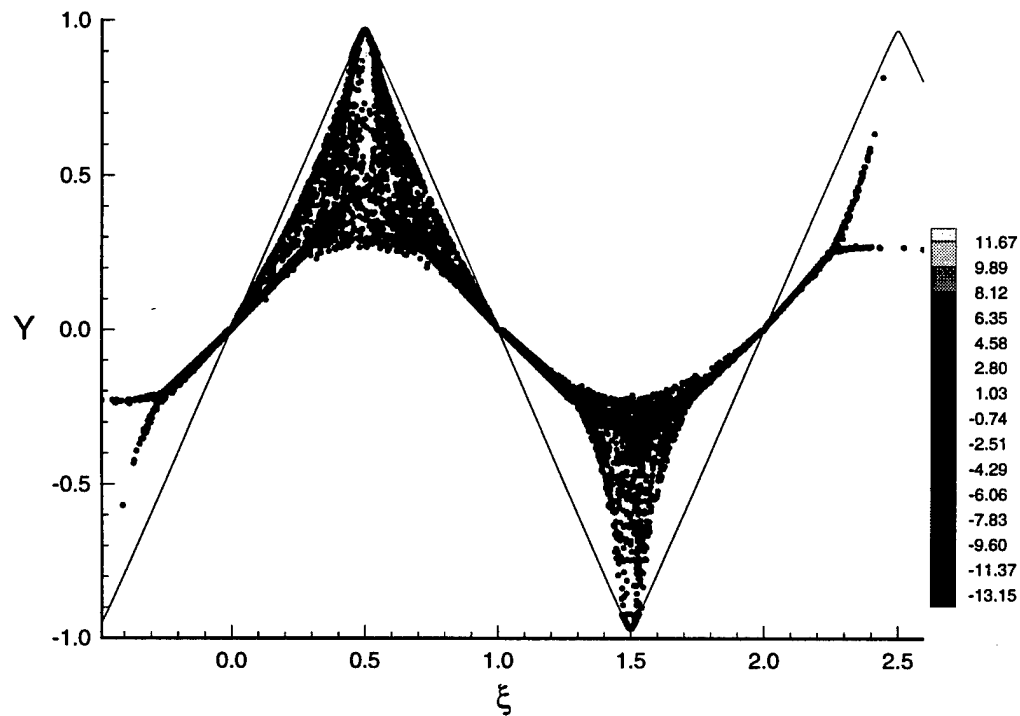


Figure 35: Scatter plot of progress variable Y vs. mixture fraction ξ for the $\hat{\xi}_r = 0.27$ case at $t = 7.29$ ($2T_t$) using the EMST mixing model. The Damköhler number for this simulation ($Da = 700$) corresponds to global extinction. The solid line is the equilibrium line $Y_e(\xi)$. The grayscale intensity of each particle represents the magnitude of the reaction rate S_Y whose scale is shown in the table on the right.

Noting $\hat{\xi} \equiv z/\Delta\xi_e$, the quantity ξ_{ss} is calculated as

$$\xi_{ss} = -\hat{\xi}_1 \Delta\xi_e,$$

where $\hat{\xi}_1$ is the solution to the equation

$$h(\hat{\xi}_1 + \frac{1}{\Delta\xi_e}) - h(\hat{\xi}_1) = -\frac{a}{b\Delta\xi_e}, \quad (82)$$

with the function $h(\hat{\xi})$ given by

$$h(\hat{\xi}) = \frac{1}{2\pi} \left[\ln(1 + \hat{\xi}^2) - 2\hat{\xi} \arctan(\hat{\xi}) \right]. \quad (83)$$

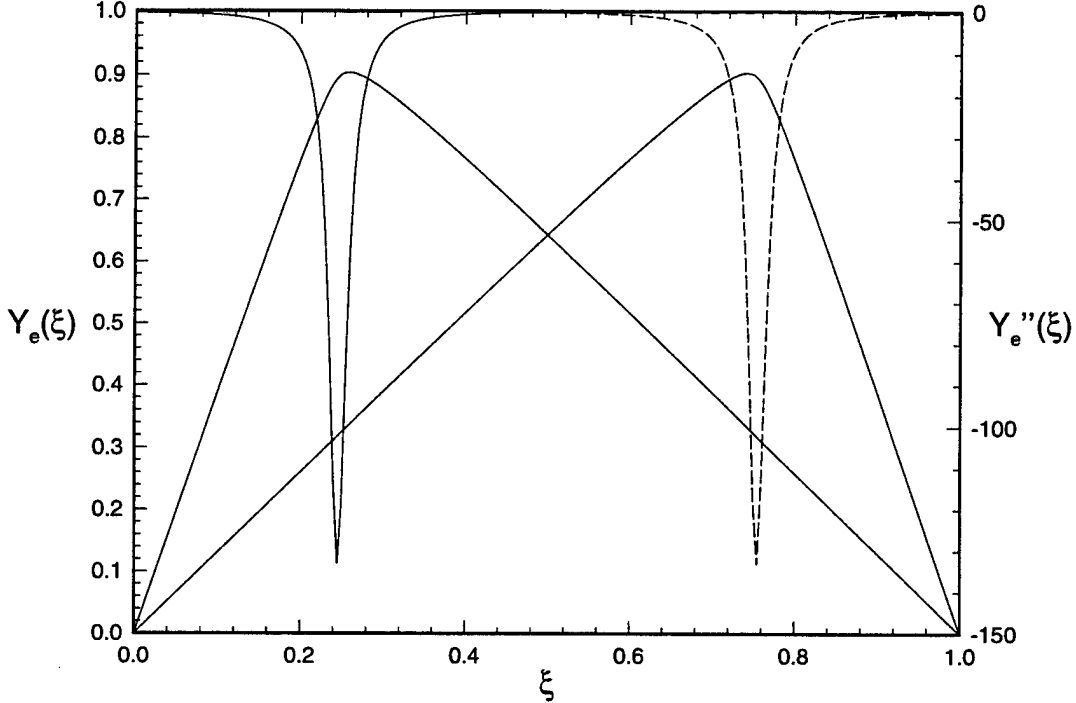


Figure 36: Equilibrium function $Y_e(\xi)$ and its second derivative $Y_e''(\xi)$ for different values of the stoichiometric mixture fraction ξ_s , in the self-similar thermochemistry: — $\xi_s = 0.25$; — — $\xi_s = 0.75$. The value of the parameter $\Delta\xi_e$ is 0.0127324.

The second derivative of the equilibrium function is again of the Cauchy form (which will asymptote to a δ function in the limit $\Delta\xi_e \rightarrow 0$):

$$\frac{d^2 Y_e}{dz^2} = -\frac{b}{\pi\Delta\xi_e} \frac{1}{\left[1 + (z/\Delta\xi_e)^2\right]}. \quad (84)$$

The maximum value of the second derivative $|Y_e''|_{\max}$ is $b/(\pi\Delta\xi_e)$. Integrating Eq. (84) once with respect to z yields $Y_e'(z)$:

$$\frac{dY_e}{dz} = a - \frac{b}{\pi} \arctan\left(\frac{z}{\Delta\xi_e}\right). \quad (85)$$

Integrating Eq. (84) twice with respect to z from z_1 (which corresponds to $\xi = 0$) to z_2 (which corresponds to $\xi = 1$) results in $Y_e(z)$:

$$Y_e(z) = Y_{\max} - \left\{ a(z_0 - z) + b\Delta\xi_e \left[h(\hat{\xi}_0) - h(\hat{\xi}) \right] \right\}, \quad (86)$$

where

$$Y_{\max} = a(z_0 - z_1) + b\Delta\xi_e \left[h(\hat{\xi}_0) - h(\hat{\xi}_1) \right]$$

and

$$z_0 = \Delta\xi_e \hat{\xi}_0 \equiv \Delta\xi_e \tan\left(\frac{a\pi}{b}\right).$$

This completes the specification of the self-similar equilibrium function for the general case. Fig. 36 shows the self-similar equilibrium function for different values of ξ_s .

8 Appendix B: Numerical solution of the CMC equation

In order to determine the critical Damköhler for a given value of $\hat{\xi}_{rss}$ in Eq. 67, which is a differential equation with a nonlinear source term, a numerical approach is adopted. The domain $0 \leq \eta \leq 2$ is discretized using N grid points such that

$$\eta_i = \frac{2(i-1)}{N-1} \quad i = 1, \dots, N,$$

and $\Delta\eta_{i+} = \eta_{i+1} - \eta_i$ and $\Delta\eta_{i-} = \eta_i - \eta_{i-1}$. The grid spacing may be non-uniform in order to resolve the reaction rate function accurately for cases with thin reaction zones in a computationally efficient manner. Function values at the i^{th} grid point are represented by subscript i ; e.g. the function $Q(\eta)$ at the i^{th} grid point is denoted Q_i . Using the three-point central-difference formula for the numerical approximation to $\partial^2 Q / \partial \eta^2$ we obtain

$$2 \left[\frac{Q_{i+1}\Delta\eta_{i-} - Q_i(\Delta\eta_{i-} + \Delta\eta_{i+}) + Q_{i-1}\Delta\eta_{i+}}{(\Delta\eta_{i+}\Delta\eta_{i-})(\Delta\eta_{i-} + \Delta\eta_{i+})} \right] + \frac{1}{\Delta\xi_e} \hat{q}_i \exp\{[-B\hat{q}_i - CG(\hat{\eta}_i)]\} \text{Da} \hat{\xi}_{rss}^2 \left(\frac{8C}{\pi} \right) = 0. \quad (87)$$

A numerical technique to compute simple turning points of nonlinear equations [3] based on a pseudo-arc length method is used to solve Eq. 87 for $\text{Da}_{\text{crit}}(\hat{\xi}_{rss})$.

As $|Y_e''|_{\max}$ is increased, higher grid density in the neighborhood of $\eta = \xi_s$ is required to resolve the solution to the CMC equation accurately. For this purpose a non-uniform grid is generated in η space using the following transformation from a uniformly spaced grid in z space:

$$\eta = 0.5 + \left\{ z - \frac{\Delta\xi_e}{\sqrt{W}} (1 - \rho\Delta\xi_e) \arctan\left(\frac{z\sqrt{W}}{\Delta\xi_e}\right) \right\}, \quad -z_0 \leq z \leq z_0, \quad (88)$$

where z_0 is determined by the requirement that η take the values 0 and 1 at $z = -z_0$ and $z = z_0$ respectively. This value is easily obtained by solving the transcendental equation

$$z_0 - \frac{\Delta\xi_e}{\sqrt{W}} (1 - \rho\Delta\xi_e) \arctan\left(\frac{z_0\sqrt{W}}{\Delta\xi_e}\right) = 0.5$$

The parameters W and ρ can be used to control the width of the fine grid and the grid density respectively. For all the test cases the grid was generated with $N = 180$, $\rho = 1$, and $W = 0.005$. This ensured there were at least 45 points in the $\Delta\xi_e$ neighborhood of ξ_s for the most demanding case with $|Y_e''|_{\max} = 120$.

9 Appendix C: Analytic Integration of the Reaction Rate

In the simulations particle properties are advanced over a time step Δt which is chosen to be small compared to the the physical time scales of the problem. Changes in the reaction progress variable Y due to reaction occur on the order of the chemical timescale τ^* . In general, time-accurate solutions are obtained by advancing the change in Y over a series of fractional sub-steps Δt_r for each Δt , such that the chemical timescale is also resolved. This is a computational overhead characteristic of reactive flows which scales as the Damköhler number. In the present work, this expensive sub-stepping is avoided by noting that the self-similar thermochemistry reaction rate (and in fact, even the Lee-Pope thermochemistry reaction rate) admits an analytic solution.

The evolution of the reaction progress variable Y due to reaction can be written as:

$$\frac{dY}{dt} = S_Y(\xi, Y) = S(\xi, y) = f(y)g(\xi)/\tau_c. \quad (89)$$

In practice it is easier to solve for the perturbation from equilibrium y , which evolves by

$$\frac{dy}{dt} = -y \exp(-B^* y)g(\xi)/\tau^*, \quad (90)$$

where $\tau^* = \tau_c/Be$ and $B^* = B/\Delta\xi_e$. This equation can be integrated the beginning of the time-step (t_0) to the end of the time step ($t_0 + \Delta t$) to yield

$$\text{Ei}(B^* y(t_0 + \Delta t)) = -\frac{g(\xi)}{\tau^*} \Delta t + \text{Ei}(B^* y(t_0)), \quad (91)$$

where

$$\text{Ei}(x) = \int_{-\infty}^x \frac{e^t}{t} dt, \quad x > 0,$$

is the standard exponential integral which is easily evaluated numerically [17]. Since the perturbation y is non-negative in the flame zones and $B^* = B/\Delta\xi_e$ is always a positive quantity, Eq. 91 can be solved using a root-finder for all positive values of y (the special case of $y = 0$, in which case $Y = Y_e(\xi)$ and there is no change in the progress variable is handled by a conditional statement). For the “anti-flame” zones where the perturbation is negative, the same equation Eq. 91 holds for the absolute value of the perturbation.

10 Appendix D: Numerical resolution and convergence testing of the PDF simulations

When using a Monte Carlo solution procedure for the pdf transport equation, it is important to ensure that the numerical estimates of flow statistics of interest are converged with respect to the number of particles per cell N_{pc} used in the simulation. For the present problem, the statistic of interest is defined in terms of the mean perturbation from equilibrium of the progress variable conditioned on the reaction zone $\langle y|R \rangle(t)$, which is defined as

$$\langle y|\xi_R \rangle(t) \equiv \langle (Y_e(\xi^{(i)}(t)) - Y^{(i)}(t)) | \xi_l \leq \xi^{(i)}(t) \leq \xi_r \rangle. \quad (92)$$

This quantity attains a stationary state after one transport timescale T_t has elapsed and time-averaging may be performed for $t > T_t$. This time-averaged quantity, $[\langle y|R \rangle]_T$, is used to determine convergence of the simulations.

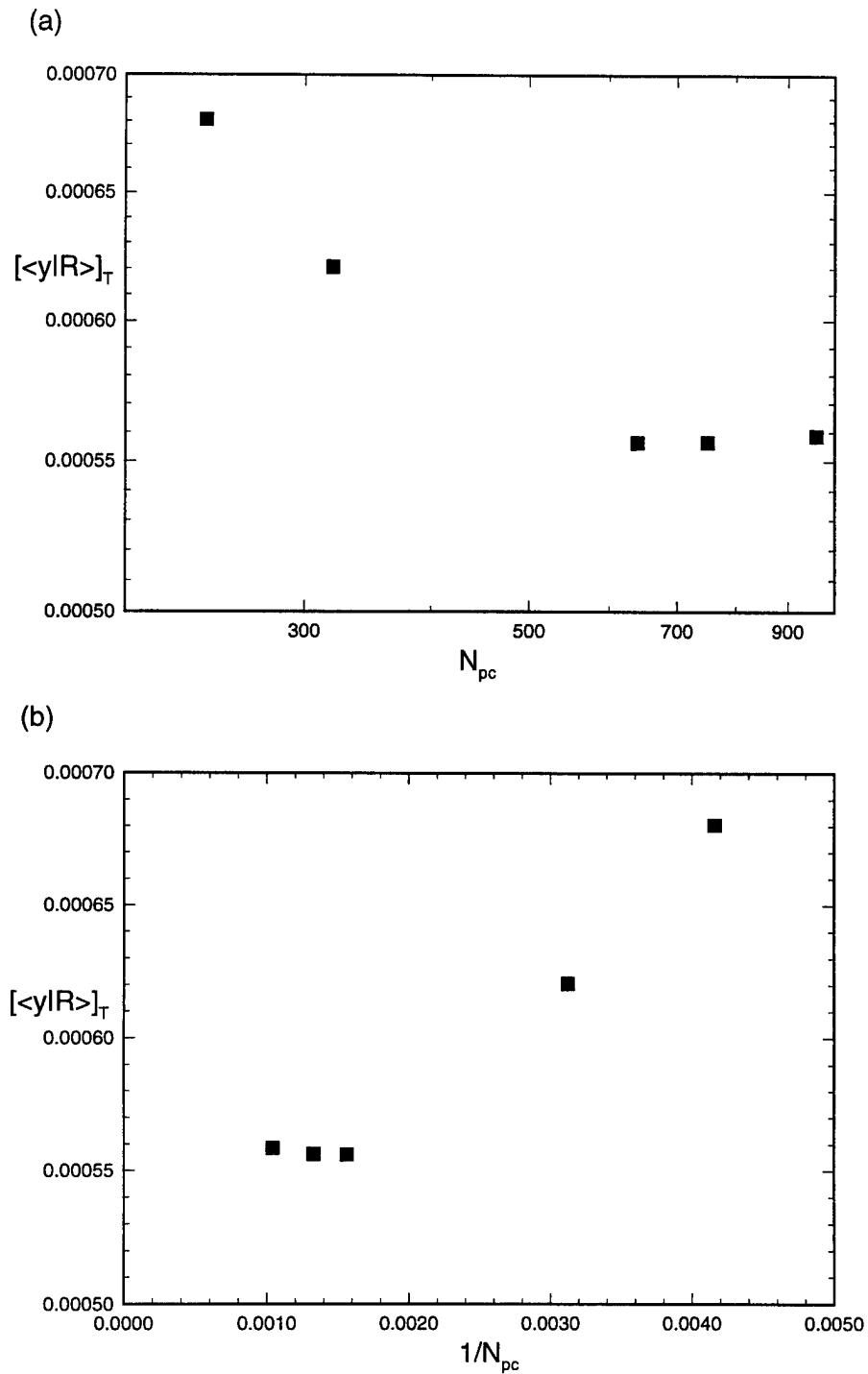


Figure 37: Convergence of $[\langle y | \xi_R \rangle]_T$ and for the $\hat{\xi}_r = 1$ case. EMST model, $Da = 500$ (stable reaction): (a) logarithmic plot showing the $1/N_{pc}$ behavior. (b) plot vs. $1/N_{pc}$, with the origin corresponding to $N_{pc} = \infty$.

For the $\hat{\xi}_r = 1$ case, simulations are performed at a Damköhler number corresponding to stable combustion for different N_{pc} values and the variation of $[\langle y|R \rangle]_T$ is shown in Fig. 37. It is clear that $[\langle y|R \rangle]_T$ converges with respect to N_{pc} and this convergence is reached around $N_{pc} = 640$. Based on this result, the value of N_{pc} for simulations of the $\hat{\xi}_r = 1$ case is chosen to be 750.

From this result, an empirical rule for the resolution (in terms of N_{pc}) required in the $\hat{\xi}_r = 10$ simulation may be deduced. If the particles in a cell are assumed to be uniformly distributed in mixture fraction space, then the average spacing between two particles in mixture fraction space may be estimated as

$$\Delta\xi \sim \xi'/N_{pc},$$

where ξ' is the r.m.s. mixture fraction. The resolution requirement may be expressed as

$$\Delta\xi < \text{constant} \min(\Delta\xi_e, \Delta\xi_r).$$

From the $\hat{\xi}_r = 1$ convergence test this constant is determined to be 0.0625. Using this rule it is found that the minimum N_{pc} for converged simulations for $\hat{\xi}_r = 10$ is 76. Based on this the simulations for the $\hat{\xi}_r = 10$ case are performed with $N_{pc} = 80$.

For the $\hat{\xi}_r = 0.27$ case, since the value of the thermochemical constant C is different from the other two cases, a separate convergence test is performed. These results are shown in Fig. 38. For this case also it is clear from the results that $[\langle y|R \rangle]_T$ converges with respect to N_{pc} and this convergence is reached around $N_{pc} = 960$. Based on this result, the value of N_{pc} for simulations of the $\hat{\xi}_r = 0.27$ case is chosen to be 1120.

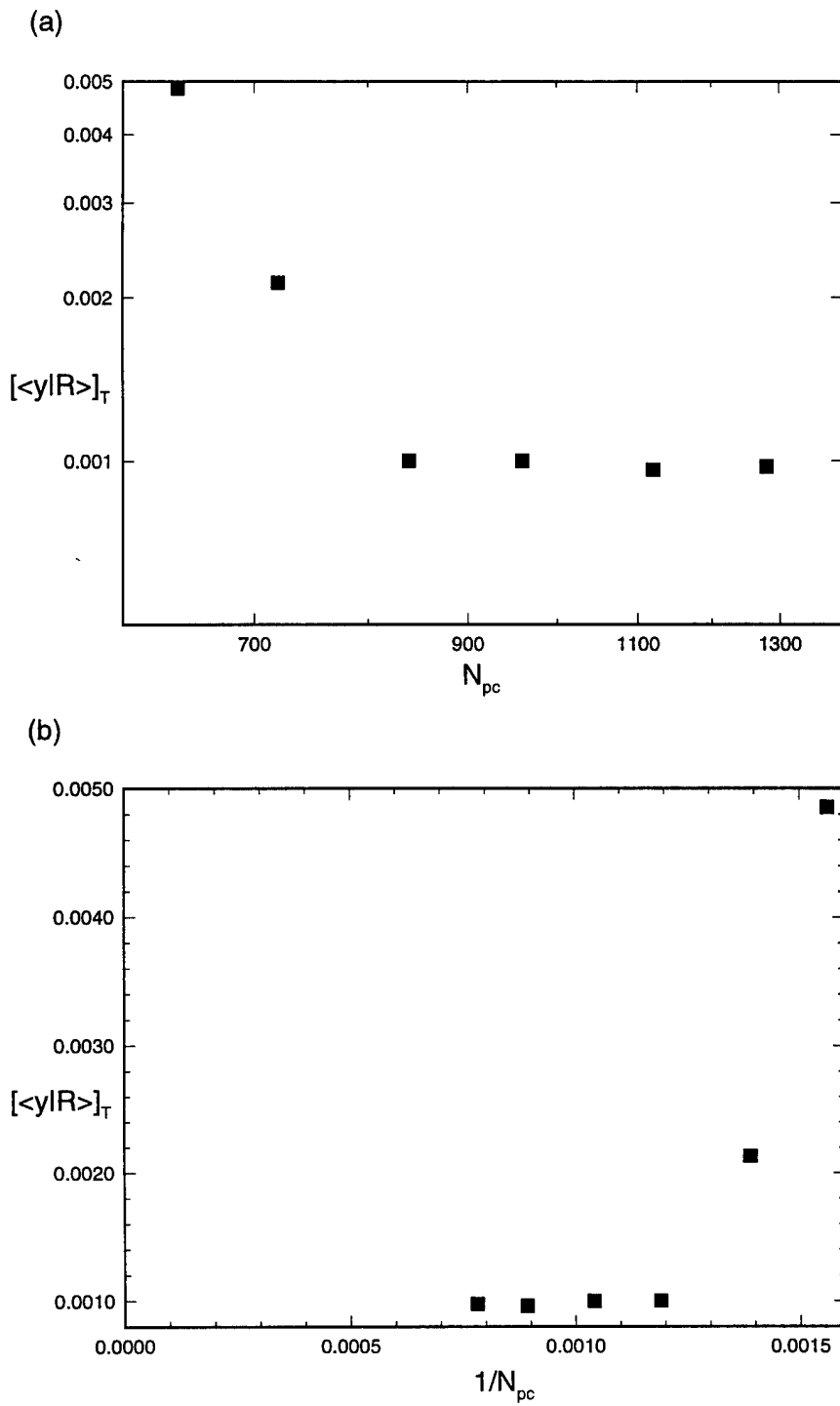


Figure 38: Convergence of $[\langle y | \xi_R \rangle]_T$ and for the $\hat{\xi}_r = 0.27$ case. EMST model, $Da = 2000$ (stable reaction): (a) logarithmic plot showing the $1/N_{pc}$ behavior. (b) plot vs. $1/N_{pc}$, with the origin corresponding to $N_{pc} = \infty$.

References

- [1] R. W. Bilger. Turbulent flows with nonpremixed reactants. In P. A. Libby and F. A. Williams, editors, *Turbulent Reacting Flows*, chapter 3, pages 65–113. Springer-Verlag, 1980.
- [2] R. W. Bilger. Conditional moment closure for turbulent reacting flow. *Phys. Fluids A*, 5(2):436–445, 1993.
- [3] T. F. Chan. Newton-like Pseudo–Arclength Methods For Computing Simple Turning Points. *SIAM J. Sci. Comput.*, 5(1):135–148, 1984.
- [4] J.-Y. Chen and W. Kollmann. PDF Modeling of Chemical Nonequilibrium Effects in Turbulent Nonpremixed Hydrocarbon Flames. In *Twenty-Second Symposium (International) on Combustion*, pages 645–653. The Combustion Institute, Pittsburgh, 1988.
- [5] C. Dopazo. Probability density function approach for a turbulent axisymmetric heated jet. centerline evolution. *Phys. Fluids*, 18:397–404, 1975.
- [6] D. C. Haworth and S. B. Pope. A generalized Langevin model for turbulent flows. *Phys. Fluids*, 29:387–405, 1986.
- [7] Jayesh and S. B. Pope. Stochastic model for turbulent frequency. Technical Report FDA 95-05, Cornell University, Oct 1995.
- [8] Y. Y. Lee and S. B. Pope. Nonpremixed Turbulent Reacting Flow near Extinction. *Combustion and Flame*, 101:501–528, 1995.
- [9] Masri, A. R., Dibble, R. W. and Barlow, R. S. Chemical Kinetic Effects in Non-premixed Flames of H_2/CO_2 Fuel. *Combustion and Flame*, 91:285–309, 1992.
- [10] A. T. Norris and S. B. Pope. Turbulent Mixing Model Based on Ordered Pairing. *Combustion and Flame*, 83:27–42, 1991.
- [11] A. T. Norris and S. B. Pope. Modeling of extinction in turbulent diffusion flames by the velocity–dissipation–composition pdf method. *Combustion and Flame*, 100:211–220, 1995.
- [12] M. R. Overholt and S. B. Pope. Direct numerical simulations of a passive scalar with imposed mean gradient in isotropic turbulence. *Phys. Fluids A*, 8(11):3128–3148, November 1996.
- [13] S. B. Pope. PDF2DV: A FORTRAN code to solve the modeled joint pdf equations for two-dimensional recirculating flows. Unpublished, Cornell University.
- [14] S. B. Pope. PDF Methods for Turbulent Reactive Flows. *Prog. Energy Combust. Science*, 11:119–192, 1985.
- [15] S. B. Pope. On the relationship between stochastic Lagrangian models of turbulence and second-moment closures. *Phys. Fluids*, 6(2):973–985, 1986.

- [16] S. B. Pope. Computations of turbulent combustion: Progress and challenges. In *Twenty-Third Symposium (International) on Combustion*, pages 591–612. The Combustion Institute, 1990.
- [17] Press, W. H.. Teukolsky, S. A.. Vetterling, W. T.. Flannery, B. P. *Numerical Recipes in FORTRAN. The Art of Scientific Computing*. Cambridge University Press, second edition, 1992.
- [18] S. Subramaniam and S. B. Pope. A Turbulent Mixing Model Based on Euclidean Minimum Spanning Trees. *Combustion and Flame*. (to be submitted).
- [19] Masri A. R. Taing, S. and S. B. Pope. PDF Calculations of Turbulent Nonpremixed Flames of H_2/CO_2 Using Reduced Chemical Mechanisms. *Combustion and Flame*. 95:133–150, 1993.
- [20] B. Yang and S. B. Pope. An Investigation of the Accuracy of Manifold Methods and Splitting Schemes in the Computational Implementation of Combustion Chemistry. *Combustion and Flame*. submitted.

Acknowledgements

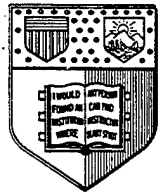
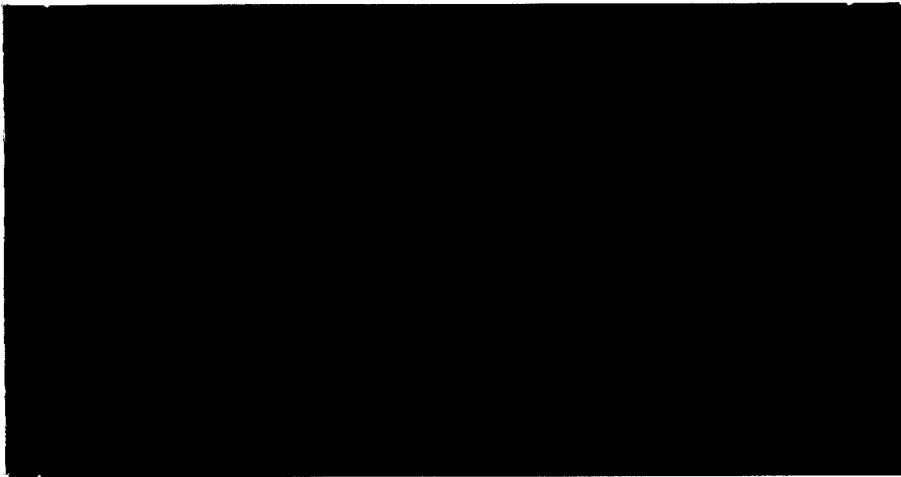
This work was supported by the Air Force Office of Scientific Research, Grant F49620-94-1-0098.

Table 6: Comparison of stationary values of $\langle y | \xi_R \rangle$ from the PDF simulations using IEM and EMST methods with the mean value of $q(\eta)$ in the reaction zone obtained from CMC.

	CMC	EMST	IEM
$\hat{\xi}_r = 10$ Da = 0.527	0.14	0.066	0.075
$\hat{\xi}_r = 1$ Da = 2000 Da = 175	2.5×10^{-4} 3.98×10^{-3}	1.03×10^{-2}	0.10 —
$\hat{\xi}_r = 0.27$ Da = 2000	2.42×10^{-3}	9.98×10^{-4}	—

Table 7: Summary of numerical parameters for each case in the CMC solution.

	$\hat{\xi}_r = 10$	$\hat{\xi}_r = 1$	$\hat{\xi}_r = 0.27$
N —number of grid points in $0 \leq \eta \leq 1$	240	240	240
N_r —number of grid points in $[\xi_s - \Delta\xi_r/2, \xi_s + \Delta\xi_r/2]$	169	71	81
ρ —grid density parameter	1.0	1.0	0.2
W —non-uniform grid width parameter	0.005	0.005	1×10^{-5}
$\Delta\eta_{\min}/\Delta\xi_e$ —resolution in mixture fraction space	6.28×10^{-3}	7.4×10^{-3}	2.99×10^{-3}



Fluid Dynamics and Aerodynamics Program

**Sibley School of
Mechanical and Aerospace Engineering**

Cornell University Ithaca, New York 14853

SOURCES OF BIAS IN PARTICLE-MESH METHODS FOR
PDF MODELS FOR TURBULENT FLOWS

by

Jun Xu and Stephen B. Pope

FDA 97-01

January, 1997

Abstract

Numerical errors, in particular bias, in PDF-based particle-mesh methods for turbulence modeling have been explored. It is shown that bias decreases linearly with the increase of the number of particles, but increases with grid refinement. The fluctuations in mean fields which are fed back into the coefficients of stochastic differential equations are attributed to be the sources of bias. The *Frozen Coefficient* approach has been proposed and adopted to pinpoint the sources of bias in detail. These results provide guidelines for improving the numerical accuracy of PDF models for turbulent flows.

INTRODUCTION

For complex turbulent reactive flows, probability density function (PDF) methods have been well developed and offer great potential [4] [5]. In the application of these methods, a particle-mesh method is used to solve a modeled equation for the evolution of a PDF, e.g., the joint velocity-frequency-composition PDF. This is a Monte-Carlo method in which the PDF is represented by a large set of particles distributed in the physical space. This space is divided into a number of cells in order to estimate the mean fields such as the mean velocity as a function of position. Such a method has been implemented in the PDF2DV code [8] which is a Fortran code to calculate the properties of statistically two-dimensional (plane or axi-symmetric) turbulent reactive flows using the joint velocity-frequency-composition PDF model. In the present work, numerical errors, in particular bias, in PDF2DV are investigated.

The numerical accuracy and convergence of PDF methods have been discussed by Pope [6] and Welton et.al. [9]. Usually, weak convergence, i.e., the convergence of expectations instead of the PDF, is sought for PDF methods. Four different types of numerical errors have been identified by considering estimating a mean quantity: statistical error, spatial discretization error, temporal discretization error and bias. The convergence of numerical solutions to the modeled equations, which are stochastic differential equations (SDE), requires that numerical errors vanish as the particle number per cell N tends to infinity, and as the time step Δt and grid size h approach to zero. It has been shown that statistical error (SE) scales as $1/N^{1/2}$ [6]. It is reasonable to postulate that temporal error and spatial error, behave as that in finite difference method, i.e., both vanish as Δt and h tend to zero for fixed N .

However, in early experiences with the PDF2DV code it has been observed that there appeared to be relatively large bias. The bias is the deterministic error resulting from using a finite number of particles. Its features in the PDF methods are not very clear yet. This study is devoted to understanding the behavior and the sources of bias in PDF2DV, which will provide one of the guidelines for improving the accuracy of the code.

The description of bias in PDF2DV is presented in the next section, and then the strategies for pinpointing the sources of bias is described in the following section. Two test cases are used to search for the sources of bias: stationary homogeneous turbulence and Couette flow. Results for these cases are discussed. Conclusions are drawn in the final section.

DESCRIPTION OF BIAS IN PDF2DV

Before presenting the behavior of bias in PDF2DV, the model equations and some numerical techniques are introduced. A Lagrangian approach is taken both in the modeling and in the numerical method which is a Monte-Carlo particle-mesh method. The fluid-particle possesses properties: velocity $\mathbf{u}^+(t)$ and turbulence relaxation rate (turbulence frequency) $\omega^+(t)$. These properties are then modelled by the corresponding stochastic processes $\mathbf{u}^*(t)$ and $\omega^*(t)$ based on the idea of the stochastic Lagrangian modeling approach [7]. (If combustion is considered, the stochastic models for scalar fields are needed.) In PDF2DV, $\mathbf{u}^*(t)$ evolves according to the simplified Langevin equation (SLM, [7])

$$d\mathbf{u}^*(t) = -\nabla \langle p \rangle dt - \left(\frac{1}{2} + \frac{3}{4} C_0 \right) \Omega (\mathbf{u}^*(t) - \langle \mathbf{U} \rangle) dt + (C_0 k \Omega)^{1/2} d\mathbf{W}, \quad (1)$$

where \mathbf{W} is Wiener process, $\omega^*(t)$ is solved by the Ito stochastic differential equation [2]

$$d\omega^* = -C_3 (\omega^* - \langle \omega \rangle) \Omega dt - \langle \omega \rangle \omega^* S_\omega dt + (2C_3 \sigma^2 \Omega \langle \omega \rangle)^{1/2} dW. \quad (2)$$

The non-dimensional source term S_ω is defined as:

$$S_\omega = C_2 - C_1 S_{ij} S_{ij} / \langle \omega \rangle^2, \quad (3)$$

where S_{ij} is the mean rate of strain. For all other terms, model constants and the definition for conditional mean of turbulence frequency Ω in (1) and (2), refer to [2] [7].

In PDF2DV, the expectation of a random variable, e.g. $\langle \mathbf{U} \rangle$, is approximated by an ensemble mean estimated by the cloud-in-cell method. Because the number of samples, i.e., the number of particles per cell N is finite, the ensemble mean itself is a random variable. Of course, it also depends on time step Δt and grid size h . Several numerical techniques, e.g., variance reduction (VR) and time averaging (TAV), are adopted to reduce the statistical fluctuations in the mean fields [8].

The bias B_Q of a statistics $\langle Q \rangle$, e.g. $\langle U \rangle$, is the deterministic error caused by N being finite. Using $\langle Q \rangle_{N,\Delta t,h}$ to represent the ensemble-average of Q calculated by finite N , Δt and h , B_Q can be written as,

$$B_Q = \langle \langle Q \rangle_{N,\Delta t,h} \rangle - \langle Q \rangle_{\infty,\Delta t,h}. \quad (4)$$

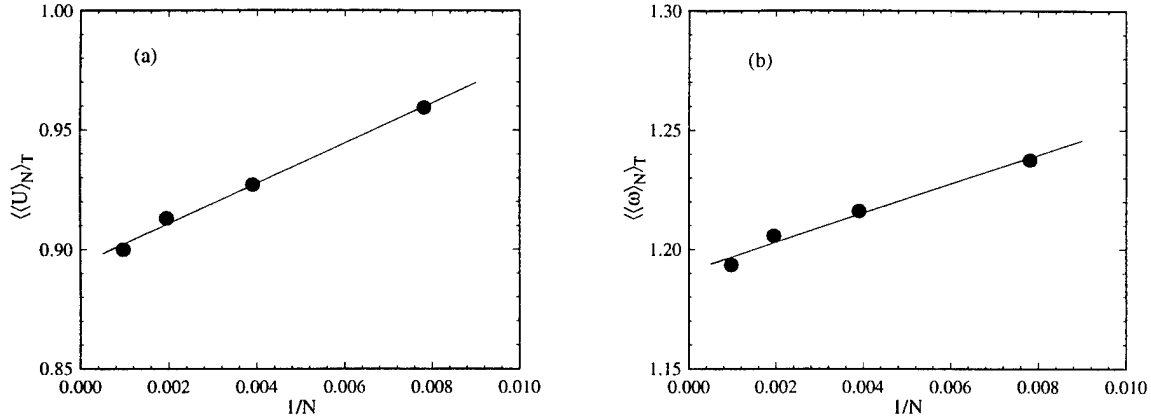


Figure 1: Time-averaged mean values vs. N in Couette flow: (a) Mean Velocity; (b) Mean $\langle\omega\rangle$. Grids in y direction $N_g = 21$, both VR and TAV are off, $y/H = 0.033$.

A simple analysis by Pope [6] suggests that bias B_Q scales as N^{-1} , so B_Q can be expressed as:

$$B_Q = \frac{b}{N}, \quad (5)$$

where b may be a function of other factors affecting bias, e.g., grid size and other numerical techniques in the code.

As an example, Couette flow (for flow descriptions refer to appendix A) is calculated using PDF2DV. With the same grid size, time step and numerical techniques, the time averages $\langle\langle U_N \rangle\rangle_T$ and $\langle\langle\omega\rangle\rangle_T$ of one point, which are equivalent with the ensemble mean of $\langle U \rangle_N$ and $\langle\omega\rangle_N$ respectively according to the ergodic assumption, are shown in Figure 1 as a function of the number of particles per cell. Since temporal error and spatial error are independent of particle number, the linear relationship in the figure implies that bias scales as (5). This behavior of bias is common in PDF2DV. The scale of bias as (5) ensures that bias approaches zero as N goes to infinity and thus leads to convergence of the scheme with respect to particle number per cell.

On the other hand, the slopes of the lines in Figure 1 provide the value of b in (5) which determines the magnitude of bias. For specific Δt and h (and for all other aspects of the

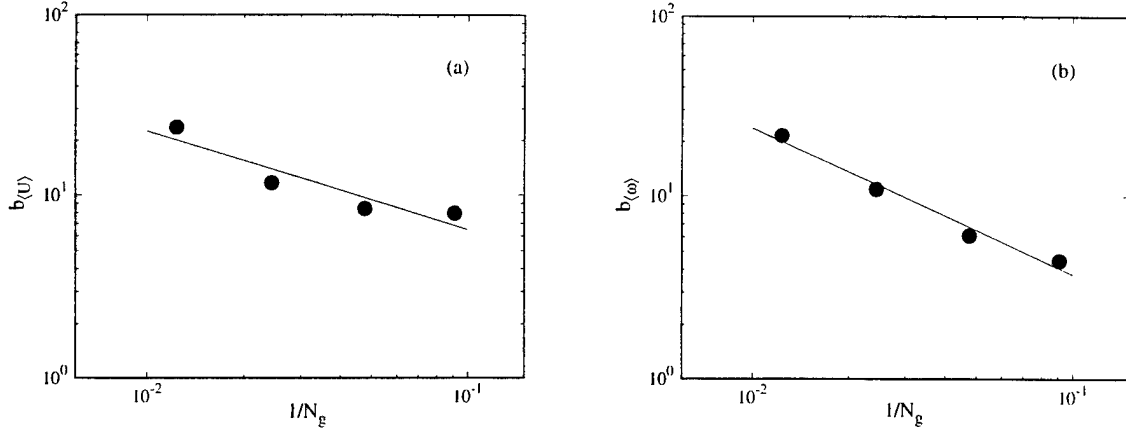


Figure 2: Bias vs. grid size in Couette flow: (a) Mean Velocity, the slope is -0.55 ; (b) Mean $\langle \omega \rangle$, the slope is -0.80 . Both VR and TAV are off, $y/H = 0.033$.

numerical method fixed), we have

$$\langle Q \rangle_{N_1, \Delta t, h} - \langle Q \rangle_{N_2, \Delta t, h} = B_{Q_{N_1}} - B_{Q_{N_2}} = b \left(\frac{1}{N_1} - \frac{1}{N_2} \right), \quad (6)$$

A formula for b is thus obtained

$$b(\Delta t, h) = \frac{N_2 N_1}{N_2 - N_1} (\langle Q \rangle_{N_1, \Delta t, h} - \langle Q \rangle_{N_2, \Delta t, h}). \quad (7)$$

Consequently, using two different particle numbers per cell, b and B_Q can be calculated for a specific grid size. By fixing the time step and the numerical techniques, b for different grid sizes in Couette flow is obtained by (7) and is plotted against $1/N_g$ in Figure 2, where N_g is the number of cells or grids in the domain. Since nonuniform grids are used in this calculation, $1/N_g$ is used here to represent the averaged grid size. Figure 2 shows that b increases with grid size. This behavior is observed in homogeneous stationary turbulence (described in appendix A) as well. In this case, bias is the deviation of turbulence energy and turbulence frequency from the stationary solutions. As shown in Figure 3, increasing the number of cells results in larger bias.

The fact that the bias increases with grid size is of great concern to PDF2DV. If b explodes faster with grid size than the convergence of bias due to increasing N , bias will not

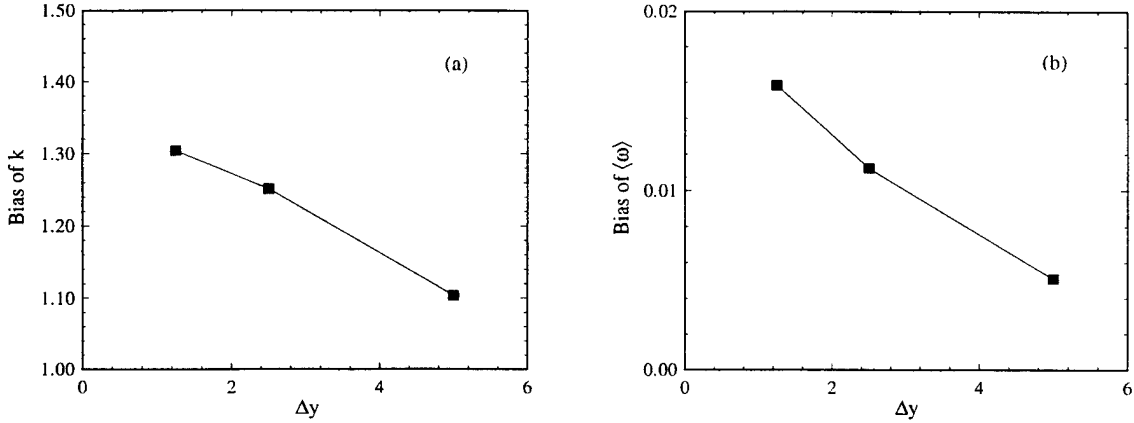


Figure 3: Bias vs. grid size in Homogeneous Stationary Turbulence: (a) Turbulence Energy k ; (b) Mean $\langle \omega \rangle$. Time step $\Delta t = 0.1s$, for 4000 steps.

vanish as h approaches zero and N goes to infinity. In the view of numerical computations, to minimize the total numerical error, one might want to increase N_g to reduce the spatial discretization error, which unfortunately causes larger bias. Therefore, N must increase as N_g increases in order to prevent the bias from exploding and to get the total error converged, which thus leads to unacceptably high computational cost.

STRATEGIES FOR EXPLORING BIAS

Theoretically, the statistical fluctuations in the coefficients of the stochastic differential equations, e.g., the Langevin equation, are the major sources of bias. The numerical solutions to (1) and (2) are essentially different from the following standard problem: given coefficients $a(x, t)$ and $b(x, t)$, an initial condition $X(0) = x_0$, and a stopping time $T > 0$, integrate the stochastic differential equation

$$dX(t) = a(X(t), t)dt + b(X(t), t)dW(t), \quad (8)$$

which has been well studied [3]. This is because in (1) and (2), the coefficients depend on the mean of a function of the process, e.g., $\langle \mathbf{U} \rangle$, which needs to be estimated in numerical

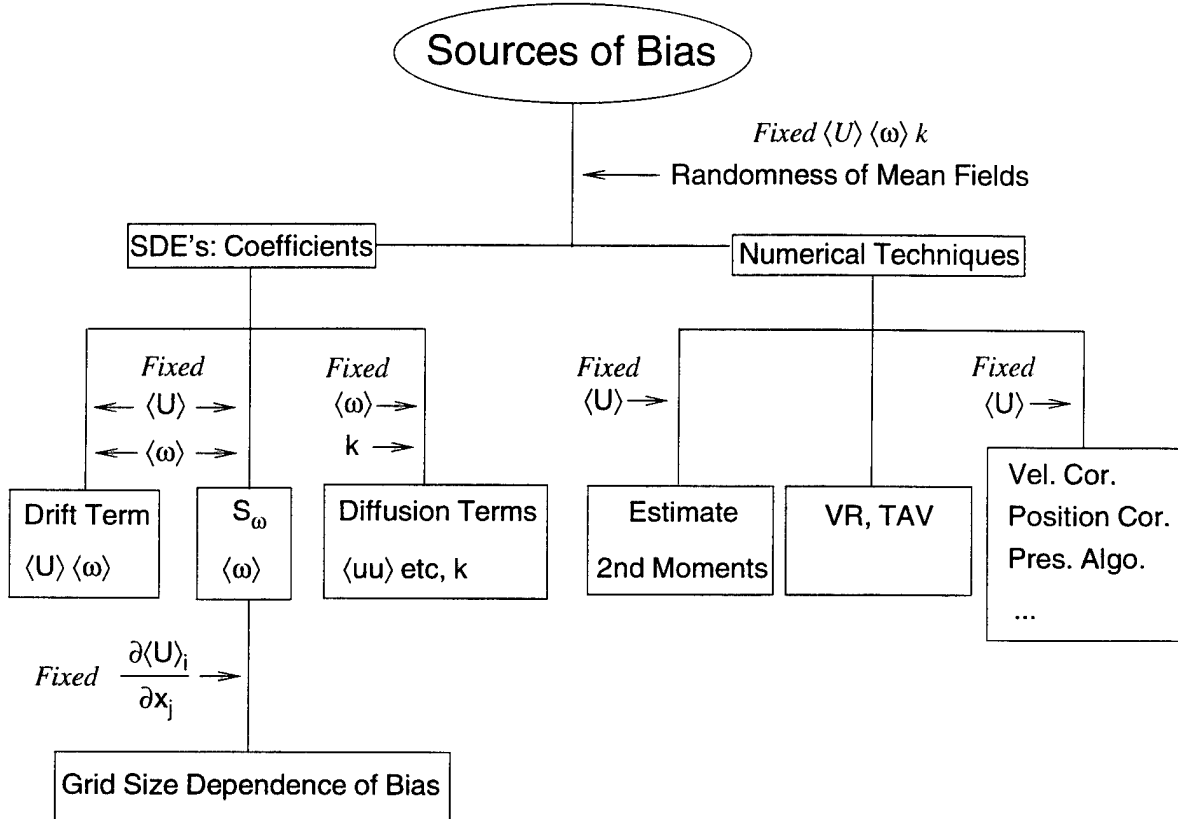


Figure 4: Strategies for exploring bias in PDF2DV

computation and inevitably carries numerical fluctuations. The mean fields in PDF2DV are calculated by cloud-in-cell method and fed back into the coefficients. This feedback causes bias. The two questions to be addressed are:

1. Which coefficients associated with mean fields yield bias ?
2. Why does bias increase with finer grids ?

For the PDF2DV code, all mean fields, terms in the SDE's and numerical techniques which may be related to the above two issues are sketched in Figure 4.

If, instead, the coefficients were non-random, independent of particle properties, the computed particle properties at any time would be independent, identically distributed,

and independent of N . It follows then there would be no bias. Therefore, if the estimate of mean field is replaced by a non-random input (say fixed or frozen $\langle U \rangle$), there is no corresponding statistical fluctuation in that mean field and related terms in the SDE's so that the contribution of statistical errors in the mean field to bias will be prevented. According to this *Frozen Coefficient* approach, a mean field or a term in the SDE's is justified as a source of bias if freezing it results in no bias. The things to be tested, which are possibly the sources of bias, and associated methods, are also shown in Figure 4.

NUMERICAL TESTS AND RESULTS

The approach of *Frozen Coefficient* is accomplished step by step through numerical tests. Because the fluctuations in the mean fields are suspected to be the major sources of bias, first of all the calculations are made by fixing mean fields in all coefficients of the SDE's to check the behavior of bias. If it disappears, then we can conclude that bias arises entirely from the fluctuations in the coefficients and no more calculations are needed to search for other sources of bias due to the numerical techniques. Several cases are calculated and compared to the base case; namely, the result from the original code without VR and TAV. The conditions for different cases are presented in Table I.

1 Sources of Bias: General Views

In the calculation of case 1, it is not the estimates from cloud-in-cell method that are used but constant values for mean fields. No bias is expected if bias is only related to the statistical fluctuations in the mean fields. The result compared to the base case (case 0) is shown in Table I. Obviously, bias of velocity and $\langle \omega \rangle$ are much smaller than case 0 and almost zero after fixing mean fields globally. Therefore bias of these two variables is because of the fluctuations in the estimates of mean fields. However, because the ensemble mean of velocity is used to estimate second moments, bias of turbulent energy is increased instead, which implies that the fluctuations in the first moments are the source of bias for the second moments. This will be discussed further in other cases.

2 Source of Bias for Velocity

Fixing Mean Fields for Coefficients in Eq.(1)

To clarify further that bias of velocity comes from Eq.(1), case 2 is calculated by fixing all mean fields in this equation. As in Table I, this case shows that the bias of the mean velocity is in the same order as case 1, which indicates that the bias of velocity is due to the fluctuations in the mean fields fed back into the coefficients of Eq.(1). This is consistent with the analysis in the previous section. To distinguish the influence on bias of drift term from diffusion term in Eq.(1), the following cases are designed.

Fixing Mean Velocity for Drift Term

The mean velocity is a critical variable in Eq.(1) because the particle velocity is forced to relax to it, and the particle velocity, in turn, is used to estimate the mean velocity. This means that there must be a very strong interaction between them. As shown in Table I (case 3), the bias of velocity resulting from fixing the mean velocity for the drift term in Eq.(1) is very small. Hence, the fluctuation in mean velocity is a major source for bias of velocity. One more interesting observation is that the bias of $\langle \omega \rangle$ becomes very small in this case as well. It seems that the behavior of the bias of $\langle \omega \rangle$ is dominated by the mean velocity although Eq.(2) is the same in the form as Eq.(1). This will be further discussed later.

It may be noticed that in case 3 there is a huge bias of k . However, this phenomenon should not be paid too much attention. When the drift term is frozen while the diffusion term is not, in the equation for k derived from Eq.(1), $-\frac{3}{4}C_0\Omega(\mathbf{u}^* - \langle \mathbf{U} \rangle)dt$ in the drift term will not still balance with the diffusion term, which may cause a large bias of k .

Fixing Ω and k

In order to determine the effect of fluctuations in the diffusion coefficients, a calculation was attempted in which Ω and k were fixed only in the diffusion term in Eq.(1). It turns out that the solution is not stable. The explanation could be that different values of Ω in the drift and diffusion terms give rise to an instability of numerical solutions to the equation. This case is then modified to let Ω take fixed values both for the drift term and the diffusion term

and k be fixed for the diffusion term so that a stationary solution is obtained. Thus, in this case 4, k and Ω (but not $\langle U \rangle$) are fixed throughout Eq.(1). The bias of velocity is almost the same as in case 0. The bias of $\langle \omega \rangle$ is not much reduced either. This case demonstrates that the diffusion term of Eq.(1) is not the source of significant bias for the velocity or for $\langle \omega \rangle$.

3 Source of Bias for $\langle \omega \rangle$

Fixing Mean Fields for Coefficients in Eq.(2)

In case 5, the coefficients in Eq.(2) are fixed. The bias of $\langle \omega \rangle$ is very small (Table I). Therefore, the bias of $\langle \omega \rangle$ stems from the fluctuations in the coefficients of Eq.(2).

Fixing Mean Velocity Gradient for Turbulent Frequency Equation

An analysis given in Appendix B shows that bias in the source term S_ω in the turbulent frequency model increases with grid refinement because of the fluctuations in the mean velocity. This may be the reason for the dependence of bias on grid size, which can be demonstrated by fixing the mean velocity gradient to calculate S_ω . The results in this case (case 7) are compared with the results of original model. Figure 5 shows that the dependence of bias on grid size almost disappears when a fixed mean velocity gradient is used to calculate S_ω . Therefore, the reason that bias increases when grid size are decreased is that the fluctuations in the mean velocity bring about an additional source into the turbulent frequency model because of the square of velocity gradient in S_ω . In addition to this observation, it is shown in Figure 5 and Table I that bias of $\langle \omega \rangle$ is almost zero. Consequently, the bias of $\langle \omega \rangle$ is dominated by the fluctuations in the mean velocity.

4 Source of Bias for Turbulent Energy k

Homogeneous Flow: Fixing Mean Velocity for Estimate of Second Moments

In this case (case H-1 in Table II), the fixed no-random first moment (the mean velocity) is used to estimate second moments. Table II shows that bias reduces by about half in

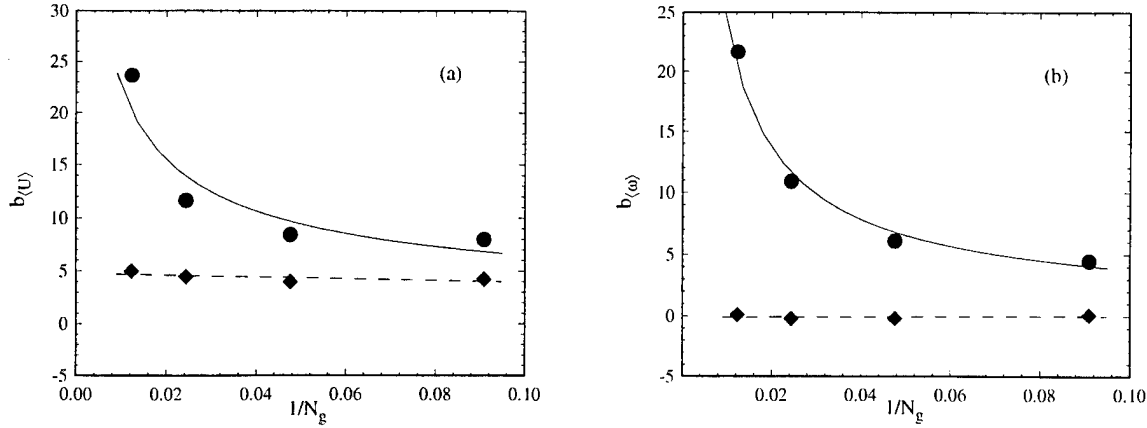


Figure 5: Comparison of the dependence of Bias on grid size in Couette flow: (a) Mean Velocity; (b) Mean $\langle \omega \rangle$; solid line, base case (case 0); dashed line, calculation by fixing velocity gradient (case 7). Both VR and TAV are off, $y/H = 0.033$.

comparison with case H-0. As pointed out before, the fluctuations carried by first moments are the sources of bias for k .

Couette Flow: Fixing k for Diffusion Term

This case is to test whether the fluctuation in k which is fed back into the diffusion term of Eq.(1) is the source of bias in k or not. The result is shown in Table I (case 6). Apparently, fixing k for the diffusion term does not reduce the bias of k . Case 4 shows, however, that by fixing both Ω and k in diffusion term, bias of k is indeed reduced. Therefore, the diffusion term is a source of bias in k due to the fluctuations in both Ω and k .

Homogeneous Flow: Fixing Mean Velocity for Estimate of Second Moments and Ω , k for Eq.(1)

The case H-2 is calculated to clarify further that the total bias of k is contributed by the above sources: the fluctuations in the first order moments which are used to estimate the second moments; the fluctuations in Ω and k which are feeded back into Eq.(1) (Table II).

Table I: Bias in Couette Flow: Test Cases and Results

Cases		0	1	2	3	4	5	6	7	8
Drift Term in the Equation for \mathbf{u}^*	$\langle U \rangle$		×	×	×					
	Ω		×	×		×				×
Diffusion Term in the Equation for \mathbf{u}^*	Ω		×	×		×				×
	k		×	×		×		×		
Drift Term in the Equation for ω^*	Ω		×				×			
	$\langle \omega \rangle$		×				×			
Diffusion Term in the Equation for ω^*	Ω		×				×			
	$\langle \omega \rangle$		×				×			
Source Term S_ω in the Equation for ω^*	$\frac{\partial \langle U \rangle}{\partial y}$		×			×			×	
	$\langle \omega \rangle$		×			×				
Evaluation of k	$\langle U \rangle$									
Measurement of Bias	$b_{\langle U \rangle}$	8.42	0.14	0.23	0.37	7.70	3.94	21.53	3.95	5.58
	$b_{\langle \omega \rangle}$	6.10	-0.23	1.26	-0.96	4.85	0.38	10.03	-0.20	4.66
	b_k	0.6	-1.96	-2.76	-12.0	0.14	0.81	1.03	-0.03	-0.39

Note. All calculations are made on the conditions: $N_g = 21$, neither VR nor TAV, $y/H = 0.033$. b 's are normalized by mean fields at the wall. 'x' denotes the parameter is fixed.

Table II: Bias in Stationary Homogeneous Turbulence

Case	Description	Bias of k	Bias of $\langle \omega \rangle$
H-0	No any coefficients fixed	1.103	0.0051
H-1	Fix $\langle U \rangle$ for estimate of second moments	0.54	0.0071
H-2	Fix $\langle U \rangle$ for estimate of second moments and fix Ω, k for Eq.(1)	0.004	0.010

Note. All calculations are made on the conditions: $N_g = 3$, neither VR nor TAV, time step $\Delta t = 0.1s$, for 4000 steps.

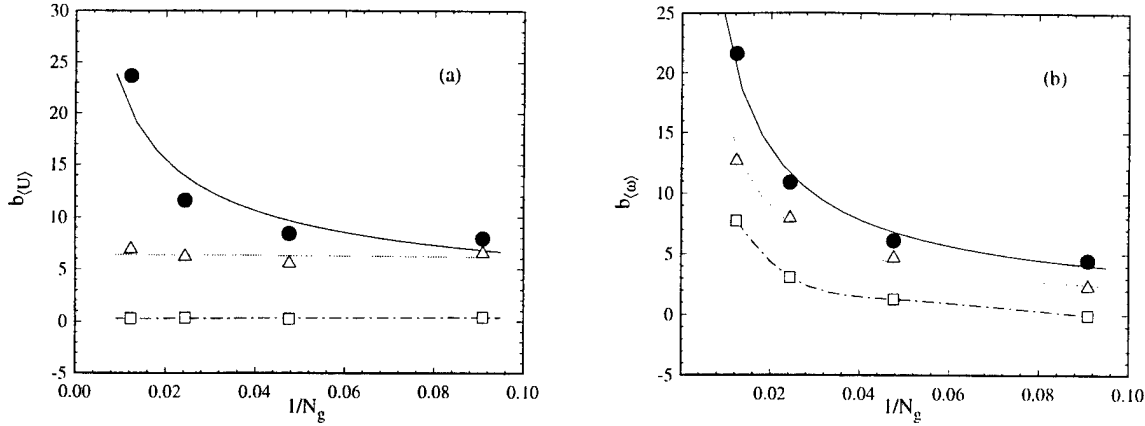


Figure 6: Comparison of the dependence of Bias on grid size in Couette flow: (a) Mean Velocity; (b) Mean $\langle \omega \rangle$; solid line, base case (case 0); dot-dashed line, calculation by fixing all mean fields for Eq.(1) (case 2); dotted line, calculation by fixing Ω for Eq.(1) (case 8).

5 Dependence of Bias on Grid Size

In the case of fixing velocity gradients for the turbulent frequency model, it has been shown that the source term S_ω in this model introduces the dependence of bias on grid refinement. Here two more cases are set up to confirm this further.

Fixing All Mean Fields for Eq. (1)

It has been shown in Table I that the bias of velocity almost disappears in this case (case 2). Here, it can be seen further from Figure 6 that the bias of velocity is apparently independent of the grid size while the bias of $\langle \omega \rangle$ still increases as the grid is refined.

Fixing Ω for Eq. (1)

By fixing Ω in Eq.(1), the contribution of the turbulent frequency model to the dependence of bias on grid refinement can be further clarified. In this case (case 8), the bias of $\langle \omega \rangle$ still increases with the grid refinement (Figure 6). In contrast, the bias of velocity does not exhibit such a behavior anymore.

From the above two cases and the case of fixing the velocity gradients for the turbulent frequency model, it can be concluded that the source term S_ω causes the bias of $\langle \omega \rangle$ to depend on the grid size and increase when the grid size is refined. Then, the bias of velocity is affected by $\langle \omega \rangle$ or Ω through Eq.(1) so that it increases with the finer grids as well.

6 Summarization

The sources of bias in the PDF2DV code have been summarized in Figure (7) which provides a general picture of the sources of bias.

CONCLUSIONS

In PDF particle-mesh methods for turbulence modeling, three types of numerical errors are identified: statistical error, truncation error, and bias. The behavior and the sources of bias in the PDF2DV code applying such a method have been studied in detail by numerical experiments.

It has been verified that bias is linearly proportional to N^{-1} so that bias decreases with increasing particle number, which is consistent with analysis. Another observation is that bias increases when the grid size is decreased. This is significant because it could lead to unacceptably high computational cost.

The *Frozen Coefficient* approach has been proposed to pinpoint the sources of bias in PDF2DV. According to this approach, the sources of bias are found through fixing or freezing the mean fields that appear in the stochastic differential equations, i.e. using non-random value instead of estimates by cloud-in-cell method. This procedure is implemented by isolating each term in the stochastic differential equations. The source of bias in velocity is found to be associated with the fluctuations in the estimated mean of velocity. In other words, the drift term in the Langevin equation for velocity is the major source of bias for velocity. As for the turbulent frequency $\langle \omega \rangle$, the bias is mostly dominated by the mean velocity and its gradient. On the other hand, the bias of second moments (or turbulence energy k) has two sources: the diffusion term of the Langevin equations for velocity which is related to the fluctuations in $\langle \omega \rangle$ and k , and the estimation of second moments based on the first moments

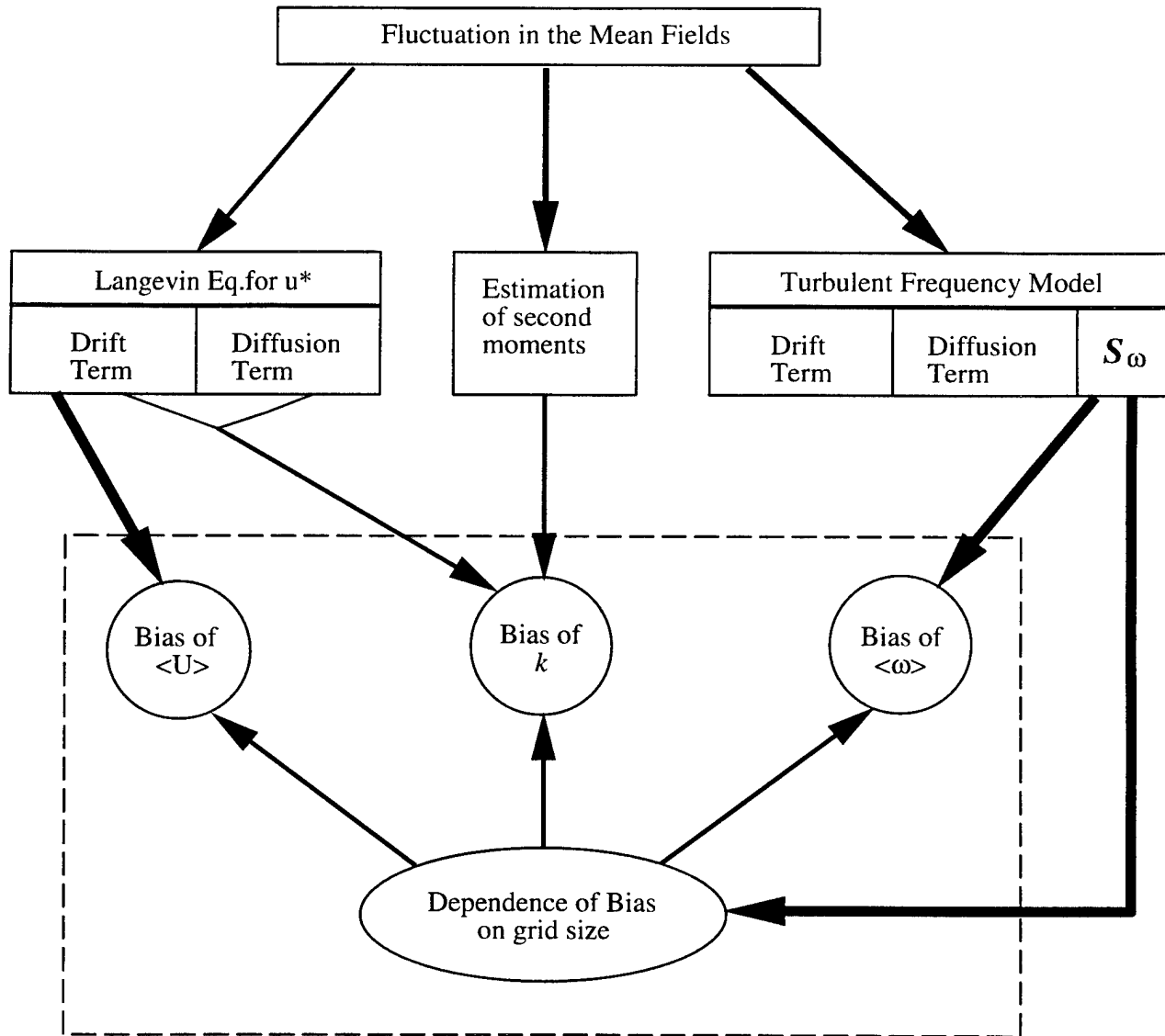


Figure 7: The chart describing the sources of bias

which of course carry fluctuations. Lastly, the dependence of bias on grid size has been attributed to the source term S_ω in the turbulent frequency model. The analysis also shows that the bias of S_ω increases with grid refinement. This leads to the dependence of bias of $\langle \omega \rangle$ and thus Ω on grid size, which furthermore affect the mean velocity through Eq.(1) so that it also depends on the grid size. The fact that bias increases as the grid size is decreased implies the PDF2DV code is not unconditionally convergent and is not acceptable.

Discovering the sources of bias provides a guideline for reducing bias and removing the dependence of bias on grid size. Partially time averaging, variance reduction techniques and modification of turbulent frequency model are possible approaches to improve the accuracy of this PDF particle method. This will be discussed in another report.

Acknowledgements

This work was supported by the Air Force Office of Scientific Research, Grant F49620-94-1-0098.

APPENDIX A: TEST FLOWS

The test flows used in this study are Couette flow and stationary homogeneous flow. Both of them have the following features

- (i) they are 0-D or 1-D problem,
- (ii) they exhibit easily understandable physics, and
- (iii) they are statistically stationary.

Because of these features, many calculations are feasible during a reasonable time; the sources of bias are distinguishable from other issues in the code and some numerical techniques, e.g. time-averaging, can be tested. The two flows are described in this appendix.

(1) Couette Flow

Couette flow is defined as the flow between two flat plates which move in the opposite direction at velocity U_w (Figure 8). The flow is one dimensional. No pressure gradient in x direction is needed to drive the flow.

For such a flow, boundary conditions need to be defined on the wall. Since only the lower half of the domain is calculated, the boundary conditions are defined at the center line and at the lower wall. In the frame of a particle method, the physical condition is imposed through specifying the particle properties. The following boundary conditions for the particle may not give the exact solution to Couette flow. However, because we are mostly interested in the numerical features of PDF2DV, we can put aside the physical consistency of calculation with real world. The issues we are concerned with should be whether these conditions give a stable and stationary solution.

(a) Center Line

At the center line, the physical conditions are

$$\langle U \rangle = 0, \quad \frac{\partial \langle uv \rangle}{\partial y} = 0, \quad (9)$$

and

$$\frac{\partial \langle \omega \rangle}{\partial y} = 0. \quad (10)$$

so that the particle conditions are imposed as

$$u_R^* = -u_I^*, \quad (11)$$

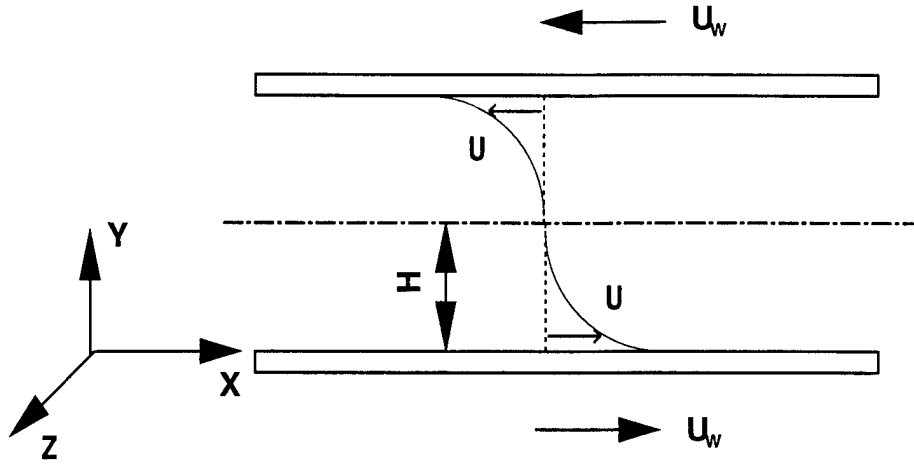


Figure 8: Couette flow configuration

$$v_R^* = -v_I^*, \quad (12)$$

$$\omega_R^* = \omega_I^*, \quad (13)$$

where 'I' denotes particles which are incident to the boundary and 'R' denotes particles which are "reflected" from the boundary. The mean conditions are obtained as the average of the condition before and after reflection. It can be shown readily that particle conditions are consistent with physical conditions.

(b) Wall Conditions

The boundary conditions at the wall are more difficult to define for particles than at the center line. A modified wall function proposed by Dreeben [1] is used in this study.

The conditions for the mean velocities are

$$\langle U \rangle = U_w, \quad \langle V \rangle = 0. \quad (14)$$

The velocities of particles hitting the wall satisfy the following conditions:

$$u_R^* = u_I^* + \alpha v_I^*, \quad (15)$$

$$v_R^* = -v_I^*, \quad (16)$$

where α can be calculated from the wall function. To be consistent with the mean conditions

at the wall, α must satisfy

$$\alpha = \frac{-2\langle uv \rangle_w}{\langle v^2 \rangle_w}, \quad (17)$$

where 'w' stands for values at the wall. Using the wall function, a formula for α can then be deduced,

$$\alpha = \frac{C_w \langle U \rangle_w / k_w^{1/2}}{\kappa U_w / \hat{u} - \ln(E \lambda \hat{u} / \nu)}, \quad (18)$$

where the friction velocity \hat{u} is calculated by

$$\hat{u} = C_\mu^{1/4} k^{1/2}. \quad (19)$$

All other model constants are chosen as

$$C_\mu = 0.0841, \quad \kappa = 0.4, \quad (20)$$

$$C_w = 0.76, \quad E = 8.0, \quad (21)$$

$$\lambda = 0.05. \quad (22)$$

As for conditions for turbulence frequency at the wall, a modified form of the model proposed by Dreeben et.al. [1] is adopted. The particle condition is

$$\omega_R = e^{\beta \frac{v_I}{\lambda \langle \omega \rangle}} \omega_I. \quad (23)$$

Dreeben et.al. deduce the following formula for β [1]

$$\beta = \frac{-2\lambda \langle \omega \rangle \langle \omega v \rangle}{\langle \omega v^2 \rangle} + O(\beta^3). \quad (24)$$

Here a simplified form for β , i.e. a constant, is used

$$\beta = -0.5. \quad (25)$$

The above boundary conditions indeed yield a stable and stationary solution to Couette flow. The profiles of the mean velocity and the mean turbulence frequency from the above boundary conditions are shown in Figure 9.

(2) Stationary Homogeneous Turbulence

The coefficient $(\frac{1}{2} + \frac{3}{4}C_0)$ in SLM (Eq. (1)) causes the turbulence energy to be dissipated at the rate $\langle \epsilon \rangle$ or $k \langle \omega \rangle$. If the $\frac{1}{2}$ is omitted, the equation (1) will pertain to the hypothetical

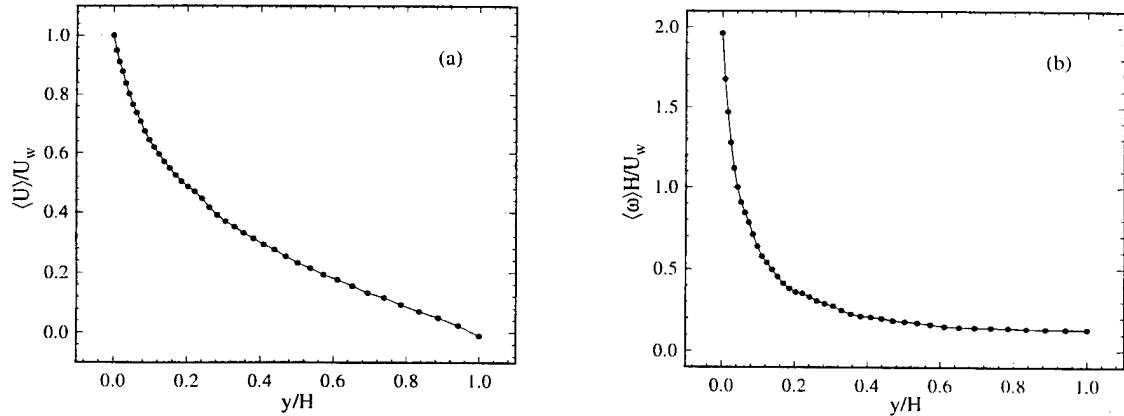


Figure 9: Calculated profiles of Couette flow: (a) Mean Velocity; (b) Mean $\langle \omega \rangle$. Calculation conditions: Half width of channel $H = 1$, Wall velocity $U_w = 1$, Grids in y direction $N_g = 41$

case of stationary (i.e. non-decaying) homogeneous (isotropic) turbulence. In this flow, as turbulence energy does not decay and there does not exist production either, theoretically the solutions to this flow are constant against time, i.e. stationary solutions are expected. To assure a stationary solution for $\langle \omega \rangle$ as well, in Eq.(3) constant C_2 is set to be zero. Because the mean rate of strain S_{ij} is zero (ideally), a stationary solution to $\langle \omega \rangle$ is expected. To see the effect of grid size on bias, we treat this flow as 1-D flow instead of 0-D, i.e. in one direction, say y direction, multiple grids instead of one grid are used.

APPENDIX B: DEPENDENCE OF BIAS IN S_ω ON GRID SIZE

As in Eq.(3), S_ω is involved with the square of the strain rate. In Couette flow and stationary homogeneous turbulence it reduces to

$$S_\omega = C_2 - \frac{1}{2} C_1 \left(\frac{\partial \langle U \rangle}{\partial y} \right)^2 \frac{1}{\langle \omega \rangle^2}. \quad (26)$$

In the numerical calculation, the differentiation is replaced by finite difference. According

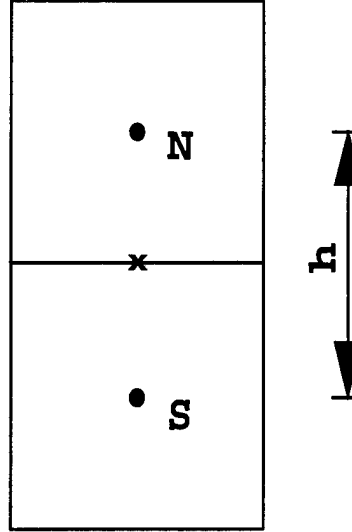


Figure 10: Cell and Node Structure

to Figure 10,

$$\left(\frac{\partial \langle U \rangle}{\partial y} \right)^2 \sim \left(\frac{\langle U \rangle_n - \langle U \rangle_s}{h} \right)^2. \quad (27)$$

And then, $\langle U \rangle$ is approximated by the corresponding ensemble mean $\{U\}$ estimated by cloud-in-cell method. The bias of $\left(\frac{\partial \langle U \rangle}{\partial y} \right)^2$ is defined as

$$B_{u,y} = \left\langle \left(\frac{\langle U \rangle_n - \langle U \rangle_s}{h} \right)^2 \right\rangle - \left(\frac{\langle U \rangle_n - \langle U \rangle_s}{h} \right)^2. \quad (28)$$

This can be rewritten as

$$\begin{aligned} B_{u,y} &= \left\langle \frac{\langle U \rangle_n^2 + \langle U \rangle_s^2 - 2\langle U \rangle_n \langle U \rangle_s}{h^2} \right\rangle - \frac{\langle U \rangle_n^2 + \langle U \rangle_s^2 - 2\langle U \rangle_n \langle U \rangle_s}{h^2}, \\ &= \frac{1}{h^2} (\langle \langle U \rangle_n^2 \rangle - \langle U \rangle_n^2) + \frac{1}{h^2} (\langle \langle U \rangle_s^2 \rangle - \langle U \rangle_s^2) - \frac{2}{h^2} (\langle U \rangle_n \langle U \rangle_s - \langle U \rangle_n \langle U \rangle_s), \\ &= \frac{1}{h^2} [Var(\{U\}_n) + Var(\{U\}_s)] - \frac{2}{h^2} Cov(\{U\}_n, \{U\}_s), \\ &= \frac{1}{h^2} \left[\sqrt{Var(\{U\}_n)} - \sqrt{Var(\{U\}_s)} \right]^2 + \frac{2}{h^2} [Var(\{U\}_n)Var(\{U\}_s)]^{1/2} (1 - \rho), \\ &\geq \frac{2}{h^2} [Var(\{U\}_n)Var(\{U\}_s)]^{1/2} (1 - \rho), \end{aligned} \quad (29)$$

where ρ is the correlation coefficient between $\{U\}_n$ and $\{U\}_s$. In most of the cases, ρ is less than one, so bias of $\left(\frac{\partial \langle U \rangle}{\partial y} \right)^2$ or S_ω is not zero and determined by the variance of the estimate

of the mean velocity and the grid size. As far as there exists fluctuations in the estimate of the mean velocity, $B_{u,y}$ increases with grid size refinement. Consequently, the bias of S_ω depends on the grid size.

REFERENCES

- [1] T.D. Dreeben and S.B. Pope. Wall-function treatment in pdf methods. *Physics of Fluids*, To be published.
- [2] Jayesh and S.B. Pope. Stochastic model for turbulent frequency. Technical Report FDA 95-05, Cornell University, 1995.
- [3] P.E. Kloeden and E. Platen. *Numerical Solution of Stochastic Differential Equations*. Springer-Verlag, 1992.
- [4] S.B. Pope. Pdf methods for turbulent reactive flows. *Progress Energy and Combustion Science*, 11:119–192, 1985.
- [5] S.B. Pope. Computations of turbulent combustion: Progress and challenges. In *Proceedings of the Twenty-Third Symposium on Combustion*, pages 591–612, 1990. Actual booktitle unknown.
- [6] S.B. Pope. Particle method for turbulent flows: Integration of stochastic differential equations. *J. Comput. Phys.*, 117:332–349, 1992.
- [7] S.B. Pope. Lagrangian pdf methods for turbulent flows. *Annual Review of Fluid Mechanics*, 26:23–63, 1994.
- [8] S.B. Pope. *pdf2dv*. Cornell University, Sibley School of Mechanical Engineering, Ithaca, NY 14853, 1994.
- [9] W.C. Welton and S.B. Pope. A PDF-based particle method for compressible turbulent flows. *AIAA Paper No. 95-0804*, 1995.

A MIXING MODEL TO IMPROVE THE PDF SIMULATION OF TURBULENT DIFFUSION FLAMES

A. R. MASRI

*Department of Mechanical and Mechatronic Engineering
The University of Sydney
NSW, 2006, Australia*

S. SUBRAMANIAM AND S. B. POPE

*Department of Mechanical and Aerospace Engineering
Cornell University
Ithaca, NY 14850, USA*

A new mixing model based on Euclidean minimum spanning trees (EMST), which has been developed by Subramaniam and Pope, is used in the PDF simulation of pilot-stabilized turbulent non-premixed flames. A model equation is solved for the joint PDF of velocity composition and turbulence frequency using a particle mesh method. Simulations using the EMST mixing model and the IEM (interaction by exchange with the mean) mixing model are compared. A simple thermochemistry equivalent to one-step reaction is used in the calculations. Comparisons are made with experimental measurements in the upstream regions of piloted H_2/N_2 flames. This fuel is chosen because its chemistry is simple and may be adequately represented by a single-step mechanism. It is found that the EMST model gives the correct mixing pattern for the reactive scalar, as well as the conserved scalar, especially in the early parts of the jet where mixing is most difficult to represent. This result is not achieved by the IEM model. The success of the EMST mixing model is attributable to its satisfying a "localness" condition that other models violate. This is a significant advance that will enable the PDF approach to simulate complex flows with finite rate chemical kinetics.

Introduction

The main advantage of using the joint PDF approach in the simulation of turbulent combustion lies in its capability to represent chemical reaction exactly. However, the accuracy of the approach depends also on the modeling of molecular mixing. In reacting flows, mixing of both reactive and conserved scalars occurs and modeling such processes must be adequate, particularly if finite-rate chemistry effects are involved. This is especially important close to the exits of fuel and pilot jets, where the gradients are steep and the scalars are evolving in time under significant turbulent mixing rates. It is also important at the base of lifted flames. Some previous attempts to compute the structure of pilot-stabilized non-premixed flames close to blow off have not been successful despite the use of realistic chemistry [1]. This is mainly due to the fact that just downstream of the pilot flame gases, mixing of reactive scalars is incorrectly represented, leading to largely nonreactive fluid mixtures that prevent ignition further downstream.

Central to the development of mixing models are important questions about how multiscalar mixing

occurs. The simple particle interaction model developed by Curl [2] has undergone various modifications [3,4] and has been used with limited success [5]. The IEM model developed by Dopazo [6] represents a significant improvement in computing the structure of turbulent pilot-stabilized flames [4]. Both Curl's model and the IEM model perform poorly on the simple test case of a conserved scalar decaying to Gaussian in homogeneous, isotropic turbulence [7]. But for inhomogeneous flows, the production of scalar fluctuations by mean gradients ameliorates this deficiency. More important in the present context is that neither model satisfies the "localness principle," namely that mixing occurs locally in composition space [4]. Mapping closure methods [8] give excellent results for the simple test cases and satisfy the localness principle. Although there have been various efforts to extend this approach to multiscalar mixing [9,10-12], significant problems are encountered, particularly in its numerical implementation. The linear eddy mixing approach developed by Kerstein [13-15] shows promising results and has the unique advantage of being capable of accounting for differential diffusion ef-

fects. It has been used by Menon et al. [16] to compute the structure of jet flames.

The issue of multiscalar mixing remains unresolved and is the subject of intense research. Recently, a mixing model based on EMST has been developed by Subramaniam and Pope [17]. The EMST is used to identify neighboring fluid particles in composition space, and mixing then occurs only between these particles. The model satisfies Pope's rules of boundedness [18] and localness [4]. A version of the model that satisfies Pope's linearity principle [18] has also been developed but is not used in this paper. The model has been validated satisfactorily with the simple test problems of multiple scalars decaying in homogeneous isotropic turbulence and the evolution of a scalar field in an imposed mean scalar gradient. Further details about the model, its performance, and its convergence and numerical characteristics may be found elsewhere [17].

The purpose of this paper is to demonstrate that the new EMST mixing model gives a realistic representation of mixing in the early region of pilot-stabilized flames. This is particularly important for obtaining the correct flame structure further downstream. The model is coupled to a new stand-alone PDF code developed for two-dimensional turbulent reacting flows [19]. The joint PDF of velocity, composition, and frequency are solved using the particle-mesh method. The single-step chemistry used in these simulations is rather simple but is adequate to demonstrate the different performance of the mixing models. The reaction rate is a function of mixture fraction, ξ , and a reaction progress variable, b . Computations using both the EMST and IEM mixing models are compared with experimental measurements in a pilot-stabilized turbulent diffusion flame of H_2/N_2 fuel mixture.

Numerical Considerations

The PDF Code

The approach is based on the transport equation for the joint PDF of velocity, composition, and turbulent frequency. A Lagrangian method is used to solve the Eulerian PDF transport equation, and stochastic models are used for the velocity, dissipation, and molecular mixing terms. The evolution of the fluid particle velocity is represented by the simplified Langevin model [7], and a new stochastic model for turbulent frequency is employed [20]. Constants $C_{\omega 0}$, $C_{\omega 1}$, and C_ϕ in the turbulent frequency and composition equations are valued at 2.1, 0.04, and 2.00, respectively. The sensitivity of the solution to these constants is yet to be investigated, but Norris and Pope [21] have found that a higher value of $C_{\omega 0}$ is more appropriate for axisymmetric jets. The scalar mixing models are addressed in the next subsection.

The new code solves the PDF equations for two-dimensional flows and uses a particle-mesh numerical method [19]. A rectangular grid is used, and the mean properties are determined for each grid node. The instantaneous properties are carried by stochastic particles within each cell. The code can and has been implemented with parallel processing. This facilitates accurate calculations with many particles in a reasonable amount of elapsed time. Although used here for parabolic flows, the main virtue of this new code is that it allows, for the first time, the use of full PDF approach to compute the structure of recirculating flows.

The Piloted Flame

The pilot-stabilized burner has been used extensively as a model problem for simple parabolic flows with small and extreme departures from chemical equilibrium. The burner consists of a central fuel tube 7.2 mm in diameter, surrounded by an 18-mm annulus for the premixed flame pilot. A large body of experimental data is available for piloted flames over a range of fuel mixtures [22]. The initial and boundary conditions for the flames are well-known and these are described elsewhere [5]. To validate the numerical simulations, pilot-stabilized flames of H_2/N_2 (1/1 by vol.) fuel are investigated experimentally. Joint images of temperature and mixture fraction are collected in these flames just downstream from the jet exit plane. The Raman-Rayleigh technique, which is fully described elsewhere [23], is used for these measurements. Hydrogen-nitrogen fuel is used because it has moderately fast chemistry and the dilution with nitrogen increases the stoichiometric mixture fraction to $\xi_s = 0.305$ and forces the reactive zone into the shear layer. Measurements are taken in the region in which the pilot stream is still separating the fuel and airstream and further downstream in the region where fuel, air, and pilot gases are mixing together.

The Thermochemistry

Detailed chemical kinetics may be implemented easily in the PDF code and are not required here since only fast chemistry is considered. A very simple thermochemical model that simulates one-step chemical reaction is used in the simulations. The reaction rate is given as a function of two variables (ξ and b), where b is a reaction progress variable that varies from 0 for fully frozen to 1 for fully reacted fluid particles. Four parameters are needed to specify the reaction rates: a stoichiometric mixture fraction, ξ_s , a chemical time scale, τ_c , the curvature of the progress variable in mixture fraction space, at equilibrium, $\Delta\xi_c$, and a rich mixture fraction limit, ξ_r . The thermochemistry is self-similar and may be applied over a range of ξ values. Figure 1 shows

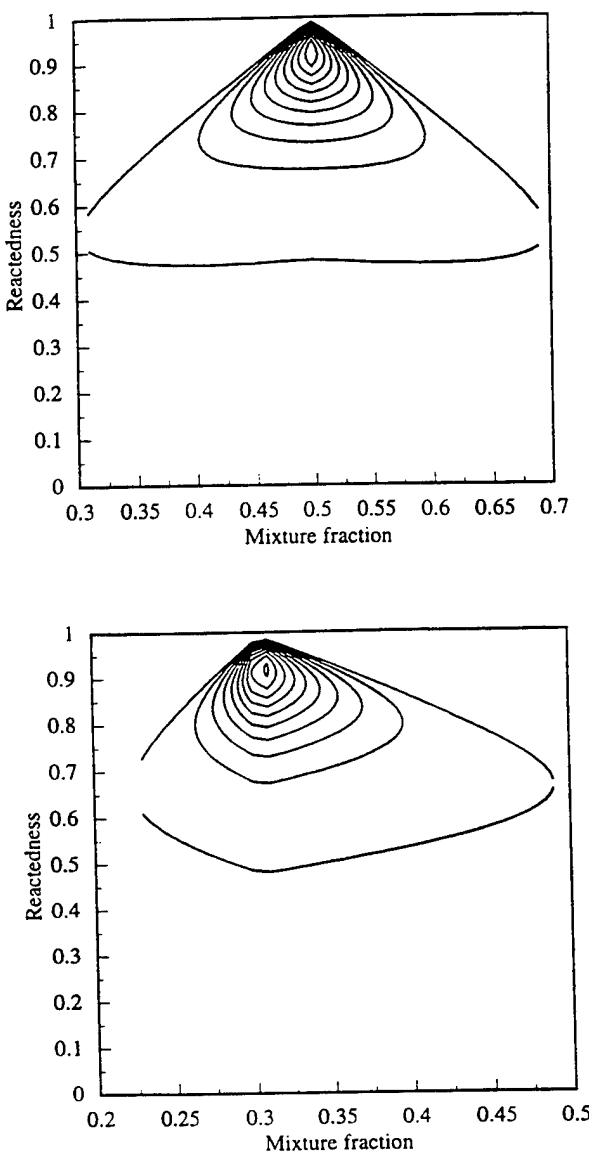


FIG. 1. Contours of normalized reaction rate plotted with respect to reaction progress variable b and mixture fraction ξ for two fuels with stoichiometric mixture fractions $\xi_s = 0.305$ and 0.5 .

contour plots of the rates obtained for two “fuels” with $\xi_s = 0.305$ and 0.5 , respectively. The first stoichiometry ($\xi_s = 0.305$) matches the H_2/N_2 fuel mixture for which experimental data are presented here. The case of $\xi_s = 0.5$ is used because the chemistry is symmetric, as shown in Fig. 1. The nonlinearity of the rates for all “fuels” is obvious and the modeled rate function peaks closer to stoichiometric, which is consistent with actual chemical kinetic rates. The lean and rich reactive limits, ξ_L, ξ_R are set where the rate drops to 1% of the peak value, and the contours shown in Fig. 1 are limited to this range. The chemical parameters used here for both “fuels” are $\tau_c =$

2.0×10^{-9} and $A\xi_r = 1.0 \times 10^{-3}$. This corresponds to a chemical timescale that is short enough to simulate the fast chemistry studied in this paper and represented by the H_2/N_2 fuel mixture. More details on this self-similar thermochemistry may be found elsewhere [24].

The EMST Mixing Model

The EMST model has the unique advantage of adequately representing the mixing of reactive and conserved scalars. At a given time, and within a given grid cell, a new “tree” is formed to account for the mixing that occurs between the particles in the cell. With σ being the number of compositions considered and N the number of particles in the cell, the composition of the i th particle ($i = 1, \dots, N$) is denoted by $\phi_{(i)}^\sigma$, $\beta = 1, \dots, \sigma$. The particle compositions evolve by interactions with “neighbor” particles, which are defined by the EMST according to their proximity in composition space. A “tree” is formed with a set of edges (unordered pair of points defining a particle and its neighbor) connecting all particles such that the total length of edges is minimized. If the number of edges incident on the i th particle is denoted E_i , then the scalar properties of particles, $\phi_{(i)}^\sigma$, evolve according to the following equation:

$$w_{(i)} \frac{d\phi_{(i)}^\sigma}{dt} = -\alpha \sum_{v=1}^{E_i} B_v (\phi_{(i)}^\sigma - \phi_{(i,v)}^\sigma) \quad (1)$$

where i_v represents the i th particle’s neighbor in the v th edge. This is illustrated in Fig. 2, which shows a typical EMST formed in two-dimensional composition space using 800 stochastic particles. The model parameter α controls the rate of variance decay of the scalars. The numerical weight of the particle is denoted by $w_{(i)}$, and the model coefficients B_v associated with the edges determine the evolution of the scalar PDF with time. One disadvantage of the EMST is that its computational cost scales as N^2 . Details about the model and its performance characteristics in a number of test conditions are given elsewhere [17].

Results and Discussion

All computations are performed for the following conditions: bulk jet velocity, $\bar{u}_j = 41$ m/s, burned pilot velocity, $\bar{u}_{pb} = 24$ m/s, co-flow air velocity, $\bar{u}_a = 15$ m/s. The initial conditions for the velocity and turbulence profiles are identical to those specified earlier for similar jet flames [5]. The mixture fraction at the jet exit plane in the jet, pilot, and air streams is $1, \xi_s$, and 0 , respectively. The solution grid covers the region from $x/D = 0-25$ and $r/D = 0-10$, where D is the fuel jet diameter ($D = 7.2$ mm). This is considered adequate since the region of interest is

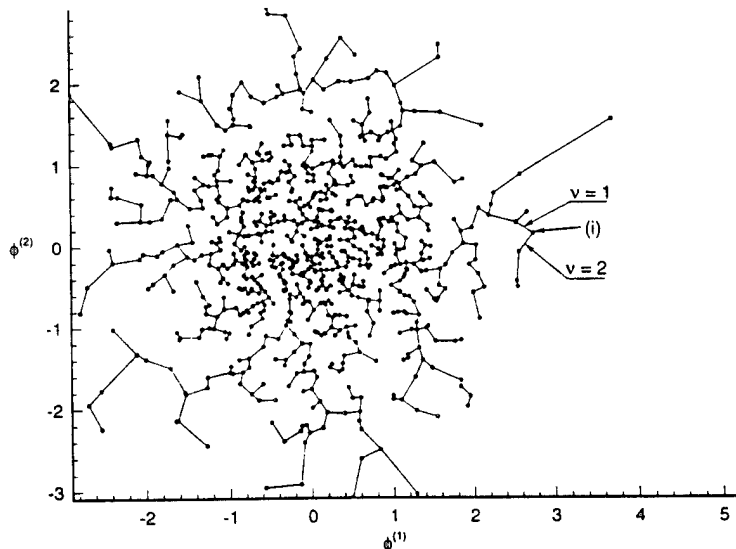


FIG. 2. The EMST formed from 800 particles in a two-dimensional composition space, showing the general particle i that in this case has two edges $v = 1$ and $v = 2$.

TABLE 1

Stoichiometric mixture fraction, ξ_s , X-Y grid size, lean and rich reactive limits, ξ_L and ξ_R , for the flames for which PDF simulations are performed

ξ_s	ξ_L	ξ_R	X-Y Nodes
0.055	0.045	0.185	31×21
0.305	0.225	0.495	31×21
0.5	0.305	0.695	31×21

centered just downstream of the pilot flame "shroud" that generally extends for a few jet diameters. (Before it is completely mixed, the pilot flame provides a shroud in the sense that it physically separates the fuel stream from the airstream.)

Numerical tests were performed to determine the choice of numerical parameters that minimize the computational cost of obtaining converged solutions that are reasonably independent of the grid size and the number of stochastic particles. At each time step, computations are carried out for all the particles in the solution domain. The time step is chosen to be the shortest of the convective, mixing, and reactive timescales. This ensures that these processes are resolved properly. It should be noted that using the same time increment for velocity and scalar mixing is justified for this type of shear flows because of the multistream geometry with different velocities and compositions. The solution is carried out over a long enough time to ensure convergence. With the EMST model, both mixing and reaction are performed simultaneously. This is a considerable advantage over previous approaches where these processes are computed separately.

Computations are performed for the same flame

using three different grid sizes with X-Y nodes: 31×21 , 46×31 , and 61×41 . This corresponds to 600, 1250, and 2400 cells, respectively, with 100 particles in each cell. The computed mean axial velocity, \bar{u} , and mean mixture fraction, $\bar{\xi}$, have been compared for the three grid sizes, and the 31×21 grid is found to be adequate. Computations with the EMST mixing model take about 2.5 times the CPU time required for a similar calculation using the IEM mixing model. Simulations performed with double the number of particles revealed little difference. The 31×21 grid with 100 particles per cell is, therefore, used in all further computations that are performed for three different stoichiometries with the conditions shown in Table 1.

Measurements of the velocity, turbulence, and mixing fields are available only for a piloted flame of methane fuel with $\xi_s = 0.055$. Computations are performed for a flame with the same stoichiometry and the results are then compared with the measurements (not shown here). The agreement is found to be adequate, considering the difference between the simple chemistry used here and that of methane fuel.

Figures 3 and 4 show computed scatter plots of progress variable b versus mixture fraction for two flames with $\xi_s = 0.305$ and 0.5, respectively. The computations are repeated using the IEM and EMST mixing models, and the results are shown in Figs. 3 and 4 for the ranges of $x/D = 0-5$, $5-15$, and $15-25$ of the solution domain. The first range from $x/D = 0-5$ corresponds to the region where the pilot shroud is still separating the fuel from the airstream and is shown in Figs. 3a and 4a. In this range, mixing mainly occurs between the pilot gases and either air or pure fuel. Originally, fluid particles issuing from the pilot stream with composition ($\xi = \xi_s$, $b = 1$), mix either with air ($\xi = 0$, $b = 0$) or with fuel (ξ

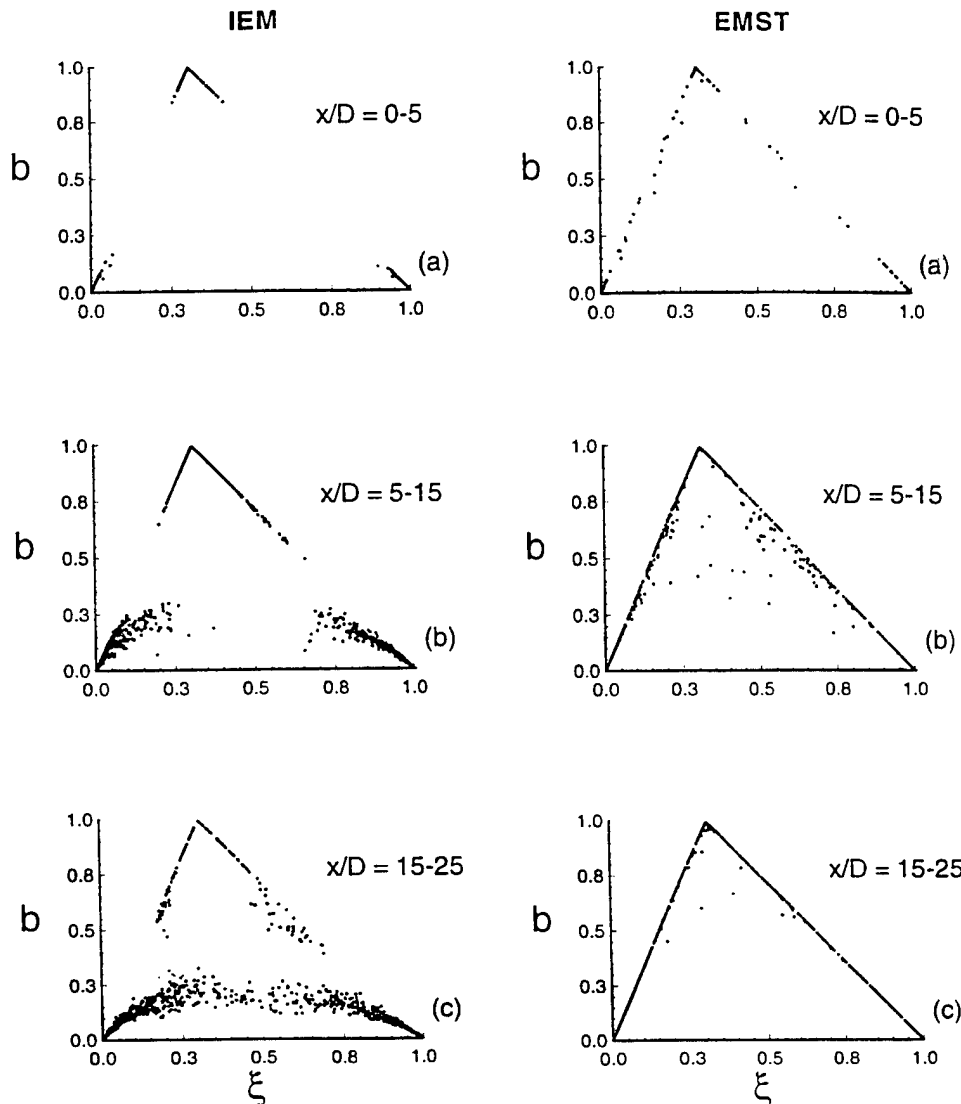


FIG. 3. Computed scatter plots of progress variable b versus mixture fraction ξ for the flame with $\xi_s = 0.305$ using the IEM and EMST mixing models. Each plot covers a specific axial range extending from (a) $x/D = 0-5$; (b) $x/D = 5-15$; (c) $x/D = 15-25$.

$= 1, b = 0$). Resulting particles populate the composition space that joins the following vertices: $(\xi = \xi_s, b = 1)$, $(\xi = 0, b = 0)$, $(\xi = 1, b = 0)$. Figures 3 and 4 show that both the IEM and EMST models give comparable results in this region of the flow. This is expected considering that mixing is done mainly in one-dimensional scalar space where both models perform adequately.

Further downstream of the pilot flame shroud, fluid particles that originated from the pilot, air, and fuel streams may coexist in the same cell and are therefore likely to mix. It is in these regions of the flows that the mixing models are put to the test since two-dimensional mixing is more likely between particles with a range of conserved and reactive scalars.

Figures 3b and 4b show a comparison between the IEM and EMST models for flame with $\xi_s = 0.305$ and 0.5 in the range $x/D = 5-15$. It is clear that the compositions resulting from the IEM model deviate from the fully burned compositions and start to populate the intermediate region. Fully burned compositions are those that lie on the line extending from $(\xi = 0, b = 0)$ to $(\xi = \xi_s, b = 1)$ to $(\xi = 1, b = 0)$. The EMST model results in compositions that remain on the fully burned line regardless of the axial location. It should be noted that identical conditions are used for both the IEM and EMST simulations. The same trend continues further downstream as is shown in Figs. 3c and 4c for the range $x/D = 15-25$. It is also clear that these results

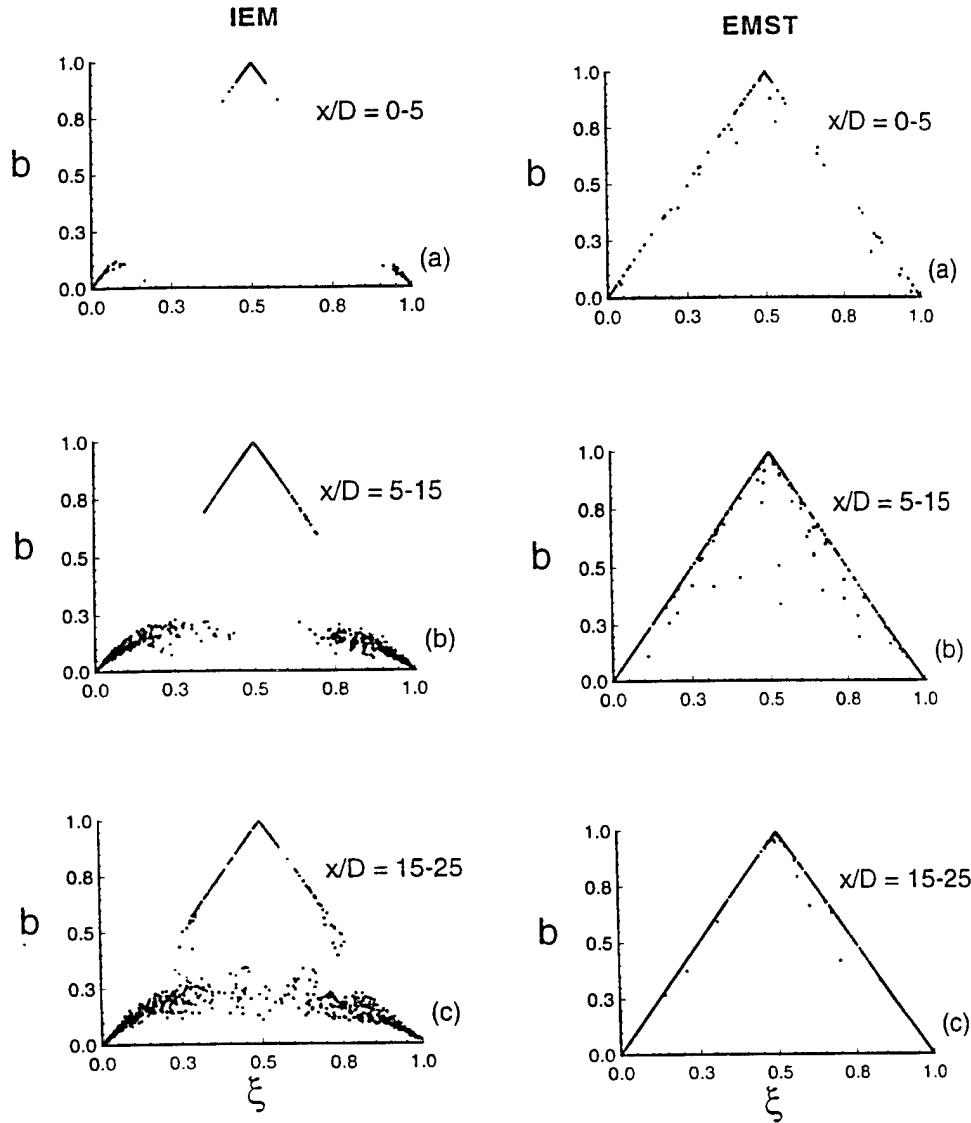


FIG. 4. Computed scatter plots of progress variable b versus mixture fraction ξ for the flame with $\xi_s = 0.5$ using the IEM and EMST mixing models. Each plot covers a specific axial range extending from: (a) $x/D = 0-5$; (b) $x/D = 5-15$; (c) $x/D = 15-25$.

are independent of the stoichiometry of the fuel mixture.

To validate these computations, joint imaging of temperature and mixture fraction has been performed in a pilot-stabilized flame of $H_2/N_2 = 1/1$ (by vol.). The fuel mixture has a stoichiometric mixture fraction of 0.305 and the chemistry is relatively fast. Temperature here may be thought of as a progress variable (b) with a value of 1 when the temperature corresponds to that of fully reacted fluid and a value of 0 when the temperature is that of unreacted fluid at 300 K. Contour plots representing the joint PDF of measured temperature and mixture fraction are shown in Fig. 5 for a range of axial locations in the H_2/N_2 flame. These measurements

should be compared with simulations for the flame with $\xi_s = 0.305$ shown in Figs. 3a and 3b for similar axial locations. It is evident from these plots that the EMST mixing model is showing the correct trend of mixing as opposed to the IEM model, which fills up the entire domain within the fully reactive and frozen limits. Although measurements do not extend further downstream, the trend is expected to be the same since the flames studied here are very far from blow off. It should be noted here that the pilot in the H_2/N_2 flame is shorter than that of the computed flame and extends for only about 3 jet diameters.

The IEM model mixes particles that may be well apart in composition space as long as these particles are in the same cell. This implies that particles with

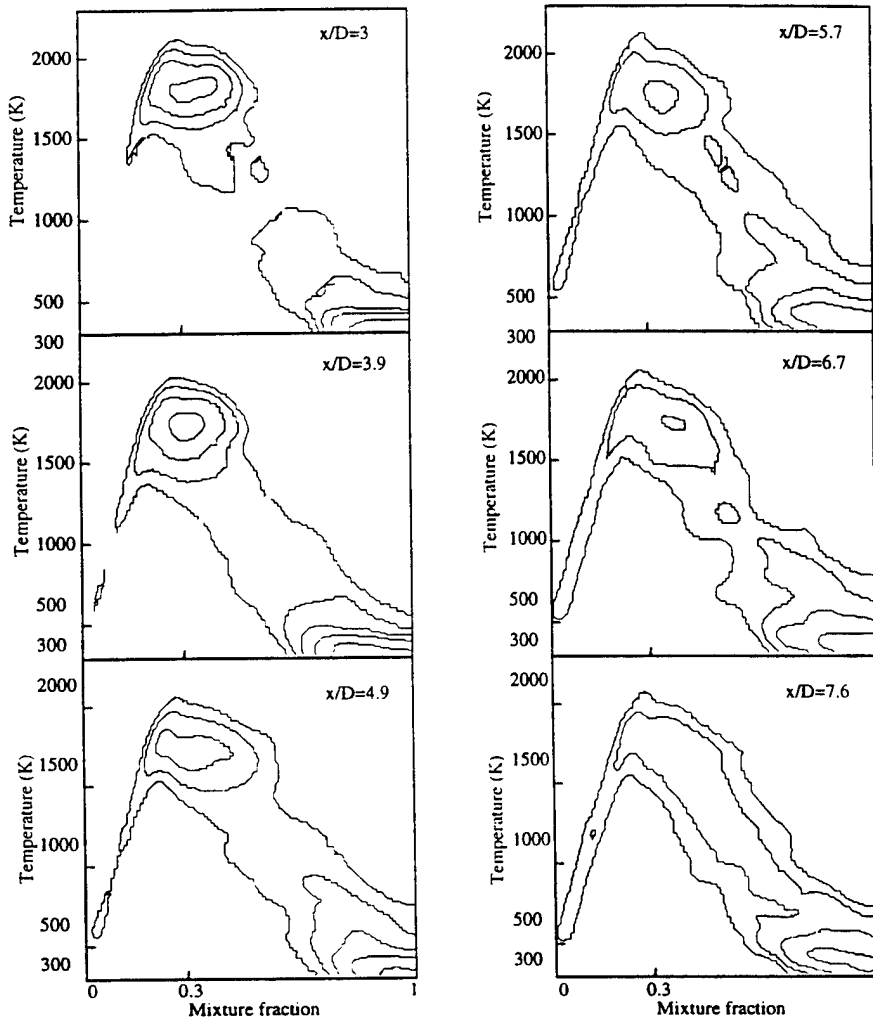


FIG. 5. Contours of the joint PDF of temperature and mixture fraction imaged at various axial locations in a jet flame of H_2/N_2 fuel with $\xi_c = 0.305$. Each image covers a range of 12 mm (1.6 diameters), and the axial location quoted on each plot corresponds to the center of the image.

compositions, say ($\xi = 0.75, b = 0.50$) and ($\xi = 0.15, b = 0.25$) may mix, leading to intermediate compositions that are well away from the fully burned line. With the EMST model, these particles will not mix together but will mix with others that are closer in composition space. It should be noted here that in the hypothetical case of very fast chemistry and very broad reactive limits, particles will be pushed immediately to the fully burned limit because of the fast reactions and the results will be similar regardless of the mixing model. On the other extreme, when three-scalar mixing occurs without reaction, the IEM and EMST models will give different results, especially in the region close to the jet exit plane. This forms an interesting test case that could be used to further validate these mixing models. Imaging experiments applied to a nonreacting, three-stream/three-scalar mixing test case will be very useful in revealing the mixing pattern and fur-

ther validating the multiscalar mixing aspect of the model.

(Previously, Norris and Pope [21] applied PDF methods using the IEM mixing model to pilot-stabilized jet flames close to extinction. In view of the current findings, it is somewhat surprising that their results compare favorably with the experimental data. Although they used a different PDF model and different thermochemistry, it is not clear which specific difference is responsible for the different behavior observed.)

Conclusions

A new code that uses a particle-mesh method to solve the transport equation for the joint PDF of velocity composition and turbulent frequency has been used with a new mixing model based on EMST

and simple, one-step thermochemistry. Comparison with experimental measurements in pilot-stabilized flames demonstrate that the EMST successfully models multiscalar mixing, and, in particular, it overcomes serious defects in IEM and Curl's models arising from their violation of the localness principle.

The success of the EMST model marks a significant advance in the modeling of turbulent combustion with PDF methods. It is well-known that the weak link in this approach lies in the modeling of mixing, and success in this regard brings us closer to the goal of the accurate simulation of complex turbulent reacting flows with detailed chemical kinetics. The extensive computational requirement, however, remains a drawback that is addressed elsewhere [25]. Bluff-body stabilized flames and lifted flames are two cases in which the PDF approach incorporating the EMST mixing model is likely to make a significant impact.

Acknowledgments

Dr. Masri is grateful for the support provided while on sabbatical leave at Cornell University by Prof. Pope. Dr. Masri is also supported by the Australian Research Council. The work at Cornell is supported by Air Force Office of Scientific Research, Grant F49620-94-1-0098. Thanks to Dr. J. B. Kelman and Mr. F. C. Christo for producing some of the figures.

REFERENCES

1. Taing, S., Masri, A. R., and Pope, S. B., *Combust. Flame* 95:133–150 (1993).
2. Curl, R. L., *A I Chem. E J.* 9:175–181 (1963).
3. Pope, S. B., *Combust. Sci. Technol.* 28:131–145 (1982).
4. Norris, A. T. and Pope, S. B., *Combust. Flame* 83:27–42 (1991).
5. Masri, A. R. and Pope, S. B., *Combust. Flame* 81:13–29 (1990).
6. Dopazo, C., *Phys. Fluids* 18:397–404 (1975).

7. Pope, S. B., *Prog. Energy Combust. Sci.* 11:119–192 (1985).
8. Chen, H., Chen, S., and Kraichnan, R. H., *Phys. Rev. Lett.* 63(24):2657–2660 (1989).
9. Pope, S. B., *Theoret. Comput. Fluid Dynamics* 2:255–270 (1991).
10. Valino, L., *Phys. Fluids* 7:144–152 (1995).
11. Gao, F., *Phys. Fluids* 3(5):956–959 (1991).
12. Girimaji, S. S., *Phys. Fluids A* 4:2875–2886 (1992).
13. Kerstein, A. R., *Combust. Sci. Technol.* 60:391–421 (1988).
14. Kerstein, A. R., *Combust. Sci. Technol.* 81:75–96 (1992).
15. Kerstein, A. R., *J. Fluid Mech.* 240:289–313 (1992).
16. Menon, S., Callwoon, W. H., Goldin, G., and Kerstein, A. R., *Twenty-Fifth Symposium (International) on Combustion*, The Combustion Institute, Pittsburgh, 1994, pp. 1125–1131.
17. Subramaniam, S. and Pope, S. B., “Model for Turbulent Mixing Based on Euclidean Minimum Spanning Trees,” (in preparation).
18. Pope, S. B., *Phys. Fluids* 26:404–408 (1983).
19. Pope, S. B., “PDF2DV: A Fortran Code to Solve the Modelled Joint PDF Equations for Two-Dimensional Recirculating Flows,” Unpublished, Cornell University, 1994.
20. Jayesh and Pope, S. B., “Stochastic Model for Turbulent Frequency,” Cornell University Report FDA 95-05, 1995.
21. Norris, A. T. and Pope, S. B., *Combust. Flame* 100:211–220 (1995).
22. Masri, A. R., Dibble, R. W., and Barlow, R. S., *Prog. Energy Combust. Sci.* (in press).
23. Masri, A. R., Dibble, R. W., and Barlow, R. S., *Combust. Flame* 91:285–309 (1992).
24. Subramaniam, S. and Pope, S. B., “Self-Similar Thermochemistry for Turbulent Combustion Studies,” (in preparation).
25. Christo, F. C., Masri, A. R., Nebot, E. M., and Pope, S. B., *Twenty-Sixth Symposium (International) on Combustion*, The Combustion Institute, Pittsburgh, 1996, pp. 43–48.

COMMENTS

J.-Y. Chen, University of California-Berkeley, USA.
Have the authors carried out PDF simulation using modified Curl's mixing which is inexpensive relative to EMST?

Author's Reply. Not in this work, but in an earlier study [1], both Curl's model and the modified Curl model were applied to a zero-dimensional nonpremixed test case. As here, in that study it was demonstrated that these non-local models yield qualitatively incorrect behavior in the fast-chemistry limit.

REFERENCE

1. Norris and Pope, *Combust. Flame* 83:27–42 (1991).

Norberto Fueyo, University of Zaragoza-LITEC, Spain.
My impression is that you are using a rather coarse mesh. For the flames you have simulated, our experience is that, for coarse meshes, the flame does tend to be extinguished, regardless of the mixing model (or even the chemistry model) that one uses. Once the mesh is adequately refined

and a grid-independent solution reached. the problem disappears and then the flame does burn. Have you tested your computations for mesh independence?

Your mixing model seems to do a good job at keeping the reaction going; how does it perform when it comes to predicting extinction?

Author's Reply. We do not agree that extinction here is due to the coarse mesh rather than the mixing model. For the IEM mixing model, the grid was refined from 31×21

to 91×61 and the flame remained extinguished resulting in the same scatter plots as shown in Figs. 3 and 4 of the paper.

The EMST does indeed give a good representation of the mixing and hence it sustains reaction as illustrated in the paper using relatively fast and simple thermochemistry. Predicting extinction requires the implementation of realistic chemistry into the code. This is currently being done and, in conjunction with the EMST, it is expected to give good results.

COMBINED AIR FORCE SCIENTIFIC RESEARCH (AFSC)

Approved and is
190-12

Approved for public release
Distribution unlimited